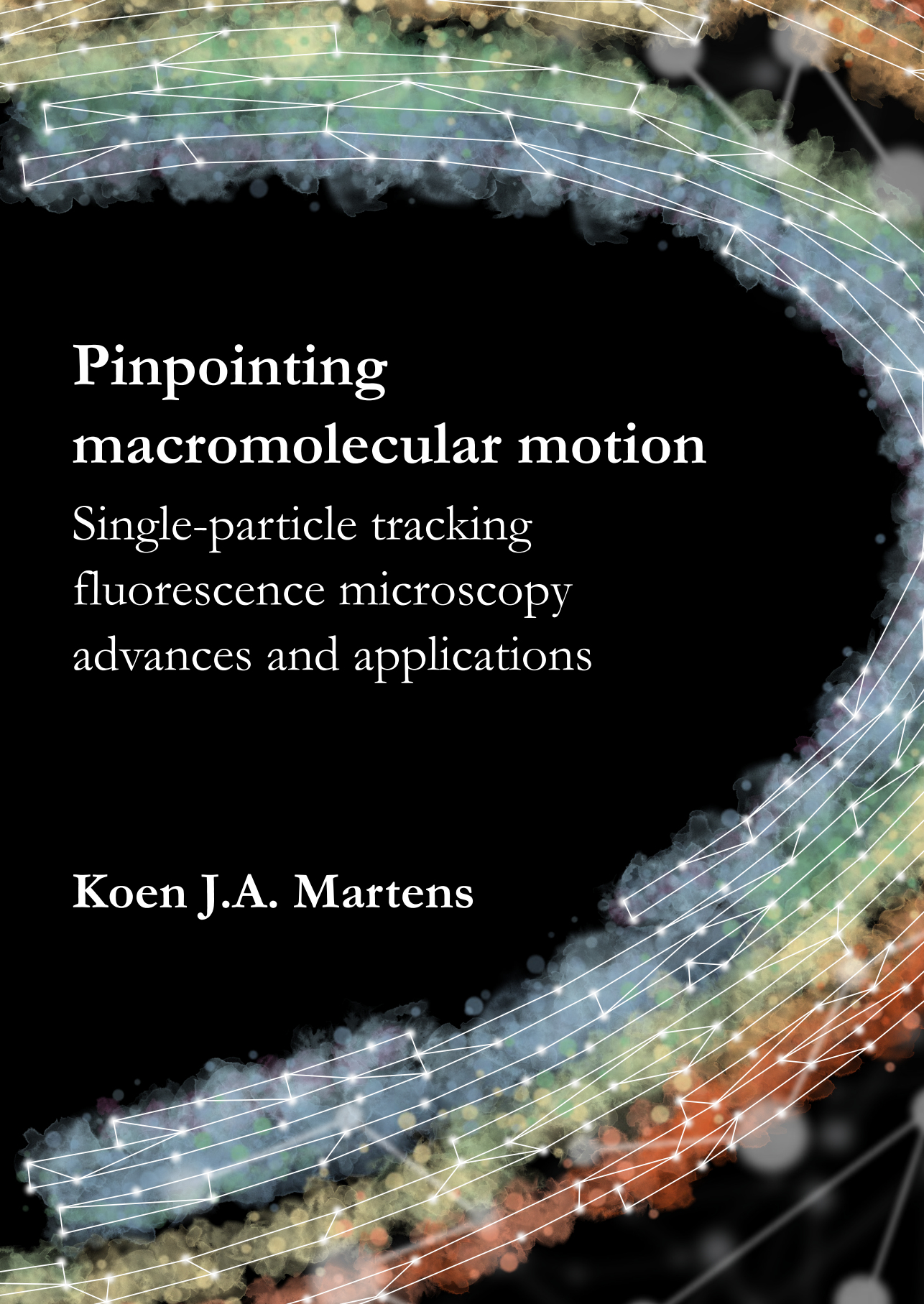

Pinpointing macromolecular motion

Single-particle tracking fluorescence microscopy advances and applications

Koen J.A. Martens

Pinpointing macromolecular motion

Single-particle tracking fluorescence microscopy advances and applications

Koen J.A. Martens

Propositions

1. Temporal resolution is more valuable than spatial resolution in single particle tracking fluorescence microscopy (this thesis).
2. The current spatiotemporal resolution of super-resolution microscopy is not the limiting factor anymore for broad application (this thesis).
3. A citation limit in peer-reviewed journal articles leads to a winner-take-all citation distribution not truly representative of actual value.
4. The differentiation between life and non-life bears no value in modern science.
5. Long-term research planning hinders investigation of unexpected novel scientific discoveries.
6. Virtual scientific conferences are not a satisfactory replacement for physical scientific conferences.
7. Commercialization of news outlets impairs objective reporting.

Propositions belonging to the thesis entitled

"Pinpointing macromolecular motion: single-particle tracking fluorescence microscopy advances and applications"

Koen J.A. Martens
Wageningen, 8 October 2020

Thesis committee

Promotors:
Prof. Dr J.P.M. van Duynhoven
Special professor of Biophysics
Wageningen University & Research

Prof. Dr A.H. Velders
Professor of BioNanoTechnology
Wageningen University & Research

Co-promotor:
Dr J. Hohlbein
Associate professor, Laboratory of Biophysics
Wageningen University & Research

Other members:
Prof. Dr M. Dogterom, Technical University Delft
Dr S. Holden, Newcastle University, United Kingdom
Prof. Dr E. van der Linden, Wageningen University & Research
Prof. Dr N. Loren, RISE Agrifood and Bioscience, Gothenburg, Sweden

This research was conducted under the auspices of the Graduate School VLAG
(Advanced studies in Food Technology, Agrobiotechnology, Nutrition and Health Sciences).

Pinpointing macromolecular motion

Single-particle tracking fluorescence microscopy advances and applications

Koen J.A. Martens

Thesis
submitted in fulfilment of the requirements for the degree of doctor at
Wageningen University
by the authority of the Rector Magnificus
Prof. Dr A.P.J. Mol,
in the presence of the
Thesis Committee appointed by the Academic Board
to be defended in public
on Thursday 8 October 2020
at 11 a.m. in the Aula.

Koen J.A. Martens
Pinpointing macromolecular motion:
single-particle tracking fluorescence microscopy advances and applications
200 pages

PhD thesis, Wageningen University, Wageningen, The Netherlands (2020)
With references, with summary in English and Dutch

ISBN: 978-94-6395-503-4
DOI: 10.18174/529415

Contents

1

Introduction

1

1.1 Macromolecular behaviour in life science and soft matter is governed by diffusion

The biochemical complexity in life is astounding. Individual micrometre-sized cells house millions of proteins[1], as well as genomic information with a physical length orders of magnitude greater than the cell itself[2]. Despite this enormous search space, protein-protein and protein-DNA interactions are specific and efficient enough to allow the cell to proliferate. For example, many prokaryotic cells have an anti-viral defence mechanism called CRISPR-Cas (clustered regularly interspaced short palindromic repeats and their associated proteins), which is burdened with searching and destroying genomic elements belonging to invaders, while leaving the host DNA intact. A single CRISPR-Cas protein is not only able to pinpoint the genomic element belonging to the invader while bypassing the ∼100,000 times more abundant DNA of the host cell, but does this in the timespan of only a few minutes[3].

Likewise in the field of soft matter, complexity can be found on the same spatial scale. Polymer-network gels, model systems for soft matter, show diverse and heterogeneous nanoscopic architectural complexity, affecting many attributes of the material[4,5]. This is directly relevant for their applications in for example food products, pharmaceuticals, and matrices in the analytical sciences. Specifically, in κ-carrageenan hydrogels, which are widely used as a thickener agent in many food products, long chains of monosaccharides form double helices with one other[6]. These helices then further aggregate with the assistance of ions to form a gel that can hold up to hundred times its own weight in water[7].

The crucial building blocks in both these fields are large molecules known as macromolecules, with sizes in the ∼5-100 nm regime. The interactions between macromolecules on the nanoscale are governed by Van der Waals, electrostatic, and hydrophobic/hydrophilic interactions, but the majority of the accessible volume is explored via diffusion, making this the main underlying process leading to macromolecular interactions. As macromolecular diffusion is fundamentally similar in life science and soft matter, techniques focused on characterising this movement can reveal fundamental insights in both of these fields when relating diffusional behaviour to the function of the macromolecule of interest[8,9], or to the surrounding medium[4,10]. Fundamental insights can lead to a bottoms-up understanding of the complexity in life and soft matter, and the revealed knowledge is very valuable for a wide range of applications, such as in the fields of biotechnology and intelligent food design.

1.1.1 Diffusion

Diffusion is an inherent random motion of entities caused by collisions with molecules in the surrounding medium, which themselves are mobile due to heat. The first observation of diffusion was the jittery and random motion of 5 - 6 µm diameter granules by Robert Brown[11,12]. The underlying mechanism based on molecular collisions was proposed by Albert Einstein in one of his four papers published in his *annus mirabilis* 1905, and independently by Sutherland and Smoluchowski, and provided a statistical framework for experimental validation on the existence of molecules[13–15]. Importantly, a mathematical relationship between the particle size and its displacement over time

was proposed by Einstein, Smoluchowski, and Stokes:

$$D = \frac{k_B T}{6\pi\eta r} \tag{1.1}$$

and

$$< r^2 >= 2dD\Delta t \tag{1.2}$$

in which D denotes the diffusion coefficient, k_B Boltzmann's constant, T the temperature, η the solvent viscosity, r the particle radius, $< r^2 >$ the mean-squared displacement, d the dimensionality of the system, and Δt the time interval. Equation 1.1 assumes spherical particles.

1.1.2 Quantification of macromolecular diffusion

Since their conception, equations 1.1 and 1.2 have gained large experimental support. Importantly, it indicates that the diffusive movement of macromolecules in water exceeds their diameter by an order of magnitude or more in the timespan of a millisecond. Characterisation of macromolecular diffusion therefore requires techniques that are capable of both a spatial resolution at ∼10-1000 nm, known as the mesoscale, as well as a temporal resolution in the milliseconds. Moreover, ideally, disturbing of natural processes is prevented, information can be obtained from a small spatial region (e.g. a single cell in life science), molecular selectivity is achieved, quantitative data is obtained, and a lower technological barrier of entry is provided. Whilst this is an extensive list of criteria, they are imperative for fundamental research on the complex dynamic processes in life science and soft matter.

Various methodologies that can reveal (sub-)mesoscale spatial information exist. First, electron microscopy (EM)[16,17] can achieve atomic resolution, although it requires long sampling times, has scarce selectivity, and often invasive sample preparation, making it impossible to study dynamic macromolecular diffusion via EM. Second, small-angle scattering techniques via X-rays[18] (SAXS) or neutrons[19] (SANS) can also provide nanoscale resolution and can perform measurements on a sub-millisecond timescale. However, it requires expensive equipment and has limited specificity combined with substantial spatial averaging, making it challenging to use SAXS/SANS to study natural processes. Last, nuclear magnetic resonance (NMR)[20,21] has various implementations, and contains methodologies that can directly assess the diffusion of (macro)molecules within a sample. While NMR has been used to successfully characterise diffusion in life science and soft matter[20,22], it requires expensive equipment, is subject to substantial spatiotemporal averaging, and poses challenges with introducing specificity, especially in life science.

The ideal combination to study macromolecular diffusion in life science and soft matter, consisting of mesoscale spatial resolution, millisecond temporal resolution, molecular selectivity, non-invasive and non-destructive sample preparation, low spatial averaging, and accessible equipment has not yet been achieved. Optical microscopy is a strong contender to resolve these shortcomings. It inherently has good spatiotemporal resolution, does not require destructive sample preparation, and can be used on a wide range of samples. Furthermore, the technique can be expanded to have molecular selectivity (via fluorescence), to nanometre and millisecond resolution (via super-resolution microscopy techniques), and possibly to considerably more accessible equipment. The advancements required for optical microscopy to fully comply with the demands to study macromolecular diffusion are therefore further explored.

1.2 Optical microscopy

Microscopy has its origin in the Ancient Greek words *mikros* ("small things") and *scopein* ("looking at"). While this is an extremely simple description, it encompasses the desired macromolecular research. One of the most well-known microscopists is the draper Antoni van Leeuwenhoek, who developed the field in a desire to analyse the quality of his cloth. He created single-lens microscopes with magnification powers of 50-250x[23–25], and investigated nearly everything he could place under his microscope, in this way making the first observations of bacteria. His work directly showcases the applicability of optical microscopy both in life- and material sciences.

In its simplest form, a microscope creates a magnified image of a specimen by employing a set of lenses. The specimen can be illuminated with white light, and the transmitted light is then projected on a detector, which can be a human eye or a camera. While this brightfield microscopy allows for good magnification of the specimen, the obtained contrast is determined solely by attenuation of light through the specimen[25]. The contrast is therefore dictated by the sample rather than by the observer: there is no specificity. In the case of ideal specificity, only the (macro)molecules that are of interest to the researcher are visualised, while the rest of the sample remains invisible.

This lack of specificity can be resolved by introducing fluorescent molecules (fluorophores), which can specifically emit light while the rest of the specimen remains dark. Light emission is a consequence of electron energy transitions within molecules. In fluorophores, an external photon can excite an electron from a lower energy level to a higher energy level. This new electron state is unstable, causing it to quickly (ns timescale) 'relax' to the lower energy level, which releases energy from the molecule. This excitation-emission cycle contains some non-radiative processes, leading to a lower emitted energy compared to the excitation energy. A photon of a longer wavelength (more red-shifted) than the excitation photon will be produced, because a photon's wavelength is inversely proportional to its energy ($E = h \cdot c/\lambda$, where E is energy, h the Planck constant, c the speed of light, and λ the wavelength). Moreover, the quantum nature of the electron's energy levels only allows a specified range of excitation photons, leading to specified excitation and emission spectra of fluorophores.

Incorporating fluorescence into microscopy allows the observer to differentiate between structures within a specimen. Some (biological) structures are autofluorescent, but most samples require the introduction of fluorophores, which can be achieved in two possible ways. First, a fluorophore that has a non-specific interaction with part of the sample can be introduced to provide some specificity, although not on the molecular level. Examples of this are molecules that are only fluorescent in a certain local environment such as an apolar medium[26]; or electrostatic attraction between a fluorophore and structures of interest[27]. Second, labelling specific molecules of interest with fluorophores can ensure better specificity. Examples of this are antibody conjugation, in which a fluorophore-labelled antibody with high specificity and affinity for a structure of interest is added to the sample[28]; and in vivo protein fusion, in which a fluorescent protein is genetically fused to a protein of interest, after which this chimera is expressed in living cells[29,30].

1.3 Diffraction limit of microscopy

While fluorescence microscopy solves the specificity problem of optical microscopy, there is a more fundamental limit caused by the wave-nature of light. When photons from a coherent light source are conceived at an infinitesimal point, such as provided by a single molecule, these photons will interfere. In microscopy, this interference results in a pattern called the point spread function (PSF; Figure 1.1a), which can be mathematically described by an Airy disc[25]. The PSF size is dependant on the wavelength of the light λ, as well as the collection angle of the microscope's objective lens α, normally rephrased as the Numerical Aperture (NA):

$$NA = n \cdot sin(0.5 \cdot \alpha) \tag{1.3}$$

in which n is the refractive index of the medium the objective is working in ($\sim$1.52 for immersion oil). The PSF size follows equation 1.4, with the full width at half maximum (FWHM) of the main peak of the PSF being[31]:

$$FWHM_{PSF} \approx \frac{0.59 \cdot \lambda}{NA} \tag{1.4}$$

This equation also indicates that if two molecules are placed close enough together that their respective PSFs overlap substantially, they cannot be individually resolved. This fundamental diffraction limit r has been calculated slightly differently due to conflicting opinions in the required contrast between the maximum and minimum intensities[32,33], but follows equation 1.5:

$$r \approx \frac{[0.5 - 0.61] \cdot \lambda}{NA} \tag{1.5}$$

Due to the fundamental nature of this diffraction limit, it was predicted for centuries that this was an unsolvable, fundamental limit, with no possibility of having far-field optical microscopy with a resolution below $\sim$200 nm. Therefore, the diffraction limit was minimized as much as possible by reducing λ and increasing NA. Smaller wavelengths have been realised by opting for electrons rather than photons - creating electron microscopy (EM)[16]. While EM does indeed substantially increase resolution, it lacks good temporal resolution and can therefore not provide direct feedback on dynamic macromolecular processes[34]. Larger NA has been realised to some extend, with currently $NA \geq 1.40$ being commonplace in fluorescence microscopy, but further increase is restricted by the refractive index of the objective medium (equation 1.3).

1.4 Super-resolution microscopy surpasses the diffraction limit

Despite the aforementioned presumed fundamental resolution limit in microscopy, a few pioneering researchers simultaneously developed optical microscopy methods shattering this limit, culminating in the 2014 Nobel prize in Chemistry[36–39]. The methods developed by the laureates, as well as derived techniques, are collectively known as super-resolution microscopy or nanoscopy[25,40–42]. While they all obtain spatial resolution on the low end of the mesoscale ($\sim$5-100 nm), the underlying methodologies are very diverse. The most striking difference is whether a sub-diffractive excitation profile is used, or whether single fluorescent molecules are individually localized. Both these options are further discussed.

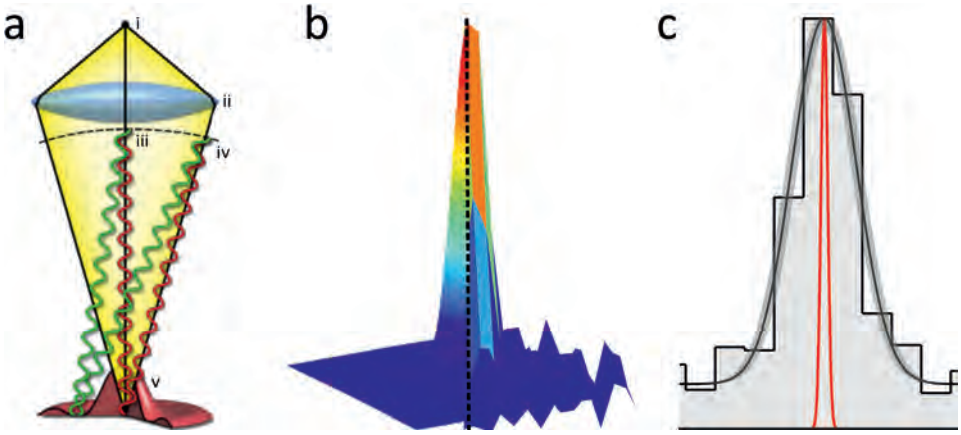

Figure 1.1: Point spread function formation and analysis. **a** Formation of the point spread function (PSF). Photons originating from a point-like source (i) are dispersed by the objective (ii), causing collimated light at different positions (iii, iv) interfering constructively (red) or destructively (green), resulting in a PSF (v). Figure adapted from [35]. **b** The original PSF (left half) when observed on a detector (right half) is noisy and binned in pixels. **c** Fitting of the pixelated information (grey step-wise pattern) is often performed with a Gaussian profile (black curve), which has a certain uncertainty on the fit (dark grey outline). This uncertainty on the fit results in an uncertainty in the position of the emitter (red profile) which is much smaller than the original PSF size.

1.4.1 Microscopy with sub-diffractive excitation profiles

If a sub-diffractive excitation profile is used, only emitters present in this profile are allowed to emit photons, thereby leading to sub-diffraction spatial resolution. First, in stimulated excitation and depletion (STED) microscopy[37,43], a diffraction-limited excitation profile is combined with a doughnut-shaped stimulated depletion profile, which causes non-radiative energy loss of excited fluorophores. The combination of these profiles results in a sub-diffraction limited region where fluorescence is achieved, generally realising spatial resolutions of 20-50 nm[43]. Second, in structured illumination microscopy (SIM), series of structured excitation profiles are used to sub-diffractively illuminate parts of the sample, resulting in ∼100 nm lateral resolution[44].

1.4.2 Single-molecule localization microscopy

Individual localization of single fluorescent molecules is defined by using *on*/*off*-switching of individual fluorophores, while imaging on a typical fluorescence microscope[39,45]. The core concept of these techniques is to elucidate the location of single emitters underlying a single PSF by fitting a mathematical model function to the noisy fluorescence pattern formed on the microscope detector (Figure 1.1b,c). This elucidation of single emitters is called 'localization', defining this technique as single-molecule localization microscopy (SMLM). The procedures for localization will be discussed in detail below. Sufficient (∼2-3 PSF sizes) spatial separation of individual single emitters is a requirement for these approaches, with sample coverage being achieved by temporally changing which emitters are activated.

Briefly, three methodologies have been developed to combine good coverage with non-overlapping emitting patterns. First, in (d)STORM, or (direct) stochastic optical reconstruction microscopy, fluorophores are chosen or designed to create chemical equilibria between a fluorescent and a non-fluorescent version of the fluorophore[45–47]. Normally, *cis*/*trans*-isomerisation, nucleophilic addition/removal, or carbon ring-opening/closing creates or destroys a conjugated system in a fluorophore, allowing energy transitions for excitation and emission in the visible spectrum[48,49]. These fluorophores are conjugated to a structure of interest and turned to their *off*-state, after which many rounds of stochastic activation, localization, and de-activation or bleaching occur. Over time, most fluorophores will have been activated, without having multiple active fluorophores closer together than the diffraction limit. This approach will result in super-resolved imaging of the structure of interest with good coverage[28,42,45,46,50,51].

Second, in (F)PALM ((fluorescence) photo-activation localization microscopy) a very similar concept as STORM is used, but the *on*/*off*-transition stems from a photo-induced chemical transition. Importantly, photo-activatable fluorescent proteins allow PALM to be used for in vivo super-resolution[3,29,30,39,52].

Last, in PAINT (points accumulation for imaging in nanoscale topography), the *on*/*off*-switching is achieved by individual fluorophores changing between diffusive and selectively bound states. Diffusing fluorophores will move enough during acquisition of a single frame to cause a blur rather than a well-formed PSF, and will consecutively be excluded from localization[53,54]. Selectively bound fluorophores, on the other hand, are spatially stable for (the majority of) single frame acquisitions, and thus procure PSFs which can be localized. The most-commonly used method to induce the selective, non-convalent, temporary binding of individual molecules is via DNA complementarity (DNA-PAINT)[53–55].

All SMLM techniques have a resolution limit dictated by the localization precision of the individual fluorophores. Importantly, the lateral localization accuracy $\sigma_{x,y}$ is inversely proportional to the square root of the number of photons emitted by the molecule, leading to the development of fluorophores with higher and higher photon budget[56,57]. With the fluorophores frequently used in SMLM, it is possible to obtain localization accuracies of ∼10-40 nm[31,42,58–60].

Recently, the concepts of sub-diffractive excitation profiles and SMLM have been united in MINFLUX (minimal photon fluxes microscopy) and further derived techniques such as SIMFLUX and ROSE (repetitive optical selective exposure)[61–64]. MINFLUX combines an excitation doughnut profile with single activated fluorophores, with the general principle that this emitter emits zero photons only when being in the exact centre of the profile. By slightly moving the excitation doughnut around the single emitter, an accurate localization can be procured while minimally depleting the photon budget of the emitter. SIMFLUX and ROSE combine spatial information of SIM-like illumination with single-molecule localization methodologies, in this manner increasing the spatial resolution further than either individual technique can realise. These techniques provide good spatiotemporal resolution but are challenging to assemble, and thus limit accessibility of this technique to expert laboratories.

Of the mentioned super-resolution techniques, SMLM is capable of effectively probing the desired millisecond and mesoscale spatiotemporal regime, whilst remaining accessible for a broad

user base in terms of instrumental complexity and costs, and is therefore further used throughout this thesis.

1.5 Single-molecule localization microscopy hardware and software

In SMLM, an inverse epi-fluorescence microscope is typically used (Figure 1.2a,b). Briefly, a laser, producing monochromatic light with defined wavelength, is collimated to procure a parallel light beam. This beam is then focussed via a doublet lens on the back focal plane of a high NA ($\gtrapprox 1.4$), high magnification (60x or 100x) objective. Focused light in the centre of the back focal plane of an objective realises a parallel beam as output. Importantly, the excitation light crosses a dichroic mirror before entering the objective. This ensures that emission light from the specimen (which by definition has a longer wavelength than the excitation light) can be directed towards the emission pathway of the microscope. The emission pathway simply consists of a tube lens which focuses the obtained emission light on an EMCCD (electron-multiplied charge-coupled device) or sCMOS (scientific complementary metal–oxide–semiconductor) camera for image formation.

This basic design can be expanded where desirable. In the excitation path, moving the entry location of focused light out-of-centre on the back focal plane will lead to a slanted beam coming out of the objective. A slanted beam will create highly inclined illumination (HiLo) or total internal reflection (TIR) microscopy, which will lead to a decreased axial penetration depth ($\sim$µm range for HiLo, $\sim$100s of nm for TIR). In turn, this increases the obtained signal-to-noise ratio by removing background fluorescence and enhancing the electric field intensity[65,66]. Optical filters can be introduced in the emission path. Moreover, cylindrical lenses or more advanced optical components such as phase masks or deformable mirrors can be introduced to obtain axial-position dependant deformations of PSFs, which allows for 3-dimensional SMLM[50,51,67–71].

Data acquisition consists of capturing camera frames while the sample is excited. Important parameters that can be altered are camera frame time, laser excitation duration, and excitation laser power. Frame time is normally in the range of 1 to 100 ms, limited on the low end by hardware limitations, and limited on the high end by a too high density of molecules in the *on*-state, and thus depends on the specific experiment. The laser excitation duration is either as long as the full frametime, or shorter than the full frame to reduce blurring artefacts[72]. The excitation laser power influences the obtained signal-to-noise ratio of single PSFs, as well as certain photophysical characterisations of the single emitters such as bleaching time and blinking behaviour[47]. Recording a series of many frames (i.e. a movie) then realises the possibility of temporal separation of spatially overlapping PSFs. Because of this, imaging experiments require immobile samples, otherwise excessive motion blur would render the obtained image useless. Optimising these data acquisition parameters is key in obtaining good SMLM data, and is equally important as sample preparation.

1.6 Data analysis of single-molecule localization microscopy

Principally, analysis of SMLM data is performed in 3 steps: molecule identification, sub-pixel localization, and data interpretation (Figure 1.2c). Molecule identification is a collection of methods that pinpoint where a PSF is likely present. Generally, this is done via image filtering techniques,

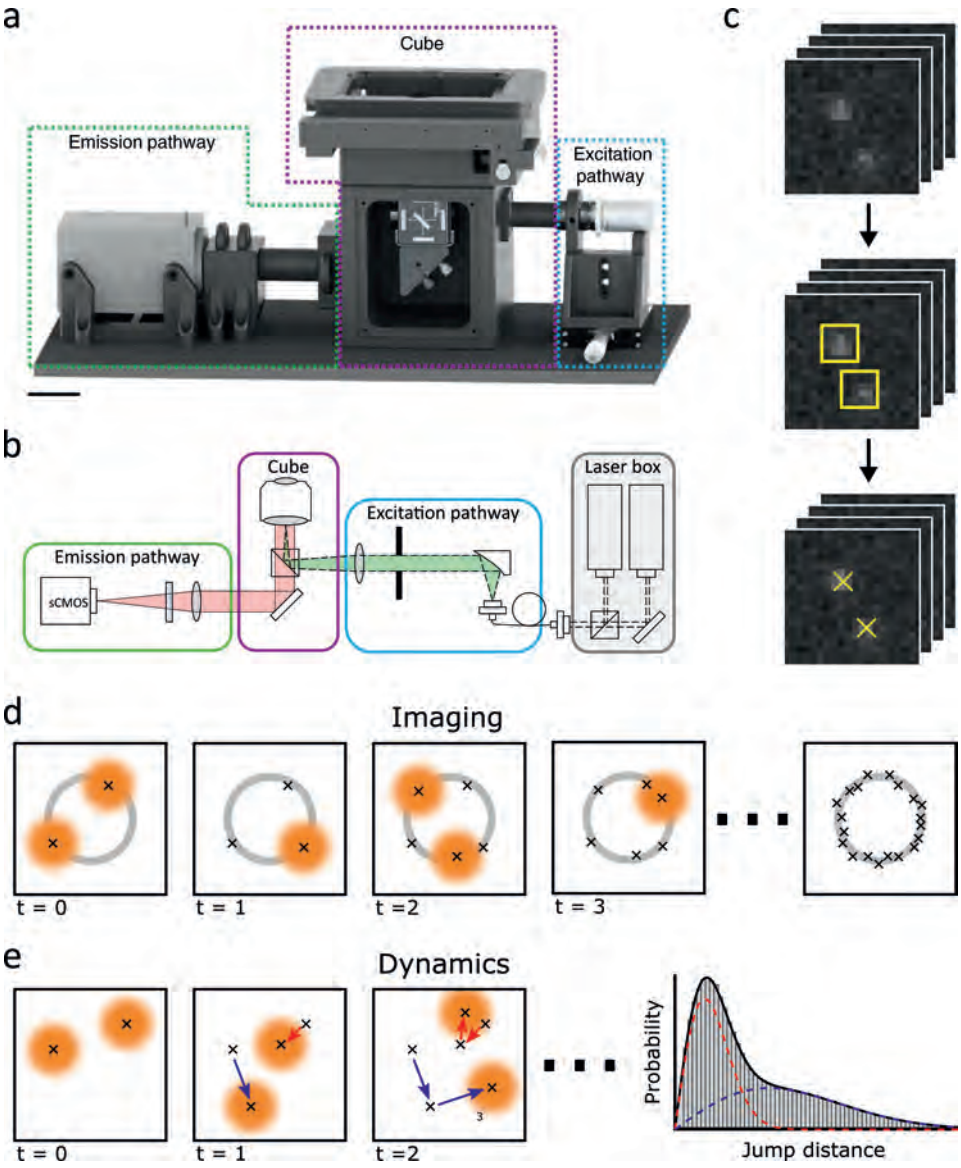

Figure 1.2: Hardware and software underlying single-molecule localization microscopy (SMLM) **a** Example of an inverted fluorescence microscope capable of SMLM: the miCube[3]. Scale bar represents 5 cm. **b** Optical path corresponding to the microscope shown in a. The excitation light originating in the laser box is adjusted in the excitation path (cyan) and focused on the back focal plane of an objective via an aperture and doublet lens. *(Continued on next page)*

Figure 1.2 ***(previous page)*****:** In the cube (magenta), the excitation light is directed via a dichroic mirror to the objective. Emission light originating from the sample (not depicted) is collected by the objective, and directed towards the emission pathway (green). It is focused via a tube lens to a detector (sCMOS). **c** Raw data analysis. Top: a section (∼2.5 x 2.5 µm) of a typical raw frame. Middle: PSF identification. Bottom: sub-pixel localization of individual PSFs. See the text for more details. **d** Typical SMLM imaging procedure. An unknown structure (grey circle) with many blinking fluorophores (orange profiles) is imaged over many time points, and the PSFs of the individual fluorophores are localized (black crosses). Taken together, the localizations reveal the underlying structure. **e** Typical single-particle tracking procedure. Individual molecules are followed over multiple frames. Their PSFs (orange profile) are localized (black crosses) and linked together (blue/red arrows). The jump distances (JD) originating from these linked particles are then analysed via for example a jump distance histogram (right). The histogram is fitted with equation 1.10 to reveal the diffusive states of the original particles (red and blue profiles).

where the background noise is suppressed, while potential PSFs are accentuated, followed by a local maxima finder[73,74].

After outlining the position of PSFs, more accurate localization is performed in the sub-pixel localization step. Regions of interest (ROIs) positioned around the found local maxima are analysed with a mathematical equation to obtain the centre of the PSF with sub-pixel accuracy. Historically, this has been done by fitting a 2-dimensional Gaussian profile, as the central lobe of a PSF is Gaussian-shaped. In the fitting procedure, the error of the Gaussian profile is estimated either via least-squares error estimation (LS) or via maximum likelihood estimation (MLE). This fitting is repeated with different parameters until a best fit is obtained.

The accuracy of the sub-pixel fitting depends on the experimental procedure, as well as on the fitting algorithm. A fundamental limit on the localization accuracy on all fitting routines is given by the Cramer-Rao lower bound (CRLB)[59,75]. Most modern algorithms are capable of nearing the CRLB, with a maximum likelihood estimator (MLE) fitting procedure with Gaussian profiles reaching this first[8,50,58,59,76]. The CRLB of 2-dimensional, in-focus PSFs can be analytically described by[58,59]:

$$\Delta x = \sqrt{\frac{\sigma^2 + a^2/12}{N}(1 + 4\tau + \sqrt{\frac{2\tau}{1+4\tau}})} \tag{1.6}$$

with

$$\tau = \frac{2\pi b(\sigma^2 + a^2/12)}{Na^2} \tag{1.7}$$

in which Δx is 1-dimensional localization accuracy, σ the PSF width, a the pixel size, N the signal photon count, and b the number of background photons per pixel. While localization often falls short of reaching the CRLB, either due to non-optimal localization settings, inhomogeneous background, or overlapping signals, equation 1.6 still provides excellent optimization strategies for localization accuracy. Most importantly, the accuracy scales proportional to the square root of the photon number N. Next, there is an optimum in pixel size a, depending on PSF width σ (which depends on emission wavelength λ (equation 1.4)). A minimum for a can be found analytically, and for typical settings in SMLM, a value of $a \approx$ 100-130 nm is optimal[76]. Last, an increased signal-to-noise ratio (i.e. decreased b) intuitively also leads to a better localization precision. A higher

signal-to-noise ratio can be realised experimentally by using HiLo or TIR illumination, removing (auto-)fluorescence from the sample[65], or computationally by applying temporal median filters, to accurately determine and subtract the background level of every pixel[77].

The obtained list of localizations can now be used for further data interpretation. While this step is very experiment dependant, the first step of data interpretation generally falls in one of two categories (Figure 1.2d,e): image generation, or single-particle tracking (spt; combined with fluorescence microscopy forming sptFM). Studies that create images from single-molecule data normally do so to visualise and quantify structures, such as microtubules[28,50], nuclear pore complexes[78] and synthetic materials[79].

To combine mesoscale spatial resolution with millisecond temporal resolution, spt can be used, in which a single emitter is free to move around either by itself or bound to an object of interest such as proteins[8,30,68,80,81]. This movement is then quantified and analysed further. Spt is often combined with PALM if it is employed in vivo[30], providing an excellent combination of non-overlapping single PSFs, high intracellular copy numbers of the protein of interest, and molecular specificity.

1.7 Single-particle tracking analysis of diffusion

Obtained localizations in an spt experiment are collected into separate tracks by linking localizations in consecutive frames, often limited by a maximum possible displacement between frames (Figure 1.2e). Interpretation of single-particle tracks for diffusion-based experiments is based on equation 1.2. Computationally, this can be achieved by calculating the step-wise displacement for every step of every frame, after which these displacements are binned. This procedure results in a so-called jump distance histogram.

To obtain confidence in the value of the diffusion coefficient of single populations, the jumping distance histogram obtained from many individual molecules should be compared to a theoretical distribution. The corresponding cumulative probability distribution function (CDF) is based on equation 1.2 and on Fick's second law of diffusion[82], and follows[83]:

$$P(r^2, \Delta t) = 1 - e^{-\frac{r^2}{4D\Delta t}} \tag{1.8}$$

in which r^2 indicates 2-dimensional displacement. The stochastic and random nature of diffusion, leading to the broadness of the populations (Figure 1.2e), indicates that recording of sufficient tracks (ideally > 10.000) is needed to obtain reliable results in spt(PALM) experiments[9,84]. Equation 1.8 can be expanded to facilitate multiple populations as follows:

$$P(r^2, \Delta t) = 1 - \sum_{i=1}^{j} f_i e^{-\frac{r^2}{4D\Delta t}} \tag{1.9}$$

in which i represents one of the j multiple populations, each with fraction f_i. For incorporation in single-particle tracking experiments, equation 1.8 is changed to a probability distribution function, and altered for the influence of statistical dependence within single tracks and for a localization uncertainty (equation 1.6)[3,52,85,86]:

$$P(r^2, \Delta t, n) = \frac{(\frac{n}{D+\sigma^2/\Delta t})^n \cdot (r^2)^{n-1} \cdot e^{-\frac{n \cdot r^2}{D+\sigma^2/\Delta t}}}{(n-1)!} \tag{1.10}$$

in which n is the length of individual tracks, and σ is the localization uncertainty. Equation 1.10 can be used to precisely extract apparent diffusion coefficient data from experimental data (Figure 1.2e).

Importantly, jump distance histograms are not capable of extracting state transitions. If a particle can occasionally transition between a slow-diffusive and a fast-diffusive state, jump distance histograms provide information on either state without information on the transition rate. If the transitions are fast (i.e. on the same time scale as the frame time), jump distance histograms will fail to work correctly as these will provide an 'intermediate' diffusion coefficient[3,52]. This limitation currently bounds the temporal resolution by the camera frame time.

1.8 Aim and outline of this thesis

Single-molecule localization microscopy combined with single-particle tracking has the prospect of being a strong framework to study macromolecular diffusion and interactions in the mesoscale and millisecond spatiotemporal regime. However, the spatiotemporal limit of SMLM has not yet been reached, and an increase in this respect would allow possible further fundamental research in life science and soft matter. Moreover, SMLM is only seldom used by non-experts in microscopy, due to a high barrier of entry with respect to required experimental expertise, hardware, and computational power. The aim of this thesis is therefore to increase the spatiotemporal resolution and accessibility of SMLM/sptFM and to provide insights in its ability to study macromolecular interactions in life science and soft matter.

In this thesis, methodological improvements are described to better approach quantification of macromolecular diffusion, both in microscopy hardware and in the downstream data analysis. These improvements have a focus on increasing the accessibility of SMLM/sptFM, and to increase the full potential and wide-spread use of the techniques. With these methodological improvements, the diffusion of macromolecules in relation to their interactions was investigated.

A novel single-molecule localization algorithm is introduced (**Chapter 2**) and expanded upon (**Chapter 3**). The localization of PSFs is performed via a Fourier-transform based phasor approach (phasor-based single-molecule localization microscopy or pSMLM). This method drastically improves localization rates ($\sim$3 orders of magnitude) on a CPU-based system, while retaining excellent localization accuracies. Furthermore, pSMLM is expanded to perform axial localization of PSFs that are shaped by astigmatic, double-helix, saddle-point, or tetra-pod optical pathways. The algorithms are incorporated in multiple software packages, which are described and quantitatively tested against other state-of-the-art software.

Chapter 4 expands the ability of SMLM to allow for spectral discrimination with minimal losses in the achievable accuracy and density. To create this, a simple and low-dispersion grating ensemble is added to a microscope, which causes a single-molecule spectral pattern to appear alongside the original PSF on the camera. By performing sub-pixel fitting routines on the PSF and the corresponding spectral pattern, $\sim$20 nm spectral resolution, alongside $\sim$20 nm spatial resolution, can be achieved, with minimal compromises to single-molecule density and camera field of view.

In **Chapter 5**, a biological system is described in which single-particle tracking photoactivation localization microscopy (sptPALM) of inactivated ('dead') Cas9 is realised. The food-

related lactic acid producing *L. lactis* is genetically modified to house a dCas9 fused to different (photo-activatable) fluorescent proteins. Induction and photo-activation of the chimeras is described. For the first time, photo-activatable fluorescent proteins are shown to be functional in *L. lactis*. Moreover, single-particle tracking of dCas9-PAmCherry2 is performed and quantified to reveal multi-state behaviour of dCas9 in vivo.

Chapter 6 continues the single-particle tracking of dCas9-PAmCherry2 in *L. lactis*, combined with a description of the modular and accessible single-molecule microscope 'miCube'. The dynamics of dCas9 PAM screening are investigated with a novel diffusional state analysis technique, termed Monte-Carlo Diffusion Distribution Analysis, or MC-DDA. It is found that dCas9 transitions from freely diffusing to PAM screening with a rate of $\sim$40 s^{-1}, while the reverse has a rate of $\sim$60 s^{-1}. Furthermore, target-bound properties of dCas9 are investigated, which show that dCas9 will, on average, be removed from plasmid DNA after $\sim$100 minutes, possibly due to hindrance of the DNA replication machinery.

In **Chapter 7**, sptFM is employed to quantitatively characterise the spatial heterogeneity of κ-carrageenan hydrogels. This hydrogel is routinely used to provide structure to a wide variety of food and healthcare products. The average fibre diameter of κ-carrageenan strands in the bulk network is found to be $\sim$3.2 nm, in agreement with other techniques. Moreover, spatial mapping of dense network structures of $\sim$1 µm diameter is performed, and it is shown that these dense networks are mobile on the seconds-to-minutes timescale.

In **Chapter 8** a general discussion on the findings presented in this thesis is provided.

References

1. Ho, B., Baryshnikova, A. & Brown, G. W. Unification of Protein Abundance Datasets Yields a Quantitative Saccharomyces Cerevisiae Proteome. *Cell Systems* **6,** 192–205.e3 (2018).
2. Blattner, F. R., Plunkett, G., Bloch, C. A., *et al.* The Complete Genome Sequence of Escherichia Coli K-12. *Science* **277,** 1453–1462 (1997).
3. Martens, K. J. A., van Beljouw, S. P. B., van der Els, S., *et al.* Visualisation of dCas9 Target Search in Vivo Using an Open-Microscopy Framework. *Nature Communications* **10,** 3552 (2019).
4. Saalwächter, K. & Seiffert, S. Dynamics-Based Assessment of Nanoscopic Polymer-Network Mesh Structures and Their Defects. *Soft Matter* **14,** 1976–1991 (2018).
5. Lorenzo, F. D. & Seiffert, S. Nanostructural Heterogeneity in Polymer Networks and Gels. *Polymer Chemistry* **6,** 5515–5528 (2015).
6. Morris, E. R., Rees, D. A. & Robinson, G. Cation-Specific Aggregation of Carrageenan Helices: Domain Model of Polymer Gel Structure. *Journal of Molecular Biology* **138,** 349–362 (1980).
7. Martens, K., van Duynhoven, J. & Hohlbein, J. Spatiotemporal Heterogeneity of κ-Carrageenan Gels Investigated via Single-Particle-Tracking Fluorescence Microscopy. *Langmuir* (2020).
8. Shen, H., Tauzin, L. J., Baiyasi, R., *et al.* Single Particle Tracking: From Theory to Biophysical Applications. *Chemical Reviews* **117,** 7331–7376 (2017).
9. Kapanidis, A. N., Uphoff, S. & Stracy, M. Understanding Protein Mobility in Bacteria by Tracking Single Molecules. *Journal of Molecular Biology. Plasticity of Multi-Protein Complexes* **430,** 4443–4455 (2018).
10. de Kort, D. W., van Duynhoven, J. P. M., Van As, H., *et al.* Nanoparticle Diffusometry for Quantitative Assessment of Submicron Structure in Food Biopolymer Networks. *Trends in Food Science & Technology* **42,** 13–26 (2015).
11. Brown, R. XXVII. A Brief Account of Microscopical Observations Made in the Months of June, July and August 1827, on the Particles Contained in the Pollen of Plants; and on the General Existence of Active Molecules in Organic and Inorganic Bodies. *The Philosophical Magazine* **4,** 161–173 (1828).
12. Mehrer, H. & Stolwijk, N. A. Heroes and Highlights in the History of Diffusion. *Diffusion Fundamentals* **11,** 1–32 (2009).
13. Einstein, A. Über Die von Der Molekularkinetischen Theorie Der Wärme Geforderte Bewegung von in Ruhenden Flüssigkeiten Suspendierten Teilchen. *Annalen der physik* **322,** 549–560 (1905).
14. Von Smoluchowski, M. Zur Kinetischen Theorie Der Brownschen Molekularbewegung Und Der Suspensionen. *Annalen der Physik* **326,** 756–780 (1906).
15. Sutherland, W. LXXV. *A Dynamical Theory of Diffusion for Non-Electrolytes and the Molecular Mass of Albumin. The London, Edinburgh, and Dublin Philosophical Magazine and Journal of Science* **9,** 781–785 (1905).
16. Bozzola, J. J. & Russell, L. D. *Electron Microscopy: Principles and Techniques for Biologists* (Jones & Bartlett Learning, 1999).
17. Hermansson, A. .-M., Eriksson, E. & Jordansson, E. Effects of Potassium, Sodium and Calcium on the Microstructure and Rheological Behaviour of Kappa-Carrageenan Gels. *Carbohydrate Polymers* **16,** 297–320 (1991).
18. Hura, G. L., Menon, A. L., Hammel, M., *et al.* Robust, High-Throughput Solution Structural Analyses by Small Angle X-Ray Scattering (SAXS). *Nature Methods* **6,** 606–612 (2009).
19. Hammouda, B. SANS from Polymers—Review of the Recent Literature. *Polymer Reviews* **50,** 14–39 (2010).
20. de Kort, D. W., Schuster, E., Hoeben, F. J., *et al.* Heterogeneity of Network Structures and Water Dynamics in κ-Carrageenan Gels Probed by Nanoparticle Diffusometry. *Langmuir* **34,** 11110–11120 (2018).
21. Tyszka, J. M., Fraser, S. E. & Jacobs, R. E. Magnetic Resonance Microscopy: Recent Advances and Applications. *Current Opinion in Biotechnology. Analytical Biotechnology* **16,** 93–99 (2005).
22. Caizán-Juanarena, L., Krug, J. R., Vergeldt, F. J., *et al.* 3D Biofilm Visualization and Quantification on Granular Bioanodes with Magnetic Resonance Imaging. *Water Research* **167,** 115059 (2019).
23. Leeuwenhoek van, A. Letter No. 26 (1679).
24. Gest, H. The Discovery of Microorganisms by Robert Hooke and Antoni van Leeuwenhoek, Fellows of The Royal Society. *Notes and Records of the Royal Society of London* **58,** 187–201 (2004).
25. Vangindertael, J., Camacho, R., Sempels, W., *et al.* An Introduction to Optical Super-Resolution Microscopy for the Adventurous Biologist. *Methods and applications in fluorescence* **6,** 022003 (2018).
26. Greenspan, P. & Fowler, S. D. Spectrofluorometric Studies of the Lipid Probe, Nile Red. *Journal of lipid research* **26,** 781–789 (1985).
27. Zhang, Z., Yomo, D. & Gradinaru, C. Choosing the Right Fluorophore for Single-Molecule Fluorescence Studies in a Lipid Environment. *Biochimica et Biophysica Acta (BBA) - Biomembranes* **1859,** 1242–1253 (2017).

28. Jimenez, A., Friedl, K. & Leterrier, C. About Samples, Giving Examples: Optimized Single Molecule Localization Microscopy. *Methods* (2019).
29. Van Beljouw, S. P. B., van der Els, S., Martens, K. J. A., *et al.* Evaluating Single-Particle Tracking by Photo-Activation Localization Microscopy (sptPALM) in Lactococcus Lactis. *Physical Biology* **16** (2019).
30. Manley, S., Gillette, J. M., Patterson, G. H., *et al.* High-Density Mapping of Single-Molecule Trajectories with Photoactivated Localization Microscopy. *Nature Methods* **5,** 155–157 (2008).
31. Stallinga, S. & Rieger, B. Accuracy of the Gaussian Point Spread Function Model in 2D Localization Microscopy. *Optics express* **18,** 24461–24476 (2010).
32. Abbe, E. Beiträge Zur Theorie Des Mikroskops Und Der Mikroskopischen Wahrnehmung. *Archiv für mikroskopische Anatomie* **9,** 413–418 (1873).
33. Rayleigh, L. XV. On the Theory of Optical Images, with Special Reference to the Microscope. *The London, Edinburgh, and Dublin Philosophical Magazine and Journal of Science* **42,** 167–195 (1896).
34. Hauser, M., Wojcik, M., Kim, D., *et al.* Correlative Super-Resolution Microscopy: New Dimensions and New Opportunities. *Chemical Reviews* **117,** 7428–7456 (2017).
35. *The Diffraction Barrier in Optical Microscopy* https://www.microscopyu.com/techniques/super-resolution/the-diffraction-barrier-in-optical-microscopy.
36. Betzig, E., Hell, S. & Moerner, W. *The Nobel Prize in Chemistry 2014* https://www.nobelprize.org/prizes/chemistry/2014/summary/.
37. Hell, S. W. & Wichmann, J. Breaking the Diffraction Resolution Limit by Stimulated Emission: Stimulated-Emission-Depletion Fluorescence Microscopy. *Optics letters* **19,** 780–782 (1994).
38. Dickson, R. M., Cubitt, A. B., Tsien, R. Y., *et al.* On/off Blinking and Switching Behaviour of Single Molecules of Green Fluorescent Protein. *Nature* **388,** 355 (1997).
39. Betzig, E., Patterson, G. H., Sougrat, R., *et al.* Imaging Intracellular Fluorescent Proteins at Nanometer Resolution. *Science* **313,** 1642–1645 (2006).
40. Schermelleh, L., Ferrand, A., Huser, T., *et al.* Super-Resolution Microscopy Demystified. *Nature Cell Biology* **21,** 72 (2019).
41. Heilemann, M. Fluorescence Microscopy beyond the Diffraction Limit. *Journal of Biotechnology. BioImaging - Contributions from Biology, Physics and Informatics* **149,** 243–251 (2010).
42. Patterson, G., Davidson, M., Manley, S., *et al.* Superresolution Imaging Using Single-Molecule Localization. *Annual Review of Physical Chemistry* **61,** 345–367 (2010).
43. Hell, S. W. Toward Fluorescence Nanoscopy. *Nature biotechnology* **21,** 1347 (2003).
44. Gustafsson, M. G. Surpassing the Lateral Resolution Limit by a Factor of Two Using Structured Illumination Microscopy. *Journal of microscopy* **198,** 82–87 (2000).
45. Rust, M. J., Bates, M. & Zhuang, X. Sub-Diffraction-Limit Imaging by Stochastic Optical Reconstruction Microscopy (STORM). *Nature methods* **3,** 793 (2006).
46. Heilemann, M., van de Linde, S., Schüttpelz, M., *et al.* Subdiffraction-Resolution Fluorescence Imaging with Conventional Fluorescent Probes. *Angewandte Chemie International Edition* **47,** 6172–6176 (2008).
47. Lin, Y., Long, J. J., Huang, F., *et al.* Quantifying and Optimizing Single-Molecule Switching Nanoscopy at High Speeds. *PLOS ONE* **10,** e0128135 (2015).
48. Heilemann, M., Margeat, E., Kasper, R., *et al.* Carbocyanine Dyes as Efficient Reversible Single-Molecule Optical Switch. *Journal of the American Chemical Society* **127,** 3801–3806 (2005).
49. Li, H. & Vaughan, J. C. Switchable Fluorophores for Single-Molecule Localization Microscopy. *Chemical reviews* **118,** 9412–9454 (2018).
50. Martens, K. J. A., Bader, A. N., Baas, S., *et al.* Phasor Based Single-Molecule Localization Microscopy in 3D (pSMLM-3D): An Algorithm for MHz Localization Rates Using Standard CPUs. *The Journal of Chemical Physics* **148,** 123311 (2018).
51. Martens, K. J. A., Jabermoradi, A., Yang, S., *et al.* Integrating Engineered Point Spread Functions into the Phasor-Based Single-Molecule Localization Microscopy Framework. *In preparation* (2020).
52. Vink, J. N. A., Martens, K. J. A., Vlot, M., *et al.* Direct Visualization of Native CRISPR Target Search in Live Bacteria Reveals Cascade DNA Surveillance Mechanism. *Molecular Cell* **77,** 39–50.e10 (2020).
53. Schnitzbauer, J., Strauss, M. T., Schlichthaerle, T., *et al.* Super-Resolution Microscopy with DNA-PAINT. *Nature protocols* **12,** 1198 (2017).
54. Jungmann, R., Avendaño, M. S., Woehrstein, J. B., *et al.* Multiplexed 3D Cellular Super-Resolution Imaging with DNA-PAINT and Exchange-PAINT. *Nature methods* **11,** 313 (2014).
55. Spahn, C. K., Glaesmann, M., Grimm, J. B., *et al.* A Toolbox for Multiplexed Super-Resolution Imaging of the E. Coli Nucleoid and Membrane Using Novel PAINT Labels. *Scientific Reports* **8,** 14768 (2018).
56. Grimm, J. B., Muthusamy, A. K., Liang, Y., *et al.* A General Method to Fine-Tune Fluorophores for Live-Cell and in Vivo Imaging. *Nature Methods* **14,** 987–994 (2017).
57. Grimm, J. B., English, B. P., Choi, H., *et al.* Bright Photoactivatable Fluorophores for Single-Molecule Imaging. *Nature Methods* **13,** 985–988 (2016).

58. Mortensen, K. I., Churchman, L. S., Spudich, J. A., *et al.* Optimized Localization Analysis for Single-Molecule Tracking and Super-Resolution Microscopy. *Nature methods* **7,** 377 (2010).
59. Rieger, B. & Stallinga, S. The Lateral and Axial Localization Uncertainty in Super-Resolution Light Microscopy. *ChemPhysChem* **15,** 664–670 (2014).
60. Sage, D., Pham, T.-A., Babcock, H., *et al.* Super-Resolution Fight Club: Assessment of 2D and 3D Single-Molecule Localization Microscopy Software. *Nature Methods* **16,** 387 (2019).
61. Balzarotti, F., Eilers, Y., Gwosch, K. C., *et al.* Nanometer Resolution Imaging and Tracking of Fluorescent Molecules with Minimal Photon Fluxes. *Science* **355,** 606–612 (2017).
62. Gwosch, K. C., Pape, J. K., Balzarotti, F., *et al.* MINFLUX Nanoscopy Delivers 3D Multicolor Nanometer Resolution in Cells. *Nature Methods* **17,** 217–224 (2020).
63. Cnossen, J., Hinsdale, T., Thorsen, R. Ø., *et al.* Localization Microscopy at Doubled Precision with Patterned Illumination. *Nature Methods* **17,** 59–63 (2020).
64. Gu, L., Li, Y., Zhang, S., *et al.* Molecular Resolution Imaging by Repetitive Optical Selective Exposure. *Nature Methods* **16,** 1114–1118 (2019).
65. Tokunaga, M., Imamoto, N. & Sakata-Sogawa, K. Highly Inclined Thin Illumination Enables Clear Single-Molecule Imaging in Cells. *Nature Methods* **5,** 159–161 (2008).
66. Martin-Fernandez, M. L., Tynan, C. J. & Webb, S. E. D. A 'Pocket Guide' to Total Internal Reflection Fluorescence. *Journal of Microscopy* **252,** 16–22 (2013).
67. Huang, B., Wang, W., Bates, M., *et al.* Three-Dimensional Super-Resolution Imaging by Stochastic Optical Reconstruction Microscopy. *Science* **319,** 810–813 (2008).
68. von Diezmann, A., Shechtman, Y. & Moerner, W. E. Three-Dimensional Localization of Single Molecules for Super-Resolution Imaging and Single-Particle Tracking. *Chemical Reviews* **117,** 7244–7275 (2017).
69. Pavani, S. R. P., Thompson, M. A., Biteen, J. S., *et al.* Three-Dimensional, Single-Molecule Fluorescence Imaging beyond the Diffraction Limit by Using a Double-Helix Point Spread Function. *Proceedings of the National Academy of Sciences* **106,** 2995–2999 (2009).
70. Shechtman, Y., Sahl, S. J., Backer, A. S., *et al.* Optimal Point Spread Function Design for 3D Imaging. *Physical Review Letters* **113,** 133902 (2014).
71. Shechtman, Y., Weiss, L. E., Backer, A. S., *et al.* Precise Three-Dimensional Scan-Free Multiple-Particle Tracking over Large Axial Ranges with Tetrapod Point Spread Functions. *Nano letters* **15,** 4194–4199 (2015).
72. Farooq, S. & Hohlbein, J. Camera-Based Single-Molecule FRET Detection with Improved Time Resolution. *Physical Chemistry Chemical Physics* **17,** 27862–27872 (2015).
73. Ovesny, M., Křížek, P., Borkovec, J., *et al.* ThunderSTORM: A Comprehensive ImageJ Plug-in for PALM and STORM Data Analysis and Super-Resolution Imaging. *Bioinformatics* **30,** 2389–2390 (2014).
74. Izeddin, I., Boulanger, J., Racine, V., *et al.* Wavelet Analysis for Single Molecule Localization Microscopy. *Optics Express* **20,** 2081–2095 (2012).
75. Smith, C. S., Joseph, N., Rieger, B., *et al.* Fast, Single-Molecule Localization That Achieves Theoretically Minimum Uncertainty. *Nature Methods* **7,** 373–375 (2010).
76. Thompson, R. E., Larson, D. R. & Webb, W. W. Precise Nanometer Localization Analysis for Individual Fluorescent Probes. *Biophysical Journal* **82,** 2775–2783 (2002).
77. Isaacoff, B. P., Li, Y., Lee, S. A., *et al.* SMALL-LABS: Measuring Single-Molecule Intensity and Position in Obscuring Backgrounds. *Biophysical Journal* **116,** 975–982 (2019).
78. Thevathasan, J. V., Kahnwald, M., Cieśliński, K., *et al.* Nuclear Pores as Versatile Reference Standards for Quantitative Superresolution Microscopy. *Nature Methods* **16,** 1045–1053 (2019).
79. Pujals, S., Feiner-Gracia, N., Delcanale, P., *et al.* Super-Resolution Microscopy as a Powerful Tool to Study Complex Synthetic Materials. *Nature Reviews Chemistry* **3,** 68–84 (2019).
80. Stracy, M., Uphoff, S., de Leon, F. G., *et al.* In Vivo Single-Molecule Imaging of Bacterial DNA Replication, Transcription, and Repair. *FEBS letters* **588,** 3585–3594 (2014).
81. Uphoff, S., Sherratt, D. J. & Kapanidis, A. N. Visualizing Protein-DNA Interactions in Live Bacterial Cells Using Photoactivated Single-Molecule Tracking. *Journal of Visualized Experiments : JoVE* (2014).
82. Fick, A. Ueber Diffusion. *Annalen der Physik* **170,** 59–86 (1855).
83. Schütz, G. J., Schindler, H. & Schmidt, T. Single-Molecule Microscopy on Model Membranes Reveals Anomalous Diffusion. *Biophysical Journal* **73,** 1073–1080 (1997).
84. Uphoff, S., Reyes-Lamothe, R., de Leon, F. G., *et al.* Single-Molecule DNA Repair in Live Bacteria. *Proceedings of the National Academy of Sciences* **110,** 8063–8068 (2013).
85. Qian, H., Sheetz, M. P. & Elson, E. L. Single Particle Tracking. Analysis of Diffusion and Flow in Two-Dimensional Systems. *Biophysical journal* **60,** 910 (1991).
86. Vrljic, M., Nishimura, S. Y., Brasselet, S., *et al.* Translational Diffusion of Individual Class II MHC Membrane Proteinsin Cells. *Biophysical Journal* **83,** 2681–2692 (2002).

2

Phasor based single-molecule localization microscopy in 3D (pSMLM-3D): An algorithm for MHz localization rates using standard CPUs

A version of this chapter has been published as:

Koen J.A. Martens, Arjen N. Bader, Sander Baas, Bernd Rieger, and Johannes Hohlbein. Phasor based single-molecule localization microscopy in 3D (pSMLM-3D): an algorithm for MHz localization rates using standard CPUs *The Journal of chemical physics* **148**, no. 12 (2018)

2

Abstract

We present a fast and model-free 2D and 3D single-molecule localization algorithm that allows more than $3{\cdot}10^6$ localizations per second to be calculated on a standard multi-core central processing unit with localization accuracies in line with the most accurate algorithms currently available. Our algorithm converts the region of interest around a point spread function to two phase vectors (phasors) by calculating the first Fourier coefficients in both the x- and y-direction. The angles of these phasors are used to localize the centre of the single fluorescent emitter, and the ratio of the magnitudes of the two phasors is a measure for astigmatism, which can be used to obtain depth information (z-direction). Our approach can be used both as a stand-alone algorithm for maximising localization speed and as a first estimator for more time consuming iterative algorithms.

2.1 Introduction

Single-molecule localization microscopy (SMLM) has become a widely used technique in the biomolecular sciences since seminal contributions successfully demonstrated a roughly ten-fold improvement in spatial resolution over conventional fluorescence microscopy[1–3]. The key concept of SMLM is that the position of a single fluorescent emitter can be determined with an accuracy exceeding the diffraction limit as long as the emission of different molecules is sufficiently separated in time and space[4–6]. To localize the individual particles with sub-diffraction accuracy in two or three dimensions, a number of approaches have been developed[7]. Frequently employed localization algorithms involve the use of two-dimensional Gaussian functions to fit the intensity profile of individual emitters with high precision. These approaches, however, tend to be slow due to their iterative nature[8,9], albeit data analysis in real time using graphics processing units (GPUs) has been successfully demonstrated[10]. Faster localization algorithms using, for example, centre of mass (CoM) calculations[11] or radial symmetry[12,13] tend to have lower localization accuracy or lack the ability to assess 3D information at $>10^5$ localizations per second[14]. Although a Fourier domain localization scheme for non-iterative 2D localization has been demonstrated theoretically, that method has not been widely adopted as it did not offer significant improvements in either localization speed or accuracy compared to iterative algorithms[15].

Here, we introduce a simple and non-iterative localization algorithm with minimal computation time and high localization accuracy for both 2D and 3D SMLM. Our approach is based on the phasor approach for spectral imaging[16]. In pSMLM-3D, we calculate the location and astigmatism of two-dimensional point spread functions (PSFs) of emitters. The real and imaginary parts of the first coefficients in the horizontal and vertical direction of the discrete Fourier transformation represent coordinates of the x- and y-phasor in a phasor plot. The associated angles provide information on the x- and y-position, while the ratio of their magnitudes is a measure for astigmatism that can be used to determine the z-position of the emitter after introducing a cylindrical lens in the detection pathway of the microscope[17,18]. Our analysis of simulated PSFs with different photon counts indicates that phasor-based localization achieves localization rates in the MHz range, using only the central processing unit (CPU) rather than requiring a GPU implementation, with similar localization accuracy as Gaussian-based iterative methods. Next to this, we localized microtubules in dendritic cells in three dimensions obtaining similar results with pSMLM-3D as with an iterative Gaussian-based algorithm. Finally, we implemented our algorithm both as a stand-alone MATLAB script and into the freely available ImageJ[19] plug-in ThunderSTORM[20] to which we further added the possibility to calculate intensity and background levels of emitters based on aperture photometry[21].

2.2 Methodology

Data analysis in SMLM consists of the following steps: Identifying potential molecules and selecting regions of interests (ROIs) around their approximate location, sub-pixel localization within the ROI, and visualization of results (Figure 2.1a).

Here, we will only focus on the sub-pixel localization step. We simulated the intensity pattern of a point source emitter using a full vectorial model of the PSF as described previously[22] and depict it pixelated and with shot noise, mimicking a typical camera acquisition under experimental

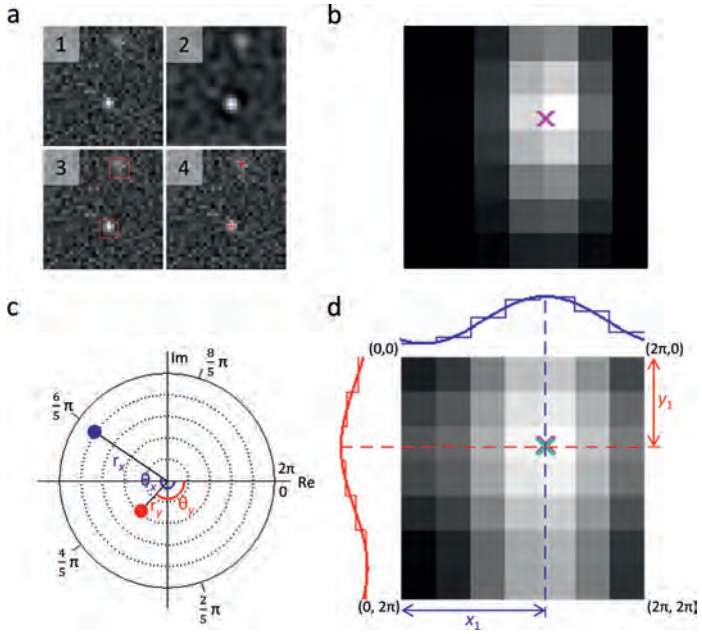

Figure 2.1: Illustration of sub-pixel localization using the phasor approach. **a** Standard workflow in single-molecule localization microscopy: 1. Acquisition of raw image data; 2. image filtering; 3. approximate localization of emitters: obtaining ROIs; 4. sub-pixel localization. **b** Strongly pixelated image (7×7 pixel) including noise representing standard conditions using camera-based detection of a simulated ellipsoidal point spread function with the ground-truth localization indicated by a pink cross. **c** Phasor plot representation of the two first Fourier coefficients of the image data. By plotting their real versus the imaginary part, the angles θ_x and θ_y represent the position (phase) of the molecule in real image space as the markings on the straight circle in the Fourier domain indicate the normalised 1D position of the true centre. Furthermore, the magnitudes r_x and r_y are reciprocally related to the PSF width in x and y in real-space, respectively. Dotted lines are added for visual guidance. **d** Inverse Fourier transformation of the first two Fourier coefficients with the cumulated discrete intensity profile plotted in the x- and y-direction and fitted with a sinusoid for visual guidance. From the angles θ_x and θ_y obtained from c and plotted in d, we obtain the position of the molecule in the image domain using y_1 and x_1 marked by a green cross, with the pink cross from the ground-truth position shown for comparison.

conditions (Figure 2.1b). As our algorithm is able to utilise astigmatism commonly introduced by placing a cylindrical lens in the emission path for localization in three dimensions[17,18], we simulated the full-width at half-maximum (FWHM) of the PSF in the y-direction to be larger than the in x-direction. We then calculated the first Fourier coefficients in the x- and y-direction by isolating them from the full two-dimensional discrete Fourier transformation of the ROI (see also section 2.7.1). Although the coefficients can be calculated without computing the complete Fourier transformation, this did not improve the localization speed in the MATLAB environment. The real and imaginary parts of each first Fourier coefficient are the coordinates of a phasor, which are both fully described by their phase angles (θ_x and θ_y) and magnitudes (r_x and r_y), representing the relative position of the emitter in real space and values for the PSF ellipticity, respectively (Figure 2.1c). To aid

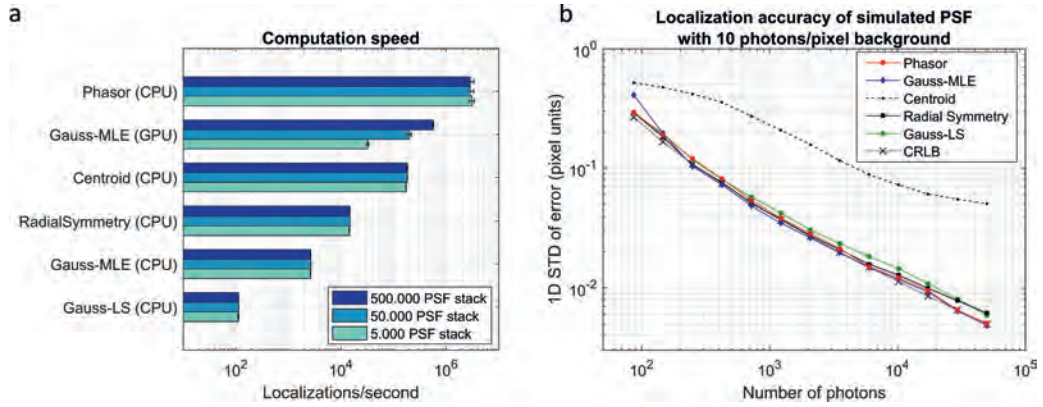

Figure 2.2: Comparison of computation speed and localization accuracy of phasor with other localization algorithms (Gaussian-MLE[10], Gaussian-LS[23], radial symmetry[12], and centroid[11,23]). **a** Speed of localization after loading the raw data in the memory in MATLAB. 7 × 7 pixel ROIs are used; the amount of PSFs at once supplied to the method is varied. **b** Accuracy comparison of phasor localization with other localization algorithms, comparing simulated PSFs with different total photon counts on a 10 photon/pixel background. Accuracy in the horizontal direction of all methods together with the Cramer-Rao lower bound24 is shown. ROI size is 5 × 5 ($<10^3$ photons) or 7 × 7 ($>10^3$ photons) pixels for the phasor algorithm and 7 × 7 pixels for all other algorithms.

the reader, we calculated the inverse Fourier transformation using only the isolated first Fourier coefficients to show the data that are used for the calculation of the emitter's position and relative widths in real-space (Figure 2.1d). We also show the localized position as determined from the phasor plot (Figure 2.1d, green cross) and the ground-truth position (Figure 2.1d, pink cross). The two elements represented in the phasor plot (Figure 2.1c) have different distances to the origin. These magnitudes are inversely proportional to the FWHM of the original PSF: $r_y < r_x$, leading to $\mathrm{FWHM}_y > \mathrm{FWHM}_x$, in agreement with the simulated data. The ratio of the PSF width in x- and y-direction can be used to calculate unknown z-positions of emitters in sample data after recording of calibration data.

2.3 Results

To assess the performance of the phasor algorithm, we analysed simulated data with a background level of 10 photons/pixels and a varying degree of total photon counts from the emitter ranging from 80 to 50,000 photons using images of 15 × 15 pixels. We compared the localization speed and accuracy of pSMLM-3D with other well established localization algorithms (for details see section 2.7.2): Gaussian-maximum likelihood estimation[10] (Gauss-MLE), Gaussian-least squares fit[23] (Gauss-LS), radial symmetry[12] (RS), and centroid[11,23] (Figure 2.2). We further included the Cramer-Rao Lower Bound (CRLB) to indicate the theoretically achievable resolution where relevant[24].

In terms of localization speed, pSMLM-3D achieved more than 3×10^6 localizations per second (3 MHz) when using ROIs with 7 × 7 pixels (Figure 2.2a). This localization rate is at least

an order of magnitude faster than our adapted implementations of other CPU-based algorithms and even significantly faster than GPU-enabled Gauss-MLE. Moreover, we found that the localization speed of GPU-based algorithms depends on the amount of data transferred to the GPU: Whereas a stack of 5000 7 × 7 pixel images was analysed at a rate of 30 kHz, a stack of 500,000 images (representing 49 MB of transferred data to the GPU) could be analysed at 600 kHz. For CPU-based algorithms, this dependency is absent, allowing fast analysis of small PSF-containing image stacks, indicative that CPU-based methods are well suited for real-time analysis.

To assess the localization accuracy of the different localization algorithms, we cropped the area around each simulated PSF (15 × 15 pixels) to create ROIs of 7 × 7 pixels (in line with the "rule of thumb" fitting region size[10] of $2 \cdot 3\sigma_{\mathrm{PSF}} + 1$) for analysis by all methods, except for phasor where we used ROIs of either 5 × 5 (for simulated photon counts $<10^3$ photons) or 7 × 7 ($\geq 10^3$ photons). We note that determining the optimal ROI size is often challenging for all localization algorithms: albeit working with larger ROIs can potentially increase the localization accuracy as more information from the PSF is extracted, larger contributions from background and near-by other emitters can have a diametric effect. Moreover, these effects depend on the photon count of the PSF and the type of the localization algorithm used for analysis (see also section 2.7.3).

The comparison showed that for PSFs consisting of 80 photon counts, the localization accuracy is around 0.3 unit pixels for Gauss-MLE, Gauss-LS, RS, and phasor and reduces to 0.005 unit pixels at 50,000 photon counts in line with the theoretically expected improvement of the localization accuracy being proportional to the square root of the photon number[25] (Figure 2.2b, Figure S2.10a). Between these outer limits, pSMLM-3D shows on average a small 3.7% decrease in accuracy compared to Gauss-MLE. We further note that the computationally inexpensive centroid-based localization algorithm has a substantially worse localization accuracy, in line with earlier results[12]. We repeated all simulations at reduced background levels of 1 or 5 photons per pixel showing that the localization accuracies of all methods improve with lower background levels (section 2.7.4).

So far, we limited our analysis to localizations in two dimensions. As our algorithm allows using the ratio of the relative widths of the PSF in the x- and y-direction introduced by astigmatism, the position of an emitter in three dimensions can be determined after performing a calibration routine in which photostable fluorescent emitters (e.g., latex beads) are imaged at different focus positions. Compared to non-astigmatic PSFs, we used larger ROIs (11 × 11 pixels for phasor, and 13 × 13 pixels for other methods, see Figure S2.4 in section 2.7.5 for details) to account for the larger PSF footprint. Comparison of phasor with other algorithms on simulated astigmatic PSFs showed that phasor remained the fastest tested algorithm whilst providing a lateral localization accuracy close to that of Gauss-MLE and better than Gauss-LS and Centroid (Figure S2.5 in section 2.7.5 and Figure S2.5b in section 2.7.8). Although RS is capable of determining the ellipticity of PSFs[14], localization rates did not exceed 10^5 Hz and the localization accuracy did not match that of Gauss-MLE.

With Gaussian-based methods, the PSF FWHM can be elucidated directly from the Gaussian fit; in our algorithm, the phasor magnitudes depend not only on the PSF FWHM in the respective directions but also on the background. This dependency can introduce a bias if the background of the calibration series differs from that of the actual data. However, the ratio of the phasor magnitude in x versus in y remained unaltered (section 2.7.6), indicating that calibration

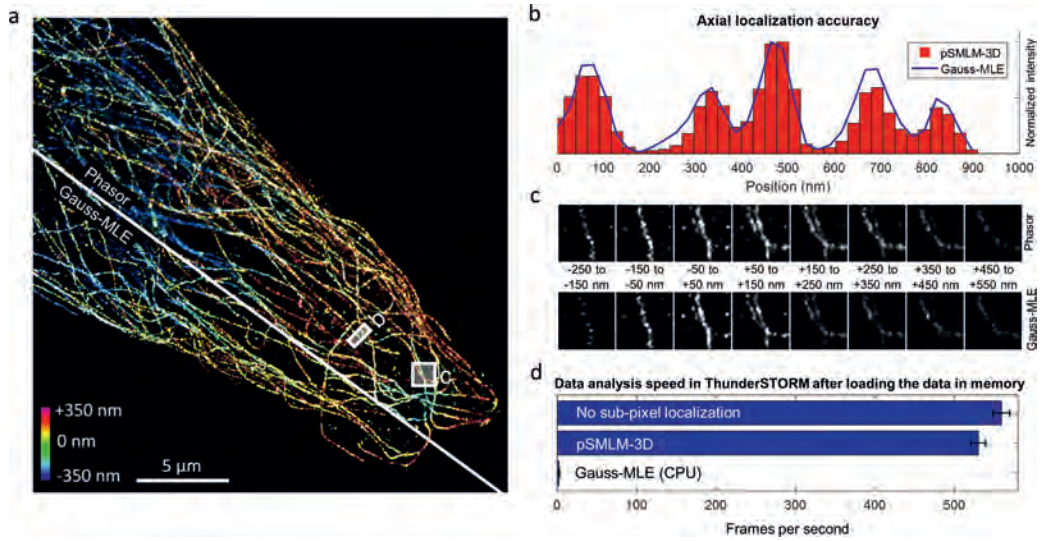

Figure 2.3: Analysis of a super-resolved microtubule network of fixed HELA cells. **a** Visualization of superresolution data after ThunderSTORM analysis using phasor (top, 7 × 7 pixel ROI) or Gauss-MLE (bottom, 11 × 11 pixel ROI) as a sub-pixel localization algorithm. Axial position is colour-coded between −350 nm and +350 nm. Note that this does not encompass all localized fluorophores. **b** Lateral resolving power of phasor (red bars) and Gaussian-MLE (blue line). Shown here are three microtubules spaced below the diffraction limit taken from panel b in a. **c** Axial resolving power of phasor (top) and Gaussian-MLE (bottom). Each subpanel shows localized fluorophores in a 100 nm window. **d** Localization speed of complete analysis (image filtering, approximate localization, and sub-pixel localization) using ThunderSTORM without sub-pixel localization (top), ThunderSTORM-Phasor (middle), and ThunderSTORM-Gauss-MLE (bottom). Error bars represent standard deviations of at least three repeats.

of the ratio between the magnitudes versus z-depth should be performed. We calculated the axial localization accuracies using phasor and Gauss-MLE both of which provide similar accuracies decreasing from around 200 nm at very low photon counts (<500 per PSF) to under 20 nm at high photon counts (>10,000 per PSF) (section 2.7.7 and Figure S2.10c in section 2.7.8).

To demonstrate the effectiveness of pSMLM-3D, we performed a standard 3D-STORM measurement of fixed immature dendritic cells with fluorescently labelled microtubules. In total, we recorded 50,000 frames (256 × 256 pixels), resulting in 6.1 GB of raw data containing roughly 2.7×10^6 localized molecules. We analysed these data with the ThunderSTORM[20] plugin for ImageJ[19] both with phasor and Gaussian-MLE (Figure 2.3a). The limited signal-to-noise ratio required changing the size of the ROIs for phasor and Gauss-MLE to 7 × 7 and 11 × 11 pixels, respectively. The lateral (Figure 2.3b) and axial (Figure 2.3c) resolving power of phasor is in line with that of Gauss-MLE. The complete analysis time using multi-core computing, including the filtering of the image to find potential single molecules and excluding the loading of the data in the computers memory, was over 5 h for Gauss-MLE, while it took only around 90 s for pSMLM-3D. Entirely omitting sub-pixel localization shortened the computation time by only ∼5 s, which

means that around 95% of the 90 s computation time is spend on image filtering and obtaining the approximate localization. Complete SMLM analysis with phasor under these conditions is at over 500 frames per second, indicative that it is fast enough for real-time analysis applications (Figure 2.3d).

2.4 Discussion and conclusion

The presented pSMLM-3D combines excellent localization accuracies in three dimensions with exceptional localization speed achievable on standard PCs. In-depth analysis of synthetic point spread functions with different photon counts and background levels indicated that pSMLM-3D achieves a localization accuracy matching that of Gaussian-based maximum likelihood estimation even at low signal-to-noise ratios. Moreover, we demonstrated localization rates above 3 MHz, which are at least one order of magnitude higher than with other CPU-based algorithms. In fact, even compared to GPU implementations of Gaussian-based localization algorithms[26], our algorithm is faster, thus significantly reducing the computational barrier and costs to analyse experimental SMLM data. Porting the phasor approach to a GPU environment is likely to achieve only marginal improvements in speed as the bandwidth of transferring raw data is becoming a limiting factor. However, implementations using field programmable gate arrays (FPGAs) directly connected to the camera chip are feasible, with real-time SMLM analysis with Gaussian methods shown before[27].

Subpixel localization rates in the MHz range satisfy even the most demanding applications as frame rates of cameras suitable for single-molecule detection are currently not above 100 Hz (full frame), indicating that phasor localization could be used in real-time environments. Moreover, some iterative localization algorithms currently use the centroid-based localization as a first estimation[10]. We believe that in that setting, the phasor approach can replace the initial step as it shows a speed as well as an accuracy improvement. We note that all necessary functions for performing the phasor algorithm are trivial, which allows for an easy upgrade of existing SMLM software packages. In computational environments in which a fast Fourier transformation function is not inherently present, a minimal algorithm to compute only the first Fourier coefficient can be written to minimize computation times, as we did for our JAVA implementation of phasor (section 2.7.9).

Compared to MLE, subpixel localization is possible in smaller areas around each emitter with good localization accuracy, allowing us to use effectively a higher concentration of fluorescently active emitters. This is especially apparent with astigmatism, where an 11×11 pixel size in the phasor approach gives similar localization accuracy as 13×13 pixel size in the Gauss-MLE approach. This directly results in a possible increase of 40% in fluorophore density with the same chance of having partial emitter overlap. However, we note that our current phasor implementation does not provide means of resolving molecules whose emission partially overlap.

Like most localization algorithms currently available, pSMLM-3D assumes well-behaved PSFs with symmetrical emission profiles. Therefore, the algorithm depends on emitters having sufficient rotational mobility as emission profiles deviating from symmetrical PSFs can result in significant localization errors as has been discussed[28–31].

In summary, we believe that pSMLM-3D holds great promise to replace or complement commonly used localization algorithms, as the combination of high localization speeds and high localization accuracy has not been shown to this extent before.

2.5 Material and methods

2.5.1 PSF simulations

PSF simulations have been performed as described earlier[22] with NA = 1.25, emission light at 500 nm, 100 nm/pixel camera acquisition, and image sizes set to 15 × 15 pixels. The centre of the PSF is within ±1 pixel of the centre of the image, and in the case of simulated astigmatic PSFs, the astigmatism has a FWHM ratio between 0.33 and 3.0. We used a full vectorial model of the PSF needed to describe the high NA case typically used in fluorescent super-resolution imaging. We accounted for the fact that in fluorescent super-resolution imaging, the emitter can rotate freely during the excited state lifetime (∼ns), so for many excitation-emission cycles, an average over randomly distributed emission dipole orientations will be observed in one camera frame (∼ms).

2.5.2 Computer and software specifications

All computational work was performed on a 64-bit Windows 7 computer with an Intel Core i7 6800K CPU @ 3.40 GHz (6 cores, 12 threads), NVIDIA GTX1060 GPU (1280 CUDA cores, 8 GHz memory speed, 6 GB GDDR5 frame buffer, driver version 376.51), and 64 GB of DDR4 RAM on a ASUSTeK X99-E WS motherboard. We used two software packages in this work: MATLAB (MathWorks, UK) version 2016b and FIJI[32]. FIJI is based on ImageJ[19] version 1.51n, using JAVA version 1.8.0_66.

2.5.3 Software scripts used

Unless specified otherwise, we used variants of the phasor script implemented in MATLAB (section 2.7.9). JAVA-implementation of the phasor approach is based around a minimal discrete Fourier transformation (section 2.7.10) and includes a aperture photometry-based method to estimate PSF intensity and background (section 2.7.11)[21]. Gauss-MLE, Gauss-RS, radial symmetry, centre-of-mass, and Cremer-Rao lower bound algorithms were adapted from earlier use[10,12]. For Gauss-MLE, 15 iterations were used[10]; Gauss-LS had 400 maximum iterations, with a tolerance of 10^{-6}.

2.5.4 Chemicals

All chemicals were purchased from Sigma-Aldrich and used without further purification, unless specified differently.

2.5.5 Labeling of in vivo microtubules

Microtubules were fluorescently labelled via a double antibody labelling; primary antibody was a mouse-anti-βtubulin, clone E7, isotype mouse IgG1; the secondary antibody was labeled with Alexa 647 (goat anti-mouse IgG (H+L) Superclonal secondary antibody, Alexa Fluor 647, ThermoFischer). HELA cells cultured on glass coverslips were fixed for 5 min with methanol at −20 °C, followed by 25 min fixation by 4% paraformaldehyde (PFA) in PBS. Next, a blocking step to prevent unspecific

adsorption was performed by adding 3% bovine serum albumin in PBS pH 7.2 + 20 mM glycine (MP Biomedicals) and incubated for 1 h. Primary antibody was added and incubated for 1 h. After washing with PBS, the secondary antibody was added and incubated for 45 min. After a final washing step, the cells were post-fixed with 2% PFA in PBS for 15 min at RT and stored in PBS with 0.05% NaN_3, with the final cells being stable for imaging for several days in PBS. During imaging, a Gloxy buffer[33] containing 35 mM β-mercaptoethanol was added to boost blinking of the fluorophores. This blinking buffer was freshly prepared on the day of imaging.

2.5.6 Single-molecule microscopy

We used a home-built microscope for imaging similar to a microscope described in more detail elsewhere[34]. Briefly, our microscope is equipped with a laser engine (Omicron, Germany), a 100× oil immersion SR/HP objective with NA = 1.49 (Nikon, Japan), and a Zyla 4.2 plus sCMOS camera for image acquisition (Andor, UK). 2 × 2 binning was used during acquisition, which resulted in a pixel size of 128 × 128 nm. A cylindrical lens with 1000 mm focal distance was placed in the emission path at 51 mm from the camera chip to enable astigmatic measurements; alignment of the lens' optical axis was performed to ensure PSF elongation in the x- or y-direction.

2.5.7 Microtubule imaging and analysis

Fully labelled cells with added blinking buffer were imaged for 50,000 frames (256 × 256 pixels) at 10 ms frame time. A 642 nm laser at 70 mW in HiLo was used for imaging of the fluorophores, a 405 nm laser at increasing power throughout the measurement was used to activate fluorophores. Analysis was performed via the ThunderSTORM[20] plugin for ImageJ[19], with phasor added as sub-pixel localization option (section 2.7.10). ThunderSTORM parameters for image filtering and approximate localization were kept constant for phasor and Gauss-MLE localization: a β-spline wavelet filter with order 3 and scale 3 was used, and approximate localization was done via an 8-neighbourhood connected local maximum, with a peak intensity threshold equal to the standard deviation of F1 of the wavelet filter. These settings are the default ThunderSTORM settings; the only difference was a β-spline wavelet filter scale of 2 rather than 3. Sub-pixel localization was performed with either elliptical Gauss-MLE (11 × 11 pixels, 1.6 pixels initial sigma) or phasor (7 × 7 pixels). Localizations for pSMLM-3D and Gauss-MLE in the acquired datasets were filtered as follows: intensity/background > 2; background standard deviation $<$ offset/2 (note that these are raw sCMOS counts rather than photon numbers). Calibration files were recorded under similar circumstances with immobilized fluorescent latex beads (560 nm emission, 50 nm diameter) and moving the piezo z-stage from -1000 nm to $+1000$ nm. These calibration files were used during the sub-pixel localization to calculate the z-position of the fluorophores. Visualization of the superresolution data was done via the average shifted histogram options, with a magnification of 3 (Figures 2.3a,c) or 5 (Figure 2.3b). No lateral or axial shifts were added. 3D was enabled and visualised coloured, after which a composite image was formed in FIJI (Figure 2.3a).

2.6 Acknowledgements

J.H. acknowledges support from a Marie Curie Career Integration Grant (No. 630992). K.M. was funded by a VLAG Ph.D. fellowship awarded to J.H. B.R. acknowledges support from European

Research Council Grant No. 648580. We thank Ben Joosten and Gert-Jan Bakker from Radboud UMC Nijmegen for kindly providing us with fixed dendritic cells and relevant labelled antibodies. We thank Sjoerd Stallinga for providing PSF simulation code. We thank Paul Reynolds and Christophe Leterrier for helpful discussions.

References

1. Betzig, E., Patterson, G. H., Sougrat, R., *et al.* Imaging Intracellular Fluorescent Proteins at Nanometer Resolution. *Science* **313,** 1642–1645 (2006).
2. Rust, M. J., Bates, M. & Zhuang, X. Sub-Diffraction-Limit Imaging by Stochastic Optical Reconstruction Microscopy (STORM). *Nature methods* **3,** 793 (2006).
3. Hess, S. T., Girirajan, T. P. K. & Mason, M. D. Ultra-High Resolution Imaging by Fluorescence Photoactivation Localization Microscopy. *Biophysical Journal* **91,** 4258–4272 (2006).
4. Deschout, H., Zanacchi, F. C., Mlodzianoski, M., *et al.* Precisely and Accurately Localizing Single Emitters in Fluorescence Microscopy. *Nature Methods* **11,** 253–266 (2014).
5. Liu, Z., Lavis, L. D. & Betzig, E. Imaging Live-Cell Dynamics and Structure at the Single-Molecule Level. *Molecular Cell* **58,** 644–659 (2015).
6. Gustafsson, N., Culley, S., Ashdown, G., *et al.* Fast Live-Cell Conventional Fluorophore Nanoscopy with ImageJ through Super-Resolution Radial Fluctuations. *Nature Communications* **7,** 12471 (2016).
7. Small, A. & Stahlheber, S. Fluorophore Localization Algorithms for Super-Resolution Microscopy. *Nature methods* **11,** 267–279 (2014).
8. Holden, S. J., Uphoff, S. & Kapanidis, A. N. DAOSTORM: An Algorithm for High- Density Super-Resolution Microscopy. *Nature Methods* **8,** 279–280 (2011).
9. Zhu, L., Zhang, W., Elnatan, D., *et al.* Faster STORM Using Compressed Sensing. *Nature Methods* **9,** 721–723 (2012).
10. Smith, C. S., Joseph, N., Rieger, B., *et al.* Fast, Single-Molecule Localization That Achieves Theoretically Minimum Uncertainty. *Nature Methods* **7,** 373–375 (2010).
11. Henriques, R., Lelek, M., Fornasiero, E. F., *et al.* QuickPALM: 3D Real-Time Photoactivation Nanoscopy Image Processing in ImageJ. *Nature Methods* **7,** 339–340 (2010).
12. Parthasarathy, R. Rapid, Accurate Particle Tracking by Calculation of Radial Symmetry Centers. *Nature Methods* **9,** 724–726 (2012).
13. Liu, S.-L., Li, J., Zhang, Z.-L., *et al.* Fast and High-Accuracy Localization for Three-Dimensional Single-Particle Tracking. *Scientific Reports* **3,** 2462 (2013).
14. Ma, H., Xu, J., Jin, J., *et al.* Fast and Precise 3D Fluorophore Localization Based on Gradient Fitting. *Scientific reports* **5** (2015).
15. Yu, B., Chen, D., Qu, J., *et al.* Fast Fourier Domain Localization Algorithm of a Single Molecule with Nanometer Precision. *Optics letters* **36,** 4317–4319 (2011).
16. Fereidouni, F., Bader, A. N. & Gerritsen, H. C. Spectral Phasor Analysis Allows Rapid and Reliable Unmixing of Fluorescence Microscopy Spectral Images. *Optics express* **20,** 12729–12741 (2012).
17. Huang, B., Wang, W., Bates, M., *et al.* Three-Dimensional Super-Resolution Imaging by Stochastic Optical Reconstruction Microscopy. *Science* **319,** 810–813 (2008).
18. Holtzer, L., Meckel, T. & Schmidt, T. Nanometric Three-Dimensional Tracking of Individual Quantum Dots in Cells. *Applied Physics Letters* **90,** 053902 (2007).
19. Schneider, C. A., Rasband, W. S. & Eliceiri, K. W. NIH Image to ImageJ: 25 Years of Image Analysis. *Nature methods* **9,** 671 (2012).
20. Ovesny, M., Křížek, P., Borkovec, J., *et al.* ThunderSTORM: A Comprehensive ImageJ Plug-in for PALM and STORM Data Analysis and Super-Resolution Imaging. *Bioinformatics* **30,** 2389–2390 (2014).
21. Preus, S., Hildebrandt, L. L. & Birkedal, V. Optimal Background Estimators in Single-Molecule FRET Microscopy. *Biophysical Journal* **111,** 1278–1286 (2016).
22. Stallinga, S. & Rieger, B. Accuracy of the Gaussian Point Spread Function Model in 2D Localization Microscopy. *Optics express* **18,** 24461–24476 (2010).
23. Cheezum, M. K., Walker, W. F. & Guilford, W. H. Quantitative Comparison of Algorithms for Tracking Single Fluorescent Particles. *Biophysical Journal* **81,** 2378–2388 (2001).
24. Van den Bos, A. *Parameter Estimation for Scientists and Engineers* (John Wiley & Sons, 2007).
25. Ober, R. J., Ram, S. & Ward, E. S. Localization Accuracy in Single-Molecule Microscopy. *Biophysical journal* **86,** 1185–1200 (2004).
26. Kechkar, A., Nair, D., Heilemann, M., *et al.* Real-Time Analysis and Visualization for Single-Molecule Based Super-Resolution Microscopy. *PLOS ONE* **8,** e62918 (2013).

27. Grull, F., Kirchgessner, M., Kaufmann, R., *et al. Accelerating Image Analysis for Localization Microscopy with FPGAs* in *Field Programmable Logic and Applications (FPL), 2011 International Conference On* (IEEE, 2011), 1–5.
28. Enderlein, J., Toprak, E. & Selvin, P. R. Polarization Effect on Position Accuracy of Fluorophore Localization. *Optics express* **14,** 8111–8120 (2006).
29. Karedla, N., Stein, S. C., Hähnel, D., *et al.* Simultaneous Measurement of the Three-Dimensional Orientation of Excitation and Emission Dipoles. *Physical review letters* **115,** 173002 (2015).
30. Stallinga, S. & Rieger, B. Position and Orientation Estimation of Fixed Dipole Emitters Using an Effective Hermite Point Spread Function Model. *Optics express* **20,** 5896–5921 (2012).
31. Lew, M., Lew*, M. D., von Diezmann*, A. R. S., *et al.* Easy-DHPSF Open-Source Software for Three-Dimensional Localization of Single Molecules with Precision beyond the Optical Diffraction Limit. *Protocol Exchange* (2013).
32. Schindelin, J., Arganda-Carreras, I., Frise, E., *et al.* Fiji: An Open-Source Platform for Biological-Image Analysis. *Nature methods* **9,** 676–682 (2012).
33. Nahidiazar, L., Agronskaia, A. V., Broertjes, J., *et al.* Optimizing Imaging Conditions for Demanding Multi-Color Super Resolution Localization Microscopy. *PLoS ONE* **11** (2016).
34. Farooq, S. & Hohlbein, J. Camera-Based Single-Molecule FRET Detection with Improved Time Resolution. *Physical Chemistry Chemical Physics* **17,** 27862–27872 (2015).
35. Shen, H., Tauzin, L. J., Baiyasi, R., *et al.* Single Particle Tracking: From Theory to Biophysical Applications. *Chemical Reviews* **117,** 7331–7376 (2017).
36. Rieger, B. & Stallinga, S. The Lateral and Axial Localization Uncertainty in Super-Resolution Light Microscopy. *ChemPhysChem* **15,** 664–670 (2014).

2.7 Supplementary information

2.7.1 Information contained in first Fourier coefficient

To show what information is present in the first Fourier coefficient in either x- or y-direction, we plotted the 1D inverse Fourier transformation of an isolated first coefficient corresponding to a PSF below (Figure S2.1). The parameters indicated by A, B, and C are related to the Fourier domain as follows:

$$A = \frac{Magn}{P^2} \tag{2.1}$$

$$B = \frac{1}{P^2} \tag{2.2}$$

$$C = \frac{Ang}{2\pi} \cdot P \tag{2.3}$$

Where P is the width of the ROI in pixels, $Magn$ the magnitude of the phasor in the Fourier domain, and Ang the angle of the element in the phasor plot in radians. Parameter C is further explored in this manuscript, as this is the direct measure for the position of a fluorophore in the direction of the first Fourier coefficient. Parameter A is influenced by the magnitude of the phasor and changes reciprocally with respect to the FWHM of the PSF.

2.7.2 Working principle of other localization algorithms

Centroid / Centre of Mass

The centroid or centre of mass algorithm[11,23] calculates the intensity-weighted centroid of the PSF. In essence, the mean pixel position is calculated, with the pixels being weighted by their respective intensities. This algorithm is fast, but sensitive to noise, the relative position of the PSF in the ROI, and even to the relative position of the centre compared to the pixel[35].

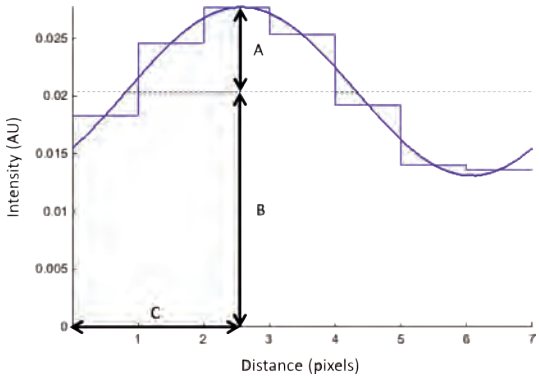

Figure S2.1: A 7 x 7 ROI containing a PSF has been Fourier transformed, after which the first Fourier coefficient is isolated (Figure 2.1c). Shown here is an inverse Fourier transformation of an isolated first Fourier coefficient (Figure 2.1d shows this in 2 dimensions). Parameters A, B, and C are explained in the text.

Radial symmetry (RS)

Radial symmetry[12] is a non-iterative method, in which the intensities at each pixel are used to calculate an intensity gradient on a displaced grid. This intensity gradient can be visualised as a set of lines on the corners of the pixels, which all have a specific slope m_k (which can be infinite for vertical lines, replaced with a large number in the software). The distance of the centre of the PSF is related to m_k and the position where the line is determined. The PSF centre is then found by minimising the intensity weighted over all distances calculated in this manner[35].

Gaussian – least squares fit (Gauss-LS)

Gauss-LS works by fitting a 2D Gaussian to a PSF[23]. Starting parameters are required, and often chosen via fast methods such as Centroid. After fitting a 2D Gaussian to the PSF, the goodness-of-fit is calculated by taking the difference between the data and the fit at each pixel. This procedure is iterated until the best goodness-of-fit is found, conditional to parameters as maximum number of iterations or a minimum required goodness-of-fit. Due to the iterative nature, the algorithm is robust albeit relatively slow.

Gaussian – maximum likelihood estimation (Gauss-MLE)

For Gauss-MLE, rather than calculating the error, the likelihood that the dataset $\vec{x}$ corresponds to parameters θ is calculated[10] via equation 2.4:

$$L(\vec{x}|\theta) = \prod_k \frac{\mu_k(x,y)^{x_k} \cdot e^{-\mu_k(x,y)}}{x_k!} \tag{2.4}$$

The parameters are then updated by calculating the derivative of the likelihood of the current iteration, and using this derivative to calculate the next iteration. Compared to Gauss-LS, this provides similar robustness, but has a significant increase in speed, as fewer iterations are necessary.

2.7.3 Determination of ideal ROI size for phasor and Gaussian-MLE

As the size of the ROI has an effect on the localization accuracy, we first determined optimal settings before comparing localization algorithms with one another. We used 5 x 5, 7 × 7, 9 × 9, and 11x11 pixels around the approximate centre of the PSF (Figure S2.2), and determined the localization accuracy of phasor and Gaussian-MLE. The same simulated data as Figure 2.2 is used (10 photons/pixels background), with the ROI reduced towards to centre.

Figure S2.2 shows that Gauss-MLE is benefiting from larger ROIs, albeit mainly between 5 × 5 pixels and 7 × 7 pixels. Phasor, on the other hand, does not benefit from the larger ROIs similarly at all photon levels. This can be explained by two counteracting processes:

1. Larger ROIs provide more information about the PSF, which results in better localization accuracies. Importantly, when the ROI is smaller than the PSFs FWHM, both phasor and Gauss-MLE start to show larger errors.

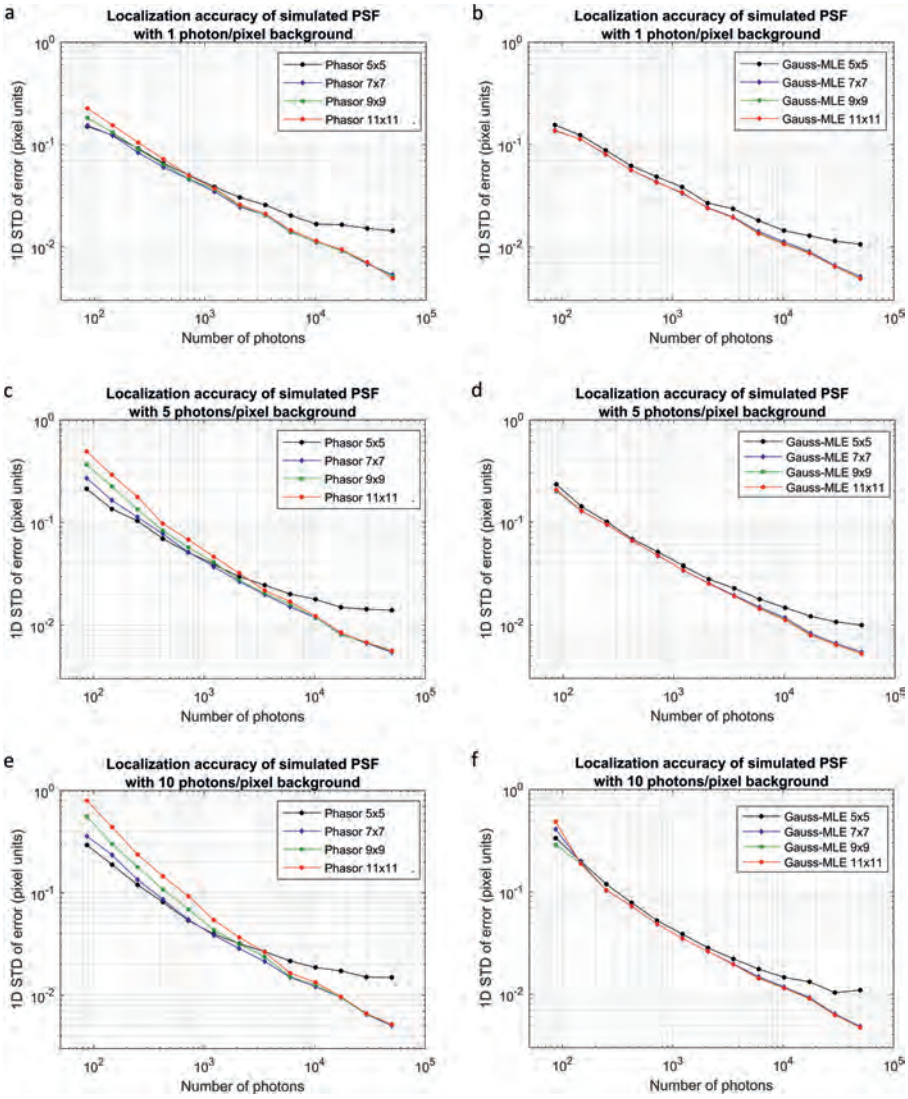

Figure S2.2: Accuracy comparison of phasor localization (**a**, **c**, **e**) and Gauss-MLE localization (**b**, **d**, **f**) of different ROI sizes (in pixels), comparing simulated PSFs with different total photon counts on a 1 photons/pixel (**a**, **b**), 5 photons/pixel (**c**, **d**) and 10 photons/pixel background (**e**,**f**).

2. Larger ROIs lead to a relatively larger contribution of the background, especially if the PSF has low photon counts. This leads to decreased phasor localization accuracy, since the first Fourier coefficient inherently provides information about a sinusoid without background levels.

As seen in Figures S2.2, enlarging the ROI beyond 7 × 7 pixels had only a visible effect of the localization accuracy at very high photon levels (50,000 photons total) and minimal photon background (1 photon/pixel). Thus, for experimentally relevant conditions, the relevant ROIs for phasor are 5 × 5 pixels and 7 × 7 pixels. Combining the presented information, we decided to use 5 × 5 pixel ROIs for PSFs with <1000 photons, and 7 × 7 pixel ROIs for PSFs with higher photon counts for non-astigmatism determination with the phasor algorithm.

2.7.4 Localization accuracy at lower background levels

In Figure 2.2, we compare different localization algorithms by simulated PSFs with 10 photons/pixel background. Here we present similar localization accuracy plots, but with lower background levels (5 photons/pixel and 1 photon/pixel compared to 10 photons/pixel (Figure S2.3)). As expected, lower background levels result in better localization accuracy for all tested methods.

2.7.5 Localization accuracy for astigmatic point spread functions

We simulated PSFs with astigmatic characteristics ($\mathrm{FWHM}_x/\mathrm{FWHM}_y$ randomly between 1/3 and 3) to compare the localization accuracy with different settings and algorithms. Here we look at the standard deviation in the lateral plane rather than in a single dimension, as the 1-dimensional error is dependent on the width of the PSF in the specified direction. Note that the shape of the PSFs has no effect on the speed of any of the algorithms. First, we look at the effect of different ROI sizes around the PSF (Figure S2.4). The same trend as non-astigmatic is observed for both phasor and Gauss-MLE, but with different optimal points. For phasor, the accuracy at high photon levels improves mostly from 7 × 7 to 9 × 9 pixels, especially at high background levels. At lower photon levels, the biggest losses are seen between 11 × 11 to 15 × 15 pixels. Therefore, a ROI of 11 × 11 pixels is used for phasor in astigmatic settings. For Gaussian-MLE, a significant improvement in localization accuracy at high photon levels is observed from 7 × 7 to 13 × 13 pixels, with a very small improvement from 13 × 13 to 15 × 15 pixels. This difference from non-astigmatic (7 × 7) is a simple result of wider PSFs, as Gaussian methods are sensitive to incomplete PSFs. A ROI of 13 × 13 pixels was used for Gauss-MLE and similar methods considering these localization accuracies and localization speed.

After determining the ideal ROI sizes, we compared the lateral localization accuracy of different algorithms (Figure S2.5). Here it can be seen that phasor has better accuracy than Gauss-MLE at low photon counts, with Gauss-MLE being slightly better than phasor at higher photon counts.

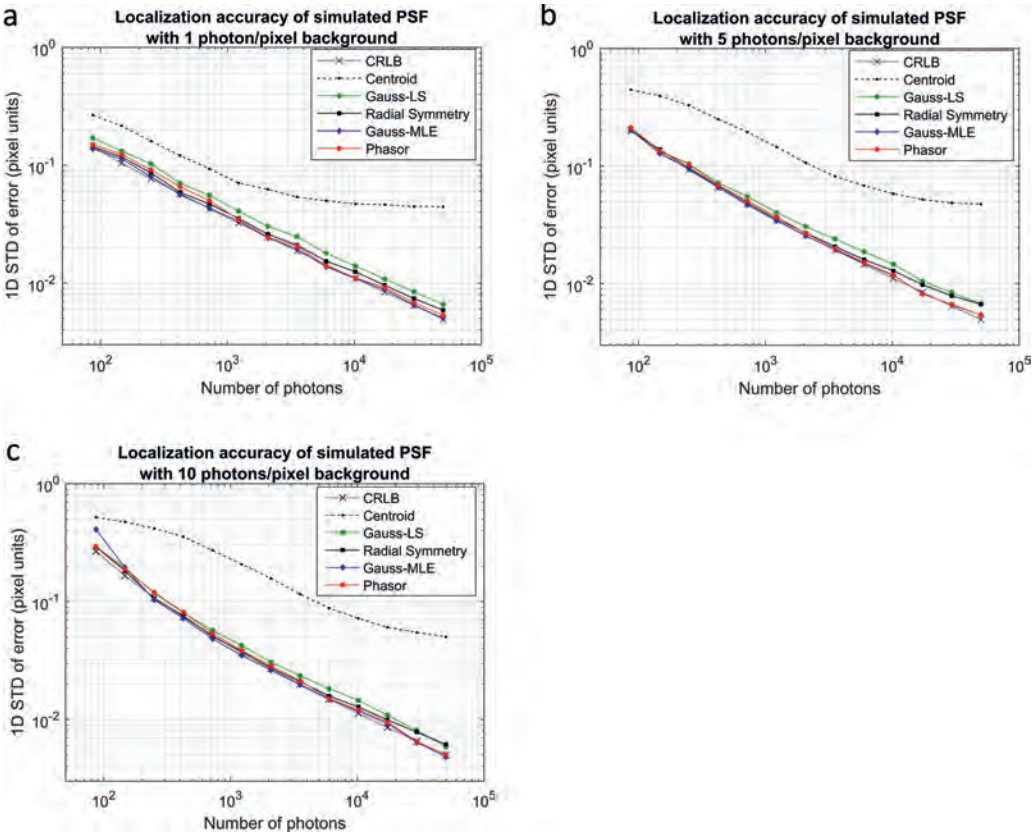

Figure S2.3: Accuracy comparison of phasor localization with other localization algorithms, comparing simulated PSFs with different total photon counts on a 1 photons/pixel background **a**, 5 photons/pixel background **b** and 10 photons/pixel background **c** Accuracy in the horizontal direction of the phasor approach (ROIs of 5 × 5 ($<10^3$ photons) or 7 × 7 ($>10^3$ photons) pixels), Gaussian-MLE[10], Gaussian-LS[23], radial symmetry[12] and centroid[11,23] (all 7 × 7 pixels) are shown, together with the Cramer-Rao lower bound[24].

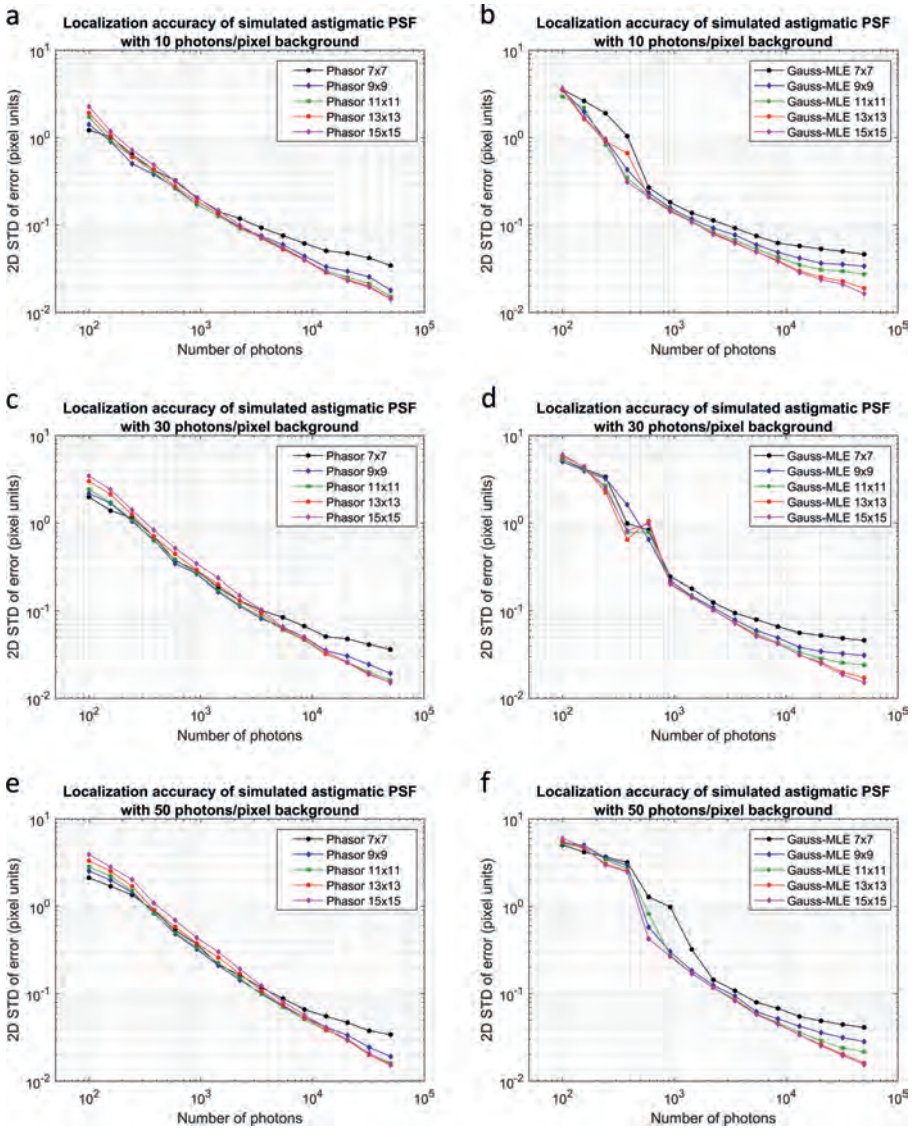

Figure S2.4: Accuracy comparison of phasor localization (**a**, **c**, **e**) and Gaussian-MLE localization (**b**, **d**, **f**) by changing the ROI size around the PSF. The combined localization accuracy in the horizontal and vertical direction of PSFs with different total photon counts on a 10 (**a**, **b**), 30 (**c**, **d**), or 50 (**e**, **f**) photons/pixel background are shown.

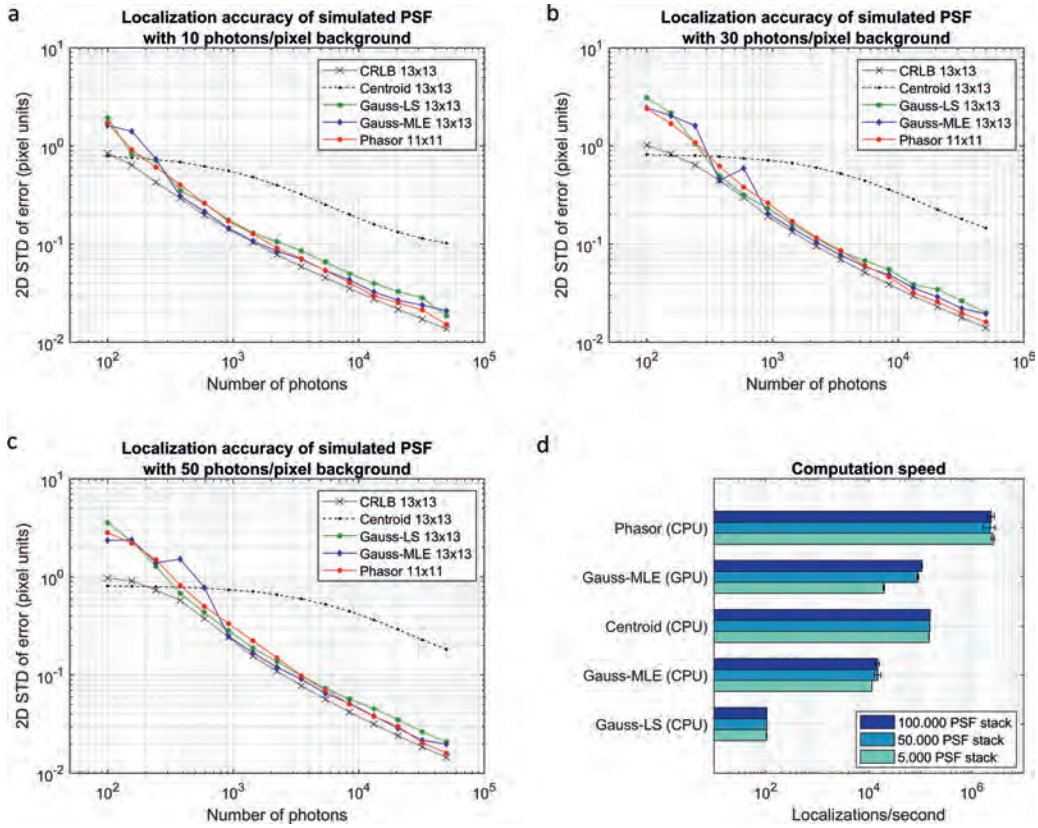

Figure S2.5: Accuracy comparison of phasor localization with other localization algorithms, comparing simulated PSFs with different total photon counts on a 10 (**a**), 30 (**b**), or 50 (**c**) photons/pixel background. Combined accuracy in the horizontal and vertical direction of the phasor approach (11x11 pixels ROI), Gaussian-MLE[10] , Gaussian-LS[23], and Centroid[11,23] (all 13 × 13 pixels ROI) are shown, together with the Cramer-Rao lower bound[24]. **d** Computation speed of the tested algorithms with the indicated ROI sizes.

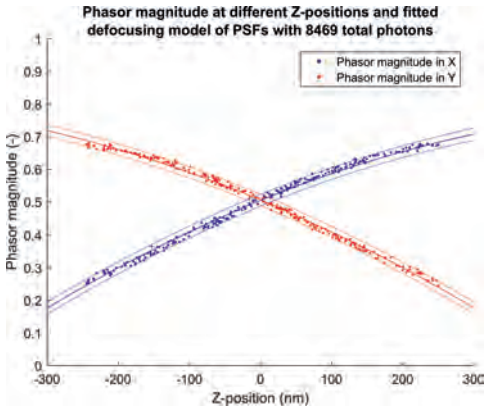

Figure S2.6: Calibration curve acquired via phasor localization. The magnitude of the phasors in x and y are fitted with curves as indicated in equation 2.5. 95% confidence interval shown in dotted lines.

2.7.6 Calibration data based on astigmatism

By introducing an astigmatic lens in the emission pathway, the PSF will be elongated in x or y depending on the position of the fluorophore in z. The axial position can be obtained by making two calibration curves (defocus model) from the FWHM in x and y of PSFs of fluorophores with known z-positions[17,20] (Figure S2.6), which is built in into the ThunderSTORM plugin. Since the PSFs are two-dimensional, two curves are found:

$$\sigma_x = a_1 \cdot (z - c_1)^2 + b_1 \text{ and } \sigma_y = a_2 \cdot (z - c_2)^2 + b_2 \tag{2.5}$$

Calculating the z-position from the width in x and y and the calibration curve is usually performed by calculating z twice, as $\sigma_{1/2}$, $a_{1/2}$ and $b_{1/2}$ are known, but give two values due to the quadration. The final z position can be elucidated from this by comparing the four solutions. For phasor, this is done slightly different because the magnitude is dependent on the background level, which might be different as the calibration series. Therefore, equation 2.6 below is used rather than using two separate equations, as the level of background noise has no effect on the ratio of σ_x divided by σ_y (Figure S2.7). This equation can provide multiple numerical solutions, but only one solution will be within the calibrated range.

$$\frac{\sigma_x}{\sigma_y} = \frac{a_1 \cdot (z - c_1)^2 + b_1}{a_2 \cdot (z - c_2)^2 + b_2} \tag{2.6}$$

2.7.7 Error in determined z-position

The accuracy of the determined z-position is dependent on the accuracy of the determined sigma in x and y. To assess this, we determined the goodness-of-fit of a defocus model (Equation 2.5) to simulated PSFs at different z-positions with different photon counts and 10 photons/pixel background. This was performed both via Gaussian-MLE and phasor (Figure S2.8). This shows the expected increase in fit certainty with higher photon counts. Next, simulated PSFs with 1435 photon counts

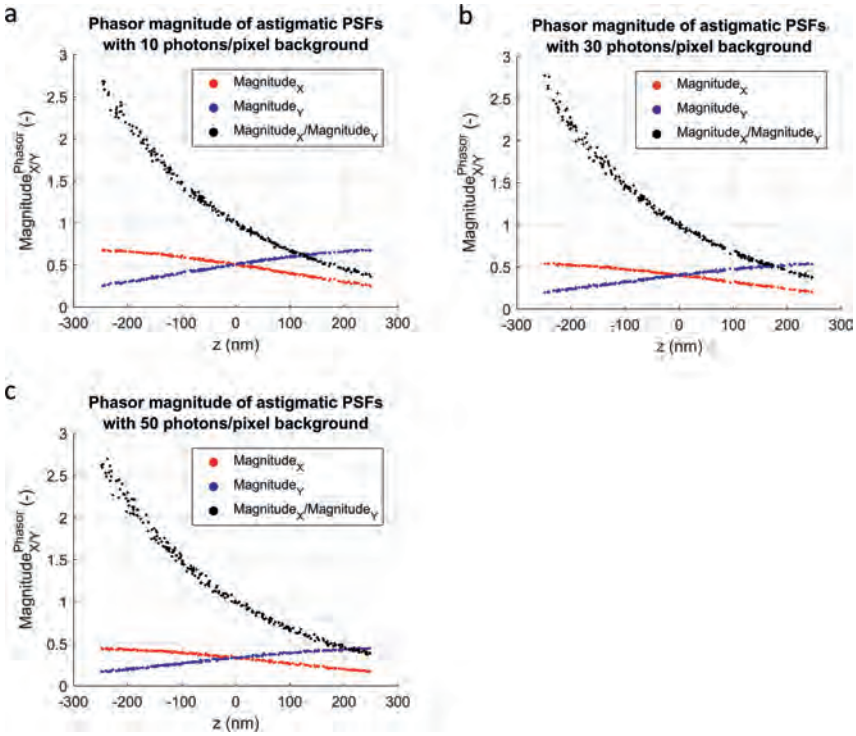

Figure S2.7: Effect of increasing background levels on the absolute phasor magnitude in x and y at simulated astigmatic PSFs with different z-positions. The phasor magnitude in x (**a**), y (**b**), or x divided by y (**c**) are shown, using simulated PSFs with 10 (red), 30 (blue), or 50 (black) photons/pixel background. A change in magnitude in both x and y can be observed with different background levels, but the ratio remains identical throughout the tested range.

provided magnitudes or FWHM that were fitted with two defocus curves (Equation 2.5). The z-position of simulated PSFs with photon counts from 100 to 50,000 were determined via Equation 2.6. The standard deviation of the error in axial plane is dependent on the PSF photon number and the background level (Figure S2.9). Phasor with an 11 × 11 ROI and Gauss-MLE with a 13 × 13 ROI provide similar accuracies in the axial plane. The CRLB in z is calculated according to [36].

2.7.8 Assessment of bias for simulated astigmatic and non-astigmatic PSFs

To be able to completely assess localization accuracy, there should be no bias introduced. We tested this for multiple circumstances by plotting the lateral localization bias of non-astigmatic and astigmatic PSFs, and the axial localization bias of astigmatic PSFs. As can be seen in the Figure S2.10, no bias is introduced by any of the localization algorithms used.

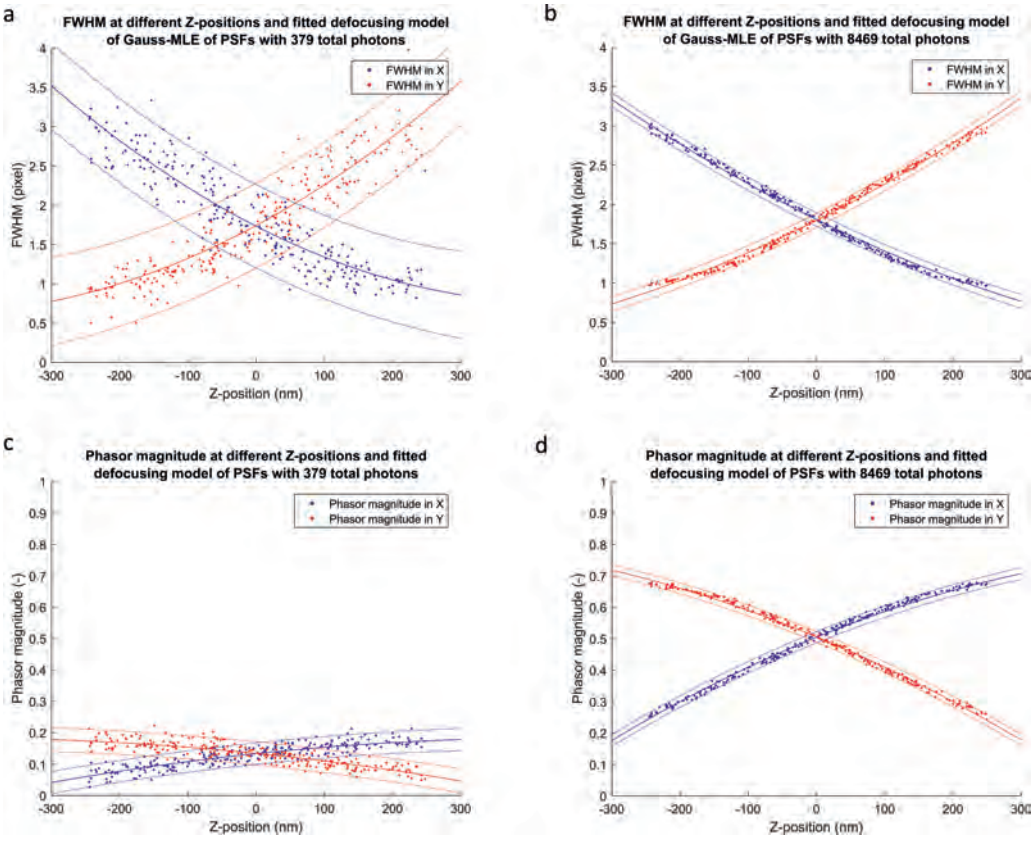

Figure S2.8: A defocus model fit with 95% confidence intervals (in dotted lines) of FWHM in x and y determined by Gauss-MLE (**a**,**b**) or of phasor magnitude in x and y (**c**,**d**), determined from simulated PSFs with 379 photons (**a**,**c**) or 8469 photons (**b**,**d**). The reciprocal relationship of phasor magnitude with PSF width is expected (main text).

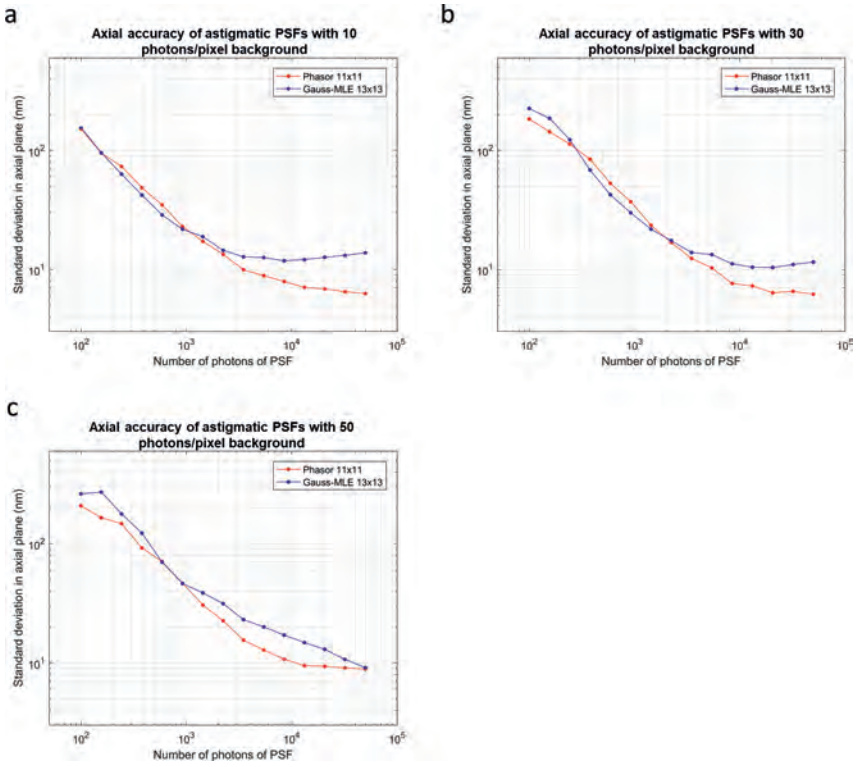

Figure S2.9: Axial accuracy as determined from simulated PSFs with photon counts from 100 to 50,000 photons and 10 (**a**), 30 (**b**), and 50 (**c**) photons/pixel background via Gauss-MLE (13 × 13 pixel ROIs) and phasor (11 × 11 pixel ROIs), and CRLB at ROI of 13 × 13 pixels indicated. Calibration curve determined from simulated PSFs with 1435 photon counts.

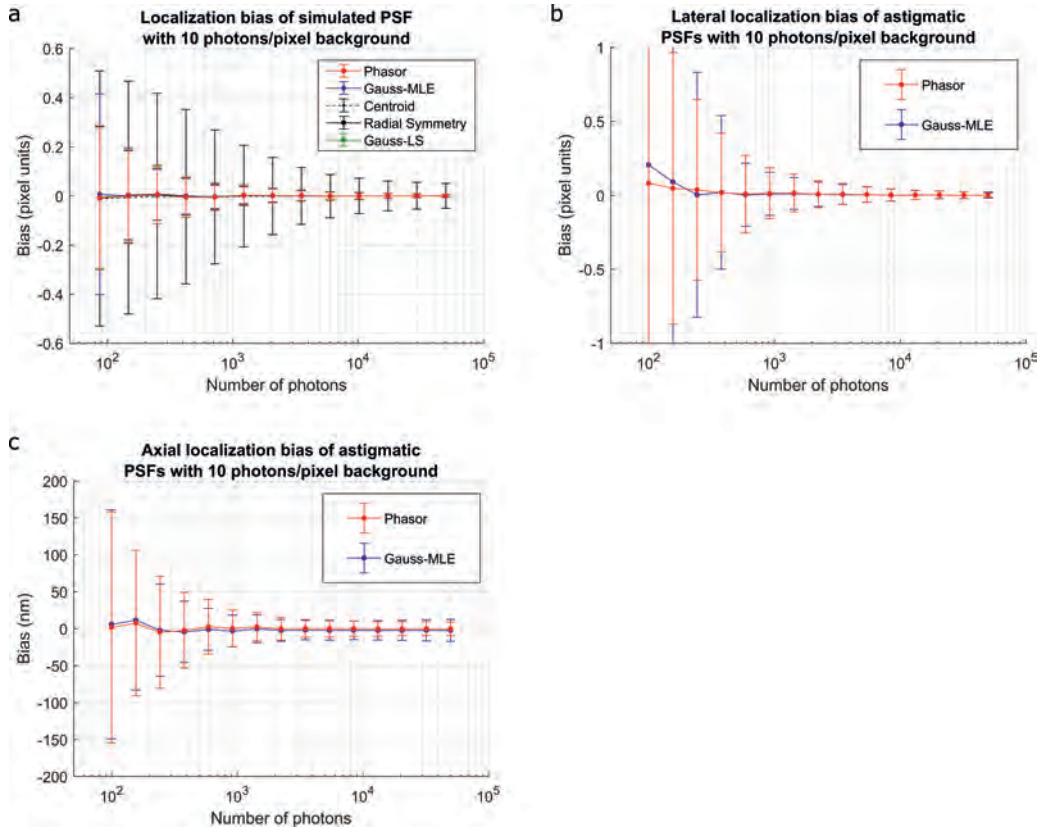

Figure S2.10: Bias of SMLM algorithms while performing localization of PSFs with 10 photons/pixel background: lateral localization bias of non-astigmatic PSFs (**a**), lateral localization bias of astigmatic PSFs (**b**), and axial localization bias of astigmatic PSFs (**c**) at total photon counts ranging from 100 to 50.000 photons. The settings of the SMLM algorithms is identical to those specified in Figure 2.2b (**a**), Figure S2.5a (**b**), or Figure S2.9a (**c**).

2.7.9 Minimal phasor calculation in MATLAB

Here we show a minimal MATLAB script for the phasor calculation of a single PSF, assuming that the data of the PSF is present in a double-precision square matrix named ROI.

```
%% Perform a 2D Fourier transformation on the complete ROI.
fft_values = fft2(ROI);

%Get the size of the matrix
WindowPixelSize = size(ROI,1);

%Calculate the angle of the X-phasor from the first Fourier coefficient in X
angX = angle(fft_values(1,2));
%Correct the angle
if (angX>0) angX=angX-2*pi; end;
%Normalise the angle by 2pi and the amount of pixels of the ROI
PositionX = (abs(angX)/(2*pi/WindowPixelSize) + 1);
%Calculate the angle of the Y-phasor from the first Fourier coefficient in Y
angY = angle(fft_values(2,1));
%Correct the angle
if (angY>0) angY=angY-2*pi; end;
%Normalise the angle by 2pi and the amount of pixels of the ROI
PositionY = (abs(angY)/(2*pi/WindowPixelSize) + 1);

%Calculate the magnitude of the X and Y phasors by taking the absolute
%value of the first Fourier coefficient in X and Y
MagnitudeX = abs(fft_values(1,2));
MagnitudeY = abs(fft_values(2,1));

%Print a line with results
fprintf('\nPosition found at X=%.2f, Y=%.2f, with phasor magnitude in
X=%.2f, phasor magnitude in Y=%.2f\n',
PositionX, PositionY, MagnitudeX, MagnitudeY);
```

2.7.10 Partial Fourier transformation in JAVA

We designed a partial Fourier transformation for use in JAVA. In its core, we have a minimal discrete Fourier transformation; with a reduction in computation time via two methods:

1. Since we are only interested in the first order harmonic, we do not need to compute the full discrete Fourier transformation.
2. As we know the size of the sub-images containing the PSF, and since this size is constant throughout the analysis, we do not need to re-calculate the value of the sine and cosine at certain positions. Instead, we can calculate these values once and then use them as input in the minimal function.

This approach does not offer an increase in speed when transcribed to MATLAB, probably due to the highly optimised fft2() function in MATLAB.

The JAVA code to calculate the sine and cosine separately is as follows:

```
//Fitradius: amount of pixels from centre pixel to edge of ROI.
//Size of ROI is fitradius*2+1
this.fitradius = fitradius;
//Calculate parts of the fitting that are only dependant on the fitradius
this.imsizeint = 2*fitradius+1; //integer
this.imsizedouble = 2*fitradius+1; //double precision
//Create and calculate the cos and sine arrays with size dependant on ROI size
this.fitomega = new double[imsizeint];
this.fitcos = new double[imsizeint];
this.fitsin = new double[imsizeint];
for (int indi = 0; indi < imsizeint; indi++){
    fitomega[indi] = (indi/imsizedouble)*2*Math.PI;
    fitcos[indi] = Math.cos(fitomega[indi]);
    fitsin[indi] = Math.sin(fitomega[indi]);
}
```

2.7.11 Aperture photometry to assess intensity and background levels

For the JAVA-based pSMLM-3D script, a aperture photometry-based method is implemented to assess values for PSF intensity and background[21] (Figure S2.11). All pixels in the ROI with a distance to the ROI centre smaller than the ROI radius minus 2 are attributed to the emitters signal, pixels with a distance to the centre between (ROI radius minus 2) and (ROI radius plus 0.5) are attributed to the background, and any other pixels are excluded. The background level is estimated by taking the 56^{th} percentile of the background pixels, while the intensity is estimated by taking the sum of the signal pixels, with the background subtracted.

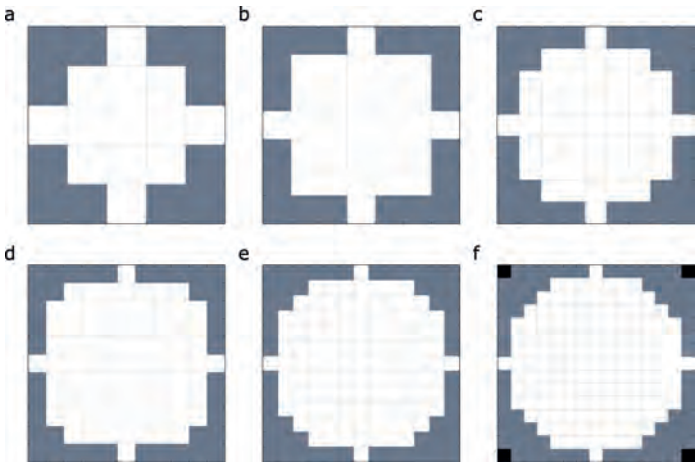

Figure S2.11: Maps of photometric aperture layout for ROIs of 5 × 5 (**a**), 7 × 7 (**b**), 9 × 9 (**c**), 11 × 11 (**d**), 13 × 13 (**e**), and 15 × 15 (**f**) pixels. White pixels are considered signal, grey pixels are considered background, and black pixels are excluded from consideration.

3

Integrating engineered point spread functions into the phasor-based single-molecule localization microscopy framework

A version of this chapter has been published as:

Koen J.A. Martens, Abbas Jabermoradi, Suyeon Yang, and Johannes Hohlbein. Integrating engineered point spread functions into the phasor-based single-molecule localization microscopy framework *Methods* (2020)

Abstract

In single-molecule localization microscopy (SMLM), the use of engineered point spread functions (PSFs) provides access to three-dimensional localization information. The conventional approach of fitting PSFs with standard Gaussian profiles, however, often falls short in analysing complex PSFs created by placing phase masks, deformable mirrors or spatial light modulators in the optical detection pathway. Here, we describe the integration of PSF modalities known as double-helix, saddle-point or tetra-pod into the phasor-based SMLM (pSMLM) framework enabling fast CPU based localization of single-molecule emitters with sub-pixel accuracy in three dimensions. For the double-helix PSF, pSMLM identifies the two individual lobes and uses their relative rotation for obtaining z-resolved localizations. For the analysis of saddle-point or tetra-pod PSFs, we present a novel phasor-based deconvolution approach entitled circular-tangent pSMLM. Saddle-point PSFs were experimentally realised by placing a deformable mirror in the Fourier plane and modulating the incoming wavefront with specific Zernike modes. Our pSMLM software package delivers similar precision and recall rates to the best-in-class software package (SMAP) at signal-to-noise ratios typical for organic fluorophores and achieves localization rates of up to 15 kHz (double-helix) and 250 kHz (saddle-point/tetra-pod) on a standard CPU. We further integrated pSMLM into an existing software package (SMALL-LABS) suitable for single-particle imaging and tracking in environments with obscuring backgrounds. Taken together, we provide a powerful hardware and software environment for advanced single-molecule studies.

3.1 Introduction

Fluorescence microscopy is frequently employed in biological sciences due to its high selectivity and non-invasiveness. Conventionally, the obtainable optical resolution in fluorescence microscopy is given by Abbe's diffraction limit which is equal to the wavelength of the light divided by double the numerical aperture of the objective (∼200 nm for visible light). However, a multitude of techniques summarised by the term super-resolution (SR) microscopy or nanoscopy[1–3] have been developed to obtain spatial information well below this limit. These techniques include (d)STORM (direct stochastic optical reconstruction microscopy)[4,5], PALM (photo-activatable localization microscopy)[6], SIM (structured illumination microscopy)[7], STED (stimulated emission depletion microscopy)[8], RESOLFT (reversible saturable optical fluorescence transitions)[9], SOFI (super-resolution optical fluctuation imaging)[10], SRRF (super-resolution radial fluctuations)[11] and MINFLUX (minimal photon fluxes localization microscopy)[12].

Single-molecule localization microscopy (SMLM) is the sub-collection of super-resolution techniques in which the fluorescent emission profile, ordinarily referred to as a point spread function (PSF), of a single fluorophore is localized with a precision (∼5 - 40 nm) that can exceed the classical resolution limit by more than one order of magnitude[13–16]. SMLM is therefore an integral part of STORM and PALM, and has been extensively used in biological research[17–19], for example to study DNA transcription[20,21], CRISPR-Cas DNA screening[22–24], nuclear pore complexes[25,26], and microtubules[27].

In a conventional fluorescence microscope, a PSF from a single emitter in focus resembles an Airy pattern, which can be approximated by a 2-dimensional Gaussian function. This approach has been the basis of the earliest localization algorithms[13,16,28], which allow for determination of the emitter locations[16] as long as overlapping of PSFs is negligible. Besides Gaussian-based methods, these symmetrical PSFs have been analysed via other mathematical frameworks, such as radial symmetry[29], cubic splines[30], or phasor (Fourier) analysis[31].

The shape of the PSF quickly deteriorates, however, if the emitter is out of focus (∼100s of nm), leading to both a limited available axial range and inaccessibility of the absolute axial position[32]. Therefore, a variety of methods have been developed to modulate the shape of the PSF depending on the emitter's axial position[33]. Historically, the first method (astigmatism; AS) introduced a cylindrical lens in the emission pathway to create ellipsoid PSFs if the emitters are out of focus[34,35]. The extent of the deformation along with its orientation allows for determination of the axial position after a calibration procedure, and fitting of these PSFs could usually be performed by derivatised localization algorithms as the ones used for 2D PSFs[28,31,36]. However, the available axial range of astigmatism is limited to less than ∼1 µm, which lead to the development of more advanced PSF shaping procedures that involve modulating the light in the pupil (Fourier) plane. Using a spatial light modulator (SLM), the principle was first employed to create a double helix (DH) pattern, in which the PSF is split in two separate lobes that non-degeneratively rotate around each other based on the emitters axial position, resulting in a usable axial range up to 2.5 µm[37]. Later, the same group theoretically maximised the information content of PSFs resulting in the Saddle-Point (SP) or Tetra-Pod (TP) designs, which are suitable for 3 µm (SP) or ≥6 µm (TP) axial ranges[38,39]. PSFs for both SP and TP are altered in the Fourier plane via a phase mask[38,39] or deformable mirror[40].

Determining the sub-pixel positions corresponding to the emitters via DH, SP, or TP PSFs, however, is more challenging than for isotropic or AS PSFs, as fitting with a single 2D Gaussian is insufficient. The current state-of-the-art fitting algorithms[41] rely on phase retrieving methods[40,42] or spline interpolation[26] to determine a PSF model based on calibration samples. A high-resolution PSF model can then be determined from these models which is fitted on experimental data. These methodologies can work with arbitrarily shaped PSFs, including DH, SP and TP. However, these methods are computationally expensive and thus time-consuming. Recently, real-time fitting localization of experimental PSFs have been achieved using graphical processing units (GPUs)[26], but this has not yet been achieved on central processing units (CPUs), which would increase the accessibility and might allow implementations directly on the camera hardware.

Here, we show fast retrieval of DH ($1.5{\cdot}10^4$ loc/s) and SP/TP ($2.5{\cdot}10^5$ loc/s) PSF localizations on a standard CPU via novel adaptations of the phasor-based single-molecule localization microscopy (pSMLM) algorithm[31]. We first explain the underlying methodology for DH and for SP/TP, termed circular-tangent (ct-)pSMLM, and then explore the performance of the methods by analysing simulated and experimental data. We have implemented all pSMLM versions (2D, AS, DH, SP/TP) in a recently published software package (SMALL-LABS[43]), resulting in user-friendly and open-source software to quickly perform sub-pixel localization including advanced background filtering options.

3.2 Methods

3.2.1 Principles of engineered PSF localization with pSMLM: Double-helix: DH-pSMLM

To localize double-helix (DH) PSFs, we rely on the fact that pSMLM-2D provides accurate lateral localization even when using a relatively small ROI around the center of an emitter[31]. Therefore, the two lobes rotating around each other (Figure 3.1a) can be localized separately. During calibration, the distance and rotation between the two lobes is plotted against the axial position (Figure 3.1b). The rotation is fitted with a third-order polynomial. This polynomial is weighted on the inverse of the standard deviation of each axial position if more than one calibration bead has been used.

The lateral position is calculated as being the average lateral position of the two lobes, corrected for a 'wobble' factor. This wobble factor is determined in x and y as function of the emitters axial position (Figure 3.1c) by comparing the lateral localization at all axial positions with the lateral localization at the axial centre of the calibration dataset. The average of this wobble factor over an axial sliding window (user-defined, default value is set to 5 axial positions) is determined during calibration and stored for future correction of lateral localization calculation (Figure 3.1d).

To extract positional information, first a standard pSMLM-2D fitting is performed[31]. The localizations in each frame are compared with each other to find pairs within the expected distance regime (determined during calibration; minimum and maximum of distance between lobe centres, with a 10% error margin), and are discarded if no pair can be found. During the linking of the lobes, priority is given to lobes that only have a single possible counter-lobe over those that have multiple options to reduce mis-fitting of closely positioned DH PSFs. The axial position is then determined from the rotation of the two lobes via the calibration curve. The obtained distance between lobes

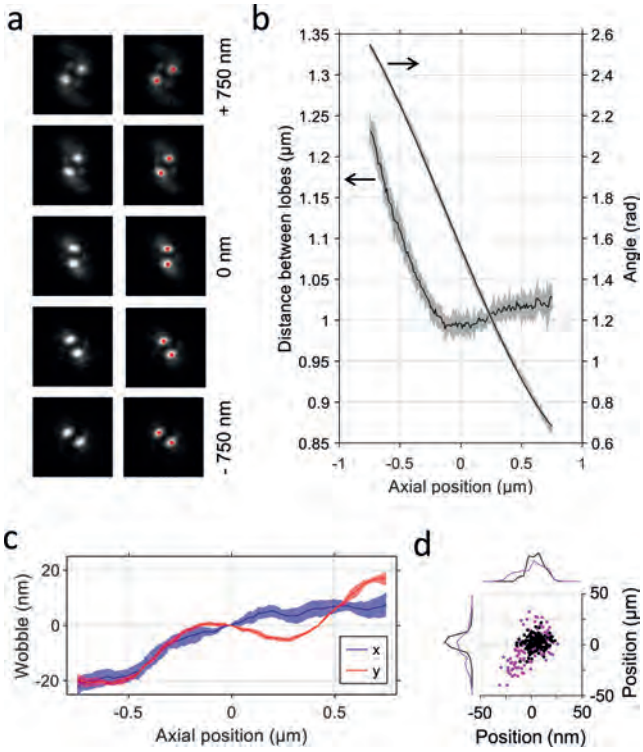

Figure 3.1: Double Helix PSF fitting via phasor-based localization. **a** Typical double helix axial position profile[41]. Red markers indicate initial 2D fits of single lobes by pSMLM. Scalebar represents 1 µm. **b** Typical calibration curve determined via DH-pSMLM. The distance between the lobes is used to link single lobes during analysis, while the angle between the lobes is used to calculate the axial position. **c** Typical wobble calculated from calibration. The solid line represents the average wobble in x or y at every axial position, the shaded area represents the standard deviation. **d** Wobble correction effect for a single calibration emitter. Magenta shows uncorrected lateral position of a fixed simulated emitter, while black shows the wobble-corrected position.

is checked against the distance determined during calibration at the found axial position, and the localization is discarded if these values differ more than ∼100 nm (user defined). Lastly, the lateral position is determined from the mean of the 2D-determined position of the two lobes, and corrected for the wobble determined during calibration (Figure 3.1d).

3.2.2 Principles of engineered PSF localization with pSMLM: Saddle-point and tetra-pod: ct-pSMLM

We analyse saddle-point (SP) and tetra-pod (TP) PSFs with an adapted phasor-based localization methodology. SP and TP have similar characteristics and show separation of a single point when in focus into two lobes above and below the focus in perpendicular directions[38,39]. Moreover, they are based on similar PSF deformations introduced by primary and secondary astigmatism Zernike coefficients[40].

We modified a spectral phasor-based approach[44] in which the convolution of arbitrary profiles in real space is a linear combination of their respective phasor representations in phasor space. In this approach, the normalised intensity ratio between the original profiles in the convolved profile (real space) is represented as the distance of the original phasor profiles to the convolved phasor profile (phasor space). This entails that if two profiles are combined with a 1:1 ratio, the

convolved phasor representation is on the mid-point of the line between the phasor representations of the original profiles.

In SP and TP PSFs, the final spatial representation of the PSF is a convolution of two separated lobes of identical intensity. Thus, SP and TP PSFs can be treated as a 1:1 ratio of arbitrary profiles that are separated at a varying distance, depending on the axial position of the emitters. Note that by orientating the respective optical components correctly, this separation can be achieved perfectly on the x- or y-axis. Therefore, the value for the separation d_{lobes}, along with the orientation of this separation provides suitable information for calibration of SP and TP PSFs.

To determine the separation d_{lobes} with phasor-based single-molecule localization microscopy (pSMLM), we assume that the width of the individual lobes in the direction of the convolution is identical to the width of the convolved PSF in the other, unconvolved spatial direction. For illustration, we show a combination of two 2-dimensional Gaussian distributions (Figure 3.2a,b,c). The phasor representation of the individual Gaussian distributions is represented by a single phasor for both dimensions, each having a certain, but different, angle representing the emitter's position in real space[31].

Then, if reasoned from the convolved PSF (Figure 3.2c) to obtain the individual lobes, the tangent at the magnitude circle in the convolved spatial dimension (broad spatial dimension; small phasor magnitude; black cross located on the red circle in Figure 3.2c) will intersect the magnitude of the smaller spatial dimension (large phasor magnitude; represented as a blue circle) at two points (Figure 3.2c; magenta and orange dots). These points are a measure for original arbitrary profiles with identical spatial sizes in both dimensions that combine in a 1:1 intensity ratio to result in the convolved profile. The angle between these two obtained intersectional points (θ_{lobes}) in phasor space is a direct normalised value for the distance d_{lobes} in real space (Figure 3.2c). We call this method circular-tangent pSMLM (ct-pSMLM).

The obtained d_{lobes} is used to create well-defined calibration curves for both SP and TP (SP shown in Figure 3.2d) that can be fitted with arbitrary functions (e.g. a fourth-order polynomial) to deduce axial positional information from experimental PSFs (Figure 3.2e). The lateral localization information of the SP or TP PSFs is still inherently present in the original phasor-representation of the complete PSF.

Determining localization of the SP or TP PSFs in the SMALL-LABS-pSMLM software consists of two parts: finding the central positions and further analysis with ct-pSMLM. The mid-points of single PSFs are determined by first checking whether two detected emitters that could represent two lobes of a single SP/TP PSF belong to the same PSF. If these emitters have little deviation in one dimension ($<$0.5 px) and are slightly separated in the other dimension (less than the calibrated maximum distance), the mid-point of these emitters is calculated and stored. If no other lobe can be found, it is assumed the located emitter is the mid-point of the SP/TP PSF. Then, ct-pSMLM is performed around the central point with a reasonably large region of interest ($>$2 µm) to obtain d_{lobes} and to calculate the axial position.

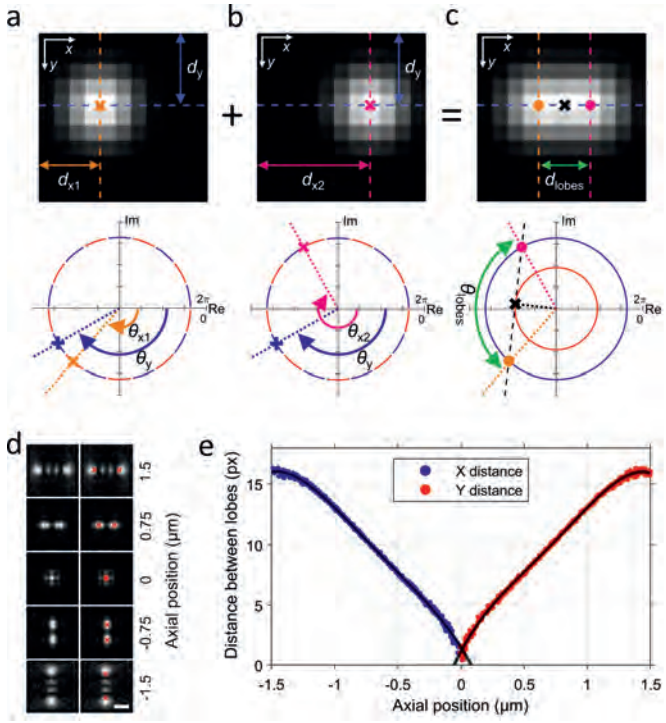

Figure 3.2: Principle of circular-tangent phasor-based single-molecule localization microscopy (ct-pSMLM) which can be used for saddle-point (SP) and tetra-pod (TP) PSF localization. **a** Single simulated 2D-Gaussian profile (top). The phasor representation (bottom) in the x dimension shows a single phasor, of which the angle θ_{x1} represents x-position d_{x1} of the emitter in real space (orange cross in both real space and phasor space). The angle θ_y in phasor space (blue plus) represents y-position d_y in real space. The magnitude of the x-dimension (red) and y-dimension (blue) are shown as circles with equal radius. **b** Identical to a, but with the 2D-Gaussian profile at a different position. **c** Top: Combination of the two Gaussian profiles shown in a and b. The wider x profile corresponds to a smaller x phasor magnitude (red circle) as compared to the profile and magnitude in y. Bottom: The phasor representation of the profile in x is represented by the black cross (the y-phasor is omitted for clarity). Next, a line (black dashed) is placed perpendicular on the x phasor magnitude circle. The positions where this line crosses the y phasor magnitude circle are indicated by the orange and magenta dots in phasor space. These values are normalised values for the single emitter positions in real space, indicated by orange and magenta dots. The angle between the two phasor angles is θ_{lobes} (green) and represents d_{lobes} in real space. **d** Representative simulated SP emitters at varying axial positions (see Methods). Red markers indicate the obtained lobe positions via ct-pSMLM. Scalebar represents 1 µm. **e** Typical calibration curve in which the separation of the lobes in x and y is plotted as a function of the z position.

3.3 Results

3.3.1 Double-helix

To evaluate the performance of DH-pSMLM, we performed fitting of simulated datasets[41] via the full pSMLM-updated SMALL-LABS software package and compared with the currently best per-

Table 3.1: Double Helix PSF fitting performance, comparing SMALL-LABS-pSMLM with SMAP.

	Low density				High density			
	High SNR		Low SNR		High SNR		Low SNR	
	pSMLM[a]	SMAP	pSMLM[a]	SMAP	pSMLM[a]	SMAP	pSMLM[a]	SMAP
RMSE *x* (nm)	10.7	9.6	24.7	8.9	32.0	37.3	53.7	57.1
RMSE *y* (nm)	7.5	6.5	16.4	6.1	21.1	23.0	35.0	41.0
RMSE *z* (nm)	15.1	13.5	34.2	12.6	35.6	36.8	70.3	65.8
RMSE *xyz* (nm)	22.9	20.5	51.3	19.0	60.8	67.0	108.2	110.1
Jaccard (%)	76	61	63	65	26	21	22	5
Analysis time (s)	52	196	58	190	9	15	9	16
Phasor time (s)	1.4		1.4		0.6		0.5	

[a] Using SMALL-LABS-pSMLM, including loading of .tiff file, excluding intermediate .mat file saving (also see Table S3.1).

forming non-machine learned localization algorithm (experimental PSF spline fitting methodology incorporated in SMAP[26]).

As the ground truth of these datasets is publicly available, we were able to extract (Table 3.1) quantitative performance parameters such as the expected deviation of localization accuracy in all three dimensions (root mean squared error, RMSE) and the Jaccard index JACC (a measure for correctly and incorrectly localized particles[41]). These performance parameters are calculated from localizations that were found in both software packages and in the Ground-Truth datasets.

We observe that both SMALL-LABS-pSMLM and SMAP have comparable RMSE errors (Table 3.1) in the order of 10-25 nm for the low density (LD), high signal to noise (SNR) dataset which are similar to the ones reported previously for SMAP[26,41]. However, at low signal to noise levels, SMAP outperforms SMALL-LABS-pSMLM on all performance indicators. This is presumably due to SMAP using the full PSF at once, while SMALL-LABS-pSMLM splits localization in two steps. This results in SMALL-LABS-pSMLM working with a lower apparent signal to noise level, causing a lower localization accuracy. We note that the reported RMSE values for SMAP analysis of the LD, low SNR dataset are counter-intuitively better than those of SMAP analysis of the LD, high SNR dataset. This is a result of the RMSE calculation methodology used (Material and methods), as only localizations that are found in both software analyses as well as in the ground-truth are used for RMSE calculations.

We observe that SMALL-LABS-pSMLM outperforms SMAP in terms of localization recall rates (Jaccard index, Table 3.1) at high SNR (23% increased), but not at low SNR (4% decrease). The Jaccard values for SMAP are slightly lower than reported earlier[41] (Material and methods), but can be compared directly with the Jaccard values for SMALL-LABS-pSMLM reported here. We note that no background subtraction is performed in SMAP, while SMALL-LABS-pSMLM subtracts the background based on foreground temporal variations (SMALL-LABS[43]).

Both software packages are not capable of recognizing HD PSFs with a good recall rate, although SMALL-LABS-pSMLM outperforms SMAP in all conditions, as single DH lobes are localized with only 5 x 5 pixel ROIs, decreasing the influence of the other nearby emitters.

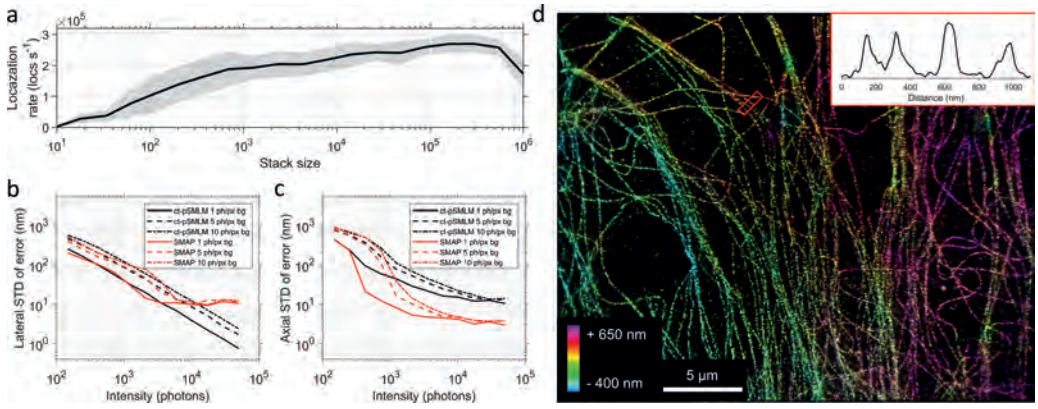

Figure 3.3: Saddle-point (SP) ct-pSMLM performance. **a** Speed of ct-pSMLM, based on a 23 x 23 pixel image stack. Shaded area indicates the standard deviation. **b,c** Localization precision of ct-pSMLM, based on simulated saddle-point point spread functions with different intensities (x axis) and background noise levels (line types). Lateral localization precision is shown in b, while axial precision is shown in c. **d** Experimental STORM microtubule network analysed with ct-pSMLM integrated in SMALL-LABS-pSMLM. Inset: Lateral profile of the red boxed outline.

SMALL-LABS-pSMLM is ~3 - 4 x faster compared to SMAP for low density datasets, and ~2x faster for high density datasets. However, most analysis time for SMALL-LABS-pSMLM (~65%) is spend on the background correction and format conversion rather than approximate localization or sub-pixel DH-pSMLM localization (Table S3.1). The localization procedure itself can achieve 1 - $1.5{\cdot}10^4$ localizations per second on a standard CPU.

3.3.2 Saddle-point and tetra-pod

The performance of the localization of saddle-point (SP) PSFs was assessed and compared to experimental PSF spline fitting[26]. As ct-pSMLM is a non-iterative method, high localization rates of up to $2.5{\cdot}10^5$ localizations per second were achieved on standard CPUs (Figure 3.3a). This is an order of magnitude lower than traditional pSMLM-3D[31], mostly due to the large required region of interest around the PSF (>2 µm; here 23 x 23 px), and partly due to the additional computations required for ct-pSMLM. Taken alone, the additional computations of ct-pSMLM compared to pSMLM-3D only result in a 10 - 40% decrease in localization rates (~10% for at a large region of interests 23 x 23 px; ~40% decrease for 7 x 7 px). The lateral localization accuracy of ct-pSMLM is in line with that of experimental PSF spline fitting (Figure 3.3b), and decreases from ~100 nm (~1 pixel) at typical (~200 - 1300) photon values for fluorescent proteins to ~10 nm (~0.1 pixels) at typical (~(2 - 11) x 10^3) photon values for organic fluorophores. The localization accuracy is roughly one order of magnitude lower than the lateral localization accuracy of non-engineered PSFs at high photon values (~0.08 pixels and ~0.01 pixels, respectively[31]), and roughly 1.5x worse than AS PSFs (~0.05 pixels[31]) caused by lower effective signal to noise ratio due to the expanded PSF. We observed a lower limit in lateral localization accuracy for SMAP fitting of ~10 nm (~0.1 pixel), which has an unknown origin.

The axial localization accuracy of ct-pSMLM increases with increasing photon values as well (Figure 3.3c). The average axial accuracy at typical photon values for organic fluorophores is ∼40 nm, which is ∼3x worse than AS PSFs with similar total photon counts and photons/pixel background[31]. The best obtainable axial accuracy is limited by the sub-optimal fitting of the calibration curve to around 11 nm, which is similar to AS PSFs (Figure 3.3c, Figure S3.2, [31]). We attribute this lower axial accuracy of SP PSFs compared to AS PSFs again to lower effective signal to noise ratios due to expanded PSFs. Up to 20% of SMAP-localized emitters had to be discarded from calculating the z offset, as these were substantially misfitted ($>$ 3 times the corresponding ct-pSMLM z offset, see Methods).

We furthermore demonstrate the implementation of ct-pSMLM in SMALL-LABS-pSMLM by analysing an experimental STORM experiment showing labelled microtubule of a Monkey cell line (Figure 3.3d, Material and methods). The total analysis time for the SMALL-LABS-pSMLM analysis for the ∼8 GB, 60.000 frames dataset containing 1.5 million localizations was ∼15 minutes on a standard CPU, including file conversion (Table S3.1), of which the ct-pSMLM sub-pixel fitting routine comprised just 77 seconds.

3.4 Discussion

Here we present integration of the phasor-based single-molecule localization microscopy (pSMLM) framework with double helix (DH), saddle-point (SP), and tetra-pod (TP) PSFs, achieving very good accuracy and speed on standard CPUs. In the current implementation, DH-pSMLM can achieve up to $1.5{\cdot}10^4$ localizations/second on a 3.10 GHz processing unit, while ct-pSMLM, the basis for SP and TP localization, can achieve up to $2.5{\cdot}10^5$ localizations/second. Specifically, ct-pSMLM is designated for real-time localization methods, combined with computationally inexpensive filtering and background subtraction methods, to better enable (automated) feedback-oriented SMLM instrumentation. Possibly a pSMLM-based methodology could be implemented on the integrated circuits of cameras to further increase end-user accessibility of advanced single-molecule techniques.

The DH-pSMLM implementation in the SMALL-LABS software has similar performance as the current state-of-the-art methods when using organic fluorophores, while decreasing the overall analysis time when ran on a CPU. We note that our implementation is not particularly sensitive to overfitting, as stringent constraints on the pair-finding are used. This allows for some false positives during the initial localization steps which are later discarded.

Ct-pSMLM improves on our previous phasor implementation[31] by offering a direct way of determining the distance between two emission peaks of a single PSF, well-suited for the quantification of the axial position in SP and TP PSFs. Here, perfect horizontal and vertical elongation of the PSFs is a requirement for ct-pSMLM to perform. Our algorithm is capable of retrieving the emitters location with a precision similar to current best non-machine learning localization algorithm[41], and is mostly limited by the fitting of the calibration curve. Naturally, for ct-pSMLM to work correctly, no other emitters or highly inhomogeneous background should be present in the fitting region. As SP and TP PSFs require large ROIs (∼23 x 23 px), this results in substantially lower accessible emitter density compared to approaches using standard and astigmatic PSFs. For high-density engineered PSF localization approaches, we point to alternative approaches such as deep learning[45,46] or matching pursuit[47].

We incorporated the novel pSMLM-derivative localization methodologies in the SMALL-LABS software[43]. The updated SMALL-LABS-pSMLM software package expands the original work with a user-friendly GUI, wavelet filtering, drift-correction in 3D, and result image generation. We believe that the software package strikes an excellent balance between fast analysis, accurate results, experimental freedom, good expandability, and hassle-free installation and operation. The software is freely available at https://github.com/HohlbeinLab/SMALL-LABS-pSMLM.

3.5 Material and methods

3.5.1 Software and hardware

All software was written and ran in MATLAB (MathWorks, UK) version 2018b on a 64-bit Windows 10 computer equipped with an Intel i5-8600 CPU @ 3.10 GHz, 16 GB RAM.

3.5.2 SMALL-LABS software

Our software package expands the original SMALL-LABS software[43] in several ways. Firstly, we added the original pSMLM-3D algorithm for 2D or astigmatism PSF sub-pixel localization, as well as the novel variations discussed in this manuscript. Next, a custom GUI was written to increase user accessibility. Lastly, the pre- and post-processing options are expanded with wavelet filtering[48], cross-correlation drift correction in three dimensions[49], and average shifted histogram result image generation[50,51].

3.5.3 Saddle-point PSF simulations

PSF simulations have been performed as described earlier[16,31] with NA = 1.25, emission light at 500 nm, 100 nm/pixel camera acquisition and 1000 PSFs for every intensity/noise combination. We used a full vectorial model of the PSF needed to describe the high NA case typically used in fluorescent super-resolution imaging. The center of the PSF is located within $\pm$ 1 pixel of the center of the image. Zernike polynomials Z_2^2 (primary astigmatism) and Z_4^2 (secondary astigmatism) are introduced in a 0.5:$-$0.65 ratio[40], and z-positions were chosen randomly between -1.5 and $+1.5$ µm away from the focal plane.

3.5.4 Sub-pixel localization of single-molecule data

For double-helix (DH) sub-pixel localization, the four datasets from the 2016 SMLM challenge[41] were analysed, which use experimental PSF models. These datasets differ in signal-to-noise (SNR) values ('high SNR', which mimics Alexa647 fluorophores, and 'low SNR', which mimics fluorescent proteins) and in emitter density ('low density' (LD) at 0.2 loc/µm^2 and 'high density' (HD) at 2 loc/µm^2).

For double-helix localization, the following settings were used. For SMALL-LABS-pSMLM-DH, the temporal window length and the minimum duration of fluorophore on-time before it is discarded were both set to 150 frames. Filtering for region-of-interest (ROI) finding was performed with a β-Spline wavelet filter with the threshold set to 1.9 times the standard deviation of a filtered frame. Single-lobe DH localization was performed with a phasor radius of 4 pixels (low

density) or 2 pixels (high density). The z-position was calculated via a calibration with identical phasor radius. For the SMAP software with fit3dSpline sub-pixel localization[26], a calibration was performed with a 33 x 33 pixel ROI. Then, localizations were identified via a mean calibrated PSF, with a 2.9 pixel Gaussian blur, using all calibrated z-positions. A threshold set to an absolute cutoff value of 86 (high SNR), 76 (low SNR, LD), or 29 (low SNR, HD) photons was used. The calibrated spline PSF was fitted with a 15 x 15 pixel ROI. Then, localizations with relative log-likelihood lower than -2 (low density) or -5 (high density) were discarded.

For the localization of simulated saddle-point PSFs, we note that in order to prevent localization artefacts at specific z-positions for ct-pSMLM (Figure S3.1), a large ROI ($> \sim$1.2x the maximum distance between the lobes) had to be used to determine lateral localization accurately, while a smaller ROI ($\sim$2.3 x 2.3 µm) was required for accurate axial localization, as ct-pSMLM with a large ROI cannot accurately describe the axial position around the focus. Then, all PSFs were localized directly with ct-pSMLM as described in the result section or via the SMAP software with fit3dSpline sub-pixel localization[26]. For ct-pSMLM, we used a 23 x 23 pixel ROI to calculate the z-position and a 43 x 43 pixel ROI to calculate the x and y position, and a 4^{th}-order polynomial was used to fit the calibration curve. For SMAP, calibration was performed with a 15-px Gaussian blur to find PSFs, a 51 x 51 pixel ROI, and 10 nm axial distance between every localization. For localization, a 10-px Gaussian blur was used to find PSFs, with a threshold of 20. A 41 x 41 pixel ROI spline fitting with 100 iterations based on the calibrated data was used to localize the PSFs.

Localization of experimental saddle-point data was performed with the SMALL-LABS-pSMLM software package. A median background subtraction with temporal window length of 150 frames and minimum duration of fluorophores to be discarded of 100 frames was used. Localizations were identified via a bandpass filter with a 95 threshold percentile. Potential lobes of saddle-point point spread functions were identified with a 3 pixel radius ROI 2D phasor fitting routine. Ct-pSMLM fitting was then performed with an 11 pixel radius ROI around the centre of localizations. Calibration was performed using simulated point spread functions at varying z-positions, consisting of 5000 photons on a noiseless background, with deformations similar to experimental data. Three-dimensional cross correlative drift correction was performed via the SMALL-LABS-pSMLM software, with 10 lateral subpixels and 10 temporal bins. The average shifted histogram image was created using ThunderSTORM[50], using 50 nm axial bins and 10 lateral subpixels.

3.5.5 Assessment of localization performance

For double-helix (DH), localizations between ground-truth (GT) and software 1 (S1; SMALL-LABS-pSMLM-DH) and between GT and software 2 (S2; SMAP with fit3dSpline) are linked on a frame-by-frame basis, with a maximum allowed lateral distance of 250 nm, and a maximum allowed axial distance of 500 nm. The median offset between GT and S1 and between GT and S2 is calculated and subtracted from the S1 and S2 datasets, to avoid introducing consistent offset errors in the RMSE calculations. The linking of localizations between GT and S1/S2 is repeated, as localizations can be shifted in/out of the maximum linking distance due to the median offset. Of this linked dataset, the Jaccard index is calculated as follows:

$$JACC = \frac{TPo}{TPo + FP + FN} \tag{3.1}$$

where TPo, FP, and FN are the true positive, false positive, and false negative localizations, respectively.

Then, only localizations that are present in all three datasets (GT, S1 and S2) are selected, and of these localizations, the root mean square error (RMSE) in a single dimension is calculated as follows:

$$RMSE = \frac{\sum_{i \in S} \sqrt{(p_i^S - p_i^{GT})^2}}{TP} \tag{3.2}$$

where p_i indicates the position of localization i in any dimension, and S indicates S1 or S2.

For saddle-point (SP), 1000 PSFs for every signal-to-noise combination were simulated (section 3.5.3), after which a calibration curve was created in SMALL-LABS-ct-pSMLM or SMAP with PSFs containing $3{\cdot}10^4$ photons on a 1 photon/pixel background. For SMAP localizations, obtained localizations well outside the expected regime (10 pixels or further removed from center) were discarded, and frames containing multiple or no localizations were fully discarded. Note, localizations obtained with SMAP that were clearly misfitted (an offset in z by at least 3 times the average z offset calculated by ct-pSMLM) were discarded; no such discarding was performed for ct-pSMLM.

For both ct-pSMLM and SMAP, the x, y and z positions were compared with the ground-truth, and the standard deviation of this offset was calculated for every intensity and background combination and is shown in the results. We note that the mean of the offset was centred around 0 for every tested intensity/noise/software combination.

3.5.6 Single-molecule microscopy

For SMLM experiments, we used a home-built super-resolution microscope similar to one reported previously[24]. Briefly, light from a fibre-coupled 642 nm laser (Omicron, Germany) was collimated using an achromatic lens (f = 30 mm, Thorlabs) and conducted to a parabolic mirror (RC12APC-P01, Thorlabs). The laser light was then focused using an achromat lens (f = 150 mm, Thorlabs) in front of a polychroic mirror (ZT532/640rpc, Chroma) into the backfocal plane of an 100x oil-immersion objective (CFI Plan Apo, NA = 1.45, Nikon Japan) such that a highly inclined illumination (HiLo) profile with a total laser power of ∼70 mW was achieved. Emitted fluorescence passing the objective, the polychroic mirror and a bandpass filter (ZET532/640m-TRF, Chroma) was then guided into a 4f geometry using the following lenses (1: f = 200 mm, 2: f = 100 mm, 3: f = 100 mm) towards a Prime 95B sCMOS camera (Photometrics, Tucson, AZ, USA), resulting in an effective 115 by 115 nm pixel size. A deformable mirror (DMP40-P01, Thorlabs) was placed in the Fourier plane between lens 2 and 3. The deformable mirror used 40 segments with bending arms for tip-tilt control to modulate and introduce different Zernike modes. After calibrating (flattening) the deformable mirror via the REALM software[52] (https://github.com/MSiemons/REALM and https://github.com/HohlbeinLab/Thorlabs_DM_Device_Adapter) we used the Zernike polynomials Z_2^2 (primary astigmatism) and Z_4^2 (secondary astigmatism) to induce saddle-point PSFs[38,40].

3.5.7 STORM experiment

A SAFe sample containing immobilised Cos7 fibroblasts from Green African Monkeys (ATCC) with Alexa Fluor 647 labelled tubulins was purchased from Abbelight (Paris, France). A nitrogen-flushed buffer containing 50 mM TRIS pH8, 10 mM NaCl, 10% glucose, 50 mM 2-mercaptoethanol, 68 µg/mL catalase, and 200 µg/mL glucose oxidase[27] was added to the sample chamber which was sealed off before the measurements. 60.000 frames of 20 ms length were recorded using the setup described in section 3.5.6. Analysis of the single-molecule data was performed as specified in section 3.5.4.

3.6 Funding

K.J.A.M was funded by a VLAG Ph.D. fellowship awarded to J.H. This work is part of the research programmes LICENSE and LocalBioFood with project numbers 731.017.301 and 731.017.204, which are financed by the Dutch Research Council (NWO).

3.7 Acknowledgements

We gratefully acknowledge Bernd Rieger and Sjoerd Stallinga (TU Delft) for sharing MATLAB code to simulate engineered point spread functions. We thank Julie Biteen, Laurent Geffroy, and Jonas Ries for helpful discussions on software. We thank Arjen Bader for fruitful discussions on applications of phasor analysis on single-molecule localization microscopy.

3.8 Author contributions

Conceptualisation: KM and JH. Data curation: KM, AJ, SY. Formal analysis: KM. Funding acquisition: JH. Investigation: KM, AJ, SY. Methodology: KM and JH. Project administration: JH. Software: KM. Supervision: JH. Visualisation: KM. Writing – original draft: KM. Writing – review & editing: All authors.

References

1. Schermelleh, L., Ferrand, A., Huser, T., *et al.* Super-Resolution Microscopy Demystified. *Nature Cell Biology* **21,** 72 (2019).
2. Vangindertael, J., Camacho, R., Sempels, W., *et al.* An Introduction to Optical Super-Resolution Microscopy for the Adventurous Biologist. *Methods and applications in fluorescence* **6,** 022003 (2018).
3. Heilemann, M. Fluorescence Microscopy beyond the Diffraction Limit. *Journal of Biotechnology. BioImaging - Contributions from Biology, Physics and Informatics* **149,** 243–251 (2010).
4. Rust, M. J., Bates, M. & Zhuang, X. Sub-Diffraction-Limit Imaging by Stochastic Optical Reconstruction Microscopy (STORM). *Nature methods* **3,** 793 (2006).
5. Heilemann, M., van de Linde, S., Schüttpelz, M., *et al.* Subdiffraction-Resolution Fluorescence Imaging with Conventional Fluorescent Probes. *Angewandte Chemie International Edition* **47,** 6172–6176 (2008).
6. Betzig, E., Patterson, G. H., Sougrat, R., *et al.* Imaging Intracellular Fluorescent Proteins at Nanometer Resolution. *Science* **313,** 1642–1645 (2006).
7. Gustafsson, M. G. Surpassing the Lateral Resolution Limit by a Factor of Two Using Structured Illumination Microscopy. *Journal of microscopy* **198,** 82–87 (2000).
8. Hell, S. W. & Wichmann, J. Breaking the Diffraction Resolution Limit by Stimulated Emission: Stimulated-Emission-Depletion Fluorescence Microscopy. *Optics letters* **19,** 780–782 (1994).
9. Hell, S. W. Toward Fluorescence Nanoscopy. *Nature biotechnology* **21,** 1347 (2003).
10. Dertinger, T., Colyer, R., Iyer, G., *et al.* Fast, Background-Free, 3D Super-Resolution Optical Fluctuation Imaging (SOFI). *Proceedings of the National Academy of Sciences of the United States of America* **106,** 22287–22292 (2009).
11. Gustafsson, N., Culley, S., Ashdown, G., *et al.* Fast Live-Cell Conventional Fluorophore Nanoscopy with ImageJ through Super-Resolution Radial Fluctuations. *Nature Communications* **7,** 12471 (2016).
12. Balzarotti, F., Eilers, Y., Gwosch, K. C., *et al.* Nanometer Resolution Imaging and Tracking of Fluorescent Molecules with Minimal Photon Fluxes. *Science* **355,** 606–612 (2017).
13. Smith, C. S., Joseph, N., Rieger, B., *et al.* Fast, Single-Molecule Localization That Achieves Theoretically Minimum Uncertainty. *Nature Methods* **7,** 373–375 (2010).
14. Abbe, E. Beiträge Zur Theorie Des Mikroskops Und Der Mikroskopischen Wahrnehmung. *Archiv für mikroskopische Anatomie* **9,** 413–418 (1873).
15. von Diezmann, A., Shechtman, Y. & Moerner, W. E. Three-Dimensional Localization of Single Molecules for Super-Resolution Imaging and Single-Particle Tracking. *Chemical Reviews* **117,** 7244–7275 (2017).
16. Stallinga, S. & Rieger, B. Accuracy of the Gaussian Point Spread Function Model in 2D Localization Microscopy. *Optics express* **18,** 24461–24476 (2010).
17. Sauer, M. & Heilemann, M. Single-Molecule Localization Microscopy in Eukaryotes. *Chemical Reviews* **117,** 7478–7509 (2017).
18. Baddeley, D. & Bewersdorf, J. Biological Insight from Super-Resolution Microscopy: What We Can Learn from Localization-Based Images. *Annual Review of Biochemistry* **87,** 965–989 (2018).
19. Endesfelder, U. From Single Bacterial Cell Imaging towards in Vivo Single-Molecule Biochemistry Studies. *Essays in Biochemistry* **63,** 187–196 (2019).
20. Stracy, M., Lesterlin, C., de Leon, F. G., *et al.* Live-Cell Superresolution Microscopy Reveals the Organization of RNA Polymerase in the Bacterial Nucleoid. *Proceedings of the National Academy of Sciences* **112,** E4390–E4399 (2015).
21. Stracy, M. & Kapanidis, A. N. Single-Molecule and Super-Resolution Imaging of Transcription in Living Bacteria. *Methods. Transcriptional Dynamics* **120,** 103–114 (2017).
22. Vink, J. N. A., Martens, K. J. A., Vlot, M., *et al.* Direct Visualization of Native CRISPR Target Search in Live Bacteria Reveals Cascade DNA Surveillance Mechanism. *Molecular Cell* **77,** 39–50.e10 (2020).
23. Turkowyd, B., Müller-Esparza, H., Climenti, V., *et al.* Live-Cell Single-Particle Tracking Photoactivated Localization Microscopy of Cascade-Mediated DNA Surveillance. *Methods in enzymology* **616,** 133–171 (2019).
24. Martens, K. J. A., van Beljouw, S. P. B., van der Els, S., *et al.* Visualisation of dCas9 Target Search in Vivo Using an Open-Microscopy Framework. *Nature Communications* **10,** 3552 (2019).
25. Thevathasan, J. V., Kahnwald, M., Cieśliński, K., *et al.* Nuclear Pores as Versatile Reference Standards for Quantitative Superresolution Microscopy. *Nature Methods* **16,** 1045–1053 (2019).
26. Li, Y., Mund, M., Hoess, P., *et al.* Real-Time 3D Single-Molecule Localization Using Experimental Point Spread Functions. *Nature Methods* **15,** 367–369 (2018).
27. Jimenez, A., Friedl, K. & Leterrier, C. About Samples, Giving Examples: Optimized Single Molecule Localization Microscopy. *Methods* (2019).
28. Mortensen, K. I., Churchman, L. S., Spudich, J. A., *et al.* Optimized Localization Analysis for Single-Molecule Tracking and Super-Resolution Microscopy. *Nature methods* **7,** 377 (2010).

29. Parthasarathy, R. Rapid, Accurate Particle Tracking by Calculation of Radial Symmetry Centers. *Nature Methods* **9,** 724–726 (2012).
30. Babcock, H. P. & Zhuang, X. Analyzing Single Molecule Localization Microscopy Data Using Cubic Splines. *Scientific Reports* **7,** 552 (2017).
31. Martens, K. J. A., Bader, A. N., Baas, S., *et al.* Phasor Based Single-Molecule Localization Microscopy in 3D (pSMLM-3D): An Algorithm for MHz Localization Rates Using Standard CPUs. *The Journal of Chemical Physics* **148,** 123311 (2018).
32. Franke, C., Sauer, M. & van de Linde, S. Photometry Unlocks 3D Information from 2D Localization Microscopy Data. *nature methods* **14,** 41 (2017).
33. Zhou, Y., Handley, M., Carles, G., *et al.* Advances in 3D Single Particle Localization Microscopy. *APL Photonics* **4,** 060901 (2019).
34. Huang, B., Wang, W., Bates, M., *et al.* Three-Dimensional Super-Resolution Imaging by Stochastic Optical Reconstruction Microscopy. *Science* **319,** 810–813 (2008).
35. Holtzer, L., Meckel, T. & Schmidt, T. Nanometric Three-Dimensional Tracking of Individual Quantum Dots in Cells. *Applied Physics Letters* **90,** 053902 (2007).
36. Henriques, R., Lelek, M., Fornasiero, E. F., *et al.* QuickPALM: 3D Real-Time Photoactivation Nanoscopy Image Processing in ImageJ. *Nature Methods* **7,** 339–340 (2010).
37. Pavani, S. R. P., Thompson, M. A., Biteen, J. S., *et al.* Three-Dimensional, Single-Molecule Fluorescence Imaging beyond the Diffraction Limit by Using a Double-Helix Point Spread Function. *Proceedings of the National Academy of Sciences* **106,** 2995–2999 (2009).
38. Shechtman, Y., Sahl, S. J., Backer, A. S., *et al.* Optimal Point Spread Function Design for 3D Imaging. *Physical Review Letters* **113,** 133902 (2014).
39. Shechtman, Y., Weiss, L. E., Backer, A. S., *et al.* Precise Three-Dimensional Scan-Free Multiple-Particle Tracking over Large Axial Ranges with Tetrapod Point Spread Functions. *Nano letters* **15,** 4194–4199 (2015).
40. Aristov, A., Lelandais, B., Rensen, E., *et al.* ZOLA-3D Allows Flexible 3D Localization Microscopy over an Adjustable Axial Range. *Nature Communications* **9,** 2409 (2018).
41. Sage, D., Pham, T.-A., Babcock, H., *et al.* Super-Resolution Fight Club: Assessment of 2D and 3D Single-Molecule Localization Microscopy Software. *Nature Methods* **16,** 387 (2019).
42. Petrov, P. N., Shechtman, Y. & Moerner, W. E. Measurement-Based Estimation of Global Pupil Functions in 3D Localization Microscopy. *Optics Express* **25,** 7945–7959 (2017).
43. Isaacoff, B. P., Li, Y., Lee, S. A., *et al.* SMALL-LABS: Measuring Single-Molecule Intensity and Position in Obscuring Backgrounds. *Biophysical Journal* **116,** 975–982 (2019).
44. Fereidouni, F., Bader, A. N. & Gerritsen, H. C. Spectral Phasor Analysis Allows Rapid and Reliable Unmixing of Fluorescence Microscopy Spectral Images. *Optics express* **20,** 12729–12741 (2012).
45. Nehme, E., Freedman, D., Gordon, R., *et al.* DeepSTORM3D: Dense 3D Localization Microscopy and PSF Design by Deep Learning. *Nature Methods*, 1–7 (2020).
46. Speiser, A., Turaga, S. C. & Macke, J. H. Teaching Deep Neural Networks to Localize Sources in Super-Resolution Microscopy by Combining Simulation-Based Learning and Unsupervised Learning. *arXiv:1907.00770 [cs, eess, stat].* arXiv: `1907.00770 [cs, eess, stat]` (2019).
47. Barsic, A., Grover, G. & Piestun, R. Three-Dimensional Super-Resolution and Localization of Dense Clusters of Single Molecules. *Scientific reports* **4,** 5388 (2014).
48. Izeddin, I., Boulanger, J., Racine, V., *et al.* Wavelet Analysis for Single Molecule Localization Microscopy. *Optics Express* **20,** 2081–2095 (2012).
49. Wang, Y., Schnitzbauer, J., Hu, Z., *et al.* Localization Events-Based Sample Drift Correction for Localization Microscopy with Redundant Cross-Correlation Algorithm. *Optics Express* **22,** 15982–15991 (2014).
50. Ovesny, M., Křížek, P., Borkovec, J., *et al.* ThunderSTORM: A Comprehensive ImageJ Plug-in for PALM and STORM Data Analysis and Super-Resolution Imaging. *Bioinformatics* **30,** 2389–2390 (2014).
51. Scott, D. W. Averaged Shifted Histograms: Effective Nonparametric Density Estimators in Several Dimensions. *The Annals of Statistics*, 1024–1040 (1985).
52. Siemons, M. E., Hanemaaijer, N. A. K., Kole, M. H. P., *et al.* REALM: AO-Based Localization Microscopy Deep in Complex Tissue. *bioRxiv*, 2020.06.12.147884 (2020).

3.9 Supplementary information

Table S3.1: Detailed analysis time for double-helix fitting by pSMLM-SL-DH.

	TIFF conversion	Intermediate file saving	Background subtraction	Total analysis time (s)	pSMLM-DH fitting time (s)
N1-LD	Yes	Yes	Yes	72.7 ± 1.7	1.4
(20.000 frames)	Yes	Yes	No	43.7 ± 1.0	1.4
	Yes	No	Yes	51.8 ± 0.4	1.4
	Yes	No	No	34.6 ± 0.8	1.4
	No	Yes	Yes	57 ± 1.1	1.4
	No	Yes	No	25.8 ± 0.3	1.4
	No	No	Yes	42 ± 0.2	1.4
	No	No	No	24.6 ± 0.2	1.4
N1-HD	Yes	Yes	Yes	13.4 ± 0.3	0.5
(2.000 frames)	Yes	Yes	No	5.8 ± 0.3	0.6
	Yes	No	Yes	8.5 ± 0.0	0.6
	Yes	No	No	4.2 ± 0.2	0.6
	No	Yes	Yes	11.6 ± 0.1	0.6
	No	Yes	No	3.9 ± 0.0	0.6
	No	No	Yes	8.2 ± 0.0	0.6
	No	No	No	3.8 ± 0.1	0.6

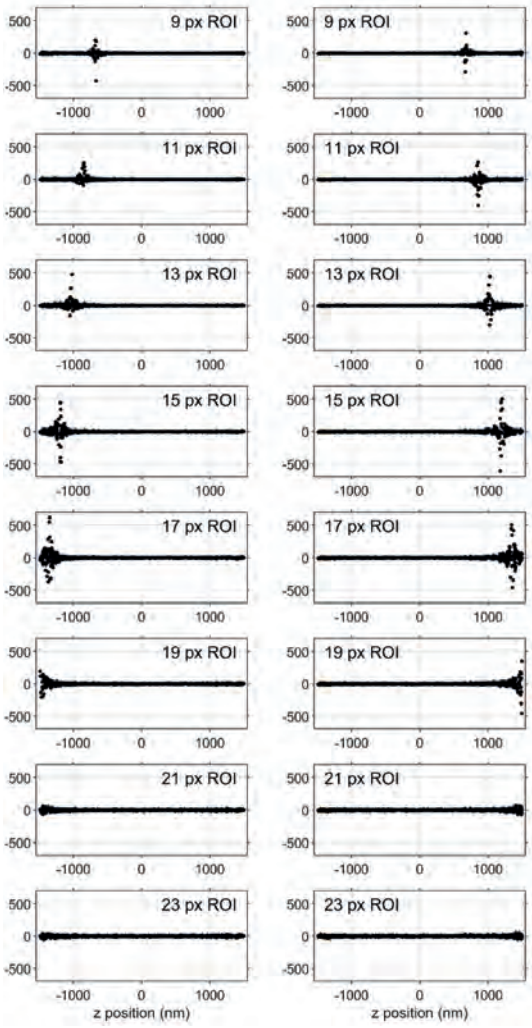

Figure S3.1: Offset (in nm) in y (left) and x (right) based on z position (x-axis) and ROI (vertical panels) used for ct-pSMLM. Note that the offset error is in the direction of the lobes (y-direction at negative z positions, x-direction at positive z positions), is very localized, and shifts with increasing ROI size towards more extreme z positions.

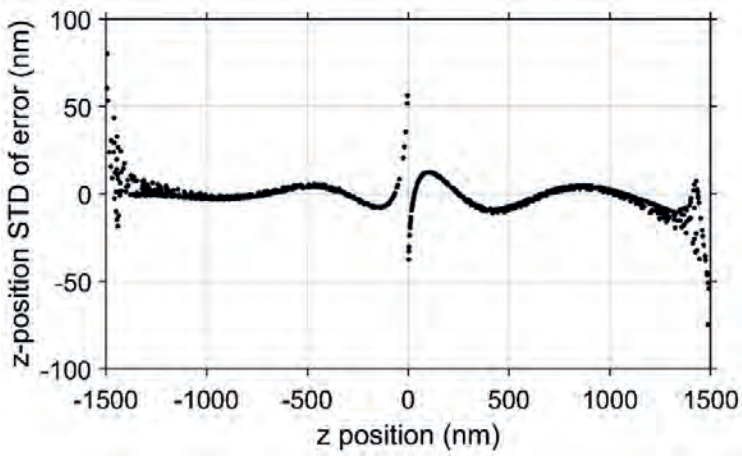

Figure S3.2: Lateral accuracy of ct-pSMLM as a function of z position, calculated via simulated PSFs without introduced noise. The mismatch between the fitted calibration curve and the actual distance is an effective lower limit of the lateral localization accuracy, and is on average 11 nm for our tested simulated PSFs.

4

Simple low-dispersion spectral single-molecule localization microscopy

Koen J.A. Martens, Emmanouil Archontakis, Roger R. Brillas, Lorenzo Albertazzi, Johannes Hohlbein

Abstract

Single-molecule localization microscopy (SMLM) is a powerful technique to elucidate structural and dynamic properties in life- and material science with sub 20 nm spatial resolution. The simultaneous acquisition of spectral information (spectral SMLM; sSMLM) can further increase the information content by providing opportunities for fluorophore multiplexing and the characterisation of local chemical environments caused by potential shifts in the emission spectra. The widespread utilisation of sSMLM, however, is hindered by an increased complexity of the optical detection pathway, lower accessible emitter densities, and compromised spatio-spectral resolution because the photon budget is spread over additional (camera) pixels. Here, we present a low-cost (∼€100) implementation of sSMLM with just 0.4 nm/pixel spectral dispersion, orders of magnitude lower than typical sSMLM implementations. We performed localization of both the spatial and spectral profiles with typical single-molecule localization algorithms, leading to a simple hardware set-up, a ∼5x increased maximum emitter density compared to existing approaches, and excellent spatio-spectral localization accuracy. We demonstrate spectral discrimination of fluorophores with just 10 nm spectral difference in dSTORM and DNA-PAINT, as well as applications in single-molecule FRET. We believe that the combination of low-cost hardware that is easy to install with straightforward data analysis via existing and future sub-pixel localization algorithms has the potential to find widespread use in microscopy.

4.1 Introduction

Super-resolution microscopy or nanoscopy has revolutionised life and material sciences as it allows surpassing the optical diffraction limit by more than an order of magnitude[1,2]. One frequently used implementation is single-molecule localization microscopy (SMLM), in which the stochastic activation of single fluorescent emitters leads to spatially separated point spread functions (PSFs) that are used to determine the position of the emitters with sub 20 nm accuracy. Localizations obtained via stochastic optical reconstruction microscopy (STORM) or point accumulation for imaging in nanoscale topography (PAINT)[1,3,4] provide access to detailed structural images, or can quantify dynamics and mobilities via single-particle tracking (spt)[5,6]. In this capacity, SMLM has led to breakthroughs in fields such as DNA replication, CRISPR-Cas, and soft matter[7–10].

Improving throughput via multiplexing of different fluorophores in SMLM, or enabling microenvironmental characterisation can be accomplished by combining SMLM with the additional spectral characterisation of emitters. Spectral information of single emitters has been acquired and analysed using various implementations that all rely on placing additional components into the optical detection pathway.

The first implementation, ratiometric distinction of spectral emission profiles, is based on placing of one (or more) suitable dichroic mirror(s) in the emission pathway[11–13]. Photons emitted from the sample are separated based on their wavelength, and directed towards two different detection channels. This entails either two separate detectors or using two areas on the same camera chip. Then, the PSFs and their integrated intensities obtained in the two channels are matched, and the intensity ratio of photons is used to discriminate between the emission spectra of different fluorophores. Importantly, this method requires photons to be directed towards each channel implicating that only a defined spectral range around the cut off wavelength of the dichroic mirror can be accessed.

In the second implementation, point spread function engineering, a spatial light modulator or a phase mask is employed in the Fourier plane of the emission path[14,15]. The introduced phase offset by these elements is depending on the incoming wavelength, which can be exploited to design a pattern so that different PSF shapes are realised when photons of different wavelength arrive at the detector. However, small spectral emission differences in the order of tens of nanometres in the peak emission cannot create sufficiently distinct PSF shapes, hindering discrimination of spectrally close fluorophores. Moreover, the voltage phase has to be specifically tuned for certain emission wavelengths, complicating this method when different fluorophores are used.

In the third implementation, spectral dispersion, a spectrally-dispersive optical element is added, after which the spatial and spectral profiles are guided to different regions on a single camera chip or to completely separate detectors[16–19]. The spatial profile is then analysed with regular single-molecule localization algorithms[20–23], while the spectral profile is spread out over tens of pixels and is used to determine the corresponding emission profile. While these approaches allow large spectral ranges to be used, and allow the discrimination of fluorophores with similar emission spectra, various downsides still exist. First, the entire emission pathway needs to be modified to allow separation of the spatial from the spectral channel. Furthermore, as the spectral channel is wide (tens of pixels), the signal-to-noise ratio obtainable in this channel is compromised,

leading to a loss in spectral accuracy[24]. The broad spreading of the emission also directly limits the usable density of emitters in the sample, as overlapping spectral profiles cannot be resolved.

Comparing these implementations, there remains a need to combine easy implementation with broad spectral range and good specificity. Here, we demonstrate spectrally resolved single-molecule localization microscopy (sSMLM) via an inexpensive (blazed) transmission grating that can be easily implemented in most microscope configurations. By using a grating with a large line pitch and placing it as close as possible to the camera, we created a low-dispersion sSMLM implementation in which the 0^{th} and 1^{st} diffraction order of every emitter is imaged in a single field of view and which does not require any additional optical elements such as mirrors, lenses, or filters. Our implementation is capable of accurately determining spectral properties of single molecules at 5x increased emitter density compared to traditional sSMLM implementations. With our sSMLM approach, we show the technical feasibility of single-excited 3-colour multiplexing and observable 0-to-15% FRET changes in single-molecule FRET experiments.

4.2 Results

4.2.1 Implementation and characterisation of minimal dispersion sSMLM

In order to maximise the achievable molecular density and the signal-to-noise ratio in spectral single-molecule localization microscopy (sSMLM), the available photon budget should be distributed over as few pixels as possible. Therefore, we opted for minimal spectral dispersion allowing to separate spatial from spectral information. In our implementation, we placed a transmission grating with the lowest commercially available diffraction (70 lines/mm) as close as possible to a camera chip ($<$ 1 cm, Figure 4.1a). This arrangement results in the minimum possible separation of 0^{th} and 1^{st} order diffraction patterns, and thus results in the highest achievable fluorophore density and signal-to-noise ratio for the 1^{st} order diffraction pattern (Figure 4.1b,c). Notably different from earlier implementations, this results in the full field of view containing both spatial and spectral information[16–19]. Our approach does not require the addition of any other optical components or secondary detectors.

Because the obtained 1^{st} order diffraction patterns behave similar to a point spread function (PSF), we employed existing super-resolution algorithms to obtain sub-pixel localizations of the 0^{th} and 1^{st} order diffraction patterns. Next, the localizations are linked with each other in the dispersion direction, with the distance between the 0^{th} and 1^{st} order diffraction patterns (d_1 and d_2 in Figure 4.1b; further called '0^{th}-to-1^{st}-order distance') being a direct measure for the emission wavelength of the emitter ($\lambda_1 < \lambda_2$ with $d_1 < d_2$). Moreover, the width of the 1^{st} order diffraction pattern, routinely used in astigmatic single-molecule fitting algorithms, is a measure for the width of the emission spectrum. This directly results in a spectral accuracy being limited solely by spatial super-resolution localization accuracy, a field which is progressing very rapidly via both software and hardware developments[20,25]. Moreover, the achievable density in our implementation without the need for specialised high-density fitting algorithms is 5x higher than earlier implementations of sSMLM, where the spectral information is spread out over 20-30 pixels[19] (Figure 4.1d, Methods).

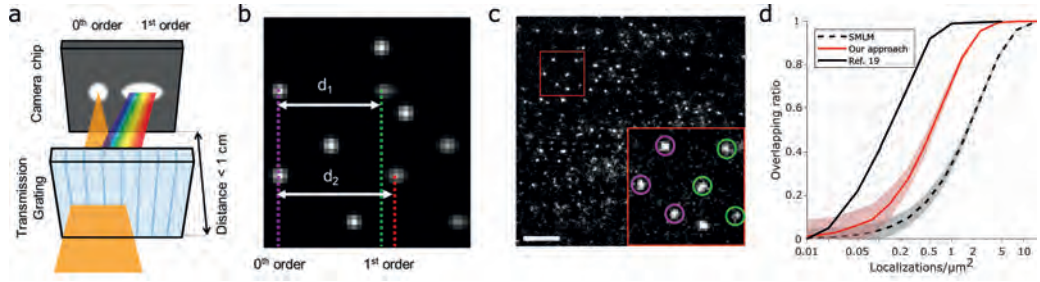

Figure 4.1: Grating based implementation of low-dispersion spectral single-molecule localization microscopy. **a** A low-dispersion transmission grating (blazed) is placed in the emission path of a typical SMLM microscopy such that the distance of the grating to the detector is as small as possible (<1 cm). Around 50% of the emission light will pass the grating without any diffraction, causing a 0^{th} order point spread function (PSF) to appear. The other ∼50% of the emission light is dispersed based on its wavelength and will create a second, slightly elongated 1^{st} order diffraction pattern. Image not to scale. **b** Simulation of low-dispersion sSMLM data of two spectrally different emitters with λ_1 (corresponding to d_1) $< \lambda_2$ (corresponding to d_2). Six emitters create in total 10 0^{th} and 1^{st} order diffraction patterns on the detector, which can be linked together (not all 1^{st} order diffraction patterns are visualised). The obtained distances between the 0^{th} and 1^{st} order diffraction patterns (d_1 and d_2) are a measure for the mean emission wavelength. **c** Raw data as recorded by our sSMLM implementation, showing 85 spatiospectrally resolvable emitters in a 31 x 31 µm field of view. Red outline is enlarged in the inset, in which the 0^{th} order patterns are encircled in magenta, while the 1^{st} order diffraction patterns are encircled in green. Scale bar represents 5 µm. **d** Comparison of achievable density in normal (non-spectral) SMLM (black dotted line), our approach (red line), and sSMLM with 20-30 pixels spectral pattern elongation, taken from ref [19]. The shaded background indicates a single standard deviation.

We determined the distance between the dispersion-inducing optics of the grating to the camera chip to be 6.9 ± 0.1 mm in our system (Methods, Figure S4.1a,b). The spectral dispersion (SD) was determined by calculating the 0^{th}-to-1^{st}-order distance of a sample labelled with ATTO542 and ATTO655 (Figure S4.1c). From the median distance of these obtained distances and the mean emission profile of the fluorophores, a SD of ∼4.7 nm/nm (equivalent here to 0.4 nm/pixel) was determined. We further did not observe a wavelength dependency on the angle between the spatial and spectral profiles (Figure S4.1d).

4.2.2 Multiplexing of 10 nm spectrally separated fluorophores in dSTORM and DNA-PAINT

The excellent signal-to-noise ratio of the obtained 1^{st} order diffraction pattern, combined with high resolution of sub-pixel localization algorithms indicates that small spectral differences can be elucidated. With our sSMLM implementation, we imaged double-labelled fixated Cos7 cells, in which clathrin was labelled with CF660, and microtubulin with CF680. Pseudo-colour coding a super-resolved image based on 0^{th}-to-1^{st}-order distance reveals good separation of the labelled structures without further analysis (Figure 4.2a), even though these fluorophores only have a ∼10 nm intensity-weighted spectral separation in our microscope (CF660: 691.9 nm, CF680: 701.6 nm, Figure 4.2b).

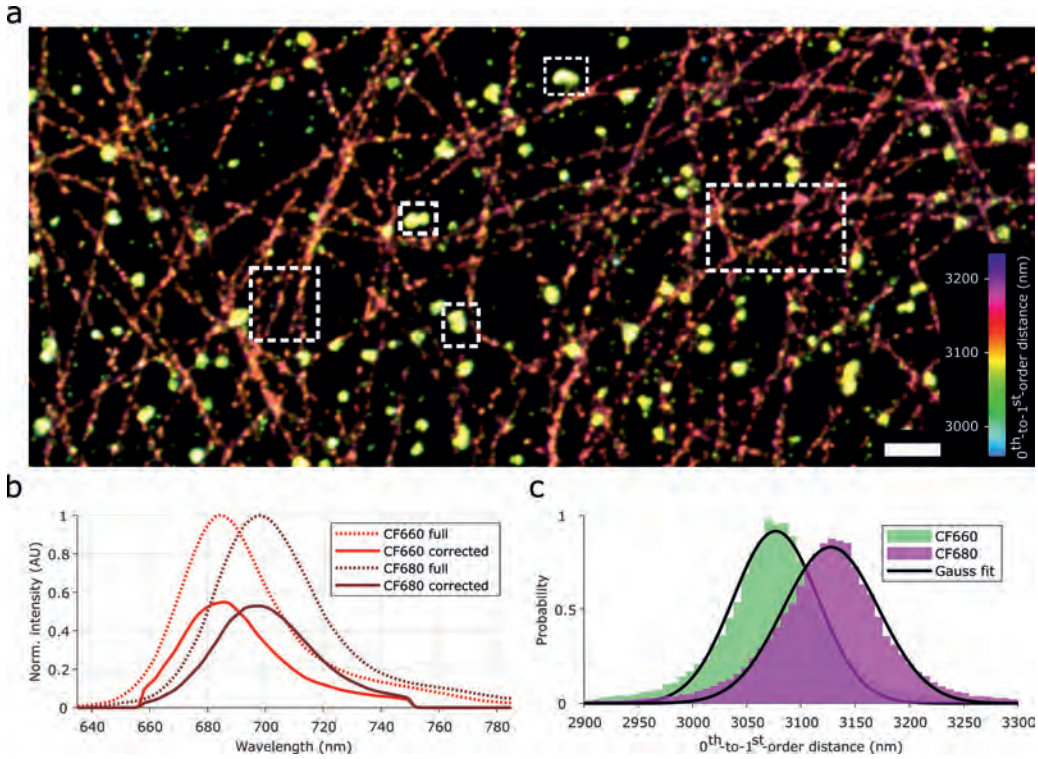

Figure 4.2: Multiplexing STORM of fixated Cos7 cells with CF660-labelled clathrin and CF680-labelled microtubules. **a** Obtained STORM image, colour-coded on 0^{th}-to-1^{st}-order distance. Separation between microtubule and clathrin can be observed without further data analysis. Scale bar represents 1 µm. **b** Emission spectra of CF660 (bright red) and CF680 (dark red). Dotted lines represent full spectra, while the solid lines represent emission spectra corrected for the transmission characteristics of the optical components present in the microscope. **c** Histograms representing 0^{th}-to-1^{st}-order distances of fluorophores belonging to areas indicated by dotted outlines in a. These populations are fitted with Gaussian curves (see main text), and attributed to CF660 (green) or to CF680 (magenta).

Binning image regions with only CF660-labelled structures or with only CF680-labelled structures (dotted outlines in Figure 4.2a), and fitting the corresponding 0^{th}-to-1^{st}-order distances with a Gaussian profile reveals that CF660 has a 0^{th}-to-1^{st}-order distance of 3077 $\pm$ 2 nm (σ = 56 $\pm$ 2 nm; mean $\pm$ 95% CI), with 3128 $\pm$ 2 nm for CF680 (σ = 62 $\pm$ 2 nm; Figure 4.2c). This is a difference of 51 $\pm$ 2 nm in the raw data, which corresponds to a spectral distance of 10.9 $\pm$ 0.4 nm, in agreement with the emission profiles.

Next, we performed a DNA-PAINT experiment with polystyrene nanoparticles (NPs) with DNA-PAINT imager strands bearing either ATTO647N or ATTO655 (Figure 4.3a). These fluorophores have a weighted average emission wavelength separated only ~9 nm (684.5 and 693.4 nm, respectively, after correcting for optical components in our microscope (Figure 4.3b)), and a peak emission wavelength separated ~16 nm (664 and 680 nm, respectively). After outlining of the in-

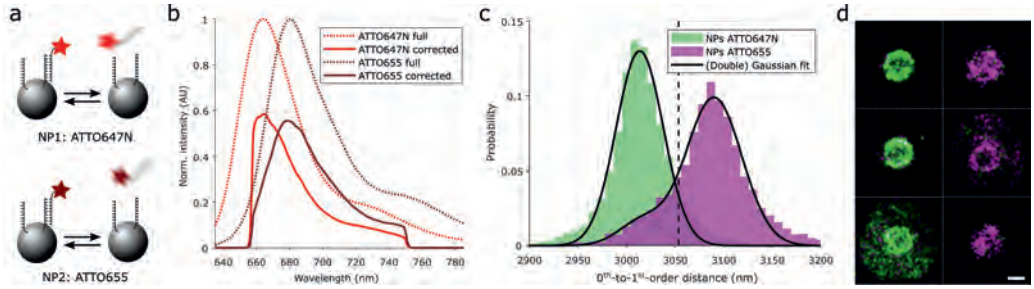

Figure 4.3: Low-dispersion sSMLM is capable of resolving ATTO647N from ATTO655 in DNA-PAINT. **a** Two different nanoparticles have associated DNA-PAINT imager strands containing either ATTO647N or ATTO655. Scheme not on scale. **b** Emission spectra of ATTO647N (bright red) and ATTO655 (dark red). Dotted lines represent full spectra, while the solid lines represent emission spectra corrected for the optical components present in the microscope. **c** Histograms representing observed 0^{th}-to-1^{st}-order distances of fluorophores belonging to individual NPs, and hand-attributed to either population. These populations are fitted with Gaussian curve(s) (see main text), and attributed to NPs accepting ATTO647N-DNA (green) or to NPs accepting ATTO655-DNA (magenta). **d** Visualisation of individual NPs, with individual localizations colour-coded based on the dotted line shown in b. Note that these NPs are spatially further separated in the original images. Scale bar represents 500 nm.

dividual beads and analysing the 0^{th}-to-1^{st}-order distances of emitters belonging to the NPs, two populations can be observed (Figure 4.3c).

The population with the lowest 0^{th}-to-1^{st}-order distance (green; Gaussian fit peak position: 3014 ± 1 nm, $\sigma = 34 \pm 1$ nm, mean ± 95% CI,) was attributed to ATTO647N fluorophores. The population with the larger distances (magenta) was fitted with a combination of the Gaussian curve fitted to the first observed population, along with a unique Gaussian curve (Gaussian fit peak position: 3090 ± 2 nm, $\sigma = 41 \pm 3$ nm). This population was attributed to ATTO655 fluorophores. The larger standard deviation of the ATTO655 population compared to the ATTO647N population can be attributed to a lower median localization accuracy (42 nm vs 50 nm), possibly caused by a difference in quantum yield (65% vs 30%). The spectral distance between these fitted peak positions (76 ± 2 nm distance; corresponding to 16.2 ± 0.4 nm spectral separation) is higher than expected from the spectra. This is possibly caused by deviations of the described wavelength-dependant efficiency of optical elements compared to our hardware implementation, which could lead to a shifted weighted mean emission wavelength of ATTO647N, as its emission maximum is close to the spectral cut-off (∼660 nm).

Next, all linked localizations were colour-coded according to their distance (cut-off at the black dotted line in Figure 4.3c at 3054 nm). Visualisation of the individual NPs (Figure 4.3d) then reveals their fluorophore distribution. This shows that the NPs are populated by either one DNA-PAINT docking strand or the other, with minimal cross-talk between the used fluorophores.

Taken together with the dSTORM data of the fixated cells, the obtained order of the mean emission wavelength of all four fluorophores (ATTO647N, CF660, ATTO655, CF680) coincided with that of the 0^{th}-to-1^{st}-order distance (mean emission wavelength: 684.6, 691.9, 693.4, 701.3 nm; mean 0^{th}-to-1^{st}-order distance: 3014, 3077, 3090, 3128 nm). The separation of these 0^{th}-

to-1st-order distances suggests that simultaneous multiplexing of at least three fluorophores with single-wavelength excitation is technically possible with our sSMLM implementation under realistic experimental conditions.

4.2.3 Elucidation of single-molecule FRET states via sSMLM

Next, we were interested whether we could expand the low-dispersion sSMLM to assess single-molecule Förster resonance energy transfer (smFRET). In a typical smFRET experiment, probes labelled with a donor and an acceptor fluorophore are immobilised on a surface, and monitored over time. Depending on the experiment, changes in FRET and/or changes in acceptor/donor activity (i.e. blinking, bleaching) can be expected. Normally, a ratiometric spectral determination method is applied to separate the donor emission from the acceptor emission on different positions on a camera chip, and the intensity ratio between these is a measure for the relative FRET efficiency E. However, in our implementation, we can use the full field of view of our camera, and determine E via the 0th-to-1st-order distance, as well as the width of the 1st order diffraction pattern.

We performed smFRET measurements on well-characterised samples[26] of immobilised double-stranded DNA strands dual-labelled with ATTO550 and ATTO647N. Two samples were used: 23-bp separation (∼8.5 nm) and 15-bp separation (∼5.6 nm), leading to FRET efficiencies of ∼0.15 and ∼0.55, respectively. First, we performed simulations (Methods; Figure 4.4a,b) based on our sSMLM implementation and the theoretical emission profiles (corrected for the fluorophore's quantum yield and the optical elements in our microscope). These simulations of donor-only, 15% FRET, and 55% FRET samples show that the 0th-to-1st-order distance follows $d_{\mathrm{donor}} < d_{15\%\mathrm{FRET}} < d_{55\%\mathrm{FRET}}$, while the width of the 1st order diffraction pattern follows $\sigma_{55\%\mathrm{FRET}} < \sigma_{15\%\mathrm{FRET}} < \sigma_{\mathrm{donor}}$.

Experimentally, the immobilised 15% FRET and 55% FRET DNA strands were imaged separately with 561 nm excitation for 250 s. Contrary to the multiplexing before, both the 0th-to-1st-order distance and the width of 1st order diffraction pattern are measures for the FRET efficiency and were therefore visualised (Figure 4.4c,d). The experimental data agrees with the simulations showing $d_{\mathrm{donor}} < d_{15\mathrm{FRET}} < d_{55\mathrm{FRET}}$ (2620 nm, 2653 nm, 2781 nm, respectively) and $\sigma_{\mathrm{donor}} < \sigma_{15\mathrm{FRET}} < \sigma_{55\mathrm{FRET}}$ (172 nm, 204 nm, 238 nm, respectively).

Next, we explored to which extend we can monitor dynamic behaviour using spectrally resolved smFRET. While no direct state transitions are expected for this sample, there is occasional acceptor fluorophore blinking or bleaching, leading to a transition of FRET emission to donor-only emission. For this, we fitted the combined [d, σ] 2-dimensional histogram with four 2-dimensional Gaussian profiles (Figure 4.4c,d black crosses and ellipses). These profiles comprise donor-only, 15% FRET efficiency, 55% FRET efficiency, and 'background' states (background state not shown). The 'background' state is attributed to nonsense linkages occurring from sparse localizations unrelated to the FRET sample.

Time traces of individual emitters were further assessed (Figure 4.4e-h). The likelihood of an emitter belonging to the states determined before was calculated (Methods), and the most likely state determines the background colour of the graphs in Figure 4.4e,g. With this methodology, we were able to determine acceptor bleaching (Figure 4.4e) and acceptor blinking (Figure 4.4g) in 15% and 55% FRET experimental data. Accurate state determination of the 15% FRET measurement

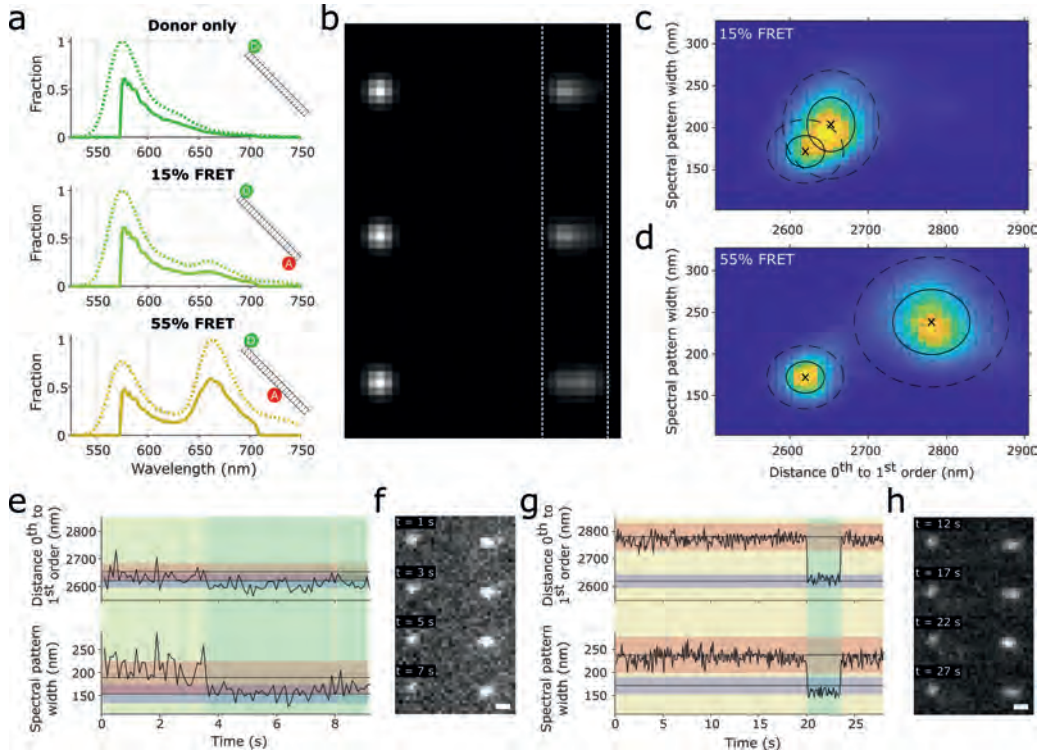

Figure 4.4: Single-molecule FRET analysis with low-dispersion sSMLM. **a** Predicted emission spectra of donor-only (top, ATTO550), 15% FRET (middle), and 55% FRET (bottom). Dotted lines represent full spectra, while the solid lines represent emission spectra corrected for the transmission characteristics of the optical components present in the microscope. Schemes represent donor (green; ATTO550) and acceptor (red; ATTO647N) fluorophore placements on a DNA strand. **b** Simulated raw data obtained in our low-dispersion sSMLM implementation, based on the emission profiles determined in a. Vertical dotted white lines are a guide for the eye. **c,d** 2-dimensional histograms of experimental data of 15% FRET (c) and 55% FRET (d). The histograms were globally fitted with multiple Gaussian functions (shown here centred around black crosses, with solid ellipses representing 1 sigma, and dotted ellipses representing 2 sigma; Methods, main text). **e-h** Single emitter time trace analysis of a bleaching acceptor fluorophore in a 15% FRET pair (e,f), and of a blinking acceptor fluorophore in a 55% FRET pair (g,h). Horizontal grey lines with red and blue shading represent 15% (e) or 55% (g) FRET populations (red) and donor-only populations (blue), determined from the fit in c,d. The vertical green, yellow, orange shading represented current FRET pair state, with green representing donor-only, yellow representing 15% FRET, and orange representing 55% FRET. The raw data corresponding to these FRET pairs throughout the observation time is shown in f,h. Scale bars in f,h represent 500 nm.

proved to be difficult due to the overlapping Gaussian profiles representing the FRET and donor-only states (Figure 4.4c), whereas this was better discriminable for 55% FRET (Figure 4.4d).

4.3 Discussion

We have demonstrated minimal-dispersion spectral SMLM (sSMLM), which fundamentally maximises signal-to-noise and emitter density due to lowest possible photon spread on the detector. In our implementation, we used a single optical component add-on to the detection path leading to a spectral dispersion of just ∼0.04 nm/pixel, orders of magnitude lower than typical grating-based sSMLM implementations. With this implementation, we realised a five times increased emitter density, achieved good separation of emitters with a ∼10 nm intensity-weighted spectral difference in STORM, and were able to observe changes between 0 and 15% FRET efficiency in smFRET.

The low spectral dispersion allows us to use sub-pixel localization algorithms, a field that is advancing rapidly[20], and all future developments are directly applicable to our sSMLM implementation. This could open up avenues for better spatial and spectral precision, more information obtained from the 1^{st} order pattern shape, and sSMLM at even higher emitter density. Recent work by Song et al employed sub-pixel localization algorithms for sSMLM based on data obtained via the -1^{st} and $+1^{st}$ orders of a non-blazed transmission grating[27]. While this solution is elegant and uses all photons that arrive on the camera chip for both spatial and spectral localization, blocking out the 0^{th} order leads to a significant loss of photons. Moreover, the implementation requires additional optical components (mirrors and lenses) to direct only the -1^{st} and $+1^{st}$ orders on the camera chip. Earlier theoretical work[24], not employing sub-pixel localization algorithms, discussed a best possible sSMLM implementation with spectral dispersions of ∼1-4 nm/pixel. This determined minimum was ultimately dependant on pixel-based analysis, but with sub-pixel localization we demonstrated accurate sSMLM with ∼2 orders of magnitude lower spectral dispersion (∼5 nm/nm, or ∼0.04 nm/pixel).

Further reduction of the spectral dispersion will depend on overcoming current practical and physical limitations. In our implementation, we have used a low-dispersion blazed grating (70 lines/mm), and placed this as close to the camera chip (6.9 mm) as possible. A blazed grating with lower line density is technically possible to create, however, its efficiency is likely to decrease, obscuring whether it will actually lead to better overall data. Placing a grating even closer to the camera chip is possible especially on lower-end (s)CMOS cameras, where the sensor is not additionally sealed as in our camera[28]. In any case, further minimisation of spectral dispersion without loss of signal would lead to higher achievable spatial and spectral precision than reported here. A trade-off of spectral dispersion minimisation is a decreased information content about the shape of the emission spectrum. In this study, we use the shape of the emission spectrum to discriminate FRET states from the donor-only state.

Taken together, we believe that our implementation of low-dispersion sSMLM will find widespread use in the life and material sciences due to its inherent simplicity and photon efficiency providing access to maximised spatiotemporal and spectral resolution. We further envision applications in which the photon efficient separation of spectrally different entities is desired, such as in low-signal flow cytometry. Here, the ideas taken from super-resolution microscopy such as sub-pixel localization and spectral peak determination can be equally applied even for low magnification configurations.

4.4 Material and methods

4.4.1 Microscopy

All microscopy is performed on a home-build super-resolution microscopy fully described elsewhere[9]. Briefly, a 561 nm and 642 nm laser line were employed in epifluorescent, HiLo, or TIRF (depending on the experiment) illumination via a Nikon 100x 1.49 NA HP/SR objective. The emission light was guided via the bypass mode of a rescan confocal microscope to a Zyla 4.2 plus sCMOS (at 2 x 2 pixel binning, 122 nm effective pixel size) controlled by the micromanager software[29]. Either a 405/488/561 dichroic mirror and filter set (ZT405/488/561rpc and ZET405/488/561m-TRF, Chroma, Bellows Falls, VT, USA) for the smFRET experiments, or a 405/488/561/642 dichroic mirror and filter set (ZT405/488/561/642rpc and ZET405/488/561/642m-TRF, Chroma) was used. The second set was only used in experiments where the 642 nm laser line was employed, unless specified differently.

Details implementation grating

A blazed transmission grating (70 grooves/mm, Edmund Optics, Barrington, NJ, USA, part nr 46-067) was housed in a 3D-printed plastic insert and was inserted in the inner tube of a Zyla 4.2 PLUS sCMOS camera. An external C-mount threaded retainer ring (Thorlabs, Newton, NJ, USA, part id CMRR) was then threaded to keep the grating in this place, and the retainer ring was glued to the plastic insert for repeatable insertion of the grating.

4.4.2 Multiplexing fixated cells

Immobilised Cos7 cells with CF660-immunostained clathrin and CF680-immunostained microtubulin (Abbelight; France) were imaged for 100.000 frames at 20 ms frametime and 80 mW 642 nm laser illumination. A STORM buffer (Abbelight) was added directly before sealing of the sample and ∼5 minutes before the start of imaging. STORM imaging was started after ∼2 minutes of 80 mW at 642 nm laser illumination to turn the molecules in their off-state.

4.4.3 Multiplexing with polystyrene nanoparticles

Streptavidin-coated polystyrene nanoparticles (NPs) with a diameter of 400-700 nm (SVP-05-10; Spherotech, Lake Forest, IL, USA) were functionalized with single-stranded DNA (ssDNA) by mixing biotinylated ssDNA (20 µM) with the NPs (10 mg/mL) for 1 hr at room temperature. Two analogue batches were created. Batch NP1 consists of nanoparticles equipped with docking strand 1 (TTATACATCTA); NP2 are equipped with docking strand 2 (TTTCTTCATTA), following earlier protocols[30]. An imager solution was prepared, containing imager strand 1 (CTAGATGTAT), which is conjugated with ATTO647N and complementary to docking strand 1, found on NP1; and imager strand 2 (GTAATGAAGA), conjugated with ATTO655 and complementary to docking strand 2, found on NP2.

A sample was created consisting of 1:1 ratio of 1 mg/ml NP1, NP2 adsorbed for ∼10 minutes between oven-cleaned coverslips (500 °C for 20 minutes to remove organic impurities[31]). Subsequently a solution containing a 1:1 ratio of 5 nM imager strand 1 and 2 was added. Imaging was

performed with a 642 nm laser in TIRF at 80 mW, with 100 ms frame time for 2500 frames, without any additional emission filter present.

4.4.4 smFRET

Biotinylated double-stranded DNA labelled with ATTO550/ATTO647N with 23-bp (15% FRET) or 15-bp (55% FRET) separation was obtained via a multi-lab study on FRET measurements (1-lo, 1-mid)[26]. PEGylated and biotinylated coverslips were created following an earlier protocol[32]. Briefly, oven-cleaned (500 °C for 20 minutes to remove organic impurities[31]) coverslips were washed in acetone, and incubated in 1:50 Vectabond (in acetone; Vector labs, Burlingame, CA, USA). Wells were created via silicone gaskets, and incubated with 200 mg/ml NHS-PEG (Laysan Bio, Arab, AL, USA) and 2.5 mg/ml NHS-biotin-PEG (Laysan Bio) in 50 mM MOPS buffer. Then, ∼20 µl 0.02 mg/ml neutravidin was added, and after rinsing, 20 pM of the biotinylated DNA was added. Four movies of 2500 frames of 100 ms each were recorded using ∼20 mW 561 nm of laser light in TIRF mode, without an additional emission filter.

4

4.4.5 General computational analysis

A single-molecule dataset was localized via ThunderSTORM[33] for FIJI[34,35], with the pSMLM plugin[22], after performing a 50-frame temporal median filter (https://github.com/marcelocordeiro/medianfilter-imagej). A β-spline wavelet filter with scale 2 and order 3, with a local maxima finder with a threshold set to the standard deviation of wave F1 of the filter multiplied by 1.5, and a non-calibrated 3D astigmatism Gaussian fitting routine or a pSMLM routine with ROI (region of interest) 11 x 11 or 5 x 5, respectively, was used. For analyses where the width of the PSFs was critical (i.e. the smFRET experiments), analysis was performed by SMAP with the fit3dSpline fitter[21] without a calibrated PSF model. Here, a difference-of-Gaussian filter with size 3 was used alongside an absolute photon cut-off value of 0.3 with a 5 pixel NMS kernel size, to identify PSFs. Fitting was performed with an elliptical PSF with a 13 pixel ROI, 30 iterations. No further filtering was performed.

Linking of the localizations found in this dataset was performed with a methodology adapted from linking individual lobes of a double-helix point spread function[36]. Briefly, the localizations in each frame are compared with each other to find pairs within a larger-than-expected distance and rotation regime. While it is expected that the localizations are not rotated with respect to each other (i.e. a rotation of 0 rad), slight inconsistencies in placing the grating can lead to small rotations (< 0.1 rad; Figure S4.1). Then, the positions of the leftmost localization (the spatial localization) is stored alongside information about the rightmost localization (the spectral localization). The final information consists of the position of the spatial localization, the distance and angle between the two localizations, and (if applicable) the obtained PSF width in both dimensions for the spatial and the spectral localizations.

4.4.6 smFRET analysis

For the spectral smFRET analysis, the general analysis workflow as presented above was used (fitted with SMAP[21]). In addition, the obtained 0^{th}-to-1^{st}-distances and the spectral widths of all

found pairs were plotted for each experiment (comprised of 4 movies of 2500 frames each) as a 2D histogram. The sum of the 2D histograms of 15% and 55% FRET was fitted with 4 Gaussian profiles, representing donor-only, 15% FRET, 55% FRET, and background populations. For visualisation, these Gaussian profiles were re-fitted to either the 15% FRET or the 55% 2D histograms, only changing the relative intensities of the profiles, but not their position or spread.

Thereafter, individual linked pairs (i.e. a 0^{th} and 1^{st} order pattern) were classified as 'FRET', 'Donor Only', or 'Background', based on the likelihood of belonging to each Gaussian profile. Individual linked pairs were furthermore linked to other linked pairs throughout time via a simple Nearest-Neighbours tracking algorithm[37], with maximum 1 pixel movement between frames. Only tracks of at least 10 positions without donor blinking events were investigated further.

4.4.7 Spectral SMLM simulation

A simulation of the expected spatial and spectral diffraction patterns was performed in MATLAB 2018b (The Matworks, Natick, MA, USA) based on physical properties of the grating and its placement. First, the emission spectrum on which the simulation is based is quantised in single wavelength units (i.e. a resolution of 1 nm). For every wavelength, the angle of the 1^{st} order diffraction with respect to the 0^{th} order diffraction is calculated (based on a specified density of grooves of the grating: 70 mm^{-1} in our implementation), and is used to gain the spatial position of the 1^{st} order diffraction pattern on the camera chip (based on a specified distance of the grating to the detector). Then, a point spread function is approximated via a 2-dimensional Gaussian function, positioned at the 0^{th} order and the 1^{st} order diffraction pattern positions, where the positions are offset by a pre-defined random position between 0 and 1 final pixel size. These are then normalised for its relative intensity (specified by the emission profile and by the efficiencies of the diffraction orders (41% and 32% for the 0^{th} and 1^{st} order, respectively)). This simulation is first done over-sampled on a grid with 1 nm^2-sized pixels, before it is binned into 122 x 122 nm pixels, corresponding to our sSMLM hardware.

4.4.8 Simulating the resolvable emitter density

The resolvable emitter density possible in our implementation was simulated in MATLAB 2019b (The MathWorks, Natick, MA, USA) with similar conditions as performed previously[19]. A 20-by-20 µm frame was filled with emitters specified by a certain density. Then, localizations that are located closer than 3 pixels (here 0.388 µm) are indicated as 'overlapping'. For our sSMLM implementation, a secondary localization was placed to the right of the primary emitter with a randomly chosen distance between 2500 and 3400 nm, and was taken into consideration for overlapping scenarios. This was repeated 500 times at every density, and the mean and standard deviation was determined.

4.4.9 Characterisation

Distance grating to camera chip

While the absolute distance between the camera chip and the grating is initially unknown, a full rotation of the C-mount thread corresponds to exactly $1/32^{\text{th}}$ inch (∼0.8 mm). Four sSMLM experiments with increasingly more full rotations of the grating away from the camera were recorded. The median value of the resulting distance between the 0^{th} and the 1^{st} order is plotted against the absolute distance that the grating is removed from the closest position. Fitting and extrapolating this curve with a 1^{st} order polynomial then reveals the distance of the grating to the chip at the crossing of the curve with the x-axis (Figure S4.1b).

Spectral dispersion

A 2D DNA-PAINT (Gattaquant, Germany) containing ATTO542 and ATTO655 fluorophores was imaged with either a 561 nm or a 642 nm laser activated. The 0^{th}-to-1^{st}-order distance was calculated, and the difference in the median distance is divided by the difference of the weighted mean of the fluorophore emission profiles. The fluorophore emission profiles were corrected for the optics and detector used in the microscopy system[9].

4.5 Competing interests

K.J.A.M. and J.H. have a manuscript and patent in preparation regarding low-dispersion spectral microscopy.

References

1. Rust, M. J., Bates, M. & Zhuang, X. Sub-Diffraction-Limit Imaging by Stochastic Optical Reconstruction Microscopy (STORM). *Nature methods* **3,** 793 (2006).
2. Hell, S. W. & Wichmann, J. Breaking the Diffraction Resolution Limit by Stimulated Emission: Stimulated-Emission-Depletion Fluorescence Microscopy. *Optics letters* **19,** 780–782 (1994).
3. Jungmann, R., Avendaño, M. S., Woehrstein, J. B., *et al.* Multiplexed 3D Cellular Super-Resolution Imaging with DNA-PAINT and Exchange-PAINT. *Nature methods* **11,** 313 (2014).
4. Sharonov, A. & Hochstrasser, R. M. Wide-Field Subdiffraction Imaging by Accumulated Binding of Diffusing Probes. *Proceedings of the National Academy of Sciences* **103,** 18911–18916 (2006).
5. Manley, S., Gillette, J. M., Patterson, G. H., *et al.* High-Density Mapping of Single-Molecule Trajectories with Photoactivated Localization Microscopy. *Nature Methods* **5,** 155–157 (2008).
6. Shen, H., Tauzin, L. J., Baiyasi, R., *et al.* Single Particle Tracking: From Theory to Biophysical Applications. *Chemical Reviews* **117,** 7331–7376 (2017).
7. Elf, J. & Barkefors, I. Single-Molecule Kinetics in Living Cells. *Annual Review of Biochemistry* (2019).
8. Wöll, D. & Flors, C. Super-Resolution Fluorescence Imaging for Materials Science. *Small Methods* **1,** n/a–n/a (2017).
9. Martens, K. J. A., van Beljouw, S. P. B., van der Els, S., *et al.* Visualisation of dCas9 Target Search in Vivo Using an Open-Microscopy Framework. *Nature Communications* **10,** 3552 (2019).
10. Uphoff, S., Reyes-Lamothe, R., de Leon, F. G., *et al.* Single-Molecule DNA Repair in Live Bacteria. *Proceedings of the National Academy of Sciences* **110,** 8063–8068 (2013).
11. Purohit, A., Benigno, S. P. C., Richtering, W., *et al.* Microgel PAINT–Nanoscopic Polarity Imaging of Adaptive Microgels without Covalent Labelling. *Chemical Science* (2019).
12. Baddeley, D., Crossman, D., Rossberger, S., *et al.* 4D Super-Resolution Microscopy with Conventional Fluorophores and Single Wavelength Excitation in Optically Thick Cells and Tissues. *PloS one* **6,** e20645 (2011).
13. Testa, I., Wurm, C. A., Medda, R., *et al.* Multicolor Fluorescence Nanoscopy in Fixed and Living Cells by Exciting Conventional Fluorophores with a Single Wavelength. *Biophysical journal* **99,** 2686–2694 (2010).

14. Shechtman, Y., Weiss, L. E., Backer, A. S., *et al.* Multicolour Localization Microscopy by Point-Spread-Function Engineering. *Nature photonics* **10,** 590 (2016).
15. Broeken, J., Rieger, B. & Stallinga, S. Simultaneous Measurement of Position and Color of Single Fluorescent Emitters Using Diffractive Optics. *Optics Letters* **39,** 3352–3355 (2014).
16. Dong, B., Almassalha, L., Urban, B. E., *et al.* Super-Resolution Spectroscopic Microscopy via Photon Localization. *Nature Communications* **7,** 1–8 (2016).
17. Mlodzianoski, M. J., Curthoys, N. M., Gunewardene, M. S., *et al.* Super-Resolution Imaging of Molecular Emission Spectra and Single Molecule Spectral Fluctuations. *PloS one* **11,** e0147506 (2016).
18. Zhang, Y. S., Ribas, J., Nadhman, A., *et al.* A Cost-Effective Fluorescence Mini-Microscope for Biomedical Applications. *Lab on a Chip* **15,** 3661–3669 (2015).
19. Bongiovanni, M. N., Godet, J., Horrocks, M. H., *et al.* Multi-Dimensional Super-Resolution Imaging Enables Surface Hydrophobicity Mapping. *Nature communications* **7,** 13544 (2016).
20. Sage, D., Pham, T.-A., Babcock, H., *et al.* Super-Resolution Fight Club: Assessment of 2D and 3D Single-Molecule Localization Microscopy Software. *Nature Methods* **16,** 387 (2019).
21. Li, Y., Mund, M., Hoess, P., *et al.* Real-Time 3D Single-Molecule Localization Using Experimental Point Spread Functions. *Nature Methods* **15,** 367–369 (2018).
22. Martens, K. J. A., Bader, A. N., Baas, S., *et al.* Phasor Based Single-Molecule Localization Microscopy in 3D (pSMLM-3D): An Algorithm for MHz Localization Rates Using Standard CPUs. *The Journal of Chemical Physics* **148,** 123311 (2018).
23. Smith, C. S., Joseph, N., Rieger, B., *et al.* Fast, Single-Molecule Localization That Achieves Theoretically Minimum Uncertainty. *Nature Methods* **7,** 373–375 (2010).
24. Song, K.-H., Dong, B., Sun, C., *et al.* Theoretical Analysis of Spectral Precision in Spectroscopic Single-Molecule Localization Microscopy. *Review of Scientific Instruments* **89,** 123703 (2018).
25. Xu, F., Ma, D., MacPherson, K. P., *et al.* Three-Dimensional Nanoscopy of Whole Cells and Tissues with in Situ Point Spread Function Retrieval. *Nature Methods* **17,** 531–540 (2020).
26. Hellenkamp, B., Schmid, S., Doroshenko, O., *et al.* Precision and Accuracy of Single-Molecule FRET Measurements—a Multi-Laboratory Benchmark Study. *Nature Methods* **15,** 669–676 (2018).
27. Song, K.-H., Zhang, Y., Brenner, B., *et al.* Symmetrically Dispersed Spectroscopic Single-Molecule Localization Microscopy. *Light: Science & Applications* **9,** 92 (2020).
28. Diekmann, R., Till, K., Müller, M., *et al.* Characterization of an Industry-Grade CMOS Camera Well Suited for Single Molecule Localization Microscopy–High Performance Super-Resolution at Low Cost. *Scientific Reports* **7,** 14425 (2017).
29. Edelstein, A. D., Tsuchida, M. A., Amodaj, N., *et al.* Advanced Methods of Microscope Control Using μManager Software. *Journal of Biological Methods* **1,** e10 (2014).
30. Schnitzbauer, J., Strauss, M. T., Schlichthaerle, T., *et al.* Super-Resolution Microscopy with DNA-PAINT. *Nature protocols* **12,** 1198 (2017).
31. Hübner, C. G., Renn, A., Renge, I., *et al.* Direct Observation of the Triplet Lifetime Quenching of Single Dye Molecules by Molecular Oxygen. *The Journal of Chemical Physics* **115,** 9619–9622 (2001).
32. Evans, G. W., Hohlbein, J., Craggs, T., *et al.* Real-Time Single-Molecule Studies of the Motions of DNA Polymerase Fingers Illuminate DNA Synthesis Mechanisms. *Nucleic Acids Research* **43,** 5998–6008 (2015).
33. Ovesny, M., Křížek, P., Borkovec, J., *et al.* ThunderSTORM: A Comprehensive ImageJ Plug-in for PALM and STORM Data Analysis and Super-Resolution Imaging. *Bioinformatics* **30,** 2389–2390 (2014).
34. Abràmoff, M. D., Magalhães, P. J. & Ram, S. J. Image Processing with ImageJ. *Biophotonics international* **11,** 36–42 (2004).
35. Schindelin, J., Arganda-Carreras, I., Frise, E., *et al.* Fiji: An Open-Source Platform for Biological-Image Analysis. *Nature methods* **9,** 676–682 (2012).
36. Martens, K. J. A., Jabermoradi, A., Yang, S., *et al.* Integrating Engineered Point Spread Functions into the Phasor-Based Single-Molecule Localization Microscopy Framework. *In preparation* (2020).
37. Isaacoff, B. P., Li, Y., Lee, S. A., *et al.* SMALL-LABS: Measuring Single-Molecule Intensity and Position in Obscuring Backgrounds. *Biophysical Journal* **116,** 975–982 (2019).

4.6 Supplementary information

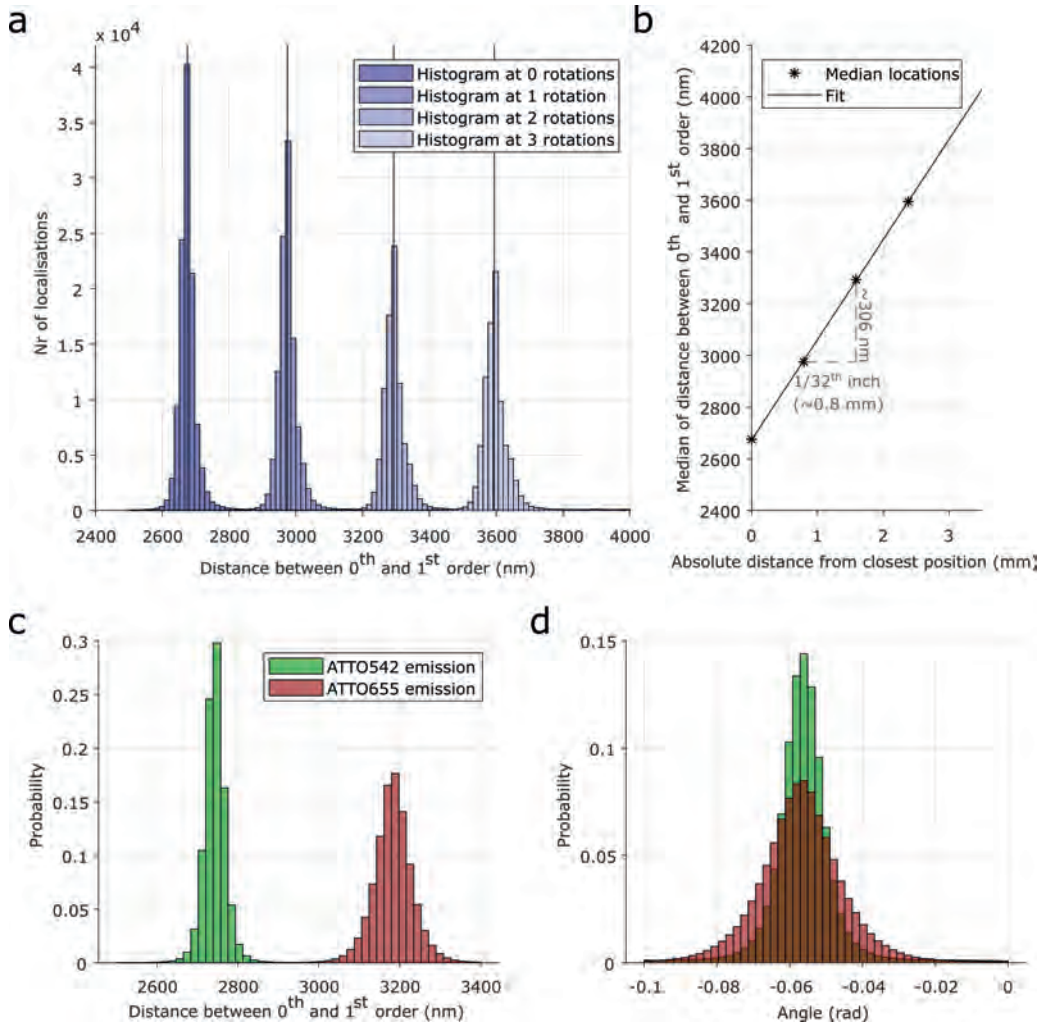

Figure S4.1: Calibration of low-dispersion sSMLM. **a,b** Determination of distance between grating and camera chip. The grating is incrementally distanced from the camera by a series of rotations (every rotation is $1/32^{\text{th}}$ inch or ~0.8 mm). The histograms of the obtained distances between the 0^{th} and 1^{st} order are plotted in a, while the linear fit of the median distances is shown in shown in b. **c,d** Determination of the spectral distance (SD). A DNA-PAINT sample with ATTO542 and ATTO655 fluorophores was imaged. The distances (c) show a clear difference between the two fluorophores, while the angle (d) is not influenced.

5

Evaluating single-particle tracking by photo-activation localization microscopy (sptPALM) in *Lactococcus lactis*

A version of this chapter has been published as:

Sam P.B. van Beljouw*, Simon van der Els*, **Koen J.A. Martens***, Michiel Kleerebezem, Peter A. Bron, and Johannes Hohlbein. Evaluating single-particle tracking by photo-activation localization microscopy (sptPALM) in *Lactococcus lactis*. *Physical biology* **16**, no. 3 (2019)

* These authors contributed equally

Abstract

Lactic acid bacteria (LAB) are frequently used in food fermentation and are invaluable for the taste and nutritional value of the fermentation end-product. To gain a better understanding of underlying biochemical and microbiological mechanisms and cell-to-cell variability in LABs, single-molecule techniques such as single-particle tracking photo-activation localization microscopy (spt-PALM) hold great promises but are not yet employed due to the lack of detailed protocols and suitable assays.

Here, we qualitatively test various fluorescent proteins including variants that are photoactivatable and therefore suitable for sptPALM measurements in *Lactococcus lactis*, a key LAB for the dairy industry. In particular, we fused PAmCherry2 to dCas9 allowing the successful tracking of single dCas9 proteins, whilst the dCas9 chimeras bound to specific guide RNAs retained their gene silencing ability in vivo. The diffusional information of the dCas9 without any targets showed different mechanistic states of dCas9: freely diffusing, bound to DNA, or transiently interacting with DNA. The capability of performing sptPALM with dCas9 in *L. lactis* can lead to a better, general understanding of CRISPR-Cas systems as well as paving the way for CRISPR-Cas based interrogations of cellular functions in LABs.

5.1 Introduction

Lactic acid bacteria are Gram-positive microbes that produce lactic acid as the main end product of sugar fermentation, thereby contributing to preservation and microbial safety of fermented foods. In addition, these bacteria are also essential for the taste, texture, and nutritional value properties of these products[1]. In particular, *Lactococcus lactis* is extensively used in the production of dairy products such as butter and cheese but also shows promise as a producer of flavour compounds, vitamins, and other nutraceuticals[2–4] . Moreover, the potential of *L. lactis* as a microbial cell factory and as vector for therapeutic protein delivery has recently been highlighted[5], suggesting that *L. lactis* approaches the applicability of other well-established biotechnological work horses such as *Escherichia coli* and *Bacillus subtilis*, while having the benefit of being a well-established food-grade bacterium. Furthermore, it is known that *L. lactis* employs bet-hedging strategies under specific conditions, resulting in high inter-cellular heterogeneity[6], emphasising the relevance of single-cell studies in *L. lactis*.

Despite great progress in the field of industrial microbiology, the function and spatial organisation of many cellular proteins remain elusive. Super-resolution microscopy is capable of detecting individual proteins in living bacteria and as such has revealed intricate cellular dynamics and organisation[7]. A promising super-resolution microscopy method to inquire molecular motion in vivo is single-particle tracking photo-activation localization microscopy (sptPALM)[8]. SptPALM allows tracking of individual entities in living cells with nanometre (∼40 nm) precision and millisecond (∼10 ms) temporal resolution[8,9], enabling the characterisation of single protein kinetics and dynamics in real time[10,11].

In typical sptPALM measurements, a photoactivatable fluorescent protein (PA-FP) is genetically fused to the protein of interest, enabling non-invasive live cell imaging[12]. As PA-FPs have the intrinsic ability to undergo 'on'-switching in the presence of activation illumination (Figure 5.1a)[13], careful tuning of the activation light intensity allows imaging of individual proteins in a sequential manner thereby avoiding overlapping emission signals. Molecules that have not yet been activated or already have been (photo-)bleached remain in a dark state. By focusing on a single particle at a time, the motion of the active particle can be determined by analysing its position in several subsequent frames until the PA-FP turns dark (Figure 5.1b). The procedure is then repeated to generate precise quantification of the proteins behaviour, often via analysis of the diffusion coefficient.

Although other industrially relevant bacteria have been tested in their compatibility with single-particle tracking and as such have revealed dynamic cellular mechanisms[14–17], single-particle tracking in *L. lactis* was reported only by us[18]. Here, we provide a detailed overview about all steps necessary to develop functional sptPALM assays and experiments in *L. lactis*. We first test various PA-FPs that can be applied in *L. lactis* (see also reference [19] for benchmarking conventional fluorescent proteins (FPs) in *L. lactis*), explain methods to label a protein of interest and elucidate quantitative information. To demonstrate sptPALM, we PAmCherry2-tagged catalytically-inactive Cas9 (dCas9), provided together with single guide RNA on a separate plasmid, and monitored its mobility in the cellular environment. The ability to perform quantitative single-particle tracking of dCas9, and more generally, of CRISPR-Cas systems, facilitates further research of the mechanistic details of these systems. As CRISPR-(d)Cas has a well-established and important role in genomic

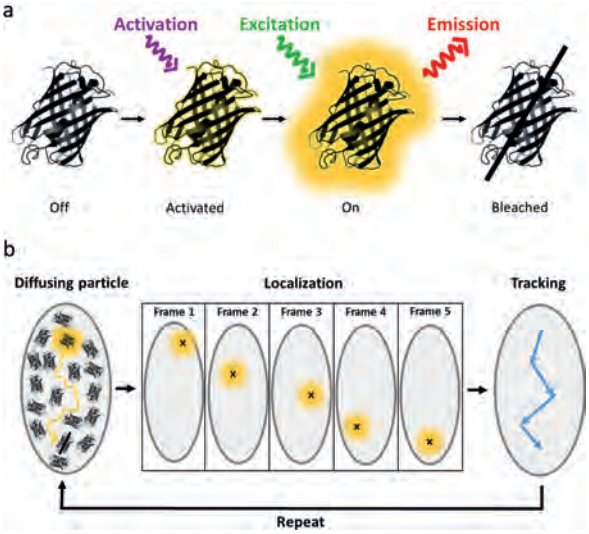

Figure 5.1: Single-particle tracking PALM. **a** Photoactivatable proteins are activated from an initial non-fluorescent state upon activation irradiation. The activated state can then be excited, after which it emits fluorescence until the fluorophore either irreversibly bleaches or returns to a long-lived dark state. **b** By controlling the activation rate, only one or a small subset of the FPs get stochastically activated per cell at a time. The majority of proteins, which have not yet been activated, remain in a dark state. The movement of the fluorescent molecule is followed by localizing its position in consecutive frames and subsequent connections of the localizations to form a trajectory. Tracks of many molecules are obtained by repeating the cycle.

5

silencing and editing[20–22], this increased understanding is especially valuable in industrially relevant organisms such as *L. lactis*.

5.2 Results

5.2.1 Evaluation of (photoactivatable) FPs in *L. lactis*

In order to test the compatibility of several FPs with *L. lactis*, we constructed strains harbouring pNZ8150 derivatives for the nisin-controlled expression of PAmCherry2, PATagRFP, mScarlet, mScarlet-I, mScarlet-H, mTurq2 or sYFP2 in the nisRK expressing host NZ9000 (Figure 5.2a). Fluorescent protein expression was evaluated with fluorescence microscopy. Low-level expression was detected in non-induced (−nisin) cells, whereas high expression (i.e. high level fluorescence) was observed in induced cells (+nisin) (Figure 5.2b). The photoactivatable FPs (PAmCherry2 and PATagRFP) responded appropriately to nisin induction and photoactivation, only becoming emissive after photoactivation with a 405 nm laser (Figure 5.2c). Multiple cell divisions were observed when the cells were grown on an agar pad under microscopy conditions at room temperature (Figure S5.1), indicating that the cells remained alive during sample preparation and imaging.

5.2.2 Genetic design of fluorescently labelled dCas9

Catalytically inactive Cas9 (dCas9) strongly binds to specific nucleotide sequences. This feature allows the employment of dCas9 for many applications, including DNA visualisation and gene silencing[21,23,24]. Moreover, dCas9 can be used as a model for normal Cas9 to elucidate mechanistic and protein behavioural details.

We designed a *L. lactis* codon-optimised plasmid encoding fluorescently labelled dCas9 (Figure 5.3). The engineered gene encodes a FP that is fused via a flexible linker (amino acid

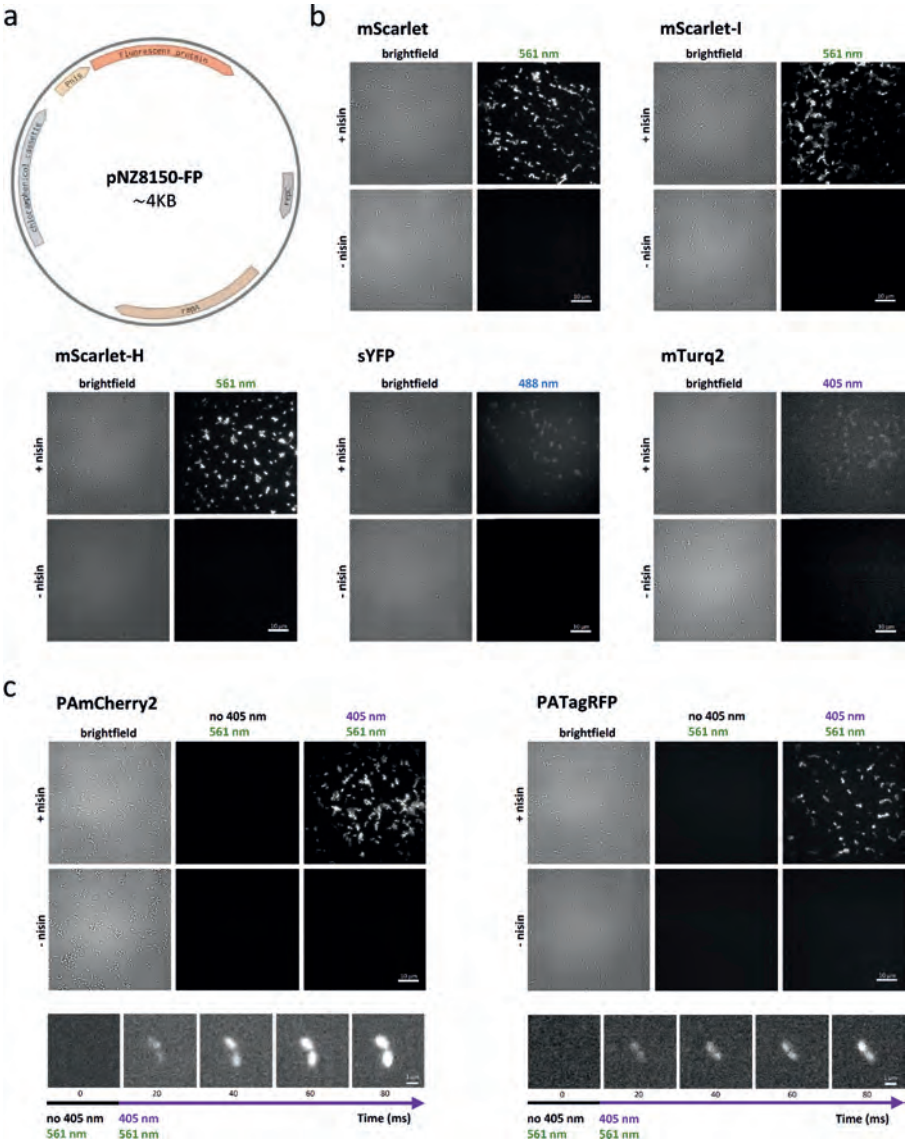

Figure 5.2: Nisin induction and photoactivation of FPs in *L. lactis*. **a** Annotated outline of the pNZ8150 derivatives for the expression of the FPs under the nisin-promoter. **b** Non-photoactivatable FP expression in cells after high induction (+nisin). Non-induced (−nisin) cells showed hardly any fluorescence. **c** PAmCherry2 and PATagRFP photoactivation after exposure to the 405 nm laser. Without 405 nm exposure, hardly any fluorescence is observed.

sequence: GSGSS) to the C-terminus of dCas9; dCas9-PAmCherry2. This gene was cloned under

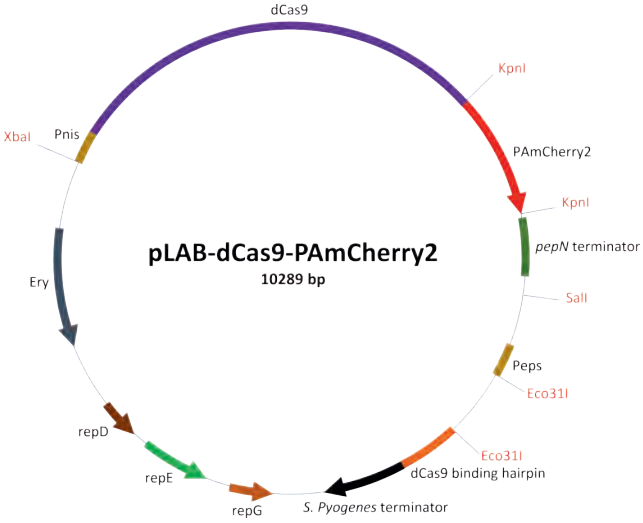

Figure 5.3: Schematic representation of pLAB-dCas9-PAmCherry2. The pIL253 derived expression vector encodes the PAmCherry2 labelled dCas9 under control of the nisin-promoter (P*nis*), contains an erythromycin resistance marker (Ery), replication genes (repD, repE and repG), and a cloning site (Eco31I) for sgRNA insertion and expression under control of the constitutive *eps* promoter (P*eps*).

transcriptional control positioned of the *nisA* promoter in a pIL253 derived vector-backbone (conferring erythromycin resistance), allowing its nisin-controlled expression (plasmid was designated pLAB-dCas9-PAmCherry2). The engineered gene contains restriction endonuclease target sites that allow interchanging of the FP and/or dCas9 encoding region by other FP encoding sequences or other CRISPR-associated nucleases, respectively. Furthermore, the plasmid contains a convenient site for sgRNA introduction and expression (driven by the eps_{b40} promoter[25] and appropriately spaced relative to the required Cas9 binding hairpin and *Streptococcus pyogenes* terminator) that was derived from the previously described pLABTarget vector[26].

5.2.3 Functional evaluation of fluorescently labelled dCas9 in *L. lactis*

In order to validate appropriate functionality of the dCas9-PAmCherry2 expression and photoactivation, cells harbouring pLAB-dCas9-PAmCherry2 were nisin-induced and imaged. Expression was evaluated with fluorescence microscopy, with a 561 nm laser for excitation and a 405 nm laser for photoactivation. Low-level fluorescence was detected in non-induced (−nisin) cells (Figure 5.4), whereas high level and fluorescence was detected following photoactivation in nisin induced cells (+nisin).

The use of protein chimeras requires verification of the activity and characteristics of both proteins. Therefore, we verified that dCas9-PAmCherry2 is still able to localize and bind target sites in a sgRNA-dependent manner, by performing CRISPR interference (CRISPRi) experiments[27]. To this end, we inserted a sgRNA in the vector that targets the major-autolysin encoding *acmA* gene that plays a critical role in proper cell segregation during cell division and mutation of this gene have been shown to result in chain formation of cells[28]. Different sgRNAs were designed to target the *acmA* gene in different ways (gene/promoter in template/non-template strand), which are expected to have different outcomes in terms of silencing of the *acmA* gene. Targeting dCas9

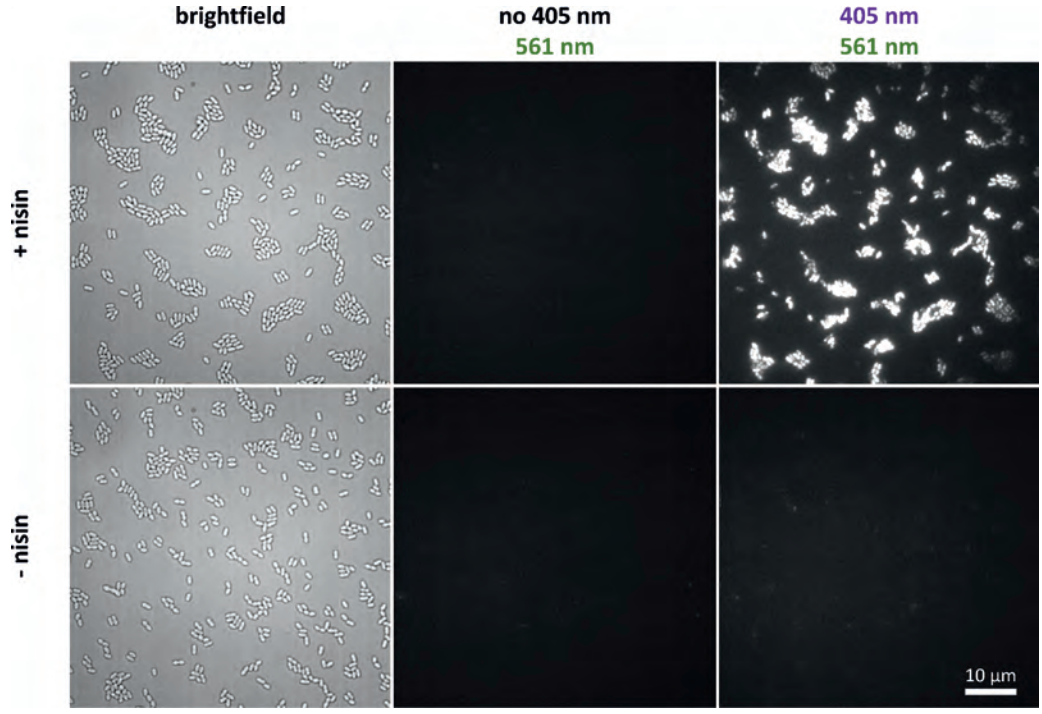

Figure 5.4: dCas9-PAmCherry2 nisin induction and photoactivation. Cells harbouring pLAB-dCas9-PAmCherry2 after 3 h of induction (+nisin) with 5 ng ml^{-1} nisin compared to non-induced (−nisin) cells. After exposure to 405 nm, substantial fluorescent signal was detected.

to the −10 and −35 promoter regions on the template as well as the non-template DNA strand is expected to block transcription initiation and thereby effectively silence the expression of *acmA*. In contrast, targeting of dCas9 to bind within the coding region of the gene is only expected to silence *acmA* expression when the sgRNA targets the non-template strand[23]. Employing sgRNAs that target dCas9-PAmCherry2 to these sites within the gene and its upstream region, we observed chain formation according to our expectation (Figure 5.5), indicating that dCas9-PAmCherry2 can effective bind its target sites, and is functioning appropriately in CRISPRi gene silencing.

5.2.4 Tracking single dCas9-PAmCherry2 molecules in *L. lactis*

After ensuring dCas9-PAmCherry2 chimeras retained their capacity to effectively bind to targeted DNA sequences in a sgRNA-dependent manner, we set out to perform single-particle tracking on these proteins to obtain more detailed information on dCas9. We used *L. lactis* containing dCas9-PAmCherry2 in combination with a sgRNA that lacks a full-length (20 bp) matching target site within the chromosomal or plasmid DNA[18]. This allows us to ensure that, with such imperfect sgRNA, dCas9-PAmCherry2 is unable to bind on a minute time-scale[21], but still allows shorter-term dCas9 binding events at PAM sites and at sites with partial sgRNA-DNA complementarity[29].

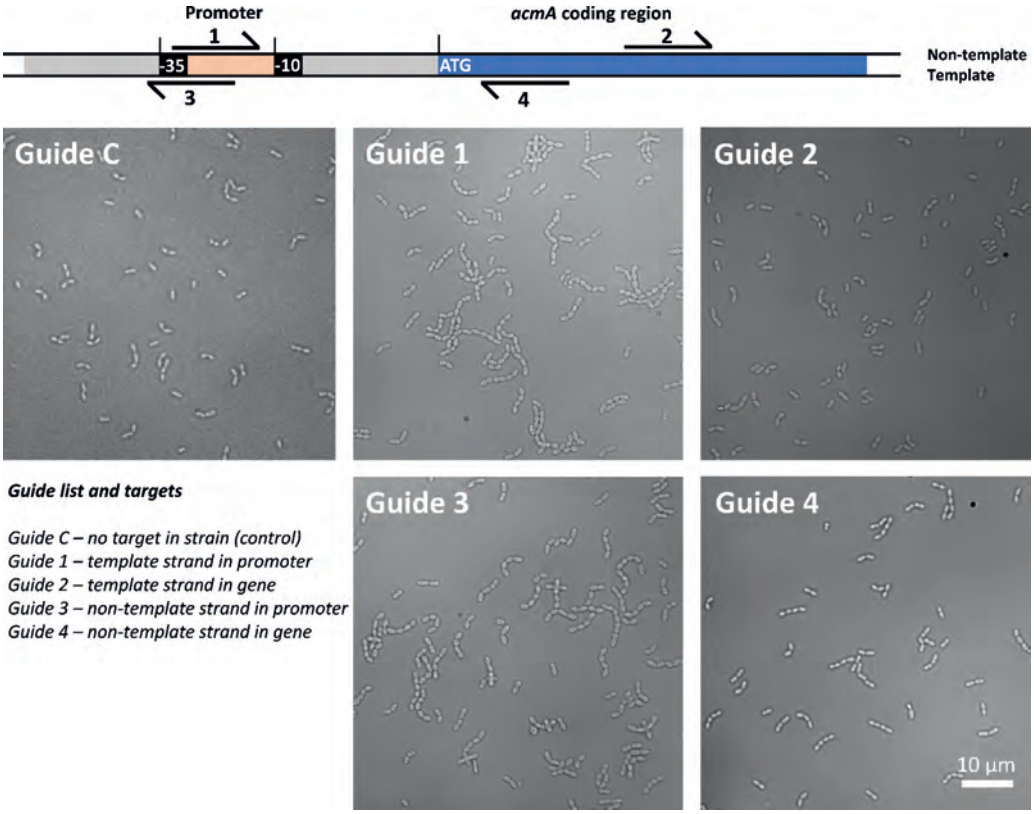

Figure 5.5: CRISPRi with dCas9-PAmCherry2. Cells expressing dCas9-PAmCherry2 guided to different sequences around the *acmA* gene. Chain formation was observed in the cells for which CRISPRi was expected. The sgRNA sequences can be found in Table 5.1.

To perform the tracking, individual fluorophores need to be activated with no overlapping signal from adjacent particles. This was achieved by using low level induction (0.4 ng ml^{-1} nisin) and low-activation laser intensity (2.7-619 µW cm^{-2}; for comparison, data shown in in Figure 5.4 was achieved using 5 ng ml^{-1} nisin and 800 µW cm^{-2} activation laser intensity) such that on average less than one photoactivated particle is present in a single cell in the same frame.

For sptPALM, we first recorded brightfield images (Figures 5.6a,b), which are used to computationally segment individual cells (c). Then, individual fluorophores are activated and localized in multiple subsequent frames until turning to dark states (d and e). The localizations of the single particles are connected if they occur in close proximity in consecutive frames within the cell outline, resulting in dCas9 trajectories per individual cell (f).

The tracks corresponding to individual particles were assessed with regards to their apparent diffusion coefficient, which is directly related to the average distance travelled per time unit. The apparent diffusion coefficients of all dCas9-PAmCherry2 particles is represented in a single his-

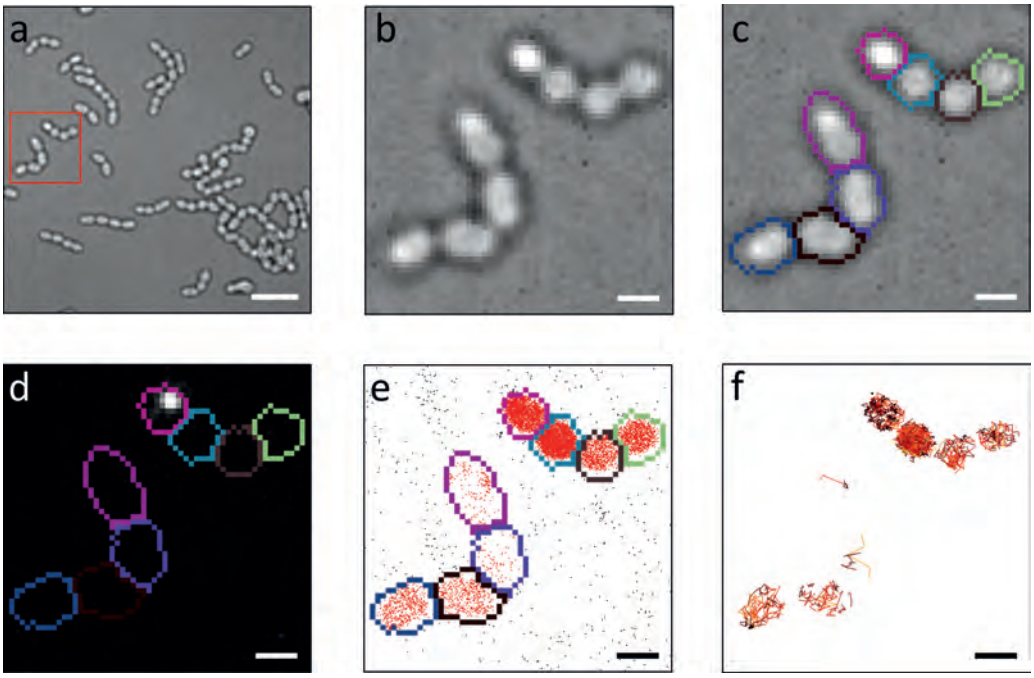

Figure 5.6: Single-particle data analysis steps. An image of the cells is made by averaging the intensities of 200 brightfield images (**a**, selection shown in the red square is enlarged in **b**), which is used as input for the Interactive Watershed plug-in in Fiji to construct a watershed image (**c**). Raw data (**d**) is localized with ThunderSTORM and filtered on the cell outline (**e**; localizations within a cell are marked in red, localizations outside a cell in black). Tracking is then performed on the localizations that were found within the cell outline (**f**). Scale bar represents 5 µm (a) or 1 µm (b)-(f).

togram (Figure 5.7a), and fitted with a combination of diffusional states. Three distinct populations were observed.

The slowest population is fully determined by the localization uncertainty inherently present in a microscopy system[30], and is therefore attributed to immobile dCas9-PAmCherry2 proteins. The fastest population agrees with diffusion of dCas9-PAmCherry2 restricted in a small *L. lactis* cell through viscous and crowded cytoplasm[18]. The remaining population is governed by transient interactions that occur on timescales of the order of the acquisition time of single frames (10 ms). These represent quick interactions to DNA, such as PAM screening or partial DNA matching[18].

Transitions between the three distinct states can be inferred from rare long-lived tracks (>250 ms, Figure 5.7b). Individual tracks indicate transitions in mobility, with state occupancies in tens of ms-range (Figure 5.7c).

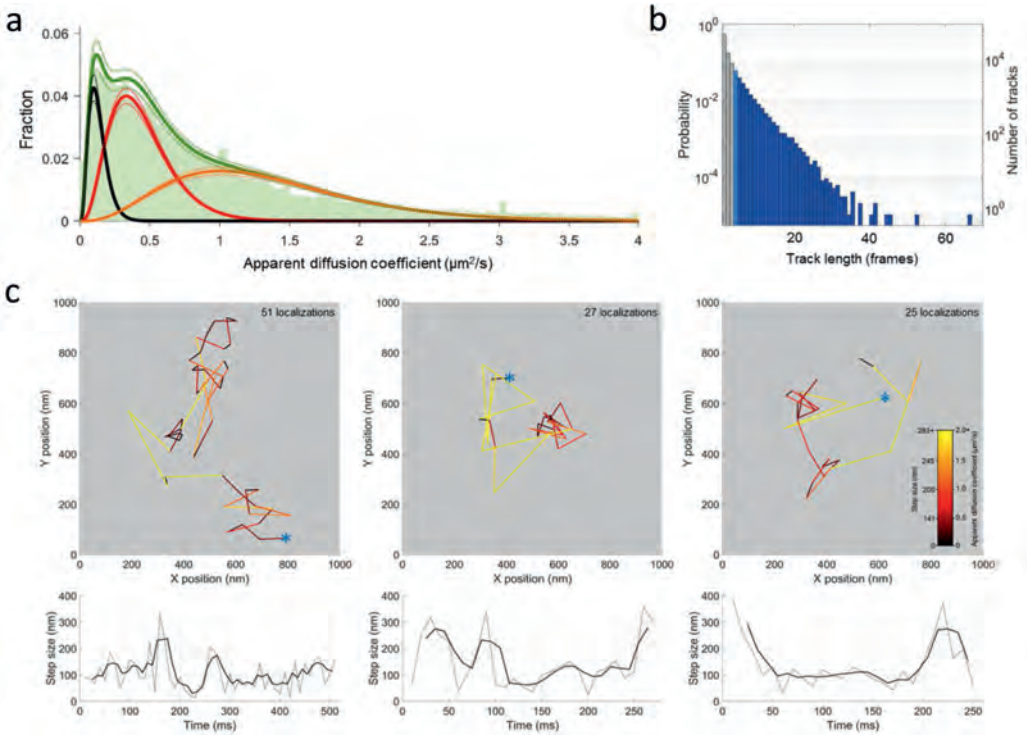

Figure 5.7: Single-particle tracking of dCas9. **a** Histogram of dCas9 diffusion coefficients in *L. lactis* (bin width = 0.05 $\mu m^2\ s^{-1}$). The three fitted populations are 0.13 ± 0.01 $\mu m^2\ s^{-1}$ (black), 0.44 ± 0.02 $\mu m^2\ s^{-1}$ (red) and 1.35 ± 0.05 $\mu m^2\ s^{-1}$ (orange) with relative occupancies of 12.4 ± 2.4%, 39.5 ± 4.8%, and 48.0 ± 7.3%, respectively. Dotted lines correspond with 95% confidence intervals of the fitted curve to the data. **b** Histogram of all track lengths. It should be noted that tracks shorter than 4 localizations (gray) are not taken into account in a, and that for all tracks longer than 4 localizations (dark blue), only the first 4 localizations are used to calculate the diffusion coefficient as shown in a. **c** Individual tracks that show state-transition behaviour. The top figures are colour-coded with respect to their apparent diffusion coefficient calculated from a single step, and the track starts at the position marked by *. The bottom figures show the step sizes as a function of time. Dotted lines indicate single step sizes, while the solid line is the floating average over 3 data points (30 ms).

5.3 Discussion and conclusion

As *L. lactis* is gaining ground in the biotechnology sector, capabilities to explore its mechanistic details and molecular behaviour on the single-cell level are highly desirable. Powerful experimental techniques for investigating protein behaviour in vivo often involve fluorescence-based approaches. For obtaining single-molecule specificity and resolution, single-particle tracking offers excellent possibilities. Here, we demonstrated the compatibility of various FPs for fluorescence microscopy and single-particle tracking in *L. lactis*.

In particular, we qualitatively tested a range of FPs (PAmCherry2, PATagRFP, mScarlet, mScarlet-I, mScarlet-H, mTurq2 and sYFP2). The plasmids encoding these FPs were successfully transformed in the cells, indicating low-level expression of these proteins is tolerated by these cells. Importantly, the observation that *L. lactis* cells succeeded to undergo division following sample preparation and mounting onto slides proves that the cells remain viable and active during these sample preparations. The signal of non-photoactivatable FPs was higher than the auto-fluorescent signal of wild-type cells and allowed for nisin induction. The photoactivatable FPs (PAmCherry2 and PATagRFP) responded appropriately to photoactivation, being switched on by irradiation with the 405 nm laser with hardly any fluorescent signal before photoactivation. sYFP and mTurq2 were less bright than the other FPs. Moreover, they are excited at low wavelength (488 nm and 405 nm, respectively), increasing the contribution of autofluorescence and toxic effects. Therefore, we consider sYFP and mTurq2 to be less-attractive candidates for fluorescence microscopy in *L. lactis*.

We analysed the behaviour of PAmCherry2-labelled dCas9 controlled via photoactivation and nisin induction. The tagged dCas9 could still successfully bind DNA target sites in a sgRNA dependent manner, as shown by the CRISPRi results targeting different sequences of the *acmA* gene and its promoter region. Interestingly, we observed chain-formation even without nisin induction, suggesting leakage of the nisin promoter. Single-particle tracking of individual dCas9-PAmCherry2 entities reveals the presence of immobile, transiently-interacting and freely diffusive dCas9 states. Apparent diffusion coefficients obtained from model simulations in which these three states were simulated agreed well with the experimentally obtained D^* values[18].

In this work, we have established and evaluated the procedure for sptPALM of labelled dCas9 in living *L. lactis*. After verifying the compatibility of various FPs as well as proper functioning of dCas9 labelled with PAmCherry2, we show that the presented single-particle tracking procedure allows distinguishing multiple diffusional dCas9 states in *L. lactis*. We anticipate that the described assays can also be adapted to molecules other than dCas9.

5.4 Material and methods

5.4.1 Bacterial strain and growth conditions

Lactococcus lactis strain NZ9000 was used in this study, based on its suitability as a host for the use of the nisin-controlled gene expression system[31]. Unless stated differently, cells were cultivated in M17 medium (Tritium, Eindhoven, The Netherlands) supplemented with 0.5% (w/v) glucose (G-M17) and grown at 30 °C without agitation. For the single-particle tracking studies, chemically defined medium for prolonged cultivation (CDMPC) was used[32]. This growth medium shows substantially less background fluorescence when compared to M17 medium. The low auto-fluorescence makes CDMPC vital for single-particle tracking in *L. lactis*.

Genes coding for the FPs were PCR amplified using plasmids containing the target genes as template. The primers were designed to contain a KpnI restriction site as overhang on the 3' end of the fragment (Table 5.1). The resulting amplicons (FP encoding gene including its stop-codon and KpnI restriction site) were digested with KpnI. The cloning vector pNZ8150[33] was ScaI-KpnI digested and ligated with the FP encoding amplicons, using T4 ligase, according to the manufacturers protocol (Thermo Fisher Scientific, Waltham, MA, USA). The resulting plasmids encode the

FP under control of the nisin-controlled *nisA* promoter[25] and were electrotransformed to *L. lactis* NZ9000[34]; transformants were selected on G-M17 agar plates containing 10 µg ml^{-1} chloramphenicol. Transformants were screened using a colony PCR (primer S15 combined with the corresponding reverse primer of each fluorescent gene insert; Table 5.1) with KOD Hot Start Mastermix according to the manufacturers instructions (Merck Millipore, Amsterdam, the Netherlands). The expected amplicon lengths were 200 bp (*nisA* promoter length) plus the base pair length of each insert.

5.4.2 FP expression, vector construction

PAmCherry2-labelled dCas9 was expressed from the pLAB-dCas9-PAmCherry2 plasmid. This pIL253-derived expression vector[36] encodes dCas9 under control of the nisin-promoter (P*nisA*), contains an erythromycin resistance marker (*ery*), replication genes (*repD*, *repE* and *repG*), and a cloning site (Eco31I) for sgRNA insertion and expression under control of the constitutive *eps* promoter (P*eps*). Details on vector construction can be found elsewhere[18].

5.4.3 Sample preparation

Cells were grown overnight from glycerol stocks in chemically defined medium for prolonged cultivation (CDMPC)[32]. Overnight cultures were subcultured (1:50 (v/v)) in CDMPC until exponential phase (∼3 h of growth) was reached. For the FP and dCas9-PAmCherry2 validation experiments, cultures were induced with a final nisin concentration of 50 ng ml^{-1} and 5.0 ng ml^{-1} (stock compound containing approximately 2.5% active component) (Sigma-Aldrich, Zwijndrecht, The Netherlands), respectively, and further grown for ∼3 h at room temperature before imaging. For the tracking experiments, cultures were induced with a final nisin concentration of 0.4 ng ml^{-1} and further grown for 1.5 h at room temperature before imaging.

Single-molecule microscopy requires samples in which cells are densely packed in a single-cell layer. In order to ensure low background fluorescence, cells were grown in CDMPC and washed three times in PBS. Cells were centrifuged and immobilised on 1.5% agarose pads between two glass coverslips (Paul Marienfeld GmbH & Co. KG; #1.5H or Menzel–Gläser, 24 × 60 mm #1.5) that were heated beforehand to 500 °C in an oven for 20 min to remove fluorescent background particles. Before single-molecule imaging, a series of brightfield images is taken which was later used to determine cell outlines. A detailed sample preparation protocol can be found elsewhere[18].

5.4.4 FPs and dCas9-PAmCherry2 imaging

The cells were imaged on a custom-built total internal reflection fluorescence (TIRF) microscope[18]. Laser beams were provided by a multilaser engine (Omicron Lighthub, available wavelengths 405 nm, 488 nm, 561 nm and 642 nm) and focused onto the sample (100× oil immersion Nikon SR HP TIRF with N.A. = 1.49). Fluorescent emission was filtered by a dichroic mirror (ZT405/488/561rpc-UF2 or ZT405/488/561/640rpc-UF2, Chroma, VT, USA) and appropriate emission filter (ZET405/488/561m-TRF or ZET405/488/561/640m-TRF, Chroma, VT, USA) and recorded with a sCMOS camera (Andor Zyla 4.2 PLUS). During acquisition, pixels were binned 2 × 2 leading to an effective pixel size of 128 × 128 nm, such that a 512 × 512 pixel centre crop led to a 65.64 × 65.64 µm field of view. Brightfield light was provided by a LED source.

Table 5.1: List of used plasmids and primers.

Plasmids

Name	Description	Reference
pNZ8150	Contains cmR and nisA inducable promoter system	[33]
pNZ8150-mScarlet	pNZ8150 with mScarlet inserted	This study
pNZ8150-mScarlet-I	pNZ8150 with mScarlet-I inserted	This study
pNZ8150-mScarlet-H	pNZ8150 with mScarlet-H inserted	This study
pNZ8150-sYFP	pNZ8150 with sYFP inserted	This study
pNZ8150-mTurq2	pNZ8150 with mTurq2 inserted	This study
pNZ8150-PAmCherry2	pNZ8150 with PamCherry2 inserted	This study
pNZ8150-PATagRFP	pNZ8150 with PATagRFP inserted	This study
pLAB-dCas9-PAmCherry2	pIL253 backbone, inserted fusion of *dspyCas9* to *PAmCherry2*, nonsense guide	This study, [35]
pLAB-dCas9-PAmCherry2-acmA1	sgRNA to target the template strand of the *acmA* promoter	This study
pLAB-dCas9-PAmCherry2-acmA2	sgRNA to target the template strand of the *acmA* gene	This study
pLAB-dCas9-PAmCherry2-acmA3	sgRNA to target the non-template strand of the *acmA* promoter	This study
pLAB-dCas9-PAmCherry2-acmA4	sgRNA to target the non-template strand of the *acmA* gene	This study

Primers

Name	Sequence	Code
mScarlet FWD	ATGGTGAGCAAGGGCGAGGCAGTGAT	S1
mScarlet REV	TTGAGGTACCTTACTTGTACAGCTCGTCCATGC	S2
mScarlet-i FWD	ATGGTGAGCAAGGGCGAGGCAG	S3
mScarlet-i REV	TTGAGGTACCTTACTTGTACAGCTCGTCCATGC	S4
mScarlet-H FWD	ATGGTGAGCAAGGGCGAGGCAGT	S5
mScarlet-H REV	TTGAGGTACCTTACTTGTACAGCTCGTCCATGCCG	S6
sYFP2 FWD	ATGGTGAGCAAGGGCGAGGA	S7
sYFP2 REV	TTGAGGTACCTTACTCGTTGGGGTCTTTGCTCA	S8
mTurq2 FWD	ATGGTGAGCAAGGGCGAGGAGCT	S9
mTurq2 REV	TTGAGGTACCTTACTTGTACAGCTCGTCCATGCCG	S10
PAmCherry2 FWD	ATGGCCATCATCAAGGAGTTC	S11
PAmCherry2 REV	TTGAGGTACCTTACTTGTACAGCTCGTCCATGC	S12
PATagRFP FWD	ATGAGCGAGCTGATTAAGGAG	S13
PATagRFP REV	TTGAGGTACCTTAATTAAGCTTGTGCCCCAG	S14
pNZ8150-Insertion FWD	CAGCTCCAGATCTAGTCTTA	S15
acmA guide 1 FWD	TGATGTCTTTTTTTAGCTTGAGGCG	SG1
acmA guide 1 REV	AAACCGCCTCAAGCTAAAAAAAGAC	SG2
acmA guide 2 FWD	TGATGAGCAGCGACTAACTCATCAG	SG3
acmA guide 2 REV	AAACCTGATGAGTTAGTCGCTGCTC	SG4
acmA guide 3 FWD	TGATGAAAAAAAGATGTCAATTTGG	SG5
acmA guide 3 REV	AAACCCAAATTGACATCTTTTTTTC	SG6
acmA guide 4 FWD	TGATGCTGGTTTATAAAAAGCGAG	SG7
acmA guide 4 REV	AAACCTCGCTTTTTATAAACCAGC	SG8

Table 5.2: Parameters during FP validation experiments.

Protein name	Excitation laser (nm)	Excitation intensity (W cm^{-2})	Photo-activation intensity (µW cm^{-2})	Emission filter (nm)	Dichroic mirror[a]	Reference
mScarlet	561	0.12	—	595 ± 25	1	[37]
mScarlet-I	561	0.12	—	595 ± 25	1	[37]
mScarlet-H	561	0.12	—	595 ± 25	1	[37]
sYFP	488	0.12	—	525 ± 25	2	[38]
mTurq2	405	0.012	—	—	2	[39]
PAmCherry2	561	0.12	800	595 ± 25	1	[35]
PATagRFP	561	0.12	800	595 ± 25	1	[40]
dCas9-PAmCherry2	561	0.12	2.7–619	—	1	[18]

[a] (1) reflecting 405 nm, 488 nm and 561 nm. (2) reflecting 405 nm, 488 nm, 561 nm and 642 nm.

Experimental conditions during the FP validation experiments (Table 5.2) are based on their spectral properties, with 10 ms frame times. Continuous laser exposure was used. For the single-molecule tracking experiments, movies were recorded at 10 ms/frame with 561 nm stroboscopic illumination (4 ms) and continuous 405 nm photoactivation increasing over time from according to an earlier described UV-increment scheme[18], all under an angle close to total internal reflection. Emission was filtered by a dichroic mirror (reflecting 405 nm, 488 nm and 561 nm) and emission filter (595 ± 25 nm).

5

5.4.5 CRISPRi experiments

Guides complementary to positions in the *acmA* gene and on its promoter, on the template strand and non-template strand[23], were designed (Table 5.1 and inserted into pLAB-dCas9-PAmCherry2 according to earlier described protocol[26]. As a control, a non-sense guide was used (Guide C) that does not have a matching target sequence. Cells were transformed with one of pLAB-dCas9-PAmCherry2-AcmA and grown overnight. Of the overnight cultures 3 µl was immobilised on 1.5% 0.2 µm-filtered agarose pads between two glass coverslips, and brightfield images were taken of these preparations.

5.4.6 Single-molecule localization and tracking

The acquisition of raw data was performed using the open source Micro-Manager software[41]. To extract single-molecule localizations, the Fiji plugin ThunderSTORM[42] with added functionality of phasor-fitting[43] with a fitting radius of 3 pixels was used. For image filtering, a β-spline wavelet filter with order 3 and scale 2 was used, and approximate localization was done via an 8-neighbourhood connected local maximum with peak intensity threshold equal to the standard deviation of F1 of the wavelet filter. Custom-written MATLAB (The MathWorks, Natick, MA) scripts were used to perform image analysis on single-molecule localizations (x, y) and particle trajectories.

Cells were segmented using the Fiji plugin Interactive Watershed (http://imagej.net/Interactive_Watershed) with an intensity average of 200 brightfield images as input. The localizations were plotted within the cell outline in order to neglect fluorophores that were localized outside the cell and to prevent trajectory construction over cell borders. Individual molecules in adjacent frames were connected into a trajectory if they were located within a radius of 1 µm to each other. An apparent diffusion coefficient (D^*) was then calculated from the mean-squared displacement (MSD) for each track[7]. The D^* values were used to discriminate between different modes of diffusion and categorise molecules as bound (low D^* values) or moving (high D^* values). The MSD was determined from the first four steps of a given track. Tracks shorter than four steps were discarded.

The apparent diffusion coefficient histogram is fitted with Equation 5.1:

$$y = \rho_1 \cdot \frac{(\frac{n}{D_1})^n \cdot x^{(n-1)} \cdot e^{-n\frac{x}{D_1}}}{(n-1)!} + \rho_2 \cdot \frac{(\frac{n}{D_2})^n \cdot x^{(n-1)} \cdot e^{-n\frac{x}{D_2}}}{(n-1)!} + \rho_3 \cdot \frac{(\frac{n}{D_3})^n \cdot x^{(n-1)} \cdot e^{-n\frac{x}{D_3}}}{(n-1)!} \quad (5.1)$$

here, ρ_1 and ρ_2 represent relative population sizes; D_1, D_2, and D_3 the apparent diffusion coefficients, n the track length (set to four here), and y the histogram count for every apparent diffusion coefficient histogram bin x.

The reported histogram containing information of apparent diffusion coefficient consists of 21,351 tracks of at least 4 track length, in total from 425 cells recorded in 2 technical duplicate measurements in 2 biologically independent experiments on 2 days (quadruplicate measurements in total).

5.5 Acknowledgements

We thank Jan Willem Borst and Jochem Vink for kindly providing us with vectors required for fluorophore expression. KJAM is funded by a VLAG PhD-fellowship grant awarded to JH. JH acknowledges funding from the Innovation Program Microbiology Wageningen (IPM-3). SvdE is funded by the BE-Basic R&D program (grant F10.002.01), which was granted a FES subsidy from the Dutch Ministry of Economic affairs.

References

1. Settanni, L. & Corsetti, A. Application of Bacteriocins in Vegetable Food Biopreservation. *International journal of food microbiology* **121,** 123–138 (2008).
2. Burgess, C., O'Connell-Motherway, M., Sybesma, W., *et al.* Riboflavin Production in Lactococcus Lactis: Potential for in Situ Production of Vitamin-Enriched Foods. *Appl. Environ. Microbiol.* **70,** 5769–5777 (2004).
3. Hugenholtz, J., Sybesma, W., Groot, M. N., *et al.* in *Lactic Acid Bacteria: Genetics, Metabolism and Applications* 217–235 (Springer, 2002).
4. van Hylckama Vlieg, J. E., Rademaker, J. L., Bachmann, H., *et al.* Natural Diversity and Adaptive Responses of Lactococcus Lactis. *Current opinion in biotechnology* **17,** 183–190 (2006).
5. Song, A. A.-L., In, L. L., Lim, S. H. E., *et al.* A Review on Lactococcus Lactis: From Food to Factory. *Microbial cell factories* **16,** 55 (2017).
6. Solopova, A., van Gestel, J., Weissing, F. J., *et al.* Bet-Hedging during Bacterial Diauxic Shift. *Proceedings of the National Academy of Sciences of the United States of America* **111,** 7427–7432 (2014).
7. Shen, H., Tauzin, L. J., Baiyasi, R., *et al.* Single Particle Tracking: From Theory to Biophysical Applications. *Chemical Reviews* **117,** 7331–7376 (2017).
8. Manley, S., Gillette, J. M., Patterson, G. H., *et al.* High-Density Mapping of Single-Molecule Trajectories with Photoactivated Localization Microscopy. *Nature Methods* **5,** 155–157 (2008).
9. Uphoff, S., Sherratt, D. J. & Kapanidis, A. N. Visualizing Protein-DNA Interactions in Live Bacterial Cells Using Photoactivated Single-Molecule Tracking. *Journal of Visualized Experiments : JoVE* (2014).
10. Elf, J. & Barkefors, I. Single-Molecule Kinetics in Living Cells. *Annual Review of Biochemistry* (2019).
11. Yao, Z. & Carballido-Lopez, R. Fluorescence Imaging for Bacterial Cell Biology: From Localization to Dynamics, from Ensembles to Single Molecules. *Annual review of microbiology* **68,** 459–476 (2014).
12. Crawford, R., Torella, J. P., Aigrain, L., *et al.* Long-Lived Intracellular Single-Molecule Fluorescence Using Electroporated Molecules. *Biophysical journal* **105,** 2439–2450 (2013).
13. Nienhaus, K. & Nienhaus, G. U. Fluorescent Proteins for Live-Cell Imaging with Super-Resolution. *Chemical Society Reviews* **43,** 1088–1106 (2014).
14. Kapanidis, A. N., Uphoff, S. & Stracy, M. Understanding Protein Mobility in Bacteria by Tracking Single Molecules. *Journal of Molecular Biology. Plasticity of Multi-Protein Complexes* **430,** 4443–4455 (2018).
15. Stracy, M., Uphoff, S., de Leon, F. G., *et al.* In Vivo Single-Molecule Imaging of Bacterial DNA Replication, Transcription, and Repair. *FEBS letters* **588,** 3585–3594 (2014).
16. Jones, D. L., Leroy, P., Unoson, C., *et al.* Kinetics of dCas9 Target Search in Escherichia Coli. *Science* **357,** 1420–1424 (2017).
17. Knight, S. C., Xie, L., Deng, W., *et al.* Dynamics of CRISPR-Cas9 Genome Interrogation in Living Cells. *Science* **350,** 823–826 (2015).
18. Martens, K. J. A., van Beljouw, S. P. B., van der Els, S., *et al.* Visualisation of dCas9 Target Search in Vivo Using an Open-Microscopy Framework. *Nature Communications* **10,** 3552 (2019).
19. Overkamp, W., Beilharz, K., Weme, R. D. O., *et al.* Benchmarking Various Green Fluorescent Protein Variants in Bacillus Subtilis, Streptococcus Pneumoniae, and Lactococcus Lactis for Live Cell Imaging. *Appl. Environ. Microbiol.* **79,** 6481–6490 (2013).
20. Doudna, J. A. & Charpentier, E. The New Frontier of Genome Engineering with CRISPR-Cas9. *Science* **346,** 1258096 (2014).
21. Vigouroux, A., Oldewurtel, E., Cui, L., *et al.* Tuning dCas9's Ability to Block Transcription Enables Robust, Noiseless Knockdown of Bacterial Genes. *Molecular systems biology* **14,** e7899 (2018).
22. Lawson, M. J., Camsund, D., Larsson, J., *et al.* In Situ Genotyping of a Pooled Strain Library after Characterizing Complex Phenotypes. *Molecular Systems Biology* **13,** 947 (2017).
23. Larson, M. H., Gilbert, L. A., Wang, X., *et al.* CRISPR Interference (CRISPRi) for Sequence-Specific Control of Gene Expression. *Nature protocols* **8,** 2180 (2013).
24. Chen, B., Gilbert, L. A., Cimini, B. A., *et al.* Dynamic Imaging of Genomic Loci in Living Human Cells by an Optimized CRISPR/Cas System. *Cell* **155,** 1479–1491 (2013).
25. Van Kranenburg, R., Marugg, J. D., Van Swam, I. I., *et al.* Molecular Characterization of the Plasmid-Encoded Eps Gene Cluster Essential for Exopolysaccharide Biosynthesis in Lactococcus Lactis. *Molecular microbiology* **24,** 387–397 (1997).
26. Van der Els, S., James, J. K., Kleerebezem, M., *et al.* Development of a Versatile Cas9-Driven Subpopulation-Selection Toolbox in Lactococcus Lactis. *Applied and Environmental Microbiology,* AEM.02752–17 (2018).
27. Berlec, A., Škrlec, K., Kocjan, J., *et al.* Single Plasmid Systems for Inducible Dual Protein Expression and for CRISPR-Cas9/CRISPRi Gene Regulation in Lactic Acid Bacterium Lactococcus Lactis. *Scientific reports* **8,** 1009 (2018).
28. Buist, G. *AcmA of Lactococcus Lactis, a Cell-Binding Major Autolysin* ([University Library Groningen][Host], 1997).

29. Singh, D., Sternberg, S. H., Fei, J., *et al.* Real-Time Observation of DNA Recognition and Rejection by the RNA-Guided Endonuclease Cas9. *Nature Communications* **7,** 12778 (2016).
30. Rieger, B. & Stallinga, S. The Lateral and Axial Localization Uncertainty in Super-Resolution Light Microscopy. *ChemPhysChem* **15,** 664–670 (2014).
31. Kuipers, O. P., de Ruyter, P. G. G. A., Kleerebezem, M., *et al.* Quorum Sensing-Controlled Gene Expression in Lactic Acid Bacteria. *Journal of Biotechnology. Genome Analysis and the Changing Face of Biotechnology* **64,** 15–21 (1998).
32. Goel, A., Santos, F., de Vos, W. M., *et al.* A Standardized Assay Medium to Measure Enzyme Activities of Lactococcus Lactis While Mimicking Intracellular Conditions. *Applied and Environmental Microbiology,* AEM.05276–11 (2011).
33. Mierau, I. & Kleerebezem, M. 10 Years of the Nisin-Controlled Gene Expression System (NICE) in Lactococcus Lactis. *Applied microbiology and biotechnology* **68,** 705–717 (2005).
34. Wells, J. M., Wilson, P. W. & Le Page, R. W. F. Improved Cloning Vectors and Transformation Procedure for Lactococcus Lactis. *Journal of Applied Bacteriology* **74,** 629–636 (1993).
35. Subach, F. V., Patterson, G. H., Manley, S., *et al.* Photoactivatable mCherry for High-Resolution Two-Color Fluorescence Microscopy. *Nature methods* **6,** 153–159 (2009).
36. Simon, D. & Chopin, A. Construction of a Vector Plasmid Family and Its Use for Molecular Cloning in Streptococcus Lactis. *Biochimie* **70,** 559–566 (1988).
37. Bindels, D. S., Haarbosch, L., Van Weeren, L., *et al.* mScarlet: A Bright Monomeric Red Fluorescent Protein for Cellular Imaging. *Nature methods* **14,** 53 (2017).
38. Nagai, T., Ibata, K., Park, E. S., *et al.* A Variant of Yellow Fluorescent Protein with Fast and Efficient Maturation for Cell-Biological Applications. *Nature biotechnology* **20,** 87 (2002).
39. Goedhart, J., Van Weeren, L., Hink, M. A., *et al.* Bright Cyan Fluorescent Protein Variants Identified by Fluorescence Lifetime Screening. *Nature methods* **7,** 137 (2010).
40. Subach, F. V., Patterson, G. H., Renz, M., *et al.* Bright Monomeric Photoactivatable Red Fluorescent Protein for Two-Color Super-Resolution sptPALM of Live Cells. *Journal of the American Chemical Society* **132,** 6481–6491 (2010).
41. Stuurman, N., Amdodaj, N. & Vale, R. μManager: Open Source Software for Light Microscope Imaging. *Microscopy Today* **15,** 42–43 (2007).
42. Ovesny, M., Křížek, P., Borkovec, J., *et al.* ThunderSTORM: A Comprehensive ImageJ Plug-in for PALM and STORM Data Analysis and Super-Resolution Imaging. *Bioinformatics* **30,** 2389–2390 (2014).
43. Martens, K. J. A., Bader, A. N., Baas, S., *et al.* Phasor Based Single-Molecule Localization Microscopy in 3D (pSMLM-3D): An Algorithm for MHz Localization Rates Using Standard CPUs. *The Journal of Chemical Physics* **148,** 123311 (2018).

5.6 Supplementary information

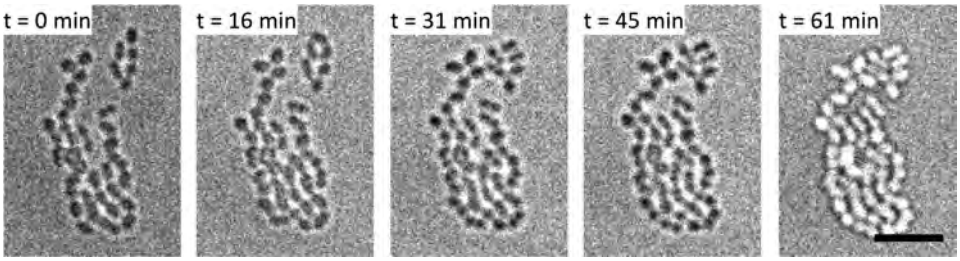

Figure S5.1: Observation of cell growth via single brightfield images. The pLAB-dCas9-PAmCherry2 *L. lactis* strain (non-induced) was typically prepared for microscopy after 3h of growth at 30 °C. Scale bar represents 5 µm.

6

Visualisation of dCas9 target search in vivo using an open-microscopy framework

A version of this chapter has been published as:

Koen J.A. Martens*, Sam P.B. van Beljouw*, S. van der Els, Jochem N.A. Vink, Sander Baas, George A. Vogelaar, Stan J. J. Brouns, Peter van Baarlen, Michiel Kleerebezem, and Johannes Hohlbein. Visualisation of dCas9 Target Search in vivo using an open-microscopy framework. *Nature Communications* **3552**, no. 10 (2019)

Abstract

CRISPR-Cas9 is widely used in genomic editing, but the kinetics of target search and its relation to the cellular concentration of Cas9 have remained elusive. Effective target search requires constant screening of the protospacer adjacent motif (PAM) and a 30 ms upper limit for screening was recently found. To further quantify the rapid switching between DNA-bound and freely-diffusing states of dCas9, we developed an open-microscopy framework, the miCube, and introduce Monte-Carlo diffusion distribution analysis (MC-DDA). Our analysis reveals that dCas9 is screening PAMs 40% of the time in Gram-positive *Lactoccous lactis*, averaging 17 $\pm$ 4 ms per binding event. Using heterogeneous dCas9 expression, we determine the number of cellular target-containing plasmids and derive the copy number dependent Cas9 cleavage. Furthermore, we show that dCas9 is not irreversibly bound to target sites but can still interfere with plasmid replication. Taken together, our quantitative data facilitates further optimisation of the CRISPR-Cas toolbox.

6.1 Introduction

The discovery of clustered regularly interspaced short palindromic repeats (CRISPR) and CRISPR-associated proteins (Cas) as a microbial defence mechanism triggered an ongoing scientific revolution, as CRISPR-Cas can be adapted to perform sequence-specific DNA modification in prokaryotes, archaea, and eukaryotes[1–4]. *Streptococcus pyogenes* Cas9 is a widely used variant[5] and an endonuclease activity-deficient version, termed dead Cas9 (dCas9), has been used to visualise endogenous genomic loci in living cells[6]. The biochemical interaction mechanisms of Cas9 are well understood[7–12]. The DNA-binding protein domain probes the DNA for a specific protospacer adjacent motif (PAM; 5'-NGG-3') via a combination of 3-dimensional diffusion and 1-dimensional sliding on the DNA[9]. Upon recognition of the PAM, the enzyme starts unwinding the DNA double helix to test for complementarity with a 20 nucleotide-long single guide RNA (sgRNA; R-loop formation). If full complementarity is found, Cas9 continues to cleave the DNA at a fixed position 3 nucleotides upstream of the PAM[13].

Optimisation of Cas9-mediated genomic engineering in a desired incubation time whilst minimising off-target DNA cleavage requires exact kinetic information. In the Gram-negative bacterium *E. coli*, an upper limit for the binding time (30 ms) of dCas9 with DNA has been determined in vivo[14], but it is unknown if such binding times are ubiquitous in prokaryotes. In addition, there is a limited understanding of the spatiotemporal relationship between cellular copy numbers of Cas9 proteins, the number of DNA target sites and the duration and dissociation mechanisms of target-bound dCas9. Since genomic engineering of food-related microbes such as Gram-positive lactic acid bacteria[15] is becoming increasingly valuable[16,17], it is important to assess whether previously determined dCas9 kinetic information can be transferred to food-related microbes.

To study the behaviour of dCas9 in vivo with millisecond time resolution, we used single-particle tracking photo-activated localization microscopy (sptPALM)[18,19]. In sptPALM, a photo-activatable fluorescent protein, which is by default not fluorescently active but can be activated via irradiation, is fused to the protein of interest, and the fusion protein is expressed in living cells. By stochastically activating a subset of the available chromophores, the signal of a single emitter is localized with high precision ($\sim$30–40 nm)[20,21] and, by monitoring its position over time, the movement of the protein fusion is followed and analysed[22].

However, sptPALM mostly provides quantitative information if the protein of interest remains in a single diffusional state for the duration of a track (e.g. $>$40 ms using at least 4 camera frames of 10 ms). As this temporal resolution is insufficient to elucidate in vivo Cas9 dynamic behaviour ($<$30 ms)[14], we developed a Monte-Carlo based variant of diffusion distribution analysis (MC-DDA, for analytical DDA see ref. [23]) to extract dynamic information on a timescale shorter than the duration of a single track.

In the experimental realisation, we refine existing single-molecule microscopy frameworks and introduce a new design, the miCube. The miCube is constructed from readily available and custom-made parts, ensuring accessibility for interested laboratories. We then use MC-DDA in combination with the miCube in an assay that employs a heterogeneous expression system in order to explore the dynamic nature of DNA-dCas9 interactions in live bacteria and their dependency on (d)Cas9 protein copy numbers. In particular, we assess dCas9 fused to photo-activatable fluorophore PAmCherry2 in the lactic acid bacterium *L. lactis*, in the presence or absence of DNA targets. With

this assay, we show that dCas9 is screening PAMs 40% of the time, with each binding event having an average duration of 17 ± 4 ms. Moreover, we show a dependency of bound dCas9 fraction on DNA target-binding sites, which allows quantification of plasmid copy numbers. This, in turn, indicates that bound dCas9 interferes with plasmid replication. These results are combined in a model that predicts Cas9 cleavage efficiencies in prokaryotes.

6.2 Results

6.2.1 Elucidation of sub 30 ms dynamic interactions with sptPALM

In the absence of cellular target sites, dCas9 is expected to be present in either one of two states (Figure 6.1a): bound to DNA (red), which results in low diffusion coefficients (∼0.2 µm^2/s); or freely diffusing in the cytoplasm (yellow), which results in high diffusion coefficients (∼2.2 µm^2/s). If the transitioning between these states is slow compared to the length of each track (here: 40 ms), diffusion coefficient histograms can be fitted with two static states (Figure 6.1b, top, Figure S6.1).

However, if transitioning between the states is on a similar or shorter timescale as the length of sptPALM tracks, these transient interactions of dCas9 with DNA (orange) will result in temporal averaging of the diffusion coefficient obtained from a single track. Therefore, we developed a Monte-Carlo diffusion distribution analysis (MC-DDA; Figure 6.1b, bottom, Methods, with an analytical approach available elsewhere[23]) that used the shape of the histogram of diffusion coefficients to infer transitioning rates between diffusional states. The analysis is based on similar approaches used to describe dynamic conformational changes observed with single-molecule Förster resonance energy transfer[24–26]. Briefly, MC-DDA consists of simulating the movement and potential interactions of dCas9 inside a cell with a Monte-Carlo approach: the simulated protein is capable of interchanging between interacting with DNA and diffusing freely, defined by $k_{\text{bound}\rightarrow\text{free}}$ and $k_{\text{free}\rightarrow\text{bound}}$. The MC-DDA diffusional data is compared with the experimental data, and by iterating on the kinetic rates and diffusion coefficients, a best fit is obtained.

6.2.2 miCube: an open framework for single-molecule microscopy

For MC-DDA to deduce high kinetic rates, experimental data with high spatiotemporal resolution ($<$ ∼50 nm, $<$ ∼20 ms) is required. This is challenging, as individual fluorescent proteins have a limited photon budget ($<$500 photons)[27], and background fluorescence is introduced by the living cells in which the fluorescent proteins are embedded. While suitable commercial microscopes are available, they often lack accessibility or are prohibitively expensive. This has led to the creation of a plethora of custom-built microscopes in the recent past[28–38], ranging from simplified super-resolution microscopes[30–34] to additions to commercial microscopes[35] or extremely low-cost microscopes[36,37].

To increase the accessibility of single-molecule microscopy with high spatiotemporal resolution further, we developed the miCube, an open-source, modular and versatile super-resolution microscope, and provide details to allow interested researchers to build their own miCube or a derivative instrument (Figure 6.1c, Figure 6.5, Methods, https://HohlbeinLab.github.io/miCube). We used 3D-printed components where possible, surrounding a custom aluminium body to minimise thermal drift and provide rigidity. All custom components are supported by technical drawings

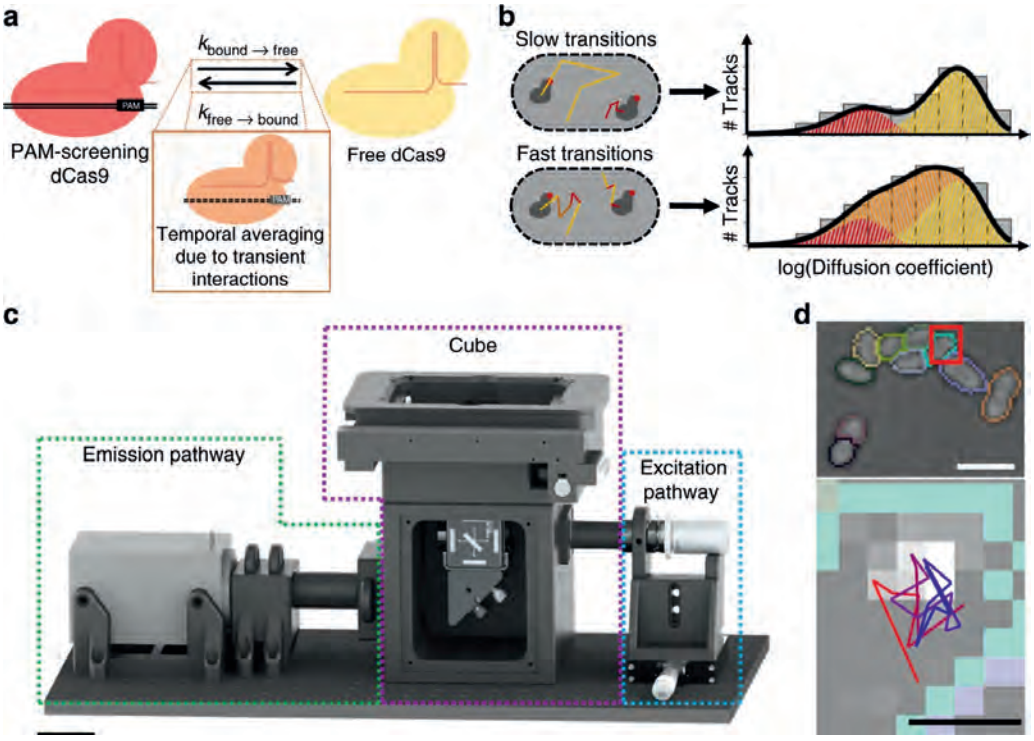

Figure 6.1: Probing cellular dynamics of dCas9 on an open-source microscope using sptPALM. **a** Simplified expected dynamic behaviour of dCas9 in absence of DNA target sites. The protein can be temporarily bound to DNA (PAM screening), or diffuse freely in cytoplasm, with two kinetic rates governing the dynamics. If the interaction is on a similar timescale as the detection time, a temporal averaging due to transient interactions is expected. **b** If the dynamic transitions are slow with respect to the camera frame time used in sptPALM, the obtained diffusional data can be fitted with a static model (top), which assumes that every protein is either free (yellow) or DNA-bound (red), but does not interchange. If the dynamic transitions are as fast or faster than the frame time used, Monte-Carlo diffusion distribution analysis (MC-DDA; bottom) can fit the diffusional data. In MC-DDA, dCas9 can interchange between the two states, resulting in a broader distribution. **c** Render of the open-source miCube super-resolution microscope. The excitation components, main cube, and emission components are indicated in blue, magenta, and green, respectively. Details are provided in the Methods section. Scale bar represents 5 cm. **d** Brightfield images of *L. lactis* used for computationally obtaining the outline of the cells via watershed (top), and raw single-molecule data (bottom; red outline in top is magnified) as obtained on the miCube as part of a typical experiment, overlaid with the determined track where this single-molecule belongs to (starting at red, ending at blue). Scale bars represent 2.5 µm (top) or 500 nm (bottom).

(Electronic Supplementary Information (ESI) Figures 10-18), along with STL files for direct 3D printing. We provide full details on the chosen commercial components, such as lenses, mirrors, and the camera. A detailed description on building a functioning miCube, along with rationale of the design choices, is given in the Methods section. Moreover, we discuss additional options for replacing expensive components with cheaper options.

To facilitate straightforward installation and flexible usability of the miCube, we simplified the alignment of the excitation module by decoupling the movement in the three spatial dimensions (Figure 6.5). A variety of imaging modalities are possible on the miCube; super-resolution microscopy in 2D and 3D[39], total internal reflection fluorescence (TIRF) microscopy, and LED-based brightfield microscopy. In its current version, the sample area fits a 96-wells plate. The excitation and illumination pathways of the microscope are fitted with 3D-printed enclosures, allowing the instrument to be used under ambient light conditions (including single-particle microscopy). Lastly, we restrained the footprint of the microscope to a 600 × 300 mm breadboard (excluding lasers; Figure 6.5), further improving accessibility.

Linear drift calculations indicate that the system experiences a drift of 13 ± 12 nm/min in the lateral plane and 25 ± 15 nm/min in the axial plane without active drift-suppressions systems in place[40] (average of three super-resolution measurements performed on three different days). A typical drift measurement is shown in Figure S6.2.

6.2.3 In vivo sptPALM in *L. lactis* on the miCube

For our sptPALM assay[41], we introduced dCas9 fused to the photo-activatable fluorophore PAmCherry2[27] in *L. lactis* under control of the inducible and heterogeneous *nisA* promoter[42] (pLAB-dCas9, Methods). On the same plasmid, a sgRNA with no fully matching targets in the genome is constitutively expressed. We immobilised the *L. lactis* cells on agarose, and using diffused brightfield LED illumination we computationally separated the cells via the ImageJ watershed[43] plugin (Figure 6.1d top). Single-particle microscopy was performed with low induction levels (0.1 ng/mL nisin) and low activation intensities (3–620 µW/cm^2, 405 nm) to obtain on average PAmCherry2 activation of <1 fluorophore/frame/cell to avoid overlapping tracks (Figure 6.1d, bottom). Single-particle tracks were limited to individual cells by using the previously obtained cell outlines.

6.2.4 dCas9 is PAM-screening for 17 ms

We first assessed the diffusional behaviour of dCas9-PAmCherry2 (hereafter described as dCas9, unless specifically mentioned) in *L. lactis* in the absence of target sites (pNonTarget plasmid; Methods). Under these conditions, dCas9 is expected to diffuse freely in the cytoplasm and screen PAM sites on the DNA for under 30 ms[14]. Under this assumption, diffusion ranges from completely immobile (and thereby fully determined by the localization uncertainty: ∼40 nm leads to ∼0.16 µm^2/s) to freely-moving. The expected free-moving diffusion coefficient can be theoretically described: the fusion protein has a hydrodynamic radius of 5–6 nm[27,44], resulting in a diffusion coefficient of 36–43 µm^2/s [45]. Cytoplasmic retardation of ∼20× due to increased viscosity and crowding effects reduces this to ∼1.8–2.2 µm^2/s [46]. We obtained diffusion coefficients in the range of ∼0–3 µm^2/s (Figure 6.2a), which is within the expected range.

We used a heterogeneous promoter (nisA, Methods), causing the apparent cellular dCas9 copy numbers to vary between 20 and ∼1000 (Figure 6.2a, Figure S6.3; cells with less than 20 copies were excluded as we corrected for ∼7 tracks (∼14 apparent dCas9) found in non-induced cells). The value of the cellular dCas9 is an approximation (Discussion), but a relative increase in cellular dCas9 copy number is certain. We then created five diffusional histograms belonging

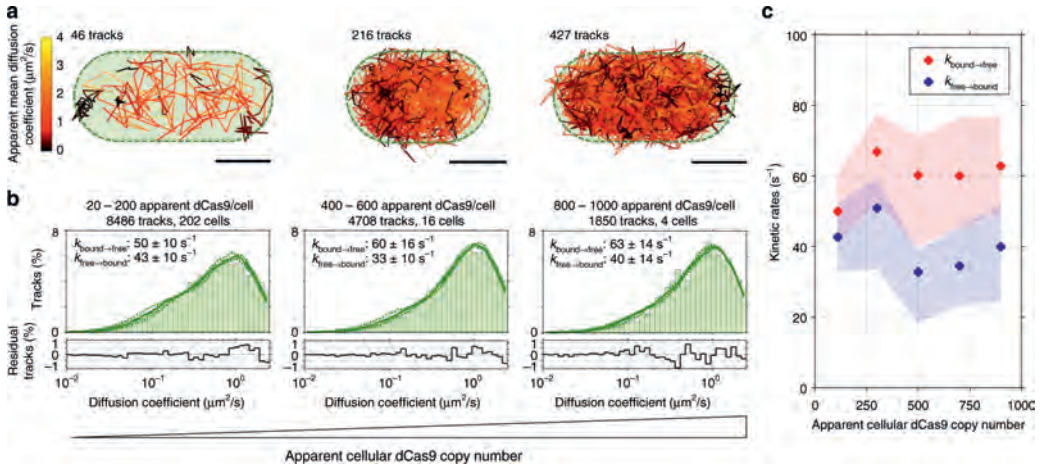

Figure 6.2: sptPALM of dCas9-PAmCherry2 in pNonTarget *L. lactis* with increasing dCas9 concentration. **a** Identified tracks in single pNonTarget *L. lactis* cells. Tracks are colour-coded based on their diffusion coefficient. Three separate cells are shown with increasing cellular concentration of dCas9. Green dotted outline is an indication for the cell membrane. Scale bars represent 500 nm. **b** Diffusion coefficient histograms (light green) belonging to 20–200, 400–600, and 800–1000 dCas9 copy numbers, from left to right. Histograms are fitted (dark green line) with a theoretical description of state-transitioning particles between a mobile and immobile state (dashed line represents 95% confidence interval based on bootstrapping the original data). Five diffusion coefficient histograms (Figure S6.3) were globally fitted with a single free diffusion coefficient (2.0 ± 0.1 μm^2/s; mean ± standard deviation), a single value for the localization error (σ = 38 ± 3 nm = 0.15 ± 0.03 μm^2/s), and 5 sets of $k_{\text{bound}\rightarrow\text{free}}$ and $k_{\text{free}\rightarrow\text{bound}}$ values (indicated in the figures). Residuals of the fit are indicated below the respective distribution. **c** $k_{\text{bound}\rightarrow\text{free}}$ (red) and $k_{\text{free}\rightarrow\text{bound}}$ (blue) plotted as function of the apparent cellular dCas9 copy number. Solid dots show the fits of the actual data; filled areas indicate the 95% confidence intervals obtained from the bootstrapped iterations of fitted MC-DDAs with 20.000 simulated proteins.

to cells with a particular apparent dCas9 copy number range (ranges of ~200 dCas9 copy number intervals; Figure 6.2b, Figure S6.3). These diffusional histograms are fitted with the aforementioned MC-DDA, where the shape of the MC-DDA is governed by the localization uncertainty, the free-moving diffusion coefficient, and the kinetic rates of PAM-screening. The localization uncertainty and free-moving diffusion coefficient are independent of cellular dCas9 copy number, since they are determined by the number of photons and a combination of hydrodynamic radius and cytoplasm viscosity, respectively. Therefore, the histograms were globally fitted with a combination of 5 MC-DDAs, each consisting of 20.000 simulated dCas9 proteins, containing a single value for free-moving diffusion coefficient (D_{free} = 2.0 ± 0.1 μm^2/s (average ± standard deviation of 4 experiments over 3 days, in total consisting of 32.971 tracks), in agreement with the theoretical expectation of ~1.8–2.2 μm^2/s), a single value for localization uncertainty (σ = 38 ± 3 nm, or D_{immobile}* = 0.15 ± 0.03 μm^2/s, expected for fluorescent proteins illuminated for 4 ms [39,41]), and five pairs of $k_{\text{free}\rightarrow\text{bound}}$ and $k_{\text{bound}\rightarrow\text{free}}$ (specified in Figure 6.2b,c).

The obtained kinetic constants of $k_{\text{free}\rightarrow\text{bound}}$ and $k_{\text{bound}\rightarrow\text{free}}$ were 40 ± 12 s^{-1} and 60 ± 13 s^{-1} (mean ± 95% CI), respectively, and did not show a significant dependence on apparent cellular dCas9 copy number (Figure 6.2c). This indicates that dCas9 is PAM-screening for 17 ± 4 ms in *L. lactis*, consisting of screening 1 or more PAMs via 1D diffusion. This value is in the same order of magnitude as the upper limit of 30 ms reported earlier for PAM-screening in *E. coli*[14], suggesting that these PAM-screening kinetics are a general feature of dCas9. Additionally, dCas9 is on average diffusing within the cytoplasm for 25 ± 8 ms before finding a new site for PAM screening. This duration is governed by the diffusion coefficient of the fusion protein, along with the average distance between DNA PAM sites. These results also entail that dCas9 is diffusing in the cytoplasm ∼60% of the time, while interacting with the DNA ∼40% of the time. Removal of the sgRNA resulted in similar diffusional data, which agrees with PAM-screening being a solely protein–DNA interaction ($k_{\text{free}\rightarrow\text{bound}}$: 34 ± 16 s^{-1}; $k_{\text{bound}\rightarrow\text{free}}$: 62 ± 21 s^{-1}; diffusion time on average 29 ± 18 ms; PAM-screening time on average 16 ± 6 ms; Figure S6.4). This also indicates that partial sgRNA-DNA matching of dCas9 with non-targets is not prevalent enough in our assay to affect the screening time significantly.

6.2.5 Target-binding of dCas9 can be observed with sptPALM

We then investigated the effect of DNA target sites complementary to the sgRNA loaded dCas9. To this end, we introduced 5 target sites on a plasmid (pTarget; Methods), which replaced the pNonTarget plasmid used so far. Qualitative visualisation of diffusion in the *L. lactis* bacteria shows tracks with small diffusion coefficients (Figure 6.3a, black tracks), indicative of target-bound dCas9. This immobile population can be observed throughout the dCas9 copy number range but is more prevalent in cells with lower cellular dCas9 copy numbers.

We expect target-bound dCas9 to move with a diffusion coefficient determined by the plasmid size, which is independent on the cellular dCas9 copy number. Therefore, we globally fitted the pTarget-obtained diffusional histograms with a combination of the corresponding pNonTarget MC-DDA fit and an additional single diffusional state belonging to target-bound dCas9 (Figure 6.3b, $D_{\text{plasmid}}{}^{*} = 0.38 \pm 0.04$ µm^2/s $= D_{\text{immobile}}{}^{*} + 0.23$ µm^2/s, which agrees with the expected diffusion coefficient from plasmids of similar size in bacterial cytoplasm[46–48]; 31.439 total tracks). The plasmid-bound dCas9 population decreases with increasing apparent cellular dCas9 copy numbers from 28 ± 3% at 105 (20–200) copies to 10 ± 5 % at 900 (800–1000) copies (Figure 6.3c left, purple squares; mean ± 95% CI). No target-binding behaviour was observed when the sgRNA was removed (Figure S6.4).

6.2.6 dCas9 does not bind targets irreversibly

This anti-correlation between dCas9 copy number and the size of the plasmid-bound population is indicative of competition for target sites by an increasing amount of dCas9 proteins. To evaluate this hypothesis, we consecutively simulated dCas9 proteins until the cellular dCas9 copy number was reached (Methods). In the simulation, every protein binds or dissociates from a PAM with the kinetic constants determined previously, and will instantly bind to a target site if it binds to a PAM directly adjacent to it. We thus disregard effects of 1D sliding on the DNA, but we believe these effects are limited, as 1D sliding between PAM sites has a low probability when PAMs are

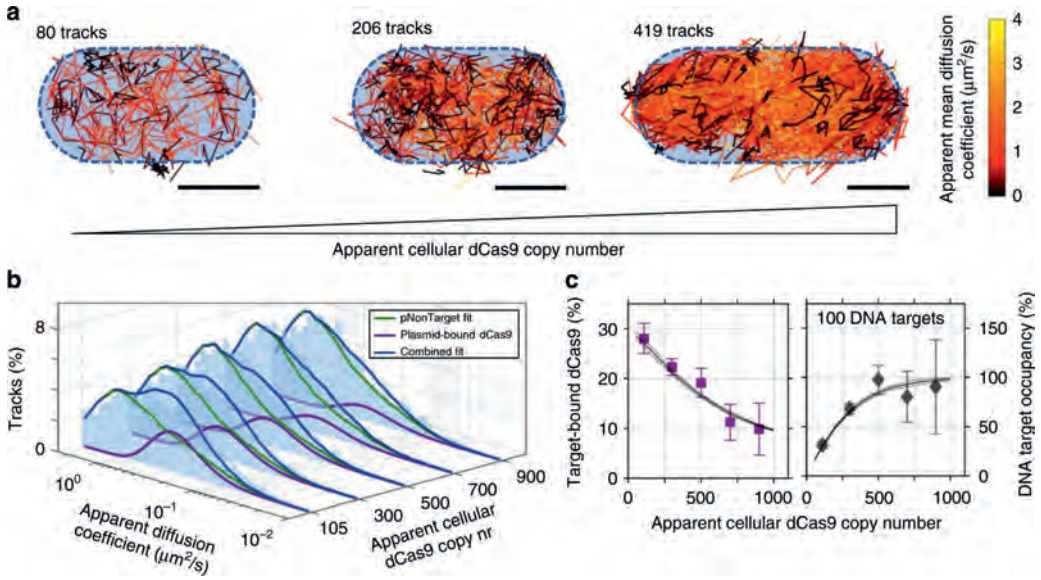

Figure 6.3: sptPALM of dCas9-PAmCherry2 in pTarget *L. lactis* shows target-binding behaviour of dCas9. **a** Identified tracks in individual pTarget *L. lactis* cells. Tracks are colour-coded based on their diffusion coefficient. Three separate cells are shown with increasing dCas9 concentration. Blue dotted outline is an indication for the cell membrane. Scale bars represent 500 nm. **b** Diffusion coefficient histograms (light blue) are fitted (dark blue line) with a combination of the respective fit of pNonTarget *L. lactis* cells (green line), along with a single globally fitted population corresponding to target-bound dCas9 (purple) at 0.38 ± 0.04 μm^2/s (mean ± standard deviation). **c** Left: The population size of the plasmid-bound dCas9 decreases as a function of the cellular dCas9 copy number. The error bar of the measurement is based on the 95% confidence interval determined by bootstrapping; the solid line is a model fit with 20 plasmids, with a 95% confidence interval determined by repeating the model simulation. Right: Occupancy of DNA targets by dCas9 based on 20 target plasmids (100 DNA target sites), based on the same data as presented in the left figure.

randomly positioned on the DNA ($<$ ∼10% at 16 bp distance average[9]). A k_{off} is introduced which dictates removal of dCas9 from the target sites.

This model fully explained the dependency of the target-bound dCas9 fraction on the cellular dCas9 copy number (Figure 6.3c left, black line). The slope of the curve towards low cellular dCas9 concentration is dependent on the total cellular number of PAM sites and k_{off}. Assuming on average 1.5 genomes worth of DNA (haploid genome replicated in half the cells) present in the cell, the k_{off} is ∼0.01 ± 0.003 s^{-1}. The number of DNA target sites determines the lower bound of the model, and ∼100 ± 50 DNA target sites (∼20 ± 10 plasmids) led to the observed bound fraction at 900 cellular dCas9 proteins. The fit of the number of target sites at high cellular dCas9 concentration is independent of k_{off}, since at the modelled concentrations and PAM-screening kinetic parameters, the target sites are essentially fully occupied (Figure 6.3c right). It thus follows that the used pTarget plasmid, a derivative of pNZ123, is present at a lower copy number than expected (∼60–80) during measurements[47]. This could hint towards interference of

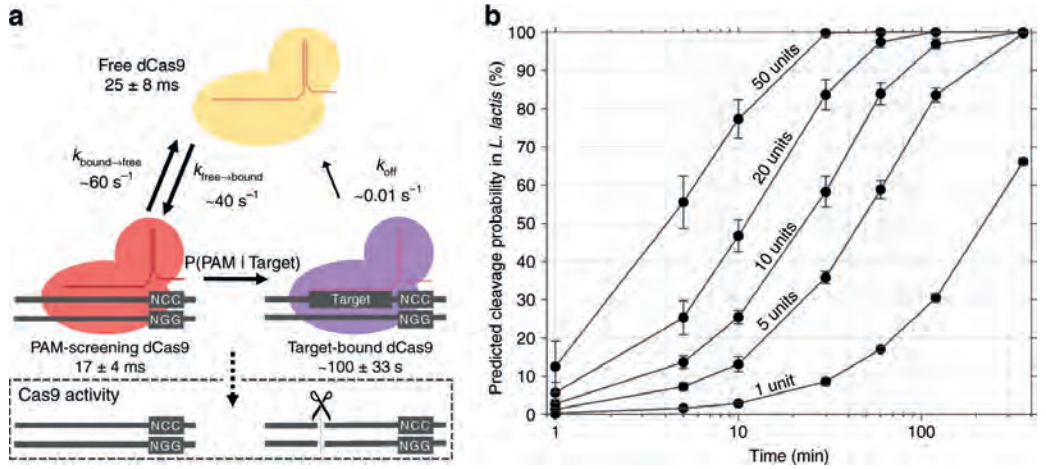

Figure 6.4: Extrapolation of the dCas9 dynamic model to assess single target cleavage by Cas9. **a** The proposed model surrounding dCas9 interaction with the obtained kinetic rates. Free dCas9 (yellow) in the cytoplasm interact with PAM sequences (5'-NGG-3') on average every 25 ms. If the PAM is not in front of a target sequence (red), only PAM-screening will occur for on average 17 ms. If the PAM happens to be in front of a target, the dCas9 will be target-bound (purple). We extend this model to predict Cas9 cleavage under conditions where target-bound Cas9 will always cleave the target DNA. **b** Calculated predicted probability that a single target in the *L. lactis* genome is cleaved after a certain period of time with a certain cellular Cas9 copy number, based on the model shown in a. Error bars indicate standard deviation calculated from iterations of the model.

plasmid replication due to dCas9 binding[49,50]. We investigated this with quantitative polymerase chain reaction (qPCR)[51], and we indeed observed a decrease in the amount of pTarget DNA with dCas9 production (Figure S6.5).

These collective results lead to the model presented in Figure 6.4a. dCas9 diffuses freely in the cytoplasm for 25 ± 8 ms on average, and will then interact with a PAM site for 17 ± 4 ms. If the PAM site is not directly adjacent to a target site, dCas9 will move back to freely diffusing in the cytoplasm. However, if the PAM site is directly followed by a target site, dCas9 will be bound to this site for 1.6 min on average, before it is removed by intrinsic or extrinsic factors.

6.2.7 A single copy of Cas9 find a single DNA target in ~4 h

We adapted the computational target-binding model to predict Cas9 cleavage in *L. lactis* and other prokaryotes with similar DNA content. We assume that all DNA is accessible to Cas9 and that Cas9 behaves identical to dCas9, but will cleave a target directly after binding. Our proposed Cas9 kinetic scheme depends only on PAM-screening kinetic rates and the ratio of total PAM sites to target sites. We predicted the incubation time-dependent probability that a certain number of cellular Cas9 proteins will bind a single target site on the *L. lactis* genome (Figure 6.4b).

The model shows that a single Cas9 protein can effectively find a single target with 50% probability in ~4 h. It also shows that an increasing cellular Cas9 copy number quickly decreases

this search time: With 10 cellular copies of Cas9, the search time is reduced to ∼25 min, and 20 copies reduce the search time to ∼10 min. Therefore, a single target is almost certainly found within a typical prokaryotic cell generation time (> ∼20 min). This agrees with in vivo data of Cas9[14] (accounting for *E. coli*'s larger genome (∼4.6 mbp versus ∼2.5 mbp)) and with in vivo data of Cascade in *E. coli*[23], though in different organisms or with different CRISPR-Cas systems.

6.3 Discussion

We have designed a sptPALM assay to probe DNA-protein interactions in vivo, and assessed the kinetic behaviour of dCas9 in *L. lactis* on the open-hardware, super-resolution microscope miCube. The high spatiotemporal resolution of the experimental data along with the heterogeneity of the used induction protocol allowed us to develop a Monte-Carlo diffusion distribution analysis (MC-DDA) of the diffusional equilibrium.

The obtained dCas9 PAM-screening kinetic rates ($k_{\text{free}\rightarrow\text{bound}} = 40 \pm 12\ \text{s}^{-1}$, $k_{\text{bound}\rightarrow\text{free}} = 60 \pm 13\ \text{s}^{-1}$) indicate that non-target binding of dCas9 has a mean lifetime of 17 ± 4 ms, and spends ∼40% of its time on PAM screening. In fact, a 1:1 ratio between diffusing and binding was shown to be optimal for target search time of DNA-binding proteins[52]. The MC-DDA further suggests that the kinetic rates governing PAM–dCas9 interactions do not depend on cellular copy number levels of dCas9.

We observed target-binding of dCas9, and showed that higher cellular dCas9 copy numbers resulted in lower probabilities of target-bound dCas9, although absolutely more targets were occupied by dCas9. We linked this finding to the previously found $k_{\text{free}\rightarrow\text{bound}}$ and $k_{\text{bound}\rightarrow\text{free}}$ rates and postulate that dCas9 dissociation from target sites is responsible for the obtained probabilities of target binding by dCas9. We made two assumptions when obtaining absolute cellular dCas9 copy numbers. Firstly, we assumed that measurements directly end after all fluorophores in the centre of the microscopy field of view have been imaged once. Secondly, we assumed a maturation grade of 50% (identical to that of PAmCherry1 in Xenopus[53]). Although an exact determination is possible[53,54], this is beyond the scope of this study.

We obtained a dCas9-target koff rate of ∼0.01 s^{-1} that is dependent on the exact cellular dCas9 copy number and total *L. lactis* genomic content. The biological cause of dissociation of target bound dCas9 from DNA remains speculative: it could be an intrinsic property, resulting in spontaneous release from target sites, or it could be caused by an extrinsic factor, such as RNA transcription or DNA replication. We do not expect RNA polymerase activity on the DNA target sites, although we did not actively block transcription. It is currently unknown whether genomic target-bound dCas9 dissociates from the DNA due to DNA replication, with studies contradictory showing that dCas9 is removed during cell duplication[14] and that dCas9 is hindering genomic DNA replication[49] or transcription[50]. We note that genomic DNA replication substantially differs from the rolling-circle DNA replication of pTarget[55].

Our data indicate that dCas9 binding to plasmid DNA hinders DNA rolling-circle replication. The pNZ123 plasmid, of which pTarget is a derivative, is believed to be high-copy[47] (60–80 plasmids per cell), although the quantification of plasmid copy numbers is challenging (discussed for the single-cell level in reference [51]). Our model suggests that pTarget is present in only ∼20 copy numbers during our measurements. Although we saw an effect of dCas9 production on pTarget

copy number via qPCR, the obtained decrease (∼20%) is not as large as observed with sptPALM (∼70%). The median cellular dCas9 copy number, however, is low (∼40; Figure S6.5) compared to most of the dCas9 copy number bins evaluated with MC-DDA. Therefore, using the averaged cellular community, not all pTarget (60–80 cellular plasmids containing 300–400 target sites), are occupied by a dCas9 protein, which would affect the ensemble qPCR results. The sptPALM plasmid copy number determination, on the other hand, is mostly determined by the *L. lactis* sub-population with high dCas9 copy numbers, for which pTarget replication is restricted more strongly.

We used our model to make predictions on Cas9 cleavage probabilities, based on kinetic values extracted from the MC-DDA, which are not influenced by the approximated cellular dCas9 copy number. The kinetic parameters of dCas9-PAmCherry2 provide estimates for those of Cas9. We reason that $k_{\mathrm{bound}\rightarrow\mathrm{free}}$ will be unchanged, since this rate is based on the duration of the PAM screening, while $k_{\mathrm{free}\rightarrow\mathrm{bound}}$ will be slightly lower for Cas9 compared to dCas9-PAmCherry2, due to the relatively higher diffusion coefficient of Cas9. The model can be expanded to incorporate a protein diffusion coefficient to obtain a modified $k_{\mathrm{free}\rightarrow\mathrm{bound}}$ rate, and to include accessibility of the DNA. These additions would allow the model to predict Cas9 behaviour in more diverse environments such as eukaryotic cells. Other computational models have taken these parameters into account[56], but these models were not based on experimental in vivo data, and were based on different assumptions.

Our open microscopy framework enables the study of in vivo protein–DNA interactions with high spatiotemporal resolution, here shown for CRISPR-Cas9 target search, and improves the general accessibility of super-resolution microscopy. Our data shows that heterogeneity in an expression system can be used to obtain new insights in any protein–DNA or protein–protein interaction in vivo, here indicating that target-bound dCas9 interferes with rolling-circle DNA replication. The derived kinetic parameters and information on target search times provide valuable practical insights in CRISPR-Cas engineering and gene silencing in lactic acid bacteria specifically, and suggest to reflect prokaryotic Cas9 search times in general.

6.4 Material and methods

6.4.1 miCube design considerations

We designed the miCube to be easy to setup and use, while retaining a high level of versatility. The instrument and its design choices will be described in three parts: the excitation path; the emission path, and the cube connecting the sample with the excitation and emission paths. Throughout this description, we will refer to numbered parts as shown in Figure 6.5a,c and described in ESI Table 1. The information on the miCube presented here can also be found on https://HohlbeinLab.github.io/miCube. The instrument is fully functional in ambient light, due to a fully enclosed sample chamber, illumination pathway and emission pathway. Moreover, the miCube has a small footprint: the final design of the miCube, excluding the lasers and controllers, fits on a 300 × 600 mm Thorlabs breadboard. We placed the whole ensemble in a transparent polycarbonate box (MayTec Benelux, Doetinchem, The Netherlands) to minimise airflow disturbing the setup during experiments.

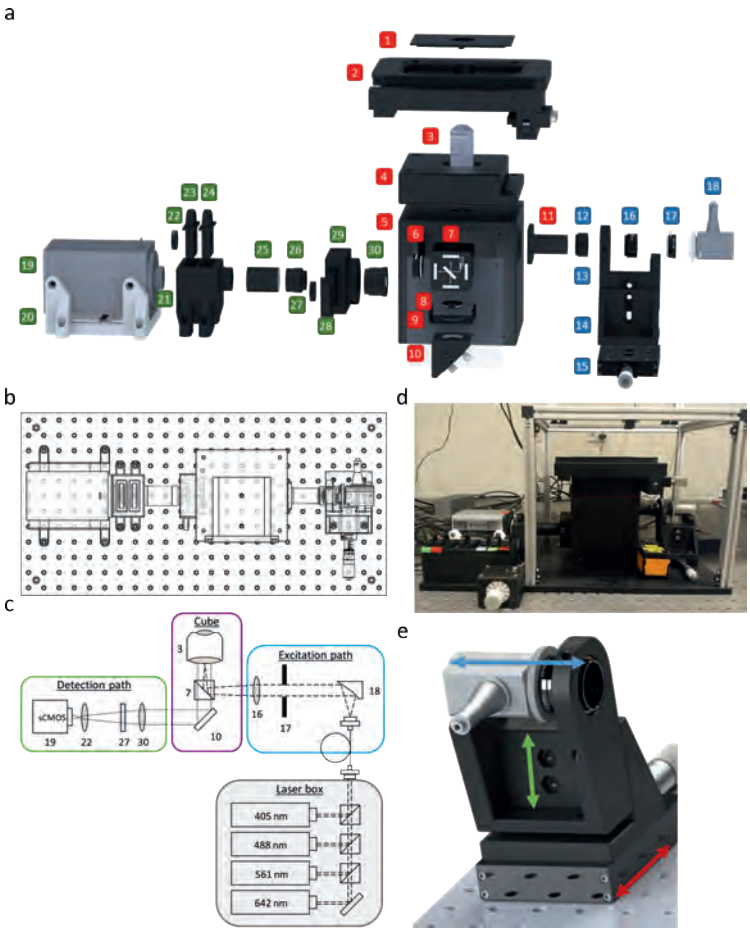

Figure 6.5: The open-source miCube single-particle microscope. **a** Exploded render of the miCube highlighting individual components. A full list of components indicated by the numbered items can be found in ESI Table 5. **b** Top-down schematic view of the miCube on the breadboard, allowing clear view of mounting positions. Distance between mounting holes on the breadboard is 25 mm. **c** Schematic overview of the miCube instrument. Numbered items correspond to the items in a and ESI Table 5. The excitation path is visualised with dashed lines, the emission path is visualised with dotted lines. **d** Photograph of the fully assembled miCube as used for measurements in this manuscript. **e** Detailed view of the miCube excitation path. This sub-assembly is comprised of numbers 12-18. Arrows indicate isolated movement in the three spatial dimensions: distance from objective (blue), height of excitation unit (green), and horizontal position with respect to the objective (red).

6.4.2 miCube excitation path

The excitation path is designed to be both robust and easy to align and adjust. The four laser sources located in an Omicron laser box are combined and guided via a single mode fibre towards a

reflective collimator (nr. 18) ensuring a well-collimated beam. The reflective collimator is attached directly to an aperture (nr. 17), a focusing lens (nr. 16, 200 mm focal length), and an empty spacer (nr. 12). This excitation ensemble is placed in the 3D-printed piece designed to hold the assembly into place (nr. 13). This holder is then attached to a right-angled mounting plate (nr. 14), which is placed on a 25 mm translation stage (nr. 15). The translation stage should be placed at such a position on the breadboard that the focusing lens (nr. 16) is exactly 200 mm separated from the back-focal plane of the objective when following the laser path.

Easy alignment and adjustment are ensured by isolating the three axes of movement of this excitation ensemble (Figure 6.5e). Adjustments of distance from objective is achieved by moving the collimator ensemble (nrs. 12, 16–18) inside its holder (nr. 13). Height of the path can be adjusted via a bracket clamp that supports the collimator ensemble (nrs. 13 and 14), and the horizontal alignment can be adjusted via a translation stage where the bracket clamp rests on (nr. 15). We note that the excitation pathway is uncoupled from any laser source due to the fibre-connection, allowing for freedom of choice for the excitation laser unit.

Additionally, the translation stage (nr. 15) can be used to enable highly inclined illumination (HiLo) or total internal reflection (TIR). The stage allows fine and repeatable adjustment of the excitation beam position on the back focal plane of the objective. By aligning the excitation beam in the centre of the objective, the microscope will act as a standard epifluorescence instrument. If the excitation beam is aligned towards the edge of the back focal plane, the miCube will operate in HiLo or TIR.

6.4.3 miCube cube and sample mount

The central component of the miCube is the cube (nr. 5) that connects excitation path, emission path, and the sample. The cube is manufactured out of a solid aluminium block maximising stability and minimising effects of drift due to thermal expansion. Black anodisation of the block prevents stray light and unwanted reflections. The illumination path is further protected from ambient light by screwing a 3D-printed cover (nr. 11) on the side of the cube, as well as a door to close the cube off.

Next, the dichroic mirror—full mirror part is assembled (nrs. 6–10). The dichroic mirror unit (nr. 7) consists of a dichroic mount that is magnetically attached to an outer holder. On the side of the dichroic mirror unit, opposing the excitation path, a neutral density filter (nr. 6) is placed to prevent scattered non-reflected light entering the miCube thereby minimising background signal being recorded by the camera. At the bottom of the dichroic mount assembly, a TIRF filter (nr. 8) is placed to remove scattered back-reflected laser light from entering the emission pathway. This ensembled dichroic mirror unit is screwed via a coupling element (nr. 9) to a mirror holder containing a mirror placed at a 45° angle (nr. 10), which reflects the emission light from the objective to the camera. This completed dichroic mirror—full mirror part is screwed into the backside of the miCube via two M6 screws, which hold the ensemble into place and directly in line with the excitation path (nrs. 12-18), the objective (nr. 3), and the tube lens (nr. 30).

Then, an objective (nr. 3) (Nikon 100× oil, 1.49 NA, HP, SR) is directly screwed into an appropriate thread on top of the cube. Around the objective, a sample mount (nr. 4) is screwed on top of the cube, which is designed to ensure correct height of the sample with respect to the

parfocal distance of the chosen objective. We opted for using a sample mount, as it can be easily swapped for another to retain freedom in peripherals. For example, only the height of the sample mount has to be changed if an objective has a different parfocal distance as the one used here. We designed two different sample mounts (nr. 4a, 4b). The first one can hold an xy-translation stage with z-stage piezo insert (nr. 2), to enable full spatial control of the sample (nr. 4a). The second one only holds the z-stage piezo insert, which decreases instrument cost (nr. 4b). In any case, the xy-translation stage with z-stage piezo insert, or only the z-stage piezo insert is screwed in place into corresponding threaded holes in the sample mount. A glass slide holder (nr. 1) is made from aluminium to fit inside a 96-wells-holder like the z-stage (nr. 2).

6.4.4 miCube detection path

A tube lens ensemble is made (nrs. 27–30) which houses a 200 mm focal length tube lens (Thorlabs) in a 3D-printed enclosure which provides space to slot in an emission filter (nrs. 27, 28). This ensemble is then attached directly to the miCube by screwing it into place with four M6 screws. The alignment of the tube lens is therefore exactly in line with the emission light, as the centre of the full mirror (nr. 10) is at the same height of the tube lens. The direction of the emission light can be aligned, which can simply be achieved by tuning the angle of the full mirror (nr. 10).

A cover (nr. 25) is attached to the tube lens ensemble to ensure darkness of the emission path, which is connected to the tube lens by a 3D-printed connector piece (nr. 26). On the other end of the cover, a 3D-printed holder for 2 astigmatic lenses (nr. 21) is placed and screwed into place in the breadboard. Astigmatic lenses (nrs. 22-24) can optionally be used to enable 3D super-resolution microscopy[57]. They can be easily changed for lenses with a different focal length or with empty holders. With this, astigmatism can be enabled or disabled, and a choice between more accurate z-positional information with a lower total z-range, or less accurate information with a larger range can be made. The Andor Zyla 4.2 PLUS camera (nr. 19) is placed behind the astigmatic lens holder, and is positioned in a 3D-printed camera mount (nr. 20) to ensure correct height and position of the camera, so that the focus of the tube lens is at the camera chip. We chose for a scientific Complementary Metal-Oxide Semiconductor (sCMOS) camera to take advantage of a larger field of view and increased temporal resolution compared to the more traditional electron-multiplying charge coupled device (EMCCD) cameras[58].

Note that the length of the cover (nr. 25) and the alignment of the holes at the feet of the 3D-printed astigmatic lens holder (nr. 21) are dependent on the focal length of the tube lens, and of the position of the chosen camera chip with regards to the 3D-printed mount for the camera. The pieces used here were designed for the Andor Zyla 4.2 PLUS, a 200 mm focal length tube lens, and the used custom-designed camera mount (nr. 20).

6.4.5 Strain preparation and plasmid construction

Lactococcus lactis NZ9000 was used throughout the study. NZ9000 is a derivative of *L. lactis* MG1363[59] in which the chromosomal *pepN* gene is replaced by the *nisRK* genes that allow the use of the nisin-controlled gene expression system[42]. Cells were grown at 30 °C in GM17 medium (M17 medium (Tritium, Eindhoven, The Netherlands) supplemented with 0.5% (w/v) glucose (Tritium, Eindhoven, The Netherlands) without agitation.

6.4.6 DNA manipulation and transformation

Vectors used in this study are listed in ESI Table 2. Oligonucleotides (ESI Table 3) and primers (ESI Table 4) were synthesised at Sigma-Aldrich (Zwijndrecht, The Netherlands). Plasmid DNA was isolated and purified using GeneJET Plasmid Prep Kits (Thermo Fisher Scientific, Waltham, MA, USA). Plasmid digestion and ligation were performed with Fast Digest enzymes and T4 ligase respectively, according to the manufacturer's protocol (Thermo Fisher Scientific, Waltham, MA, USA). DNA fragments were purified from agarose gel using the Wizard SV gel and PCR Clean-Up System (Promega, Leiden, The Netherlands). Electro competent *L. lactis* NZ9000 cells were generated using a previously described method[60]. Prior to electro-transformation, ligation mixtures were desalted for one hour by drop dialysis on a 0.025 µm VSWP filter (Merck-Millipore, Billerica, US) floating on MQ water. Electro-transformation was performed with GenePulser XcellTM (Bio-Rad Laboratories, Richmond, California, USA) at 2 kV and 25 µF for 5 ms. Transformants were recovered for 75 min in GM17 medium supplemented with 200 mM $MgCl_2$ and 2 mM $CaCl_2$. Chemically competent *E. coli* TOP10 (Invitrogen, Breda, The Netherlands) were used for transformation and amplification of the Pnis-dCas9-PAmCherry2-containing pUC16 plasmid (Figure S6.6). Antibiotics were supplemented on agar plates to facilitate plasmid selection: 10 µg/ml chloramphenicol (for pTarget/pNonTarget) and 10 µg/ml erythromycin (for pLAB-dCas9). Screening for positive transformants was performed using colony PCR with KOD Hot Start Mastermix according to the manufacturer's instructions (Merck Millipore, Amsterdam, the Netherlands). Electrophoresis gels were made with 1% agarose (Eurogentec, Seraing, Belgium) in tris-acetate-EDTA (TAE) buffer (Invitrogen, Breda, The Netherlands). Plasmid digestions were compared with in silico predicted plasmid digestions (Benchling; https://benchling.com).

6

6.4.7 pLAB-dCas9 plasmid construction

Construction of the pLAB-dCas9 plasmid[41,61] was performed by synthesising (Baseclear B.V., Leiden, The Netherlands) a codon-optimised fragment containing the sequence of Pnis-dCas9-PAmCherry2, flanked by XbaI/SalI restriction sites (Figure S6.6, ESI Note 1). This fragment was supplied in a pUC16 plasmid. After transformation in *E. coli*, the plasmid was isolated and digested with XbaI and SalI to obtain the Pnis-dCas9-PAmCherry2 fragment. From the pLABTarget expression vector[62], the Cas9 expression module was removed by digestion with XbaI and SalI, and replaced by the XbaI-SalI fragment containing Pnis-dCas9-PAmCherry2. The single-stranded guide RNA (sgRNA) for targeting *pepN* was constructed with the correct overhangs and inserted in the Eco31I digested sgRNA expression handle to yield the pLAB-dCas9 vector[62]. The plasmids used in this study, and vector maps for pLABTarget and pLAB-dCas9 are available upon request. pLAB-dCas9-PAmCherry2 was sequenced, and was confirmed to be intact in the used strains.

6.4.8 pLAB-dCas9 no-sgRNA

The pLAB-dCas9-nosgRNA plasmid was constructed by BoxI/SmaI digestion of the pLAB-dCas9-PAmCherry2 plasmid, and subsequent self-ligation. This resulted in deletion of the sgRNA handle and transcriptional terminator, successfully removing the functional sgRNA. The resulting pLAB-dCas9-nosgRNA plasmid was confirmed via sequencing.

6.4.9 pTarget and pNonTarget plasmid construction

The plasmid with binding sites for dCas9 (pTarget) was established by engineering five *pepN* target sites in the pNZ123 plasmid[63]. To this end, two single-stranded oligonucleotides (10 µl of 100 µM, each, ESI Table 3) that upon hybridisation form the a single target sequence for the *pepN*-targeting sgRNA were incubated in 80 µl annealing buffer (10 mM Tris [pH = 8.0] and 50 mM NaCl) for 5 min at 100 °C, followed by gradual cooling to room temperature. The annealed mixed multiplexed oligonucleotides were cloned in HindIII-digested pNZ123. Afterwards, we selected a derivative that contains five *pepN* target sites via colony PCR (ESI Table 4). HindIII re-digestion was prevented by flanking the *pepN* DNA product by different base pairs, changing the HindIII site. Plasmids with five *pepN* target sites were designated pTarget (Figure S6.7). Plasmids without the *pepN* target sites (the original pNZ123 plasmids) were designated pNonTarget. The vector maps for pTarget and pNonTarget are shown in Figure S6.7. Correct insertion of the five *pepN* target sites was confirmed via sequencing.

6.4.10 Construction of strains with pLAB-dCas9 and p(Non)Target

Electro competent *L. lactis* NZ9000 cells[60] harbouring pLAB-dCas9 were transformed with pTarget or with pNonTarget and subsequently used for sptPALM or stored at −80 °C.

6.4.11 Quantitative polymerase chain reaction (qPCR)

Both *L. lactis* strains containing pLAB-dCas9 and pTarget or pNonTarget were grown under similar lab conditions as the imaging experiments performed in this study ($n = 2$). After 3 h of growth, the cultures were split and dCas9 was induced (0 ng/ml nisin, 0.4 ng/ml nisin and 2 ng/ml nisin). The cells were then harvested after 12 h of growth by centrifugation. The cell pellets were washed, and DNA was extracted using InstaGene Matrix (Bio-Rad Laboratories, Richmond, California, USA).

Oligonucleotides were designed to amplify a region of spanning approximately 1000 base pairs on both pTarget and pNonTarget, and a region of similar length on the NZ9000 chromosome (Q3 + Q4 and Q7 + Q8; ESI Table 4). These oligonucleotides were used in a PCR reaction to generate templates which were diluted to function as a calibration curve in the following qPCR. Both qPCR reactions were performed on each isolated DNA sample (6 technical replicates) and the ratio between measured chromosomal amplicons (Q5 + Q6) and plasmid amplicons (Q1 + Q2) was determined. The samples which were uninduced with nisin were used to standardise the estimated pTarget and pNonTarget copy numbers.

6.4.12 Sample preparation

The strains to be used for single-molecule microscopy were grown o/n from glycerol stocks at 30 °C in chemically defined medium for prolonged cultivation (CDMPC)[64]. Then, they were sub-cultured at 5% v/v and grown for 3 h (average duplication time in CDMPC is ∼90 min (determined via OD600 measurements)), before induced with 0.1 ng/ml nisin. 90 min later, the sample preparation began (see below).

Samples were prepared as described previously[41]. Briefly, after culturing of the cells, 0.5 µg/mL ciprofloxacin (Sigma-Aldrich, Zwijndrecht, The Netherlands) was added to slightly inhibit further cell division and DNA replication for sgRNA-pTarget and sgRNA-pNonTarget experiments[65]. Then, cells were centrifuged (3500 RPM for 5 min; SW centrifuge (Froilabo, Mayzieu, France) with a CENSW12000024 swing-out rotor fitted with CENSW12000006 15 mL culture tube adaptors) and washed two times by gentle resuspension in 5 mL phosphate-buffered saline (PBS; Sigma-Aldrich, Zwijndrecht, The Netherlands). After removal of the supernatant, cells were resuspended in ∼10–50 µL PBS from which 1–2 µL was immobilised on 1.5% 0.2 µm-filtered agarose (Certified Molecular Biology Agarose; BioRad, Veenendaal, The Netherlands) pads between two heat-treated glass coverslips (Paul Marienfeld GmbH & Co. KG, Lauda-Königshofen, Germany; #1.5H, 170 µm thickness). Heat treatment of glass coverslips involves heating the coverslips to 500 °C for 20 min in a muffle furnace to remove organic impurities.

6.4.13 Experimental settings

All imaging was performed on the miCube as described at 20 °C. A 561 nm laser with ∼0.12 W/cm^2 power output was used for HiLo-to-TIRF illumination with 4 ms stroboscopic illumination[24] in the middle of 10 ms frames. Low-power UV illumination (µW/cm^2 range) was used and increased during experiments to ensure a low and steady number of fluorophores in the sample until exhaustion of the fluorophores. A UV-increment scheme was consistently used for all experiments (ESI Table 5). No emission filter was used except for the TIRF filter (Chroma ZET405/488/561m-TRF). The raw data were acquired using the open source Micro-Manager software[66]. During acquisition, 2 × 2 binning was used, which resulted in a pixel size of 128 × 128 nm. The camera image was cropped to the central 512 × 512 pixels (65.64 × 65.64 µm) or smaller. For sptPALM experiments, frames 500–55.000 were used for analysis, corresponding to 5–550 s. This prevented attempted localization of overlapping fluorophores at the beginning, and ensured a set end-time. 200–300 brightfield images were recorded by illuminating the sample at the same position as during the measurement. For the brightfield recording, we used a commercial LED light (INREDA, IKEA, Sweden) and a home-made diffuser from weighing paper.

6.4.14 Localization

To extract single-molecule localizations, a 50-frame temporal median filter (https://github.com/marcelocordeiro/medianfilter-imagej) was used to correct background intensity from the movies[67]. In short, the temporal median filter determines the median pixel value over a sliding-window of 50 pixels to determine the median background intensity value for a pixel at a specific position and time point. This value is subtracted from the original data, and any negative values are set to 0. In the process, all pixels are scaled according to the mean intensity of each frame to account for shifts in overall intensity. The first and last 25 frames from every batch of 8096 frames are removed in this process.

Single-particle localization was performed via the ImageJ[68]/Fiji[69] plugin ThunderSTORM[70] with added phasor-based single-molecule localization algorithm (pSMLM[39]). Image filtering was done via a difference-of-Gaussians filter with Sigma1 = 2 px and Sigma2 = 8 px. The approximate localization of molecules was determined via a local maximum with a peak

intensity threshold of 8, and 8-neighbourhood connectivity. Sub-pixel localization was done via phasor fitting[39] with a fit radius of 3 pixels (region-of-interest of 7 × 7 pixels). Custom-written MATLAB (The MathWorks, Natick, MA, USA) scripts were used to combine the output files from ThunderSTORM.

6.4.15 Cell segmentation

A cell-based segmentation on the localization positions was performed. First, a watershed was performed on the average of 300 brightfield-recorded frames of the cells. The watershed was done via the Interactive Watershed ImageJ plugin (http://imagej.net/Interactive_Watershed). Second, the localizations were filtered whether or not they fall in a pixel-accurate cell outline. If they do, a cell ID is added to the localization information.

6.4.16 Estimating the copy number of dCas9

The total copy number of dCas9 in a cell is not identical to the number of tracks found in each cell. Firstly, the UV illumination (405 nm wavelength) on the miCube required to photo-activate PAmCherry2 is not homogeneous over the complete field of view. To correct for this, a value for the average UV illumination experienced by each *L. lactis* cell is calculated. For this, a map of the UV intensity is made by placing a mirror on top of the objective and measuring the reflected scattering of the UV signal. Then, the mean UV intensity in the pixels corresponding to a cell according to the segmented brightfield images is stored. The cellular apparent dCas9 copy number is corrected for this normalised mean cellular UV intensity. Moreover, the cellular apparent dCas9 copy number was corrected for the average maturation grade of PAmCherry1, which is 50%[53] (shown schematically in Figure S6.8). We assume the maturation grades of PAmCherry1 and PAmCherry2 to be similar.

6.4.17 Tracking and fitting of diffusion coefficient histograms

A tracking procedure was performed in MATLAB, using a modified Particle Point Analysis script[71] (https://nl.mathworks.com/matlabcentral/fileexchange/42573-particle-point-analysis) with a tracking window of 8 pixels (1.0 µm) and no memory. Localizations corresponding to different cells were excluded from being part of the same track. As the tracking window is of similar size as the cells itself, in practice all localizations in a cell are linked together in a track if they appear in successive frames.

An apparent diffusion coefficient, D^*, was then calculated for each track from the mean-squared displacement (MSD) of single-step intervals[72]. In short, for every track with at least 4 localizations, the D^* was calculated by calculating the mean square displacement between the first four steps and taking the average of that. Qualitative tracking information in cells (Figure 6.2a, Figure 6.3a) shows that diffusion coefficients up to ~4 µm^2/s are obtained. These high diffusion coefficient tracks are caused by including false positive localizations in tracks. Therefore, tracks with a diffusion coefficient clearly caused by inclusion of false positive localizations ($D^* > 2.5$ µm^2/s) were excluded from further analysis. We then binned the diffusion coefficients in 40 logarithmic-divided bins from $D^* = 0.01$ to $D^* = 2.5$ µm^2/s. The pNonTarget diffusional information was

first corrected for the diffusion histogram obtained from a non-induced sample, subtracting the non-induced histogram from the pNonTarget histogram based on the approximated relative size of the non-induced histogram (~7.2 tracks per cell were found in non-induced cells).

Then, a Monte-Carlo diffusion distribution analysis (MC-DDA; described-below) consisting of 20.000 dCas9 proteins was fitted via a general Levenberg-Marquardt fitting procedure in MATLAB. The error of this fit was determined via a general bootstrapping approach, where a D^*-list with the same length as the original, but randomly filled with values from the original (allowing for more than one entry of the same data), was fitted via the same procedure. For the pTarget diffusional information, the pNonTarget best fitted model (calculated via the same model, but with 100.000 dCas9 proteins) was fitted and smoothed via a Savitzky-Golay filter with order 3 and length 7, to reduce noise on the fit, alongside a single population following the following equation:

$$y = \frac{\left(\frac{n}{D_{plasmid}}\right)^n \cdot x^{(n-1)} \cdot e^{-n\frac{x}{D_{plasmid}}}}{(n-1)!} \tag{6.1}$$

where D_{plasmid} is the D^*-value corresponding to plasmid-bound dCas9, n the number of steps in the trajectory (set to four in this study), y the count of the histogram, and x the D^*-value of the histogram. D_{plasmid} was kept constant in the global fit, while the size of this population and the size of the pNonTarget model were allowed to vary between apparent cellular dCas9 copy number bins. Again, the error of this fit was determined via a general bootstrapping approach.

6.4.18 pNonTarget Monte-Carlo diffusion distribution analysis

The pNonTarget data is fitted with a Monte-Carlo diffusion distribution analysis (MC-DDA), in which a variable D_{free}, localization error, $k_{\text{free}\rightarrow\text{bound}}$, and $k_{\text{bound}\rightarrow\text{free}}$ need to be provided (ESI Software). A set number of dCas9 proteins are simulated (20.000 for the fit, 100.000 for visualising the fit). These proteins are then randomly placed in a cell, which is simulated as a cylinder with length 0.5 µm and radius 0.5 µm, capped by two half-spheres with radius 0.5 µm, and the current state of the proteins is set to free or immobile, based on the respective kinetic rates ($c_{bound} = k_{free\rightarrow bound}/(k_{bound\rightarrow free} + k_{free\rightarrow bound})$, $c_{free} = 1 - c_{bound}$).

Moreover, the proteins are given a time before they are changed between states ($log(rand)/-k$, where rand is a random number between 0 and 1, and k is the respective kinetic rate). Then, the movement of the proteins is simulated with over-sampling with regards to the frame time (0.1 ms). The free proteins will move a distance equal to a randomly sampled normal distribution with $\sigma = \sqrt{2 \cdot D_{free} \cdot steptime}$, where steptime is 0.1 ms. Then, it checked if this position is still within the cell outline. If not, a new location will be pulled from the distribution and checked against the cell outline. Every time-step, the time until state-change is subtracted with the time-step, and if this value becomes ≤ 0, the proteins will switch states, getting a new diffusion coefficient and state-change time. Every 10 ms after an initial equilibrium time of 200 ms, the current location of the proteins is convolved with a random localization error, from a randomly sampled normal distribution with σ = localization error. The simulation is ended after 5 localization points are acquired for every protein. Further tracking and diffusion coefficient calculations are done the same as the experimental data.

6.4.19 Target simulation

For the target simulation, a certain number of dCas9 are simulated (similar to the average of the bins used in experiments), alongside a variable total number of PAM sites (1/16 chance at ~7.5 mln bases, or 1.5× double-stranded *L. lactis* genome[73]), plasmid copy number, target sites (5 per plasmid), incubation time (90 min), fluorophore maturation time (20 min[27]), and a k_{off} rate. The dCas9 proteins are simulated one by one. The first dCas9 will have access to all target sites, and will be simulated for [incubation time], assuming the first dCas9 was made exactly at the start of the nisin incubation. Subsequent dCas9 proteins will have access to fewer target sites, depending on whether or not earlier dCas9 proteins have ended the simulation bound to target sites. Subsequent dCas9 proteins will also be simulated for a shorter time, linearly scaling from [incubation time] to [fluorophore maturation time], which assumes that dCas9 proteins are steadily produced throughout the incubation time, but allowing for the fact that dCas9 proteins that do not yet have a matured PAmCherry2 are not visible during sptPALM.

Then, the dCas9 proteins randomly start in the free, PAM-probing, or target-bound state, based on the previously determined kinetic constants, similarly as in the pNonTarget simulation. The proteins are also given a time until state change, as was done in the pNonTarget simulation. Next, the simulation time of a single dCas9 protein was decreased by this time until state change, whereupon a new state was given to the protein: free proteins changed to PAM-probing or target-bound, with the target-bound chance being equal to nrtargetsites/totalnrofPAMsites; PAM-probing or target-bound proteins were changed to free proteins. This was continued until the end of the simulation, after which the final state was determined. If the dCas9 was bound to a target, the available target sites were decreased by 1 for the next simulated dCas9. The reported values are the mean of 50 repetitions of the simulation, with the 95% confidence interval determined via the standard deviation of these repetitions.

For simulating Cas9 cleavage rates, it was assumed that a single target site was present and that a dCas9 would never be removed from a target site. By then analysing the bound dCas9, it indicates whether the target site has been cleaved by Cas9. The other simulation parameters were kept constant.

6.4.20 miCube drift quantification

We characterised the positional stability of the miCube via super-resolution measurements of GATTA-PAINT 80R DNA-PAINT nanorulers (GATTAquant GmbH, Germany). We imaged the nanorulers in total internal reflection (TIR) mode using a 561 nm laser (~7 mW) with a frame time of 50 ms using 2 × 2 pixel binning on the Andor Zyla 4.2 PLUS sCMOS. Astigmatism was enabled by placing a 1000 mm focal length astigmatic lens (Thorlabs) 51 mm away from the camera chip. A video of 10.000 frames was recorded via the MicroManager software[66].

After recording the movie, we first localized the x, y, and z-positions of the point spread functions of excited DNA-PAINT nanoruler fluorophores with the ThunderSTORM software[70] for ImageJ[68] with the phasor-based single-molecule localization (pSMLM) add-on[39]. The ThunderSTORM software was used with the standard settings, and a 7 × 7 pixel region of interest around the approximate centre of the point spread functions was used for pSMLM. To determine the z-posi-

tion, we compared the astigmatism of the point-spread function to a pre-recorded calibration curve recorded using immobilised fluorescent latex beads (560 nm emission peak, 50 nm diameter).

After data analysis, we performed drift-correction in the lateral plane using the cross-correlation method of the ThunderSTORM software. The cross-correlation images were calculated using 10x magnified super-resolution images from a sub-stack of 1000 original frames. The fit of the cross-correlation was used as drift of the lateral plane. Drift of the axial plane was analysed by taking the average z-position of all fluorophores, assuming that all DNA-PAINT nanorulers are fixed to the bottom of the glass slide.

6.5 Acknowledgements

K.J.A.M. is funded by a VLAG PhD-fellowship grant awarded to J.H. J.H. acknowledges funding from the Innovation Program Microbiology Wageningen (IPM-3). S.v.d.E is funded by the BE-Basic R&D program, which was granted a FES subsidy from the Dutch Ministry of Economic affairs. The authors thank the WOSM (Warwick Open Source Microscope, see www.wosmic.org) for inspiration.

6.6 Author contributions

K.J.A.M., S.B., and J.H. designed, built and characterised the miCube setup. K.J.A.M., S.P.B.v.B. and G.A.V. recorded and analysed the experimental single-molecule data. J.H., S.v.d.E. and P.v.B. envisioned using *L. lactis*, dCas9, fluorescent proteins and p(Non-)Target cells to conduct super-resolution single-molecule studies. S.P.B.v.B., S.v.d.E., P.v.B., and M.K. designed the DNA vectors used in this study. S.P.B.v.B. and S.v.d.E. assembled the DNA vectors and transformed cells. K.J.A.M., J.N.A.V., and J.H. developed DDA. K.J.A.M. and J.N.A.V. wrote software for data analysis. J.N.A.V. and S.J.J.B. provided reagents and expertise for setting up the single-molecule assays. K.J.A.M. and J.H. wrote the manuscript with input from all authors. J.H. initialised the study and the collaborations, and supervised all aspects of the study.

References

1. Qi, L. S., Larson, M. H., Gilbert, L. A., *et al.* Repurposing CRISPR as an RNA-Guided Platform for Sequence-Specific Control of Gene Expression. *Cell* **152,** 1173–1183 (2013).
2. Komor, A. C., Badran, A. H. & Liu, D. R. CRISPR-Based Technologies for the Manipulation of Eukaryotic Genomes. *Cell* **168,** 20–36 (2017).
3. Jiang, W., Bikard, D., Cox, D., *et al.* RNA-Guided Editing of Bacterial Genomes Using CRISPR-Cas Systems. *Nature Biotechnology* **31,** 233–239 (2013).
4. Liu, J.-J., Orlova, N., Oakes, B. L., *et al.* CasX Enzymes Comprise a Distinct Family of RNA-Guided Genome Editors. *Nature,* 1 (2019).
5. Sapranauskas, R., Gasiunas, G., Fremaux, C., *et al.* The Streptococcus Thermophilus CRISPR/Cas System Provides Immunity in Escherichia Coli. *Nucleic Acids Research* **39,** 9275–9282 (2011).
6. Chen, B., Gilbert, L. A., Cimini, B. A., *et al.* Dynamic Imaging of Genomic Loci in Living Human Cells by an Optimized CRISPR/Cas System. *Cell* **155,** 1479–1491 (2013).
7. Bonomo, M. E. & Deem, M. W. The Physicist's Guide to One of Biotechnology's Hottest New Topics: CRISPR-Cas. *Physical Biology* **15,** 041002 (2018).
8. Anders, C., Niewoehner, O., Duerst, A., *et al.* Structural Basis of PAM-Dependent Target DNA Recognition by the Cas9 Endonuclease. *Nature* **513,** 569–573 (2014).
9. Globyte, V., Lee, S. H., Bae, T., *et al.* CRISPR/Cas9 Searches for a Protospacer Adjacent Motif by Lateral Diffusion. *The EMBO Journal,* e99466 (2018).
10. Knight, S. C., Xie, L., Deng, W., *et al.* Dynamics of CRISPR-Cas9 Genome Interrogation in Living Cells. *Science* **350,** 823–826 (2015).

11. Sternberg, S. H., Redding, S., Jinek, M., *et al.* DNA Interrogation by the CRISPR RNA-Guided Endonuclease Cas9. *Nature* **507,** 62–67 (2014).
12. Singh, D., Sternberg, S. H., Fei, J., *et al.* Real-Time Observation of DNA Recognition and Rejection by the RNA-Guided Endonuclease Cas9. *Nature Communications* **7,** 12778 (2016).
13. Gasiunas, G., Barrangou, R., Horvath, P., *et al.* Cas9–crRNA Ribonucleoprotein Complex Mediates Specific DNA Cleavage for Adaptive Immunity in Bacteria. *Proceedings of the National Academy of Sciences* **109,** E2579–E2586 (2012).
14. Jones, D. L., Leroy, P., Unoson, C., *et al.* Kinetics of dCas9 Target Search in Escherichia Coli. *Science* **357,** 1420–1424 (2017).
15. Machielsen, R., Siezen, R. J., van Hijum, S. A. F. T., *et al.* Molecular Description and Industrial Potential of Tn6098 Conjugative Transfer Conferring Alpha-Galactoside Metabolism in Lactococcus Lactis. *Applied and Environmental Microbiology* **77,** 555–563 (2011).
16. Hidalgo-Cantabrana, C., O'Flaherty, S. & Barrangou, R. CRISPR-Based Engineering of next-Generation Lactic Acid Bacteria. *Current opinion in microbiology* **37,** 79–87 (2017).
17. Zhang, C., Wohlhueter, R. & Zhang, H. Genetically Modified Foods: A Critical Review of Their Promise and Problems. *Food Science and Human Wellness* **5,** 116–123 (2016).
18. Manley, S., Gillette, J. M., Patterson, G. H., *et al.* High-Density Mapping of Single-Molecule Trajectories with Photoactivated Localization Microscopy. *Nature Methods* **5,** 155–157 (2008).
19. Uphoff, S., Reyes-Lamothe, R., de Leon, F. G., *et al.* Single-Molecule DNA Repair in Live Bacteria. *Proceedings of the National Academy of Sciences* **110,** 8063–8068 (2013).
20. Smith, C. S., Joseph, N., Rieger, B., *et al.* Fast, Single-Molecule Localization That Achieves Theoretically Minimum Uncertainty. *Nature Methods* **7,** 373–375 (2010).
21. Rieger, B. & Stallinga, S. The Lateral and Axial Localization Uncertainty in Super-Resolution Light Microscopy. *ChemPhysChem* **15,** 664–670 (2014).
22. Shen, H., Tauzin, L. J., Baiyasi, R., *et al.* Single Particle Tracking: From Theory to Biophysical Applications. *Chemical Reviews* **117,** 7331–7376 (2017).
23. Vink, J. N. A., Martens, K. J. A., Vlot, M., *et al.* Direct Visualization of Native CRISPR Target Search in Live Bacteria Reveals Cascade DNA Surveillance Mechanism. *Molecular Cell* **77,** 39–50.e10 (2020).
24. Farooq, S. & Hohlbein, J. Camera-Based Single-Molecule FRET Detection with Improved Time Resolution. *Physical Chemistry Chemical Physics* **17,** 27862–27872 (2015).
25. Santoso, Y., Joyce, C. M., Potapova, O., *et al.* Conformational Transitions in DNA Polymerase I Revealed by Single-Molecule FRET. *Proceedings of the National Academy of Sciences* **107,** 715–720 (2010).
26. Santoso, Y., Torella, J. P. & Kapanidis, A. N. Characterizing Single-Molecule FRET Dynamics with Probability Distribution Analysis. *ChemPhysChem* **11,** 2209–2219 (2010).
27. Subach, F. V., Patterson, G. H., Manley, S., *et al.* Photoactivatable mCherry for High-Resolution Two-Color Fluorescence Microscopy. *Nature methods* **6,** 153–159 (2009).
28. Arsenault, A., Leith, J. S., Henkin, G., *et al.* Open-Frame System for Single-Molecule Microscopy. *Review of Scientific Instruments* **86,** 033701 (2015).
29. Nicovich, P. R., Walsh, J., Böcking, T., *et al.* NicoLase—An Open-Source Diode Laser Combiner, Fiber Launch, and Sequencing Controller for Fluorescence Microscopy. *PLOS ONE* **12,** e0173879 (2017).
30. Auer, A., Schlichthaerle, T., Woehrstein, J., *et al.* Nanometer-Scale Multiplexed Super-Resolution Imaging with an Economic 3D-DNA-PAINT Microscope. *ChemPhysChem* (2018).
31. Babcock, H. P. Multiplane and Spectrally-Resolved Single Molecule Localization Microscopy with Industrial Grade CMOS Cameras. *Scientific reports* **8,** 1726 (2018).
32. Diekmann, R., Till, K., Müller, M., *et al.* Characterization of an Industry-Grade CMOS Camera Well Suited for Single Molecule Localization Microscopy–High Performance Super-Resolution at Low Cost. *Scientific Reports* **7,** 14425 (2017).
33. Holm, T., Klein, T., Löschberger, A., *et al.* A Blueprint for Cost-Efficient Localization Microscopy. *ChemPhysChem* **15,** 651–654 (2014).
34. Ma, H., Fu, R., Xu, J., *et al.* A Simple and Cost-Effective Setup for Super-Resolution Localization Microscopy. *Scientific Reports* **7** (2017).
35. Kwakwa, K., Savell, A., Davies, T., *et al.* easySTORM: A Robust, Lower-Cost Approach to Localisation and TIRF Microscopy. *Journal of biophotonics* **9,** 948–957 (2016).
36. Zhang, Y. S., Ribas, J., Nadhman, A., *et al.* A Cost-Effective Fluorescence Mini-Microscope for Biomedical Applications. *Lab on a Chip* **15,** 3661–3669 (2015).
37. Diederich, B., Then, P., Jügler, A., *et al.* cellSTORM—Cost-Effective Super-Resolution on a Cellphone Using dSTORM. *PLOS ONE* **14,** e0209827 (2019).
38. Aristov, A., Lelandais, B., Rensen, E., *et al.* ZOLA-3D Allows Flexible 3D Localization Microscopy over an Adjustable Axial Range. *Nature Communications* **9,** 2409 (2018).

39. Martens, K. J. A., Bader, A. N., Baas, S., *et al.* Phasor Based Single-Molecule Localization Microscopy in 3D (pSMLM-3D): An Algorithm for MHz Localization Rates Using Standard CPUs. *The Journal of Chemical Physics* **148,** 123311 (2018).
40. Coelho, S., Baek, J., Graus, M. S., *et al.* Single Molecule Localization Microscopy with Autonomous Feedback Loops for Ultrahigh Precision. *bioRxiv,* 487728 (2018).
41. Van Beljouw, S. P. B., van der Els, S., Martens, K. J. A., *et al.* Evaluating Single-Particle Tracking by Photo-Activation Localization Microscopy (sptPALM) in Lactococcus Lactis. *Physical Biology* **16** (2019).
42. Mierau, I. & Kleerebezem, M. 10 Years of the Nisin-Controlled Gene Expression System (NICE) in Lactococcus Lactis. *Applied microbiology and biotechnology* **68,** 705–717 (2005).
43. Vincent, L. & Soille, P. Watersheds in Digital Spaces: An Efficient Algorithm Based on Immersion Simulations. *IEEE Transactions on Pattern Analysis & Machine Intelligence,* 583–598 (1991).
44. Nishimasu, H., Cong, L., Yan, W. X., *et al.* Crystal Structure of Staphylococcus Aureus Cas9. *Cell* **162,** 1113–1126 (2015).
45. Edward, J. T. Molecular Volumes and the Stokes-Einstein Equation. *Journal of Chemical Education* **47,** 261 (1970).
46. Trovato, F. & Tozzini, V. Diffusion within the Cytoplasm: A Mesoscale Model of Interacting Macromolecules. *Biophysical Journal* **107,** 2579–2591 (2014).
47. Vos, D. & M, W. Gene Cloning and Expression in Lactic Streptococci. *FEMS Microbiology Reviews* **3,** 281–295 (1987).
48. Prazeres, D. M. F. Prediction of Diffusion Coefficients of Plasmids. *Biotechnology and bioengineering* **99,** 1040–1044 (2008).
49. Whinn, K., Kaur, G., Lewis, J. S., *et al.* Nuclease Dead Cas9 Is a Programmable Roadblock for DNA Replication. *bioRxiv,* 455543 (2018).
50. Vigouroux, A., Oldewurtel, E., Cui, L., *et al.* Tuning dCas9's Ability to Block Transcription Enables Robust, Noiseless Knockdown of Bacterial Genes. *Molecular systems biology* **14,** e7899 (2018).
51. Tal, S. & Paulsson, J. Evaluating Quantitative Methods for Measuring Plasmid Copy Numbers in Single Cells. *Plasmid. A Special Issue on Chromosome Dynamics in Memory of Prof. Kurt Nordstrom* **67,** 167–173 (2012).
52. Slutsky, M. & Mirny, L. A. Kinetics of Protein-DNA Interaction: Facilitated Target Location in Sequence-Dependent Potential. *Biophysical Journal* **87,** 4021–4035 (2004).
53. Durisic, N., Laparra-Cuervo, L., Sandoval-Álvarez, Á., *et al.* Single-Molecule Evaluation of Fluorescent Protein Photoactivation Efficiency Using an in Vivo Nanotemplate. *Nature methods* **11,** 156 (2014).
54. Nagai, T., Ibata, K., Park, E. S., *et al.* A Variant of Yellow Fluorescent Protein with Fast and Efficient Maturation for Cell-Biological Applications. *Nature biotechnology* **20,** 87 (2002).
55. Khan, S. A. Rolling-Circle Replication of Bacterial Plasmids. *Microbiol. Mol. Biol. Rev.* **61,** 442–455 (1997).
56. Farasat, I. & Salis, H. M. A Biophysical Model of CRISPR/Cas9 Activity for Rational Design of Genome Editing and Gene Regulation. *PLOS Computational Biology* **12,** e1004724 (2016).
57. Huang, B., Wang, W., Bates, M., *et al.* Three-Dimensional Super-Resolution Imaging by Stochastic Optical Reconstruction Microscopy. *Science* **319,** 810–813 (2008).
58. Almada, P., Culley, S. & Henriques, R. PALM and STORM: Into Large Fields and High-Throughput Microscopy with sCMOS Detectors. *Methods. Super-Resolution Light Microscopy* **88,** 109–121 (2015).
59. Kuipers, O. P., de Ruyter, P. G. G. A., Kleerebezem, M., *et al.* Quorum Sensing-Controlled Gene Expression in Lactic Acid Bacteria. *Journal of Biotechnology. Genome Analysis and the Changing Face of Biotechnology* **64,** 15–21 (1998).
60. Wells, J. M., Wilson, P. W. & Le Page, R. W. F. Improved Cloning Vectors and Transformation Procedure for Lactococcus Lactis. *Journal of Applied Bacteriology* **74,** 629–636 (1993).
61. Campelo, A. B., Roces, C., Mohedano, M. L., *et al.* A Bacteriocin Gene Cluster Able to Enhance Plasmid Maintenance in Lactococcus Lactis. *Microbial Cell Factories* **13,** 77 (2014).
62. Van der Els, S., James, J. K., Kleerebezem, M., *et al.* Development of a Versatile Cas9-Driven Subpopulation-Selection Toolbox in Lactococcus Lactis. *Applied and Environmental Microbiology,* AEM.02752–17 (2018).
63. van Asseldonk, M., Rutten, G., Oteman, M., *et al.* Cloning of Usp45, a Gene Encoding a Secreted Protein from Lactococcus Lactis Subsp. Lactis MG1363. *Gene* **95,** 155–160 (1990).
64. Goel, A., Santos, F., de Vos, W. M., *et al.* A Standardized Assay Medium to Measure Enzyme Activities of Lactococcus Lactis While Mimicking Intracellular Conditions. *Applied and Environmental Microbiology,* AEM.05276–11 (2011).
65. Drlica, K., Malik, M., Kerns, R. J., *et al.* Quinolone-Mediated Bacterial Death. *Antimicrobial Agents and Chemotherapy* **52,** 385–392 (2008).
66. Edelstein, A. D., Tsuchida, M. A., Amodaj, N., *et al.* Advanced Methods of Microscope Control Using μManager Software. *Journal of Biological Methods* **1,** e10 (2014).

67. Hoogendoorn, E., Crosby, K. C., Leyton-Puig, D., *et al.* The Fidelity of Stochastic Single-Molecule Super-Resolution Reconstructions Critically Depends upon Robust Background Estimation. *Scientific Reports* **4,** 3854 (2014).
68. Schneider, C. A., Rasband, W. S. & Eliceiri, K. W. NIH Image to ImageJ: 25 Years of Image Analysis. *Nature methods* **9,** 671 (2012).
69. Schindelin, J., Arganda-Carreras, I., Frise, E., *et al.* Fiji: An Open-Source Platform for Biological-Image Analysis. *Nature methods* **9,** 676–682 (2012).
70. Ovesny, M., Křížek, P., Borkovec, J., *et al.* ThunderSTORM: A Comprehensive ImageJ Plug-in for PALM and STORM Data Analysis and Super-Resolution Imaging. *Bioinformatics* **30,** 2389–2390 (2014).
71. Crocker, J. C. & Grier, D. G. Methods of Digital Video Microscopy for Colloidal Studies. *Journal of Colloid and Interface Science* **179,** 298–310 (1996).
72. Stracy, M. & Kapanidis, A. N. Single-Molecule and Super-Resolution Imaging of Transcription in Living Bacteria. *Methods. Transcriptional Dynamics* **120,** 103–114 (2017).
73. Linares, D. M., Kok, J. & Poolman, B. Genome Sequences of Lactococcus Lactis MG1363 (Revised) and NZ9000 and Comparative Physiological Studies. *Journal of Bacteriology* **192,** 5806–5812 (2010).

6.7 Supplementary information

Electronic supplementary information (ESI) can be found at doi:10.1038/s41467-019-11514-0, and consists of the following:
ESI Figures 10-18: Technical drawings of various miCube components.
ESI Note 1: DNA and amino acid sequences belonging to dCas9-PAmCherry2 used in this study.
ESI Table 1: Descriptive list of miCube components.
ESI Table 2: List of used vectors.
ESI Table 3: List of oligonucleotides.
ESI Table 4: List of primers.
ESI Table 5: Adjustment of the 405 nm laser power during sptPALM experiments.
ESI Software: MATLAB scripts used in this study.

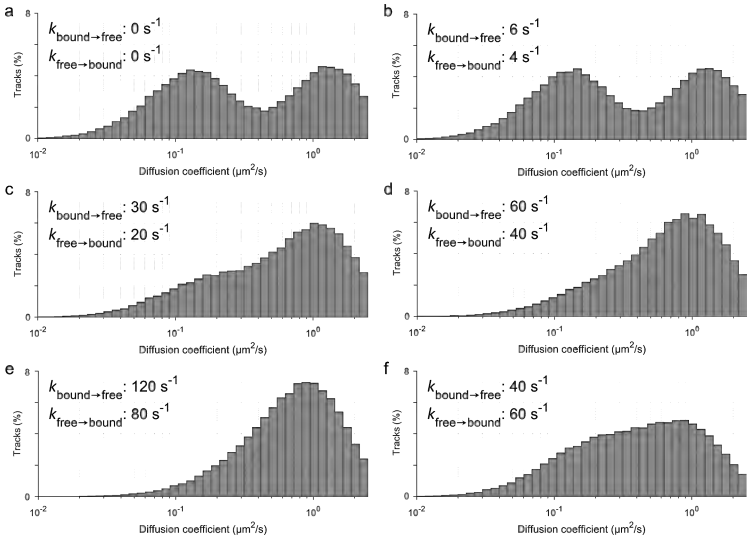

Figure S6.1: Effect of state transitions on diffusion coefficient histogram. The pNonTarget model as described in Methods was ran with varying $k_{\text{bound}\rightarrow\text{free}}$ and $k_{\text{free}\rightarrow\text{bound}}$ values as indicated in the figure, while keeping the localization error and Dfree constant at the values determined while fitting the actual data (38 nm and 2.0 $\mu m^2/s$, respectively). **a** Diffusion coefficient histogram if no state transitions would be present. **b** - **e** Diffusion coefficient histograms with the same $k_{\text{bound}\rightarrow\text{free}}$: $k_{\text{free}\rightarrow\text{bound}}$ ratio as the determined best-fitting values of ∼3:2, while varying the absolute values of the two. **f** Diffusion coefficient histogram if the kinetic parameters were swapped.

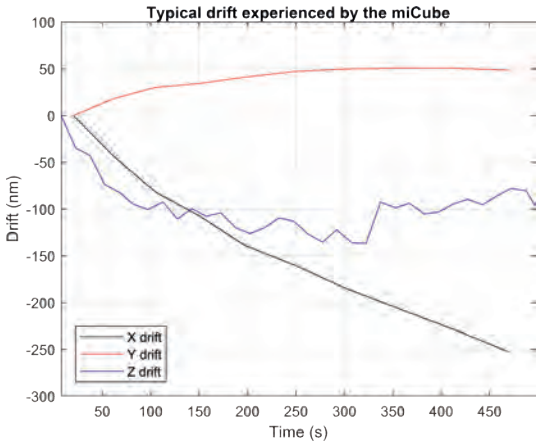

Figure S6.2: Typical drift experienced by the miCube. Typical drift in x (black), y (red), and z (blue) as experienced by the miCube used throughout this study. Repetition of this experiment led to the values specified in the main text.

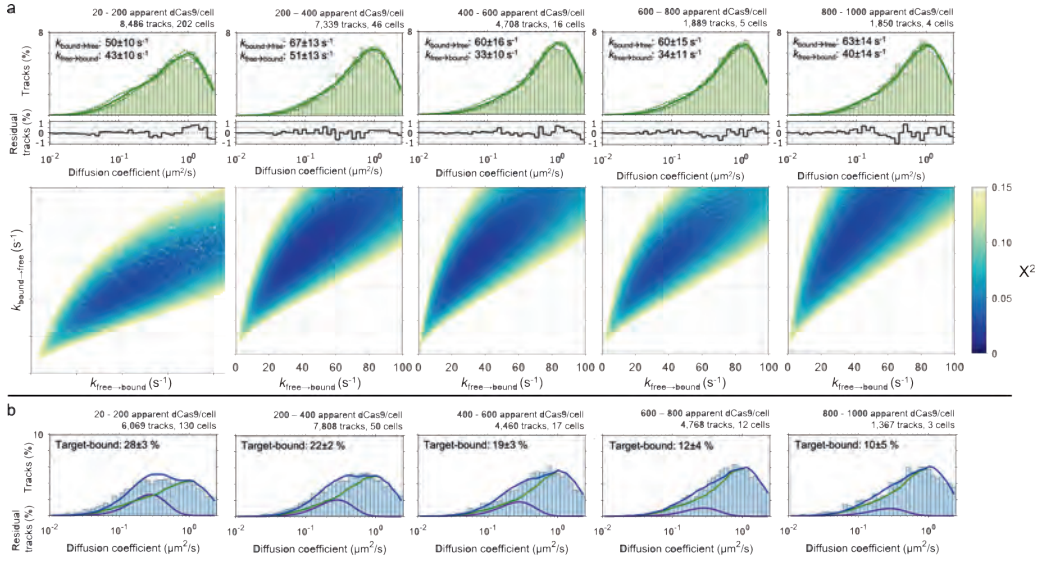

Figure S6.3: Individual pNonTarget and pTarget distributions **a** All five pNonTarget diffusional distributions fitted with MC-DDA, as explained in the main text, Methods section, and Figure 6.2. At the bottom, the Chi-squared value is plotted for a range of MC-DDAs (100.000 simulated proteins) with different $k_{\text{free}\rightarrow\text{bound}}$ and $k_{\text{bound}\rightarrow\text{free}}$. **b** All five pTarget diffusional distributions fitted with the computational target-binding model, as explained in the main text, Methods section, and Figure 6.3.

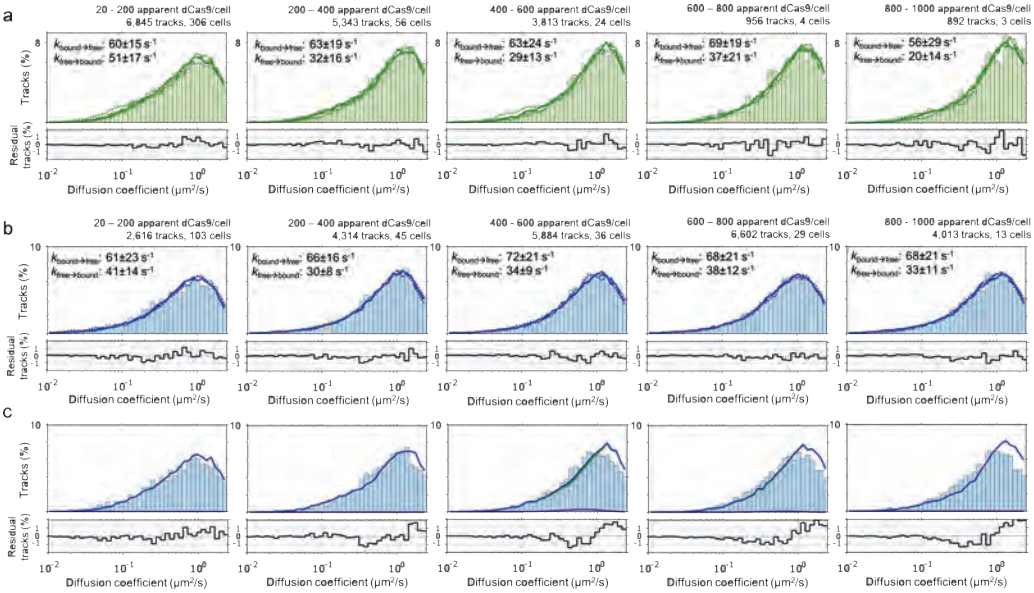

Figure S6.4: no-sgRNA distributions fitted with MC-DDA or the target-binding model **a** The five no-sgRNA pNonTarget diffusional distributions were fitted with MC-DDA as explained in the main text, Methods section. **b** The five no-sgRNA pTarget diffusional distributions were fitted with MC-DDA, as explained in the main text, Methods section. We note that the found kinetic rates are not significantly different from the no-sgRNA pNonTarget rates. **c** The five no-sgRNA pTarget diffusional distributions were fitted with a combination of the fixed no-sgRNA pNonTarget populations (from a) and a global non-fixed bound population. We note that no target-bound dCas9 population can be fitted, while the fitting methodology is identical to that of normal pTarget (Figure S6.3b).

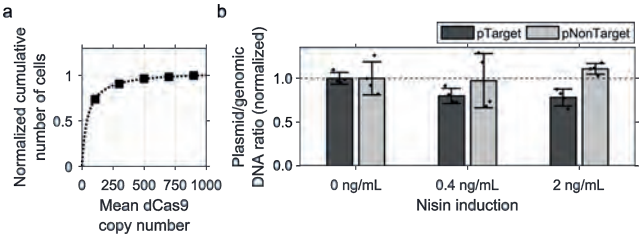

Figure S6.5: Effect of dCas9 on pTarget copy number **a** Representative normalised cumulative number of cells that have certain mean dCas9 copy numbers. Black squares are values taken from pNonTarget dataset, the dotted line is a fitted curve with equation $y = 1.05 \cdot [dCas9copynumber]/(44 \cdot [dCas9copynumber])$. **b** Normalised qPCR-determined ratio of plasmid:genome DNA for pTarget and pNonTarget for different Nisin induction. Error bars are the standard deviation determined from the average of two biological replicates (both averaged on two technical replicates). Individual data points are plotted as black circular markers.

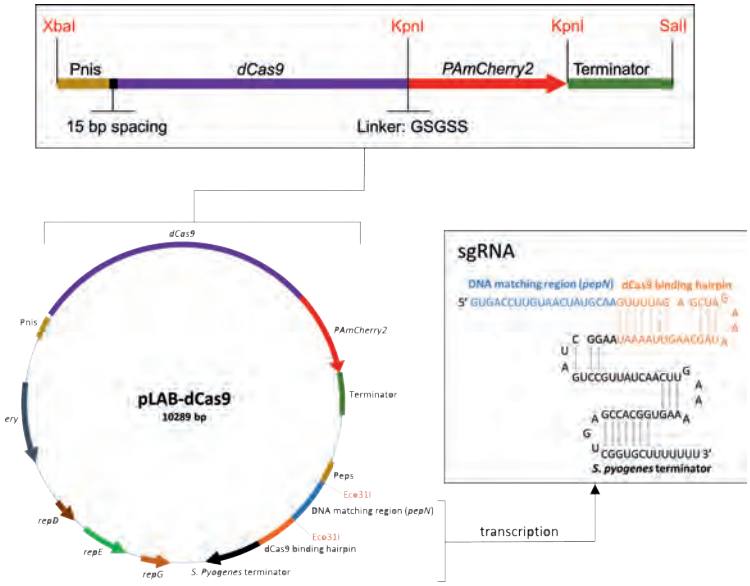

Figure S6.6: Outline of the pLAB-dCas9[1] vector **Top** The sequence encoding dCas9 (*S. pyogenes*; AddGene.org plasmid #44249) is fused to the sequence encoding PAmCherry2[27] (AddGene.org plasmid #31932) with a flexible linker (amino acid sequence GSGSS), downstream of the *nisA*-promoter (Pnis) with an ribosomal binding site (15 bp spacing) and ending with a transcriptional terminator sequence derived from a lactococcal *pepN* gene. PAmCherry2 is flanked by two KpnI sites which should allow for interchanging fluorophores. The whole sequence is flanked by XbaI and SalI restriction sites to allow convenient cloning into a (expression) vector of choice. **Bottom** The pLAB-dCas9 expression vector consists of PAmCherry2-labelled dCas9, an erythromycin resistance marker (Ery) and replication genes (*repD*, *repE* and *repG*)[61]. The *pepN* DNA matching region together with the dCas9 binding hairpin and the *S. pyogenes* terminator form the sgRNA, which is expressed under a constitutive promoter (Peps). Once the sgRNA molecule is transcribed, it folds to form the secondary structure that allows complex formation with dCas9.

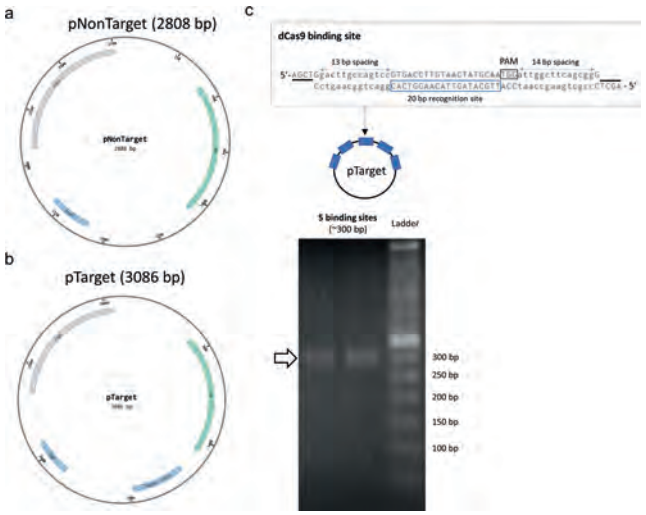

Figure S6.7: pNonTarget and pTarget construction and verification **a**,**b** Vector maps of pNonTarget and pTarget. Both targets contain *repA* and *repC* (DNA replication initiators) and a chloramphenicol-resistance marker (*cm*). Moreover, pTarget contains 5 target sites specified at 'Target Sites'. **c** dCas9 binding sites consisting of a 20 base pairs *pepN* recognition site, a 5'-NGG-3' PAM sequence, and spacing and overhang sequence motifs that are complementary to each other (indicated with black stripes) were annealed and ligated. This formed an array of five dCas9 binding sites in pNZ123, resulting in pTarget. Digestion and subsequent gel electrophoresis of plasmids isolated from two colonies revealed the expected length of the binding array in pTarget. One binding site is 54 base pairs in length, the final array of five binding sites is 278 base pairs (the expected PCR amplicon is 300 base pairs).

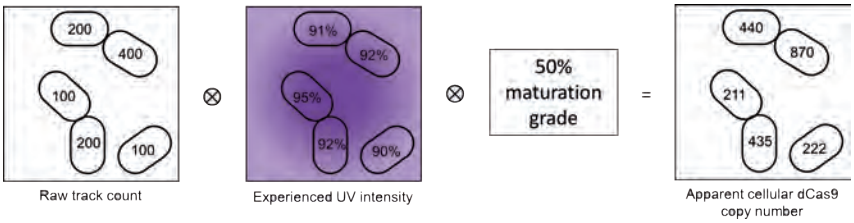

Figure S6.8: Schematic representation of obtaining cellular dCas9 copy number from number of tracks The raw track count (first subfigure) is convolved with the experience UV intensity that the cell on average experienced (second subfigure; deduced via reflective scattering of excitation lasers), and with the expected maturation grade of PAmCherry2 (Methods).

7

Spatiotemporal heterogeneity of κ-carrageenan gels investigated via single-particle tracking fluorescence microscopy

A version of this chapter has been published as:

Koen J.A. Martens, John van Duynhoven, and Johannes Hohlbein. Spatiotemporal Heterogeneity of κ-Carrageenan Gels Investigated via Single-Particle-Tracking Fluorescence Microscopy *Langmuir* **36** no. 20 (2020)

7

Abstract

Hydrogels made of the polysaccharide κ-carrageenan are widely used in the food and personal care industry as thickeners or gelling agents. These hydrogels feature dense regions embedded in a coarser bulk network, but the characteristic size and behaviour of these regions have remained elusive. Here, we use single-particle tracking fluorescence microscopy (sptFM) to quantitatively describe κ-carrageenan gels. Infusing fluorescent probes into fully gelated κ-carrageenan hydrogels resulted in two distinct diffusional behaviours. Obstructed self-diffusion of the probes revealed that the coarse network consists of κ-carrageenan strands with a typical diameter of 3.2 ± 0.3 nm leading to a nanoprobe diffusion coefficient of ∼1-5 $\mu m^2/s$. In the dense network regions, we found a fraction with a largely decreased diffusion coefficient of ∼0.1 $\mu m^2/s$. We also observed dynamic exchange between these states. The computation of spatial mobility maps from the diffusional data indicated that the dense network regions have a characteristic diameter of ∼1 µm and show mobility on the second-to-minute timescale. sptFM provides an unprecedented view of spatiotemporal heterogeneity of hydrogel networks, which we believe bears general relevance for understanding transport and release of both low- and high-molecular weight solutes.

7.1 Introduction

Carrageenan is a collection of linear sulfated polysaccharides, which are widely used as thickeners or gelling agents in food products, personal care products, and healthcare[1–3]. Gelation is induced by cooling down hot solutions of carrageenan, whereupon single helices are formed that can subsequently form double helices with other carrageenan strands under the assistance of cations such as potassium, sodium, or calcium[4–7]. This double helix formation results in cross-linking and thus thickening or gelling behaviour. Altering the precise chemical composition or concentration of carrageenan or the introduced cations results in different properties of the material[4–6]. Cations are required to induce gelation, with low concentrations of cations leading to low-strength hydrogels. Increasing the concentration of potassium, on the other hand, results in an increasing presence of stiff fiber rods, while addition of sodium ensues more flexible superstructures[5]. The degree of sulfonation dictates the exact type of carrageenan; μ, λ, and ι-carrageenans are the most common carrageenan variants, having one, two, and three sulfate ester groups, respectively[2]. In this study, we focused on the industrially relevant κ-carrageenan, for which the gel properties can readily be manipulated by specific ion additions[1,2,8].

Detailed knowledge of the structure of carrageenan hydrogels is desirable for rational design of food and personal care products. Analysis of carrageenan gels or solutions is usually performed via bulk techniques such as rheology[5], differential scanning calorimetry (used to study gel transition points[6]), scattering techniques (small angle X-ray scattering and small angle neutron scattering, used to elucidate strand thickness and behaviour[7]), and pulsed field gradient nuclear magnetic resonance (PFG NMR, used to study self-diffusion of low- and high-molecular-weight solutes[9–11]). Although these methods provide a wealth of information on the structure, formation, and behaviour of carrageenan gels, they generally do not provide spatial information on network heterogeneity.

Spatial heterogeneity is an important aspect of hydrogels: it influences rheological properties, plays an important role in the loading and releasing behaviour of solutes, and may also modulate enzyme activity during digestion[12–14]. Currently used imaging techniques (e.g. electron microscopy (EM)[5,8], raster image correlation spectroscopy (RICS)[10], or fluorescence recovery after photobleaching (FRAP)[15,16]) have indicated that dense network regions exist on a micrometre scale. However, these methods require invasive or destructive sample preparation (EM) or have limited power to quantitatively resolve spatial heterogeneity (RICS and FRAP)[11,17]. Quantitative non-destructive and non-invasive imaging techniques could prove to be valuable in confirming the existence and size of these regions. Here, we apply single-particle tracking fluorescence microscopy[18,19] (sptFM) to study κ-carrageenan networks with high spatiotemporal resolution and non-destructive sample preparation.

In subdiffraction-resolution sptFM, the positions of small (<100 nm) fluorescent particles are determined with ∼10-40 nm accuracy by fitting the emitted point spread functions (PSFs) with a mathematical model[20,21]. By assessing the position of these fluorescent particles at a high temporal resolution (∼100 Hz), the movement of the particles in the xy focal plane can be determined. While the 2D sptFM methodology can be extended to include z-positional information (3D sptFM) using engineered PSFs, this can be actually detrimental for diffusion analysis because of a lower localization accuracy in the xy plane[20,22]. Because the behaviour of the particles is directly in-

fluenced by the local environment[14,19,23–25], quantification and analysis of the movement leads to spatial characterization of the local surrounding medium. Recent sptFM performed on mixtures of ι- and κ-carrageenan gels[19,24] focused on using larger fluorescent particles (∼100 nm), effectively probing larger spatial structures than intended here. In this study, we will employ sptFM to obtain quantitative and spatially defined structural information on κ-carrageenan gels by infusing fluorescent nanoprobes of 28 nm diameter in fully gelated networks. First, we will investigate the existence and properties of κ-carrageenan gel heterogeneity and analyse the diffusional behaviour of the nanoprobes. Next, we will determine the morphology of the gel heterogeneity by evaluating nanoprobe trajectories based on their spatial position with sub-µm resolution.

Our results show the existence of primarily two nanoprobe diffusional states, which we attribute to diffusion in the coarse bulk network and in dense network regions, along with occasional switching between these states. The relationship between nanoprobe diffusion in the bulk coarse network is consistent with Johnson's obstruction model[10,26,27], describing the coarse network as consisting of 3.2 ± 0.3 nm diameter κ-carrageenan fibres independent of sodium ion concentration. Within this coarse network, regions of dense networks with ∼1 µm diameter are embedded, irrespective of the sodium ion or κ-carrageenan polymer concentration. These dense network regions occasionally show mobility on the second-to-minute timescale, which we directly observed with multiple techniques.

7.2 Results and discussion

7.2.1 κ-Carrageenan gel networks probed using fluorescent probes

κ-Carrageenan solutions were prepared at varying polymer concentrations (0.5-2.5% w/v), varying NaCl concentrations (100-200 mM), and a fixed KCl concentration (20 mM). These compositions are commonly employed in food products[28] and literature[4–6,10], and form gels throughout the parameter space. After cooling on a glass coverslip, 28 nm diameter carboxylate-modified fluorescent polymer nanospheres were infused into the gel. These probes were expected to move around in the gel network with a reduced diffusivity because of obstruction caused by the local network structure (Figure 7.1a)[26]. When we attempted to infuse nanospheres before gelation, we observed that a combination of residual salt and heating to 75 °C resulted in probe aggregation, and thus this procedure was not pursued further. Either the presence of residual salt or an increased temperature did not affect the diffusion of nanospheres, however.

Fluorescence emission from single probes could be observed using a 642 nm excitation laser light and a 5 ms camera frame time (Figure 7.1b). The PSFs were then identified and fitted (Methods; blue asterisks in Figure 7.1b,c). These positions were compared and potentially linked to those in the previous frames to create tracks. The diffusivity and jump distance of single tracks are shown as lines in Figure 7.1b,c.

7.2.2 Revealing network heterogeneity by the multimodal probe self-diffusion behaviour

Qualitatively, we could distinguish primarily two different mobilities of the fluorescent probes in the hydrogel network. We found that some of the probes were able to move around in the gel

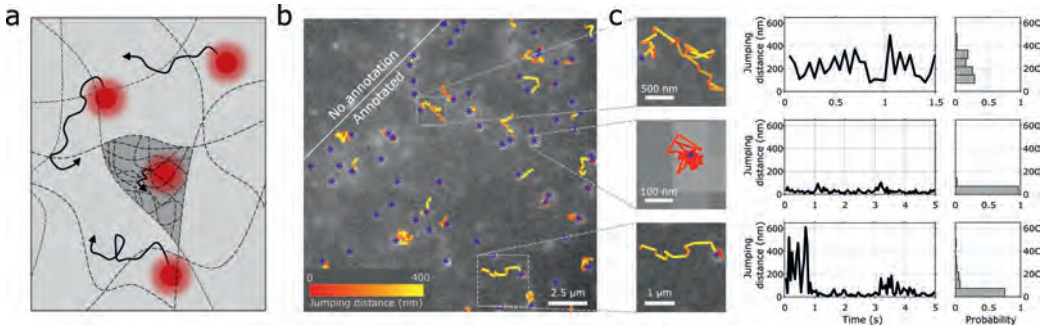

Figure 7.1: sptFM in κ-carrageenan gels. **a** Schematic representation of fluorescent probes (red), embedded in a gel matrix (dotted lines). These probes are capable of diffusion in the gel matrix (arrows). A coarse network (light grey region) allows for obstructed diffusion of the fluorescent probes, while dense network regions (dark grey region) further decrease the mobility of the probes. **b** Typical localization (blue asterisks) and tracking (yellow-red coloured lines) overlaid on a raw microscopy image. Shown here is single-particle tracking of 28 nm diameter polymer probes in a 1% κ-carrageenan gel with 200 mM NaCl, 20 mM KCl. Highlighted regions are enlarged in c. **c** Examples of obstructed diffusing (top), largely immobile (middle) or transitioning (bottom) particles. Left: the corresponding 2D movement of the single tracks. Middle: jump distance of this track plotted against the time of the track. Right: histogram created from the jump distances found in the track.

network slightly obstructed, leading to jumping distances in the order of several hundred nanometres (e.g. Figure 7.1c top). Other probes showed largely decreased self-diffusion over long time scales (>seconds; e.g. Figure 7.1c middle) in which the jumping distance is below ∼100 nm. Occasionally, probes showed interchanging behaviour between these two previous states (e.g. 7.1c bottom).

These results agree with earlier studies indicating the presence of spatial heterogeneity in the κ-carrageenan hydrogel networks[10,29,30]. The coarse network bulk is expected to have a polymer concentration-dependent mesh size of ∼100 nm, allowing slightly obstructed diffusion of the 28 nm diameter probes, in agreement with our first observed species (Figure 7.1c top). Meanwhile, distinct regions in the network exist with a much denser network with mesh size $< \sim 20$ nm[10], leading to hampered entry of the probes in the dense, but inherently flexible hydrogel network. This finding is in agreement with probes getting trapped and showing largely decreased self-diffusion (Figure 7.1c middle). Because probes are confined in both the coarse network bulk and the dense network regions, the diffusion coefficient obtained from jump distance analysis employed here is equally informative as mean squared displacement (MSD) analysis. Moreover, further quantification of the confinement effects via MSD would have to build on the assumption of spatial homogeneity[31], which is not present here.

Nonspecific chemical adsorption of the probes to network strands is unlikely because of repulsive negative charges. Moreover, similar experiments in a non-gelated κ-carrageenan polymers (because of the absence of salt) showed only a single-diffusive population (Figure S7.1), suggesting that in those experiments, diffusion is determined solely by the viscosity of a semidilute polymer solution[32].

The observation of occasional switching of the probe behaviour from the trapped state to the obstructed diffusing state or vice-versa (Figure 7.1c bottom) indicates structural rearrangement of the dense network. This finding is strengthened by the presence of trapped probes in these experiments in general, as the probes were infused after network formation and became trapped in the already gelled dense network region.

7.2.3 3.2 nm diameter κ-carrageenan network fibres hinder probe self-diffusion in the coarse network

To quantify the probe diffusion profiles, we plotted the mjd of individual tracks weighted by their corresponding number of localizations as histograms (Figure 7.2a,b, Methods). These data can be well described by two populations[30]; one corresponding to the probes trapped in the dense network (red outline in Figure 7.2a,b); and one corresponding to the probes showing obstructed self-diffusion in the coarse network (blue outline in Figure 7.2a,b). The state-switching behaviour shown in Figure 7.1c bottom should be present in these histograms as a population with a convolved mjd of the trapped and obstructed probes[33,34]. However, this behaviour is rare (<2% of all tracks longer than 20 frames likely show state-switching behaviour; Methods), and is therefore not attempted to quantify. The mjd of each population was determined by fitting logarithmic Gaussian functions on the histogram (Figure 7.2a,b).

The mjd plotted as a function of κ-carrageenan polymer and NaCl concentrations (Figure 7.2c) revealed that the population describing the trapped probes (red outline in Figure 7.2a,b) is unaffected by the polymer or NaCl concentration. The trapped probes had an average jump distance of ∼70 nm, which is higher than expected for fully immobile probes in which the measured jump distance is fully covered by the finite localization precision (22 nm; Methods). This trapped population had a self-diffusion coefficient of ∼0.1 $\mu m^2/s$, which is an inseparable convolution of probe self-diffusion and movement of the dense network region. We note that we observed a higher self-diffusion than shown previously for dendrimers trapped in κ-carrageenan gels observed via PFG NMR (10^{-14} m^2/s)[10]. We attribute this to the coating of the dendrimers used previously[10] with inert ethoxylate chains, which may entangle with polymer strands in the dense network.

The population describing the probes in the coarse network (blue outline in Figure 7.2a,b) shows a decreasing mjd with increasing κ-carrageenan polymer concentration, while it is mostly unaffected by the NaCl concentration. The mean diffusion coefficient of this obstructed population was ∼1 $\mu m^2/s$ in 2.5% κ-carrageenan gels and increased to ∼5 $\mu m^2/s$ in 0.5% κ-carrageenan gels. This relation between the probe self-diffusion coefficient and the polymer concentration can be accurately fitted by Johnson's obstruction model[10,26] (Figure 7.2d; Methods), indicating that the probe self-diffusion is obstructed by fibres of 3.2 ± 0.3 nm diameter in the coarse network. This finding agrees with earlier NMR studies in which a fibre diameter of ∼3 nm was found[10,27].

7.2.4 Dense networks span 1 µm-sized regions

Next, we were interested in the spatial distribution of the network heterogeneity, which was not yet addressed in comparable experimental settings[25,30]. To this end, the observed tracks were divided into three groups based on their respective mjd (Figure 7.3a). The first group (red) consists of

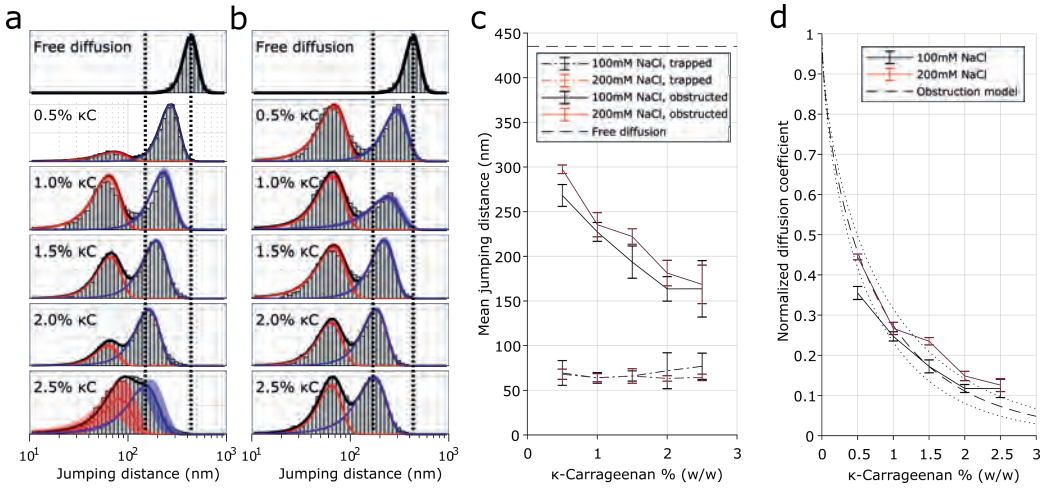

Figure 7.2: Quantification of network obstruction experienced by fluorescent probes. **a,b** Histogram of mean jump distances, weighted on track length, found for freely diffusing 28 nm probes in water (top) and in 0.5-2.5% κ-carrageenan gels with 20 mM KCl and 100 mM NaCl (a) or 200 mM NaCl (b). The histograms are fitted with 2 Gaussian profiles shown in red (trapped population) and blue (obstructed population). Vertical black-dotted lines are added as a guide to the eye, shaded red/blue profiles show the standard deviation of the fit, derived from populations fitted to individual single-particle tracking movies (each 12.5% of the complete data). **c** The mean trapped (red population in (a,b)) and obstructed (blue population in (a,b)) jump distance plotted vs the κ-carrageenan polymer content. Error bars represent the standard deviation of the fitted profile determined in (a,b). **d** Normalised diffusion coefficient corresponding to the mjd of the obstructed fraction as plotted in c, assuming a 22 nm localization uncertainty. An obstruction model (dashed line, Methods, main text; dotted lines indicate 95% confidence interval of the fit) was fitted to the data and reveals a fibre diameter of 3.2 ± 0.3 nm.

tracks that have ≥95% probability of belonging to probes trapped in the dense regions. The second group (yellow) consists of tracks that have ≥95% probability of belonging to probes in the coarse network. The third group consists of tracks that cannot be attributed clearly to either the first or second group and where therefore discarded from further analysis.

Next, we created mobility maps (Methods) in which an image with a pixel size of 61 × 61 nm is pseudo-colour coded based on the local probe behaviour (Figure 7.3b). The map shows the existence of ∼1 µm sized regions characterised by the presence of immobile probe(s), while there are no nearby mobile probe(s). Probes are trapped in these regions (red), while probes present in the coarse network surrounding the dense regions (yellow) are unable to enter (Figure 7.3c), possibly resulting in black regions indicative of the absence of any probes. These dense network regions have similar length scales to those shown previously with EM[15].

We confirmed the existence and size of these dense regions via rescan confocal microscopy (RCM)[35]. Here, the κ-carrageenan gels were infused with a higher concentration of fluorescent probes (0.03% w/v instead of 0.002%), causing fluorescence accumulation in the dense regions with respect to the coarse network[10]. As a result, the dense regions with the trapped probes were very

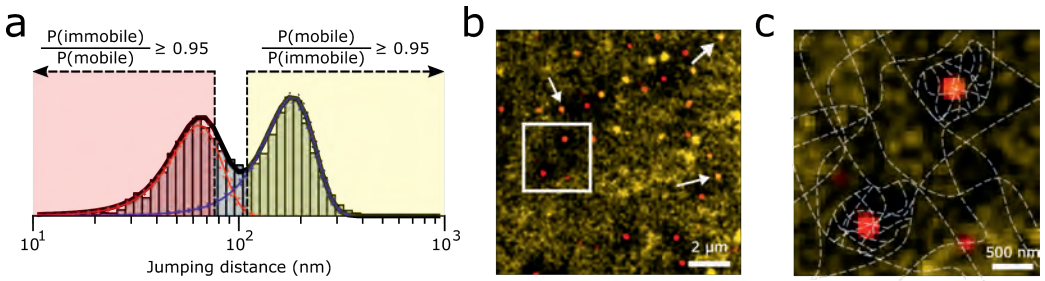

Figure 7.3: Mobility mapping of immobile and mobile regions in κ-carrageenan gels. **a** Procedure to sort single localizations in immobile (red), mobile (yellow), or intermediate (discarded) groups based on the mjd of their corresponding track. **b** Representative image of a resulting pseudocolour-coded mobility maps. Red regions are locations consisting of solely immobile particles, yellow regions are locations consisting of solely mobile particles, and orange regions (arrows) are locations where both immobile and mobile probes are present. The outlined region is enlarged in c. **c** Zoom-in from b with a proposed schematic network structure overlaid on the image. Dense network regions show translational migration in κ-carrageenan hydrogels.

bright compared to the areas in which the obstructed diffusing particles cause a heterogeneous and noisy background fluorescence. The dense regions were identified by taking a temporal median average over multiple RCM images (Figure S7.2) and had a similar size to the ones determined via sptFM. Moreover, the size and distribution of the dense regions did not seem to depend on the tested κ-carrageenan polymer concentration range (Figure S7.2).

Two species of immobile particle regions could be distinguished in the single-particle tracking derived mobility maps (Figure 7.3). First, there were regions that are characterised by the presence of immobilised probe(s) in the centre and the absence of mobile probes in the direct periphery. We attributed these regions to stable dense network regions, as these mobility maps represent a temporal integration and are therefore averaged over 40 s of each recorded movie. Second, we observed immobilised probe(s) directly adjacent to and overlapped by mobile probes (i.e. orange regions, arrows in Figure 7.3b), which could not be attributed to stable dense network regions. We hypothesised that these occurrences are caused by temporal variations in the gel network, where the dense network regions themselves are mobile within the acquisition time (40 s).

Therefore, we investigated the same mobility maps, but with a sliding temporal window. Similar dense network regions were observed, but some appear to migrate or disintegrate over time. We show an example in Figure 7.4a, where the same position in the gel is shown as a mobility map integrated over 0-20 s and 21-40 s of the same movie. During the first 20 s, a dense network region with a diameter of ∼1.5 µm is visible (dotted outline in Figure 7.4a). Later at the same position, however, only mobile particles are present. Meanwhile, a new dense region can be found ∼0.5 µm below the previous dense region. This finding suggests that dense network regions itself can migrate on the second to minute timescale even after full gelation. We note that by decreasing the temporal integration time, we are reducing the number of localizations used for creating the mobility maps. This effectively sets a lower limit to the time interval possible to be studied with mobility maps because of a decreasing signal-to-noise ratio.

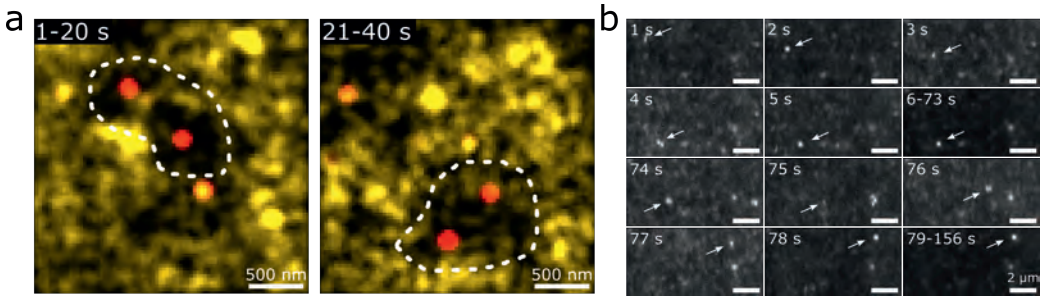

Figure 7.4: Movement of dense network regions in the coarse network. **a** Mobility maps of immobile (red) and mobile (yellow) probes in a 1% κ-carrageenan, 200 mM NaCl, and 20 mM KCl gel. The position of all particles found in the time range 1-20 s (left) or 21-40 s (right) are overlaid. The white-dotted outline represents the proposed outline of the dense region. **b** RCM images show a migrating dense network region (indicated by arrows) in a 1% κ-carrageenan, 200 mM NaCl, and 20 mM KCl gel (also see ESI Movie 1). Images represent single RCM frames, except for the 6-73 and 79-156 s images, where the median of the corresponding RCM frames is shown.

We confirmed the migration of dense regions via rescan confocal microscopy operating at 1 Hz. While the presence of immobile regions is difficult to assess in single frames because of a low signal-to-noise ratio, assessment of multiple frames shows occasional and abrupt migration of dense network regions (Figure 7.4b, ESI Movie 1). This single migration event had a diffusion coefficient of $\sim$0.4 $\mu m^2/s$; this is faster than the trapped probe fraction determined earlier, but an order of magnitude slower than probes moving in the coarse network. This indicates that the migration is not caused by diffusion of the dense regions while normally embedded in the coarse network. Identical experimental conditions of solely mobile fluorescent probes revealed no observable immobile or migrating regions as these move too fast to be captured with a frame rate of 1 Hz (ESI Movie 2).

This dense network region migration is de facto different from the trapped fluorescent probe diffusion shown earlier. The trapped probe diffusion is a convolution of probes diffusing within single immobile dense network regions and possible movement of these dense network regions. Most observed dense network regions (Figure 7.3 and ESI Movie 1) are immobile on the micrometre scale, indicating that the trapped probe diffusion is governed by probe diffusion within dense network regions rather than dense network region migration. Contrarily, mobility maps and RCM movies show movement of the dense network regions themselves, as these methods are only sensitive to movement of the complete dense network regions rather than of single probes.

Migration of dense network regions can be explained by continuous slow reorganisation of the bulk coarse network, whereupon at a certain critical reorganisation level, the dense network is allowed to suddenly migrate within the bulk coarse network. Because of the rarity of these migrating dense network regions, along with poor signal to noise levels in both the temporally limited mobility maps and the RCM images, we did not attempt further quantification of the dense network region movement in this study.

7.3 Conclusions

In this study, we qualitatively and quantitatively visualised heterogeneity present in κ-carrageenan gels with sptFM. We observed bimodal self-diffusion of inert fluorescent probes embedded in the gels with occasional switching between the two states. By analysing these states, we characterised κ-carrageenan gels as consisting of a coarse network with 3.2 ± 0.3 nm diameter fibres, in which ∼µm-sized dense network regions are present. These dense network regions showed rare and abrupt migration with a diffusion coefficient of ∼0.4 $\mu m^2/s$, suggesting continuous reorganisation of the κ-carrageenan network even after full gelation. Quantitative information on the heterogeneity and reorganisation kinetics is relevant for transport and release of low- and high-molecular-weight solutes in hydrogels, as well as for infusion and activity of digestive enzymes.

The existence and size of the dense network regions, as well as the size of the κ-carrageenan fibres, are in line with the results obtained from studies using either invasive or nonspatial techniques (nuclear magnetic resonance diffusometry or EM[5,8,10]). Our work indicates that the technique used here is reliable and has distinct advantages because of its noninvasive nature and spatial resolving power. Employment of sptFM, therefore, has potential to quantitatively and spatially assess the self-diffusion behaviour of multiscale solutes in complex heterogeneous hydrogels.

7.4 Material and methods

7.4.1 κ-Carrageenan gel creation

κ-Carrageenan (Sigma-Aldrich, Zwijndrecht, The Netherlands) was thoroughly mixed with Milli-Q water with various volumes of 1 M 0.2 µm-filtered NaCl and KCl solutions to obtain various κ-carrageenan gels (0.5-2.5% (w/v) κ-carrageenan, 20 mM KCl, and 100-200 mM NaCl). This mixture was then heated in a heat block (Dry Block Thermostat, Grant Instruments Ltd, Shepreth, UK) to 75 °C and was left at this temperature for at least 15 min while regularly vortexing the solution. Then, 20 µL of the hot κ-carrageenan solution was pipetted on a cleaned (oven-burned at 500 °C for 20 min to remove possible organic fluorescent impurities[36]) glass coverslip (Paul Marienfeld GmbH & Co. KG, Lauda-Königshofen, Germany; #1.5H, 170 µm thickness), where the sample was confined by silicone wells. The sample was then left to solidify for at least 5 min before any measurement.

7.4.2 Probe infusion in κ-carrageenan gels

After solidification of the gel and directly (∼1-5 min) before imaging, 2 µL of 0.02% w/v 28 nm diameter nanospheres (FluoSpheres carboxylate-modified dark red, Thermo Fisher Scientific, Waltham, MA, USA) solution was added to the side of the gels (leading to 0.002% w/v nanosphere concentration in the final sample volume). Single-particle tracking results shown in this study consist of two replicates with four areas characterised in every replicate.

7.4.3 Single-particle imaging

All imaging was performed on a home-built single-molecule microscope, fully described elsewhere[33]. Briefly, a 642 nm laser line was employed for epifluorescent illumination to excite the nanospheres

via a Nikon 100× 1.49 NA HP/SR objective. The emission light was then filtered via a 700 ± 75 nm bandpass filter and imaged at 200 Hz with a Zyla 4.2 plus sCMOS (at 2 × 2 pixel binning, 128 nm pixel size) controlled using the micromanager software[37]. Occasionally, the emission light was guided via the bypass mode of a rescan confocal microscope, which reduced the pixel size to 122 nm (at 2 × 2 pixel binning). Four different fields of view of every gel were recorded for 8000 frames (40 s) each and analysed.

7.4.4 Rescan confocal imaging

The home-built microscope described above was expanded with a rescan confocal microscope (RCM) unit (Confocal.nl, Amsterdam, The Netherlands)[35]. The RCM uses the same laser line, and scans the confocal excitation spot over the sample through the same objective. The resulting emission light is rescanned with a mirror with 2× the sweep length as the excitation scanning mirror, leading to a 43 nm pixel size on the sCMOS chip. In practice, RCM is capable of a ∼40% increase in resolution with respect to the classical resolution limit.

7.4.5 Single-particle tracking analysis

The raw recorded single-molecule data were analysed with the ThunderSTORM plugin[38] with pSMLM functionality[20] in FIJI[39,40]. A β-spline wavelet filter with scale 2 and order 3 was used for identification of molecules, after which a threshold of 1.25 times the standard deviation of the wavelet F1 value was used to detect single point spread functions (PSFs). Then, a 2D pSMLM sub-pixel fitting routine was employed on a 7 × 7 pixel region of interest around the centre of the PSF. These sub-pixel localizations were loaded in MATLAB (The MathWorks, Natick, MA, USA) 2018b for further analysis.

Tracking of the individual localizations was performed via the tracking methodology incorporated in the SMALL-LABS software package[41], with a minimum merit of 0.01, 5 ms integration time, a gamma of 1, a minimum track length of 2 frames, and a maximum step size of 5 pixels (0.6 µm). Then, for every track found in a movie, the mean jump distance (mjd) was calculated and a histogram of the mjd was produced, weighing the mjd on the number of localizations per track. The histograms were plotted on a logarithmic x-axis and fitted with a double log-Gaussian, constraining the peak position of the Gaussians between [7 and 148] nm, and between [55 and 1097] nm, respectively. These bounds were never limiting the fitting peak positions.

The peak positions are plotted either directly as mjd, or recalculated as the diffusion coefficient: $mjd = \sqrt{4 \cdot D \cdot \Delta t} + \sigma$, where σ is the localization uncertainty. The localization uncertainty was estimated by fitting a representative subset (∼4% of frames evenly spread over a single movie) of all localizations of all datasets with a maximum likelihood (MLE) Gaussian fitting model within ThunderSTORM[38], and extracting the calculated localization uncertainty[42]. MLE-Gauss fitting is shown to have a ∼4% difference in localization uncertainty compared to the used phasor fitting[20]. Over all localizations, a mean localization uncertainty of 22 nm was found, corrected for the difference in localization uncertainty.

7.4.6 Quantification of probe state switching

To have an indication of how many probes show behaviour characteristic of switching from obstructed diffusion in the coarse network to largely immobilised diffusion in the dense network regions (e.g. Figure 7.1c bottom), all tracks from a single movie were tested as follows: first, tracks shorter than 20 frames were discarded, as these show insufficient information to assess switching behaviour. Then, a 2-frame-moving average of the jumping distance plot was created. If this moving average plot had at least 5 consecutive frames (25 ms) of at least 150 nm jump distance (i.e. obstructed diffusion in the coarse network), along with at least 10 consecutive frames (50 ms) of at most 100 nm jump distance (i.e. largely immobile behaviour), the track was indicated to be state-switching.

7.4.7 Obstruction model

Johnson's obstruction model[10,26] was calculated according to equation 7.1:

$$\frac{D}{D_0} = \frac{e^{-0.84\cdot\alpha^{1.09}}}{1+\left(\frac{r_s^2}{\kappa}\right)^{0.5}+\frac{1}{3}\cdot\frac{r_s^2}{\kappa}} \; with\; \alpha = \phi\cdot\left(\frac{r_s+r_f}{r_f}\right)^2 \; and \kappa = 0.31\cdot r_f^2\cdot\phi^{-1.17} \tag{7.1}$$

where D is the measured diffusion coefficient, D_0 the diffusion coefficient of the probe in pure water, r_s the nanosphere radius, r_f the κ-carrageenan strand radius, and ϕ the polymer volume fraction. The κ-carrageenan strand radius is the only unknown parameter in this equation. This model is fitted to the obtained mjd log-Gaussian peak positions for both experimental conditions via a non-linear fitting procedure in MATLAB and a 95% confidence interval was obtained from this fit.

Johnson's obstruction model assumes the following conditions: (1) the collisions between the probe and network are elastic; (2) the movement of the fibres is slow compared to the interaction times of the probes; (3) the entire volume is accessible except for the volume occupied by the probes and the fibers; (4) diffusive freedom of the probes in the polymer; and (5) non-negligible hydrodynamic drag of the probes. In our setting, the use of the Johnson model is justified, as (1) the probes and polymers are both hard structures, (2) only brief (elastic) interactions between the probes and polymers occur, and (3) the probes have no expected affinity to the polymer.

7.4.8 Mobility maps

To create mobility maps, all localized particles were divided into three groups (immobile, mobile, or undefined) based on the mjd of the track to which the localizations belong. The double Gaussian fit of the mjd histograms of a single experiment (described above) was used to determine cut-off jump distances at which the ratio of the probability of the Gaussians was 0.95 for either $P(mobile)/P(immobile)$ or for $P(immobile)/P(mobile)$ (also see Figure 7.3a). Then, the localizations that correspond to tracks with jump distances lower than the jump distance found for $P(immobile)/P(mobile) = 0.95$ were termed "immobile". A similar procedure was performed to find localizations that were termed "mobile". Localizations that were neither "immobile" nor "mobile" were discarded for mobility mapping.

Next, an average shifted histogram of only the "immobile" or "mobile" localizations was created via an algorithm identical to the ThunderSTORM[38] average-shifted histogram visualisation option with a magnification of 2 and a lateral shift of 2 pixels. These "immobile" and "mobile" mobility maps were coloured and overlaid on each other.

7.5 Competing interests

J.v.D. is employed by a company that manufactures food products.

7.6 Acknowledgements

K.J.A.M. is funded by a VLAG PhD-fellowship grant awarded to J.H.

References

1. Liu, J., Zhan, X., Wan, J., *et al.* Review for Carrageenan-Based Pharmaceutical Biomaterials: Favourable Physical Features versus Adverse Biological Effects. *Carbohydrate Polymers* **121,** 27–36 (2015).
2. Campo, V. L., Kawano, D. F., da Silva, D. B., *et al.* Carrageenans: Biological Properties, Chemical Modifications and Structural Analysis – A Review. *Carbohydrate Polymers* **77,** 167–180 (2009).
3. Mihaila, S. M., Gaharwar, A. K., Reis, R. L., *et al.* Photocrosslinkable Kappa-Carrageenan Hydrogels for Tissue Engineering Applications. *Advanced Healthcare Materials* **2,** 895–907 (2013).
4. Morris, E. R., Rees, D. A. & Robinson, G. Cation-Specific Aggregation of Carrageenan Helices: Domain Model of Polymer Gel Structure. *Journal of Molecular Biology* **138,** 349–362 (1980).
5. Hermansson, A.-M. Rheological and Microstructural Evidence for Transient States during Gelation of Kappa-Carrageenan in the Presence of Potassium. *Carbohydrate Polymers* **10,** 163–181 (1989).
6. Evageliou, V. I., Ryan, P. M. & Morris, E. R. Effect of Monovalent Cations on Calcium-Induced Assemblies of Kappa Carrageenan. *Food Hydrocolloids. Gums and Stabilisers* **86,** 141–145 (2019).
7. Millane, R. P., Chandrasekaran, R., Arnott, S., *et al.* The Molecular Structure of Kappa-Carrageenan and Comparison with Iota-Carrageenan. *Carbohydrate Research* **182,** 1–17 (1988).
8. Hermansson, A. .-M., Eriksson, E. & Jordansson, E. Effects of Potassium, Sodium and Calcium on the Microstructure and Rheological Behaviour of Kappa-Carrageenan Gels. *Carbohydrate Polymers* **16,** 297–320 (1991).
9. Hu, B., Du, L. & Matsukawa, S. NMR Study on the Network Structure of a Mixed Gel of Kappa and Iota Carrageenans. *Carbohydrate polymers* **150,** 57–64 (2016).
10. de Kort, D. W., Schuster, E., Hoeben, F. J., *et al.* Heterogeneity of Network Structures and Water Dynamics in κ-Carrageenan Gels Probed by Nanoparticle Diffusometry. *Langmuir* **34,** 11110–11120 (2018).
11. de Kort, D. W., van Duynhoven, J. P. M., Van As, H., *et al.* Nanoparticle Diffusometry for Quantitative Assessment of Submicron Structure in Food Biopolymer Networks. *Trends in Food Science & Technology* **42,** 13–26 (2015).
12. Singh, H., Ye, A. & Ferrua, M. J. Aspects of Food Structures in the Digestive Tract. *Current Opinion in Food Science. Sensory Sciences and Consumer Perception • Food Physics and Material Science* **3,** 85–93 (2015).
13. Luo, Q., Boom, R. M. & Janssen, A. E. M. Digestion of Protein and Protein Gels in Simulated Gastric Environment. *LWT - Food Science and Technology* **63,** 161–168 (2015).
14. Stempfle, B., Große, A., Ferse, B., *et al.* Anomalous Diffusion in Thermoresponsive Polymer–Clay Composite Hydrogels Probed by Wide-Field Fluorescence Microscopy. *Langmuir* **30,** 14056–14061 (2014).
15. Hagman, J., Lorén, N. & Hermansson, A.-M. Probe Diffusion in κ-Carrageenan Gels Determined by Fluorescence Recovery after Photobleaching. *Food Hydrocolloids* **29,** 106–115 (2012).
16. Lorén, N., Nydén, M. & Hermansson, A.-M. Determination of Local Diffusion Properties in Heterogeneous Biomaterials. *Advances in colloid and interface science* **150,** 5–15 (2009).
17. Saalwächter, K. & Seiffert, S. Dynamics-Based Assessment of Nanoscopic Polymer-Network Mesh Structures and Their Defects. *Soft Matter* **14,** 1976–1991 (2018).
18. Shen, H., Tauzin, L. J., Baiyasi, R., *et al.* Single Particle Tracking: From Theory to Biophysical Applications. *Chemical Reviews* **117,** 7331–7376 (2017).
19. Geonzon, L. C. & Matsukawa, S. *Phase Separated Structures of Mixed Carrageenan Gels Elucidated Using Particle Tracking* in *NAC 2019* (eds Murakami, R.-I., Koinkar, P. M., Fujii, T., *et al.*) (Springer, Singapore, 2020), 41–48.

20. Martens, K. J. A., Bader, A. N., Baas, S., *et al.* Phasor Based Single-Molecule Localization Microscopy in 3D (pSMLM-3D): An Algorithm for MHz Localization Rates Using Standard CPUs. *The Journal of Chemical Physics* **148,** 123311 (2018).
21. Smith, C. S., Joseph, N., Rieger, B., *et al.* Fast, Single-Molecule Localization That Achieves Theoretically Minimum Uncertainty. *Nature Methods* **7,** 373–375 (2010).
22. Rocha, J., Corbitt, J., Yan, T., *et al.* Resolving Cytosolic Diffusive States in Bacteria by Single-Molecule Tracking. *Biophysical journal* **116,** 1970–1983 (2019).
23. Luo, Q., Sewalt, E., Borst, J. W., *et al.* Analysis and Modeling of Enhanced Green Fluorescent Protein Diffusivity in Whey Protein Gels. *Food Research International* **120,** 449–455 (2019).
24. Geonzon, L. C., Bacabac, R. G. & Matsukawa, S. Network Structure and Gelation Mechanism of Kappa and Iota Carrageenan Elucidated by Multiple Particle Tracking. *Food Hydrocolloids* **92,** 173–180 (2019).
25. Aufderhorst-Roberts, A., Frith, W. J. & Donald, A. M. A Microrheological Study of Hydrogel Kinetics and Micro-Heterogeneity. *The European Physical Journal E* **37,** 44 (2014).
26. Johnson, E. M., Berk, D. A., Jain, R. K., *et al.* Hindered Diffusion in Agarose Gels: Test of Effective Medium Model. *Biophysical Journal* **70,** 1017–1023 (1996).
27. de Kort, D. W., Van As, H. & van Duynhoven, J. P. *Estimating Microstructural Length Scales in κ-Carrageenan Hydrogels by PFG NMR Nanoprobe Diffusometry* in *Proceedings of the XIII International Conference on the Applications of Magnetic Resonance in Food Science* (IM Publications Open, 2016), 73–76.
28. Saha, D. & Bhattacharya, S. Hydrocolloids as Thickening and Gelling Agents in Food: A Critical Review. *Journal of Food Science and Technology* **47,** 587–597 (2010).
29. Bourouina, N., de Kort, D. W., Hoeben, F. J. M., *et al.* Complex Coacervate Core Micelles with Spectroscopic Labels for Diffusometric Probing of Biopolymer Networks. *Langmuir* **31,** 12635–12643 (2015).
30. Stempfle, B., Dill, M., Winterhalder, M. J., *et al.* Single Molecule Diffusion and Its Heterogeneity during the Bulk Radical Polymerization of Styrene and Methyl Methacrylate. *Polymer Chemistry* **3,** 2456–2463 (2012).
31. Stracy, M. & Kapanidis, A. N. Single-Molecule and Super-Resolution Imaging of Transcription in Living Bacteria. *Methods. Transcriptional Dynamics* **120,** 103–114 (2017).
32. de Kort, D. W., Rombouts, W. H., Hoeben, F. J. M., *et al.* Scaling Behavior of Dendritic Nanoparticle Mobility in Semidilute Polymer Solutions. *Macromolecules* **48,** 7585–7591 (2015).
33. Martens, K. J. A., van Beljouw, S. P. B., van der Els, S., *et al.* Visualisation of dCas9 Target Search in Vivo Using an Open-Microscopy Framework. *Nature Communications* **10,** 3552 (2019).
34. Vink, J. N. A., Martens, K. J. A., Vlot, M., *et al.* Direct Visualization of Native CRISPR Target Search in Live Bacteria Reveals Cascade DNA Surveillance Mechanism. *Molecular Cell* **77,** 39–50.e10 (2020).
35. De Luca, G. M., Breedijk, R. M., Brandt, R. A., *et al.* Re-Scan Confocal Microscopy: Scanning Twice for Better Resolution. *Biomedical optics express* **4,** 2644–2656 (2013).
36. Hübner, C. G., Renn, A., Renge, I., *et al.* Direct Observation of the Triplet Lifetime Quenching of Single Dye Molecules by Molecular Oxygen. *The Journal of Chemical Physics* **115,** 9619–9622 (2001).
37. Edelstein, A. D., Tsuchida, M. A., Amodaj, N., *et al.* Advanced Methods of Microscope Control Using μManager Software. *Journal of Biological Methods* **1,** e10 (2014).
38. Ovesny, M., Křížek, P., Borkovec, J., *et al.* ThunderSTORM: A Comprehensive ImageJ Plug-in for PALM and STORM Data Analysis and Super-Resolution Imaging. *Bioinformatics* **30,** 2389–2390 (2014).
39. Schindelin, J., Arganda-Carreras, I., Frise, E., *et al.* Fiji: An Open-Source Platform for Biological-Image Analysis. *Nature methods* **9,** 676–682 (2012).
40. Rueden, C. T., Schindelin, J., Hiner, M. C., *et al.* ImageJ2: ImageJ for the next Generation of Scientific Image Data. *BMC Bioinformatics* **18,** 529 (2017).
41. Isaacoff, B. P., Li, Y., Lee, S. A., *et al.* SMALL-LABS: Measuring Single-Molecule Intensity and Position in Obscuring Backgrounds. *Biophysical Journal* **116,** 975–982 (2019).
42. Mortensen, K. I., Churchman, L. S., Spudich, J. A., *et al.* Optimized Localization Analysis for Single-Molecule Tracking and Super-Resolution Microscopy. *Nature methods* **7,** 377 (2010).

7.7 Supplementary information

ESI Movie 1 and 2 are available at doi:10.1021/acs.langmuir.0c00393, and contain the following information:

ESI Movie 1: Rescan confocal microscopy operating at 1 Hz of 2% κ-carrageenan infused with 0.03% (w/v) fluorescent nanoprobes. Images shown in Figure 7.4b are extracted from this movie.

ESI Movie 2: Rescan confocal microscopy operating at 1 Hz of 0.03% (w/v) fluorescent nanoprobes in milli-Q water.

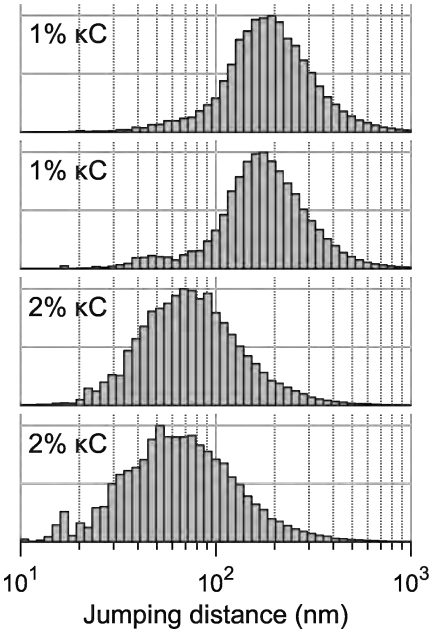

Figure S7.1: Histogram of jumping distances, weighted on track length, of probes in 1 - 2% (w/w) κ-carrageenan polymer solutions (two repetitions of each sample) without any salt addition.

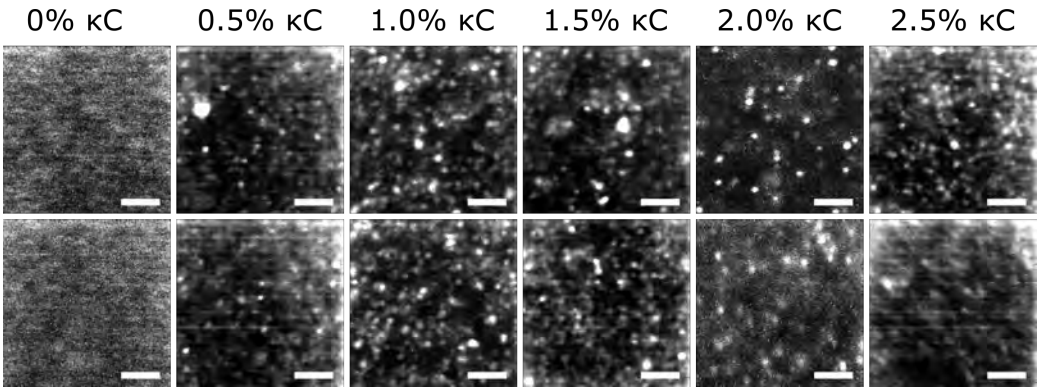

Figure S7.2: Probe infusion investigated with rescan confocal microscopy. The median value of a 50-frame window is shown, and the intensity for every individual image is rescaled to remove the highest and lowest 1% intensity values. The observed horizontal patterns represent the fast scanning direction of the RCM. Rows are repetitions of the same sample. For the 0% κ-carrageenan sample, 25% glycerol is used to decrease the diffusion coefficient of the nanosphere without introducing spatial heterogeneity. Scale bars represent 2.5 µm.

8

General discussion

8.1 Dynamic macromolecular research requires a demanding technique

A fundamental understanding of diffusion and behaviour of key macromolecules in life science and soft matter could be very influential in their respective applied fields by hypothesising and studying application-oriented effects propagating from fundamental studies. In life science, for example, good knowledge of (kinetic) interactions of CRISPR-Cas proteins with DNA can predict adverse effects as a function of protein concentration and incubation time[1–3]. This prediction allows for intelligent choices in genomic editing protocols designed for higher eukaryotes, including humans, where safe applicability is of paramount importance[4]. In the field of soft matter, a similar emphasis can be placed on fundamental knowledge. If a material can be described on the mesoscale (i.e. ∼10-1000 nm) and if the interactions of the essential macromolecules are known, the effects on for example internal solute release can be predicted[5–7]. Understanding solute release can aid in designing novel food products or pharmaceuticals, where slow release of solutes (i.e. nutrients or medicine, respectively) is required[8].

However, devising a technique that is capable of studying these dynamic macromolecular interactions is not trivial. Ideally, this technique satisfies multiple demanding criteria: 1) The sample is minimally invaded or destructed, because all samples are ideally studied in a state as natural as possible. 2) Minimal spatiotemporal averaging is taking place, to study macromolecular interactions independently of the sample spatiotemporal heterogeneity. 3) Molecular specificity is reached, to specifically study key macromolecules without noise stemming from other molecules in the sample. 4) It is as accessible as possible, because all techniques become more powerful when used by experts in specialistic fields, rather than by experts in the technique. 5) A sufficiently high spatiotemporal resolution is achieved; studying macromolecular interactions minimally requires a spatial resolution on the scale of the macromolecule (i.e. ∼1-100 nm), and a temporal resolution dictated by its diffusion (i.e. millisecond range). However, further increase in spatiotemporal resolution can open up the technique to study more exotic (macro)molecules or interactions.

Single-molecule localization microscopy (SMLM) and its derivation single-particle tracking fluorescence microscopy (sptFM) are methodologies based on localizing emission patterns of single fluorescent emitters. SptFM is a promising contender to fulfil the stated criteria (**Chapter 1**), but can be further improved by better accessibility and by an increased spatiotemporal resolution. Moreover, the application of sptFM in life science and soft matter should be investigated to accurately determine the possibilities and limitations of the technique.

This thesis is focused on these hardware and software improvements to increase the spatiotemporal resolution of sptFM, as well as to increase its accessibility. Moreover, multiple applications of sptFM in life science and soft matter are investigated. This thesis first described advances in sptFM hardware and analysis procedures. Computational ease-of-use was increased via a novel and computationally inexpensive phasor-based localization algorithm (**Chapters 2 and 3**). Next, a novel low-dispersion spectral SMLM implementation that maximises spatiospectral resolution was designed (**Chapter 4**). A large increase in temporal resolution was achieved in the form of Monte Carlo diffusion distribution analysis (MC-DDA; **Chapter 6**). Last, a modular and open-source microscope with minimal optical components was designed (**Chapter 6**). These improvements were employed to obtain high fidelity dynamic information on in vivo dCas9-DNA interactions (**Chapter**

5 and 6) and to investigate the hydrogel κ-carrageenan via sptFM (**Chapter 7**). In this chapter, the hardware and computational improvements will be discussed, followed by a discussion on the capability of SMLM and sptFM to elucidate macromolecular interactions in life science and soft matter.

8.2 SMLM adoption requires good accessibility and high spatiotemporal resolution

Currently, SMLM and sptFM are regarded as techniques usable mainly by microscopy experts. Further adoption of SMLM/sptFM broadly requires the realisation of two goals. First, it should be accessible for non-experts in microscopy, so it can be employed by experts in applied research. Increasing the accessibility of SMLM can be realised by creating robust, easy-to-install equipment and software packages, and by decreasing the associated costs. Second, SMLM/sptFM needs to be powerful enough to provide substantial incentive to use SMLM/sptFM rather than more established techniques. Specifically, the spatiotemporal resolution needs to be maximised, allowing SMLM to be used in a wider range of experimental settings. These goals can be conflicting with one another, as an increase in spatiotemporal resolution often stems from more complex hardware and more computationally expensive software and vice-versa. In this thesis, we describe various improvements in the accessibility of SMLM/sptFM while retaining maximal spatiotemporal resolution, as well as methods to increase the spatiotemporal resolution without decreasing the accessibility of SMLM/sptFM.

8.2.1 Improving computational accessibility

A more widespread use of the technique can be directly aided by an increased computational accessibility, due to more approachable and rapid processing, and due to lowering computational costs and required expertise. Moreover, better computational accessibility can be part of important incremental improvements that eventually lead to novel insights. This thesis describes an increase in the single-molecule localization rate by ∼3 orders of magnitude (reaching $\sim 3 \cdot 10^6$ localizations/s) via implementation of phasor-based algorithms in the pSMLM software suite without substantially sacrificing spatial resolution (pSMLM; **Chapter 2**). This rate is high enough for real-time localization rates on a standard central processing unit (CPU), where previously graphical processing units (GPUs) were vital to achieve this[9]. The pSMLM methodology was furthermore extended with 3-dimensional localization of engineered point spread functions (PSFs), such as astigmatic, double-helix, saddle-point, and tetra-pod point PSFs (**Chapter 3**). We integrated pSMLM in stand-alone software packages providing a complete computational pipeline to extract localizations from raw data to provide good accessibility. Implementation of real-time analysis based on pSMLM is feasible on current computer hardware, but could also possibly be implemented on the hardware of the camera itself, leading to a highly streamlined analysis pipeline in SMLM.

8.2.2 Improving hardware accessibility

Generally, microscopy hardware involves a trade-off between associated costs, required expertise, and upgradability (Figure 8.1a). Commercial instruments have high initial costs, but minimise required expertise, whilst its upgradability generally depends on external factors such as the business

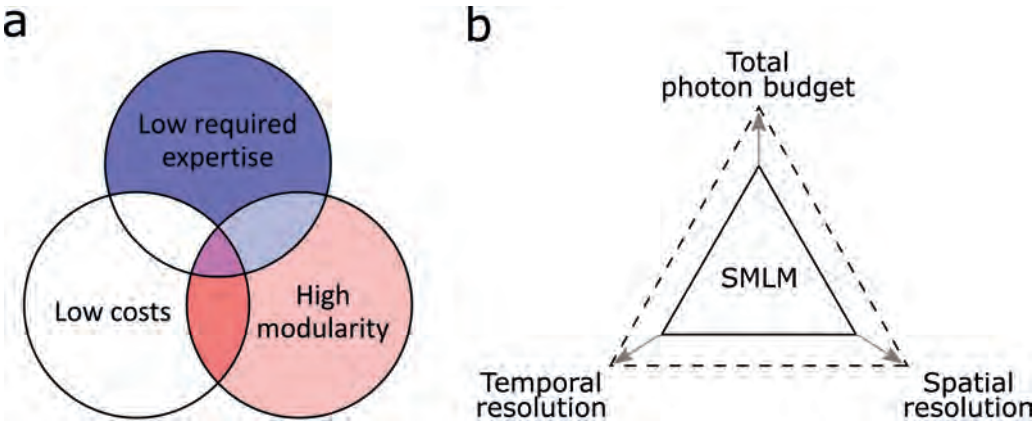

Figure 8.1: Trade-offs in the hardware (a) and experimental design (b) of SMLM. **a** SMLM microscopes have a preferred combination of low required expertise (top), low associated costs (bottom left), and high modularity (bottom right). The miCube (magenta) aims to combine all three factors. Commercial microscopes (blue) have a minimised associated expertise, but lack good cost-effectiveness, and occasionally have good modularity (light blue). Home-built microscopes (red) normally combine low costs with high modularity at the cost of higher required expertise. Some, especially complex home-built microscopes, have increased associated costs (light red). **b** The experimental parameter space in SMLM is a trade-off of total photon budget of fluorophores, temporal resolution, and spatial resolution. These three properties influence each other. Specifically, spatial resolution is directly related to photon collection per frame (Equation 1.6), which can be influenced by a higher excitation power (requiring a higher total photon budget), or by longer frame duration (sacrificing temporal resolution).

model of the vendor. Home-built instruments, on the other hand, are often characterised by lower associated costs, as well as an upgradability level fully determined by the laboratory, but requires a substantial higher level of expertise. With the miCube (**Chapter 6**), we realised a modular and upgradable SMLM-capable microscope that is fully open-source. It requires lower levels of expertise to recreate than most other home-built instruments and has lower associated costs than commercial instruments, in this manner aiding to an increased hardware accessibility in the field of SMLM. The decrease in expertise required for building the miCube mainly stems from pre-aligned optical components and detailed installation instructions. Furthermore, we designed a spectral add-on (**Chapter 4**) usable in any SMLM microscope, which minimises the required optical components to introduce spectral information in SMLM. In previous implementations of spectral SMLM (sSMLM), multiple optical components such as mirrors and lenses had to be employed in combination with a diffractive element such as a grating, a prism, or a spatial light modulator to obtain good spatiospectral resolution. In our implementation, we decreased the optical components to just the diffractive element, decreasing implementation costs and photon loss. In addition, we minimised spectral dispersion, improving the photon budget utilisation, the effects of which will be further discussed later.

Costs associated with SMLM hardware could be further decreased by employing industrial-grade CMOS or smartphone cameras, which are 10-100x cheaper than scientific CMOS

or EMCCD detectors normally employed in SMLM[10–13]. These implementations are promising in opening up opportunities for sub-diffraction resolution microscopy with a much decreased financial barrier of entry. Low-cost SMLM hardware could be useful for massively parallelised, in-field, or teaching-oriented applications. However, microscopes equipped with these alternatives currently have a decreased obtainable spatial resolution due to lower photon collection efficiency and higher background noise levels.

8.2.3 Spatiotemporal resolution increase in SMLM

The achievable data quality in SMLM fundamentally stem from a trade-off between spatial resolution, temporal resolution, and the emitter's total photon budget (Figure 8.1b). Because of this strong dependency on one another, stretching the boundaries of one property will increase the complete accessible experimental parameter space in SMLM. However, this also indicates that a true increase in spatiotemporal resolution can only be accomplished via a method that improves either spatial resolution, temporal resolution, or photon budget, without affecting the others.

Recently conceived technologies that combine SMLM with sub-diffraction illumination profile information, such as MINFLUX, SIMFLUX, and ROSE[14–17], have substantially increased the achievable spatiotemporal resolution in SMLM. In MINFLUX, high spatial resolution (<5 nm) is combined with good temporal resolution (sub-millisecond) and photon budget depletion (minimal from a technical point of view), but at the cost of a vastly decreased throughput due to sequential rather than parallel localization, and decreased accessibility due to the need for a complex and expensive microscope. SIMFLUX and ROSE achieve a ∼2x increase in spatial resolution without sacrificing temporal resolution or photon budget, but again require a complex microscope with more optical components and control elements compared to a typical SMLM microscope. The following sections will discuss spatiotemporal resolution increase without sacrificing throughput or substantially increasing the hardware complexity.

Spatial resolution increase

Spatial resolution increase in traditional SMLM can stem from more accurate sub-pixel localization procedures. In **Chapters 2 and 3**, the pSMLM sub-pixel localization algorithm framework is presented, which achieves similar spatial resolution as state-of-the-art techniques, and additionally substantially increases localization speed as discussed before. The field of sub-pixel localization algorithm development is currently advancing rapidly, and recently, many SMLM localization algorithms have been objectively compared[18]. The SMLM localization algorithms have moreover been expanded with localization algorithms based on neural networks (also known as machine-learning), which show excellent performance with regards to emitter detection and positional accuracy[19–23]. Moreover, while the network training is generally slow, neural network-based localization relies on simple mathematical operations, and can thus achieve high localization rates, outperforming non-machine-learning algorithms on all aspects. The caveat with these algorithms is their dependence on the similarity of training data to experimental data. Because the underlying mathematical steps in neural networks are generally unknown, it cannot be *a priori* assumed that small deviations between a training dataset from the experimental dataset results in negligible localization errors. This

is especially important with structured noise, inhomogeneous background fluorescence, or refractive index mismatches, which are difficult to model realistically[22].

This thesis also describes a spatio-spectral resolution improvement in spectral SMLM (sSMLM) in **Chapter 4**. By focusing on minimisation of the dispersion caused by the grating, the spectral profile results in the highest possible signal-to-noise ratio, and thus the best spectral precision when sub-pixel localization algorithms are used. In other sSMLM implementations, a ∼1:3 ratio of photons for the spatial:spectral pattern is used[24–26], but the increased attainable spectral resolution described in this thesis allows for a larger ratio of the arriving photons to inhabit the spatial pattern, thereby increasing spatial localization accuracy. Nonetheless, compared to non-spectral SMLM, the spatial localization has a little less than half of the original photons (∼1:1 ratio between spatial and spectral pattern, with additional imperfect efficiency of the dispersive element). Spectral information is therefore gained by trading only a factor of $\sim \sqrt{2}$ in spatial accuracy (Equation 1.6). Further optimisation of the data analysis of this minimum-dispersive sSMLM implementation can possibly improve spatial accuracy, especially in the direction unaffected by the spectral dispersion (i.e. the y-axis). This increased resolution can be achieved by using the 1-dimensional profile of both diffraction orders, thereby using all photons for spatial localization. A recent sSMLM method that elegantly uses the -1^{st} and $+1^{st}$ orders of a transmission grating also employs SMLM localization algorithms, and uses all photons that arrive on the detector for both spatial and spectral localization. However, it does have a higher overall photon loss because the 0^{th} order is not incorporated[26]. An intriguing possibility would be the combination of our sSMLM implementation with SIMFLUX or ROSE, which would lead to a technique that has a $\sim \sqrt{2}$ increase in spatial resolution compared to standard SMLM, as well as excellent spectral resolution.

Temporal resolution increase

Increasing temporal resolution without affecting spatial resolution in traditional SMLM can, like spatial resolution increases, be achieved via computational processing. Consider a macromolecule that changes between a fast-diffusive and a slow-diffusive state. The rate by which the state changes could previously only be quantified if both diffusive states are clearly observed in a single track, as well as at least one state change[27]. Correct state determination is complex due to the high stochasticity inherently present in diffusion (Equation 1.10). While this issue could be resolved by obtaining tracks much longer than the expected dynamics, the photon budget of existing in vivo PALM (photo-activation localization microscopy) fluorophores is insufficient to accomplish both long tracks and adequate spatial accuracy. This problem is addressed via Monte Carlo diffusion distribution analysis (MC-DDA; **Chapter 6**). MC-DDA is capable of resolving diffusive state changes on the same timescale as the frame time, even with short tracks. This enables a substantial increase in effective temporal resolution without affecting the spatial resolution or photon budget of the individual emitters. In our experimental implementation, we employed 10 ms frametimes, and were able to deduce dynamic interactions of 17 ms, with 4 ms uncertainty.

In MC-DDA, an experimentally obtained diffusion distribution histogram is compared with a simulated one, after which its parameters can be modified to find a best fitting parameter set. This allows great flexibility in MC-DDA, being theoretically unlimited in for example the number of diffusive states and complexity of the environment geometries, but does result in a com-

putationally expensive procedure. Moreover, adding more computational freedom possibly results in a redundancy of solutions, leading to multiple computationally correct, but conceptually different interpretations of the data. However, this is not the case with the current MC-DDA implementation of two diffusive states with two state-changing rate constants.

An analytic alternative to MC-DDA (analytical diffusion distribution analysis or anaDDA) was inspired by MC-DDA[3,28], and provides a computationally inexpensive method to describe the diffusion distribution histogram. However, it is currently restricted to only a single mobile and a single immobile state, and is limited to relatively simple sphere- or rod-shaped cell geometries. Other than these considerations, MC-DDA and anaDDA are fundamentally very similar and can both obtain diffusional state changes both faster and slower than the frame time, and fill slightly different niches in sptFM analysis. The DDA software suite to a certain extend uncouples the quantifiable temporal range from the experimentally employed frame time. This allows more freedom to optimise experimental frame time based on practical considerations such as hardware limitations and blurring artefacts, generally increasing applicability of sptFM.

8.3 Applications of sptFM

With the introduced advances in sptFM in terms of accessibility of soft- and hardware and of spatiotemporal resolution, we explored STORM (stocastic optical reconstruction microscopy) and PAINT (point accumulation in nanoscale tomography) imaging in **Chapters 2, 3, and 4**, predominantly demonstrating the accuracy of the presented techniques. While three-dimensional single-molecule localization was successfully used in super-resolution imaging, it was not employed in sptFM experiments. Three-dimensional localization inherently decreases lateral localization uncertainty (as studied in **Chapters 2 and 3**), while diffusional movement is dimension-independent (Equation 1.2). Adding z-positional information to sptFM experiments therefore does not provide additional dynamic information, but does decrease the localization accuracy, making it more difficult to quantitatively assess slow diffusion. Moreover, single-molecule spectral determination was not employed in the sptFM experiments, as only a single fluorophore was studied in each experimental setting.

8.3.1 Single-particle tracking of dCas9 in vivo

The dynamic behaviour of dCas9 in *L. lactis* was studied via sptFM (**Chapters 5 and 6**), leading to a novel model showing that dCas9 is in a PAM-screening configuration for ∼17 ms, and then moves to a freely diffusing state for ∼25 ms. By investigating DNA target-binding behaviour as a function of single cell dCas9 copy number, we could show a relatively short (∼100 s) dCas9-target bound time. These insights lead us to hypothesise that dCas9 target binding and plasmid replication are competing processes. Moreover, from the inferred dynamics we predicted target cleavage probability in *L. lactis* as a function of incubation time and single cell dCas9 copy number. These insights have direct applicability for safe utilisation of genome editing via CRISPR-Cas with minimal off-target effects across the domains of life, and can have a more indirect future applicability by aiding in fundamental understanding of CRISPR-Cas9 dynamic behaviour in vivo. Notably, single-protein CRISPR-Cas dynamics are currently mostly elucidated via fluorescence microscopy, with for example smFRET[29,30], DNA curtains[31] (both only in vitro), fluorescence

correlation spectroscopy[32], and sptPALM[2,3,32] being used, which provide more detailed information compared to ensemble techniques such as SDS-PAGE[31,33,34] and cell proliferation assays[3]. This showcases the strength of fluorescence microscopy in general, and sptFM in particular.

This in vivo study moreover pinpoints multiple assay designs that can be used more generally. The first utilisation of photo-activated fluorescent proteins in *L. lactis* shows that sptFM is applicable in this model food-related bacterium species (**Chapter 5**), opening possibilities for a wide range of novel studies. Next, while tracking individual dCas9 proteins in these prokaryotes, we further ascertained a pseudo-single-cell study by analysing the dCas9 based on their single-cell copy number (**Chapter 6**). In the case of dCas9 target finding, equilibrium dynamics were studied by analysing a varied protein copy number combined with an unrelated and static amount of DNA targets, revealing that dCas9 is removed from a target every ∼100 s. This method of analysing single-particle tracks based on their host cell conditions is directly extendable to more in vivo sptFM studies, as long as a cell outline can be revealed. This could prove very interesting when combined with for example single-cell transcriptome analysis[35] or single-cell growth behaviour experiments[36].

8.3.2 Nanoparticle diffusometry reveals hydrogel network structure

In **Chapter 7**, sptFM of fluorescent nanoprobes in κ-carrageenan hydrogel is performed to elucidate its mesoscale structure. This work revealed that κ-carrageenan hydrogels consist of a coarse network with ∼3.2 nm diameter fibres, in which dense regions with a diameter of ∼1 µm are embedded. Furthermore, we could show that these dense regions are mobile on a seconds-to-minutes timescale. These insights are important to intelligently design soft matter with slow release of its solutes, which is an attractive goal for food products, but also for pharmaceuticals. Some of the revelations obtained via sptFM were previously elucidated by NMR diffusometry[7], where a similar heterogeneity of bulk network with dense regions was found. However, since NMR diffusometry is a spatial-independent method, it is insensitive to movement of these dense regions. This movement was therefore not directly observed with NMR diffusometry, but it was hypothesised based on slow movement of probes trapped in dense network regions. Similarly, EM measurements of κ-carrageenan show the network with a resolution surpassing the individual strands and indicates the spatial heterogeneity[37,38], but could not show dense region movement due to the cryogenic temperatures employed. This comparison showcases both the quantitative accuracy of sptFM, as well as the advantages of a spatial technique with non-destructive sample preparation.

8.4 Challenges in sptFM

The obtainable spatiotemporal resolution of fluorescent particles employed in life science and soft matter is explored in **Chapters 5 to 7**, using very different fluorescent particles (Table 8.1). In *L. lactis*, a fluorescent protein (PAmCherry2) was conjugated to a dCas9 protein, creating a ∼12 nm diameter particle with a single fluorescence centre. In the κ-carrageenan hydrogel, however, a multi-fluorophore polystyrene nanoparticle (NP) of 28 nm diameter was used. The observed diffusion coefficients in these experiments were similar (∼1-5 $\mu m^2/s$) due to increased viscosity and molecular crowding in prokaryotic cytoplasm compared to the κ-carrageenan strands in the hydrogel, and a

Table 8.1: Comparison of the fluorescent particles used in prokaryotic life science and in soft matter sptFM in this thesis.

Name	**dCas9-PAmCherry2**	**Polystyrene nanoparticles**
Application	Life science (**Chapter 5 and 6**)	Soft matter (**Chapter 7**)
Diameter (nm)	∼12	∼28
Nr. of fluorophores	1	∼200
Laser power (J/frame)	∼0.17	∼0.4
Relative photon budget per frame	1	>400
Localization accuracy (nm)	∼40	∼22

similar frame time was used. However, the ∼2x increased localization precision does not match the attributes of the fluorescent particles and the experimental conditions (Table 8.1): the total number of fluorophores in each particle and the used excitation intensity indicates a photon budget that is >400x higher, and would therefore realise a localization precision >20x higher. This could be an overestimation, since it is assumed that no quenching takes place in the polystyrene NPs, as well as that PAmCherry2 and the unknown fluorophore in the polystyrene NPs have a similar quantum yield, but does not explain the large discrepancy. The reason that higher localization accuracy was not achieved is due to a heavy loss of signal-to-noise ratio in the more difficult to image soft matter material compared to *L. lactis* cells, which is further discussed below.

8.4.1 Practical achievable resolution in sptFM

Loss of signal-to-noise ratio in soft matter has multiple causes (Figure 8.2). First, while low HiLo conditions can be used in prokaryotic sptPALM (i.e. imaging of the ∼1 µm closest to the coverslip), soft matter such as the κ-carrageenan hydrogel needs to be imaged deeper in the material (> ∼5 µm) to prevent artefacts induced by the edge of the material, requiring epifluorescence. This causes a higher background fluorescence level in the sample due to unwanted out-of-focus fluorophores present in the sample, effectively decreasing the signal-to-noise ratio and achievable spatial resolution. Second, the inhomogeneity and low refractive index of the material below the focal plane result in optical aberrations affecting the PSFs, leading to lower accuracy in single-molecule fitting. Last, the presence of long-lasting immobile particles in the κ-carrageenan prevents the use of a temporal median filter, which substantially decreases influence of background fluorescence in single-molecule experiments. Importantly, the required imaging depth and induced optical aberrations are inherently related to soft matter studies, making this a more fundamental issue rather than a specific issue for κ-carrageenan hydrogels used in this thesis.

8.4.2 Extending the use of sptFM to complex soft matter

To investigate the possibility of using sptFM in a very challenging sample, we attempted to use a similar experimental setup described in **Chapter 7** to study an anisotropic protein-based meat analogue. Meat analogues are very promising to reduce meat intake of humanity, accordingly reducing animal suffering and environmental impact. Specifically, we tried to deduce spatial mesoscale

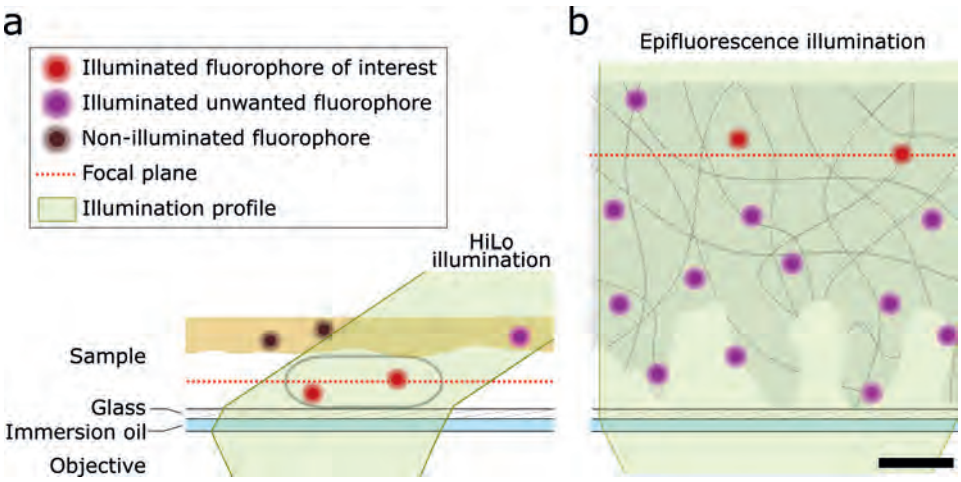

Figure 8.2: Effect of sample and illumination profile on background fluorescence. Scale bar represents 1 µm. **a** Experimental conditions of imaging in prokaryotes such as employed in **Chapter 6**. Here, the fluorophores of interest (red) are embedded in prokaryotic cells close to the objective, leading to a focal plane close to the objective (red dotted line), which allows low HiLo imaging conditions (green shading). This excitation profile in turn leads to minimal illumination of unwanted, out-of-focus spurious fluorophores (black, magenta) present in for example the agar layer on top of the prokaryotes. **b** Experimental conditions of imaging in soft matter as employed in **Chapter 7**. Because the material close to the glass can be affected (f.e. tearing or adsorption), the focal plane needs to be positioned deeper in the sample (red dotted line). A deeper focal plane in turn requires epifluorescence illumination, leading to many illuminated unwanted fluorophores (magenta).

information of a calcium caseinate (CaCas) meat alternative that attains a dense network on the microscale and a fibrous macroscale structure by shearing heated protein material via a shear cell in a cone-cone geometry[39–43]. While this provides good texture on the consumer-relevant spatial scale, it is unknown if the macroscale anisotropy propagates from underlying anisotropic mesoscale structures, or is only formed on a micro-to-macroscale level.

Fluorescent nanoparticles applicable in sptFM

A major challenge to overcome in this complex soft matter material is to find suitable nanoparticles that can be visualised on the single-molecule level via sptFM. First, the 28 nm polystyrene nanoparticles (Figure 8.3) that proved successful in κ-carrageenan hydrogel sptFM were not capable of entering the calcium caseinate meat analogue. This hints to a dense protein structure in the material, and confirms the complexity of applying sptFM on the material. Second, organic fluorophores with a size of 1-3 nm (f.e. rhodamine, Figure 8.3) were capable of entering the material, leading to homogeneous staining on the spatial scale resolvable with diffraction-limited microscopy techniques[39]. However, it proved impossible to use these fluorophores for sptFM due to the insufficient signal-to-noise ratio caused by the reasons listed earlier. Therefore, it was imperative to attempt to create ~7-10 nm diameter fluorescent nanoparticles with a substantial increase in intensity compared to

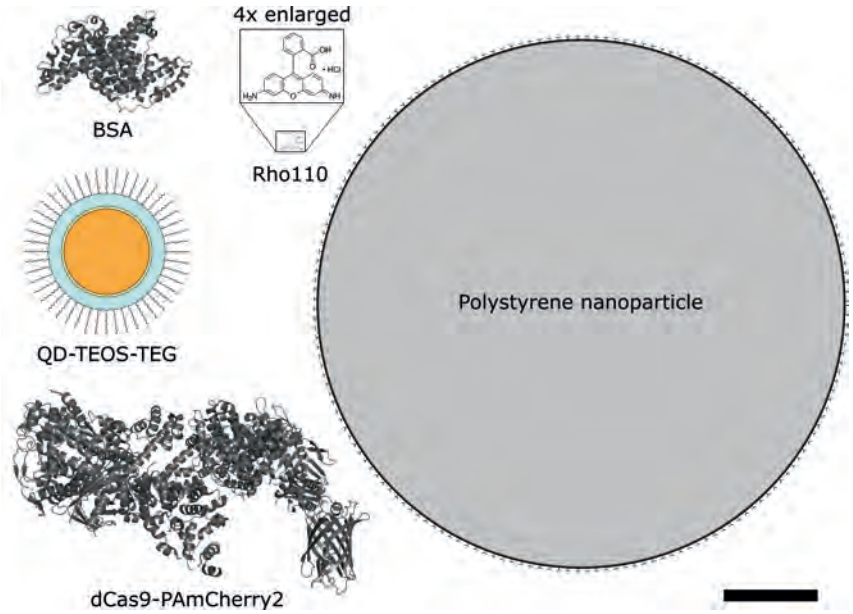

Figure 8.3: Fluorescent particles used in this thesis. BSA (bovine serum albumin; PDB 3V03[48]) was covered with multiple organic fluorophores (not depicted), and used to study dense protein networks in meat analogues. Rho110 (Rhodamine 110) is a typical organic fluorophore which could infuse in dense protein networks. Note that other organic fluorophores such as ATTO and Alexa dyes have a similar size, and have been employed in super-resolution imaging in this thesis (**Chapters 2, 3, and 4**). CdTe/CdS quantum dots (orange) were modified with a silicum-oxide shell (TEOS; blue) and a tetra-ethylene glycol (TEG) layer (to create QD-TEOS-TEG; a cross-section is depicted), but was found to blink on similar timescales as the frametime employed in sptFM. dCas9-PAmCherry2 was employed in the prokaryotic life science study and contains a single fluorophoric centre in the PAmCherry2 (**Chapters 5 and 6**; PDB 4CMP, 3KCT[49,50]). Carboxylated 28 nm diameter polystyrene nanoparticles (a cross-section is depicted here without fluorophore distribution) was used to reveal the structure of κ-carrageenan hydrogels (**Chapter 7**). Scale bar represents 5 nm.

8

individual fluorescent molecules. Dense packing of many fluorophores in a small nanoparticle can give rise to self-quenching[44], which guided us to realise nanoparticles with single fluorophore centres with high photon budget. Quantum dots (QDs) appear to be good candidates that fit this profile, and therefore I created cadmium-tellurium/cadmium-selenium (CdTe/CdS) QDs, which have a broad excitation spectrum and a narrow red emission wavelength peak with a diameter of ∼5 nm, leading to a ∼7-15 nm diameter nanoparticle after modification (Figure 8.3)[45,46]. However, these CdTe/CdS QDs proved inapplicable for our needs of sptFM at a 5-10 ms frametime, because substantial blinking was observed in this same temporal regime. Therefore, only very short tracks could be obtained, along with an increased probability of erroneously linking different QDs during tracking. While QDs have been used in sptFM studies where longer frame times were employed[47], this would result in excessive motion blur in diffusion in water-based soft matter.

Alternatives to sptFM

Because of the difficulties in designing a fluorescent nanoparticle capable of determining the mesoscale network of dense protein networks via sptFM, we attempted to use another fluorescence technique, which can provide diffusional behaviour on a meso-to-microscale based on 2-dimensional pair correlation functions (2D-PCF)[51,52]. In this technique, a temporal cross-correlation between the intensity of every pixel in a fluorescent microscopy movie is performed, and the shape of the individual pixel-to-pixel correlation curves can provide information on the local diffusive behaviour. 2D-PCF is therefore technically capable of resolving dynamic and sub-micron spatial information (with a ∼100 x 100 nm pixel size). Moreover, it does not require sufficient signal-to-noise to localize individual emitters, as the fluctuation in fluorescence intensity is directly used to deduce diffusive behaviour. This technique has for example been used to show anisotropy and barriers with sub-micron spatial resolution in vivo[51].

We attempted to perform 2D-PCF with CaCas meat analogue infused with multi-Alexa Fluor 647-labelled bovine serum albumin (BSA, Figure 8.3), creating a ∼7 nm diameter bright fluorescent particle. First, we ran simulations of the labelled BSA undergoing Brownian diffusion in liquids with varying viscosity, and of the labelled BSA confined by barriers present in CaCas with an expected ∼100 nm separation, based on EM data[39]. These simulations indicated that anisotropy on this scale should be quantifiable with nanoprobes over a broad range of diffusion coefficients. Free Brownian motion of the labelled BSA in water investigated as a control agreed with theory and with the simulations. However, experimental realisation in CaCas meat analogues proved impossible, since the obtained 2D-PCF results were distorted to the extend that no proper computational analysis could be performed. The lack of proper analysis could be due to low infusion of the nanoprobes in the material; due to poor signal-to-noise ratio originating from a high background caused by high fluorophore concentration and a deep focal plane; or due to very limited diffusion in the material, which results in bad interpretation of the cross-correlation. Limited diffusion in the material could indicate phase separation of low-density protein regions and high-density protein regions in the meat analogue. A protein-rich network would explain the difficulty in 2D-PCF together with the obtained contrast in earlier EM investigations of the material. NMR diffusometry, on the other hand, did reveal that the material has slight anisotropy (preliminary ∼1-5% difference in water diffusion in perpendicular directions) on the same spatial scale. Taken together, the practical limits of nanoprobe diffusometry by fluorescence microscopy are demonstrated, especially for the soft matter field. Possibly, sptFM in complex soft matter can be performed by combination of SMLM with light sheet microscopy and optical aberration correction, which would resolve the limited signal-to-noise ratio and induced optical artefacts[53–55].

8.5 Outlook

Single-particle tracking fluorescence microscopy (sptFM) has been advancing rapidly over the past decades. The achievable spatiotemporal resolution is increasing quickly, and can reach molecular resolution (i.e. < 5 nm), and will therefore likely not be limited by technical challenges but rather by experimental design and hard- and software accessibility. The accessibility of sptFM is similarly quickly improving: where it was a fully specialistic technique only a decade ago, super-resolution microscopy finds more and more use by non-experts in a wider variety of research. This combi-

nation could eventually lead to the possibility of direct investigation of single-molecule position and dynamics in natural environments, and can provide a fundamental approach to many research areas. The experimental developments presented in this thesis could be extended to investigation of many in vivo protein-DNA or even protein-protein interactions across the domains of life; as well as observation of the structure and dynamic properties in diverse soft matter materials with molecular resolution.

While sptFM is possibly capable of these scientific outlooks, some technical challenges have yet to be overcome. The fundamental premise of sptFM will always dictate optical transparent samples and the necessity of embedding fluorophores in the sample of interest. Next, because the resolution of sptFM is capable of surpassing the size of fluorescent probes, the distinction between fluorophore and the conjugated protein of interest is becoming relevant, and should be accounted for. This can be done computationally, but it is preferable to minimise the size of fluorophores while retaining a high photon budget. Implementation of small fluorophores in sptFM can to a certain extend be realised by nanobodies[56,57] or organic fluorophores conjugated to proteins in vivo[58] rather than fluorescent proteins. Furthermore in life science, prior knowledge of the protein of interest is required to allow for conjugation while retaining protein functionality, leading to a dependence on other techniques such as crystallography[59]. Likewise in soft matter, the fluorescent probe design is also a limiting factor, as it should have an outstanding combination of high photon budget, small physical size, and a complete lack of chemical interaction with the bulk material. Moreover, as discussed previously, sptFM in soft matter has an inherent lower signal-to-noise ratio than in life science, requiring multiple incremental advances before sptFM will be widely applicable in soft matter. If these challenges are overcome, though, the very good spatiotemporal resolution, broad applicability, non-invasiveness, and non-destructiveness will continue to make sptFM a very powerful technique in many scientific disciplines.

References

1. Martens, K. J. A., van Beljouw, S. P. B., van der Els, S., *et al.* Visualisation of dCas9 Target Search in Vivo Using an Open-Microscopy Framework. *Nature Communications* **10,** 3552 (2019).
2. Jones, D. L., Leroy, P., Unoson, C., *et al.* Kinetics of dCas9 Target Search in Escherichia Coli. *Science* **357,** 1420–1424 (2017).
3. Vink, J. N. A., Martens, K. J. A., Vlot, M., *et al.* Direct Visualization of Native CRISPR Target Search in Live Bacteria Reveals Cascade DNA Surveillance Mechanism. *Molecular Cell* **77,** 39–50.e10 (2020).
4. Komor, A. C., Badran, A. H. & Liu, D. R. CRISPR-Based Technologies for the Manipulation of Eukaryotic Genomes. *Cell* **168,** 20–36 (2017).
5. Martens, K., van Duynhoven, J. & Hohlbein, J. Spatiotemporal Heterogeneity of κ-Carrageenan Gels Investigated via Single-Particle-Tracking Fluorescence Microscopy. *Langmuir* (2020).
6. de Kort, D. W., van Duynhoven, J. P. M., Van As, H., *et al.* Nanoparticle Diffusometry for Quantitative Assessment of Submicron Structure in Food Biopolymer Networks. *Trends in Food Science & Technology* **42,** 13–26 (2015).
7. de Kort, D. W., Schuster, E., Hoeben, F. J., *et al.* Heterogeneity of Network Structures and Water Dynamics in κ-Carrageenan Gels Probed by Nanoparticle Diffusometry. *Langmuir* **34,** 11110–11120 (2018).
8. Saalwächter, K. & Seiffert, S. Dynamics-Based Assessment of Nanoscopic Polymer-Network Mesh Structures and Their Defects. *Soft Matter* **14,** 1976–1991 (2018).
9. Li, Y., Mund, M., Hoess, P., *et al.* Real-Time 3D Single-Molecule Localization Using Experimental Point Spread Functions. *Nature Methods* **15,** 367–369 (2018).
10. Babcock, H. P. Multiplane and Spectrally-Resolved Single Molecule Localization Microscopy with Industrial Grade CMOS Cameras. *Scientific reports* **8,** 1726 (2018).
11. Diederich, B., Then, P., Jügler, A., *et al.* cellSTORM—Cost-Effective Super-Resolution on a Cellphone Using dSTORM. *PLOS ONE* **14,** e0209827 (2019).

12. Diekmann, R., Till, K., Müller, M., *et al.* Characterization of an Industry-Grade CMOS Camera Well Suited for Single Molecule Localization Microscopy–High Performance Super-Resolution at Low Cost. *Scientific Reports* **7,** 14425 (2017).
13. Mao, H., Diekmann, R., Liang, H. P. H., *et al.* Cost-Efficient Nanoscopy Reveals Nanoscale Architecture of Liver Cells and Platelets. *Nanophotonics* **8,** 1299–1313 (2019).
14. Balzarotti, F., Eilers, Y., Gwosch, K. C., *et al.* Nanometer Resolution Imaging and Tracking of Fluorescent Molecules with Minimal Photon Fluxes. *Science* **355,** 606–612 (2017).
15. Gwosch, K. C., Pape, J. K., Balzarotti, F., *et al.* MINFLUX Nanoscopy Delivers 3D Multicolor Nanometer Resolution in Cells. *Nature Methods* **17,** 217–224 (2020).
16. Gu, L., Li, Y., Zhang, S., *et al.* Molecular Resolution Imaging by Repetitive Optical Selective Exposure. *Nature Methods* **16,** 1114–1118 (2019).
17. Cnossen, J., Hinsdale, T., Thorsen, R. Ø., *et al.* Localization Microscopy at Doubled Precision with Patterned Illumination. *Nature Methods* **17,** 59–63 (2020).
18. Sage, D., Pham, T.-A., Babcock, H., *et al.* Super-Resolution Fight Club: Assessment of 2D and 3D Single-Molecule Localization Microscopy Software. *Nature Methods* **16,** 387 (2019).
19. Nehme, E., Weiss, L. E., Michaeli, T., *et al.* Deep-STORM: Super-Resolution Single-Molecule Microscopy by Deep Learning. *Optica* **5,** 458–464 (2018).
20. Nehme, E., Freedman, D., Gordon, R., *et al.* Dense Three Dimensional Localization Microscopy by Deep Learning. *arXiv:1906.09957 [physics].* arXiv: `1906.09957 [physics]` (2019).
21. Speiser, A., Turaga, S. C. & Macke, J. H. Teaching Deep Neural Networks to Localize Sources in Super-Resolution Microscopy by Combining Simulation-Based Learning and Unsupervised Learning. *arXiv:1907.00770 [cs, eess, stat].* arXiv: `1907.00770 [cs, eess, stat]` (2019).
22. Möckl, L., Roy, A. R. & Moerner, W. E. Deep Learning in Single-Molecule Microscopy: Fundamentals, Caveats, and Recent Developments. *Biomedical Optics Express* **11,** 1633–1661 (2020).
23. Ouyang, W., Aristov, A., Lelek, M., *et al.* Deep Learning Massively Accelerates Super-Resolution Localization Microscopy. *Nature Biotechnology* **36,** 460–468 (2018).
24. Bongiovanni, M. N., Godet, J., Horrocks, M. H., *et al.* Multi-Dimensional Super-Resolution Imaging Enables Surface Hydrophobicity Mapping. *Nature communications* **7,** 13544 (2016).
25. Song, K.-H., Dong, B., Sun, C., *et al.* Theoretical Analysis of Spectral Precision in Spectroscopic Single-Molecule Localization Microscopy. *Review of Scientific Instruments* **89,** 123703 (2018).
26. Song, K.-H., Zhang, Y., Brenner, B., *et al.* Symmetrically Dispersed Spectroscopic Single-Molecule Localization Microscopy. *Light: Science & Applications* **9,** 92 (2020).
27. Karslake, J., Donarski, E. D., Shelby, S. A., *et al.* SMAUG: Analyzing Single-Molecule Tracks with Nonparametric Bayesian Statistics. *bioRxiv,* 578567 (2019).
28. Vink, J., Brouns, S. J. & Hohlbein, J. Extracting Transition Rates in Single-Particle Tracking Using Analytical Diffusion Distribution Analysis. *bioRxiv* (2020).
29. Singh, D., Sternberg, S. H., Fei, J., *et al.* Real-Time Observation of DNA Recognition and Rejection by the RNA-Guided Endonuclease Cas9. *Nature Communications* **7,** 12778 (2016).
30. Globyte, V., Lee, S. H., Bae, T., *et al.* CRISPR/Cas9 Searches for a Protospacer Adjacent Motif by Lateral Diffusion. *The EMBO Journal,* e99466 (2018).
31. Sternberg, S. H., Redding, S., Jinek, M., *et al.* DNA Interrogation by the CRISPR RNA-Guided Endonuclease Cas9. *Nature* **507,** 62–67 (2014).
32. Knight, S. C., Xie, L., Deng, W., *et al.* Dynamics of CRISPR-Cas9 Genome Interrogation in Living Cells. *Science* **350,** 823–826 (2015).
33. Strohkendl, I., Saifuddin, F. A., Rybarski, J. R., *et al.* Kinetic Basis for DNA Target Specificity of CRISPR-Cas12a. *Molecular Cell* **71,** 816–824.e3 (2018).
34. Brouns, S. J., Jore, M. M., Lundgren, M., *et al.* Small CRISPR RNAs Guide Antiviral Defense in Prokaryotes. *Science* **321,** 960–964 (2008).
35. Wu, A. R., Neff, N. F., Kalisky, T., *et al.* Quantitative Assessment of Single-Cell RNA-Sequencing Methods. *Nature Methods* **11,** 41–46 (2014).
36. Camsund, D., Lawson, M. J., Larsson, J., *et al.* Time-Resolved Imaging-Based CRISPRi Screening. *Nature Methods,* 1–7 (2019).
37. Hermansson, A. .-M., Eriksson, E. & Jordansson, E. Effects of Potassium, Sodium and Calcium on the Microstructure and Rheological Behaviour of Kappa-Carrageenan Gels. *Carbohydrate Polymers* **16,** 297–320 (1991).
38. Hermansson, A.-M. Rheological and Microstructural Evidence for Transient States during Gelation of Kappa-Carrageenan in the Presence of Potassium. *Carbohydrate Polymers* **10,** 163–181 (1989).
39. Wang, Z., Tian, B., Boom, R., *et al.* Air Bubbles in Calcium Caseinate Fibrous Material Enhances Anisotropy. *Food Hydrocolloids* **87,** 497–505 (2019).

40. Krintiras, G. A., Diaz, J. G., Van der Goot, A. J., *et al.* On the Use of the Couette Cell Technology for Large Scale Production of Textured Soy-Based Meat Replacers. *Journal of Food Engineering* **169,** 205–213 (2016).
41. Grabowska, K. J., Zhu, S., Dekkers, B. L., *et al.* Shear-Induced Structuring as a Tool to Make Anisotropic Materials Using Soy Protein Concentrate. *Journal of Food Engineering* **188,** 77–86 (2016).
42. Dekkers, B. L., Nikiforidis, C. V. & van der Goot, A. J. Shear-Induced Fibrous Structure Formation from a Pectin/SPI Blend. *Innovative Food Science & Emerging Technologies* **36,** 193–200 (2016).
43. Tian, B., Wang, Z., van der Goot, A. J., *et al.* Air Bubbles in Fibrous Caseinate Gels Investigated by Neutron Refraction, X-Ray Tomography and Refractive Microscope. *Food Hydrocolloids* **83,** 287–295 (2018).
44. Hamann, S., Kiilgaard, J. F., Litman, T., *et al.* Measurement of Cell Volume Changes by Fluorescence Self-Quenching. *Journal of fluorescence* **12,** 139–145 (2002).
45. Feng, H., ten Hove, J. B., Zheng, T., *et al.* All-Aqueous Synthesis of Silica-Encapsulated Quantum Dots with Functional Shells. *European Journal of Inorganic Chemistry* **2017,** 5152–5157 (2017).
46. Zou, L., Gu, Z., Zhang, N., *et al.* Ultrafast Synthesis of Highly Luminescent Green-to near Infrared-Emitting CdTe Nanocrystals in Aqueous Phase. *Journal of Materials Chemistry* **18,** 2807–2815 (2008).
47. Jin, D., Xi, P., Wang, B., *et al.* Nanoparticles for Super-Resolution Microscopy and Single-Molecule Tracking. *Nature Methods,* 1 (2018).
48. Majorek, K. A., Porebski, P. J., Dayal, A., *et al.* Structural and Immunologic Characterization of Bovine, Horse, and Rabbit Serum Albumins. *Molecular Immunology* **52,** 174–182 (2012).
49. Subach, F. V., Patterson, G. H., Manley, S., *et al.* Photoactivatable mCherry for High-Resolution Two-Color Fluorescence Microscopy. *Nature methods* **6,** 153–159 (2009).
50. Jinek, M., Jiang, F., Taylor, D. W., *et al.* Structures of Cas9 Endonucleases Reveal RNA-Mediated Conformational Activation. *Science* **343,** 1247997–1247997 (2014).
51. Malacrida, L., Hedde, P. N., Ranjit, S., *et al.* Visualization of Barriers and Obstacles to Molecular Diffusion in Live Cells by Spatial Pair-Cross-Correlation in Two Dimensions. *Biomedical optics express* **9,** 303–321 (2018).
52. Di Rienzo, C., Cardarelli, F., Di Luca, M., *et al.* Diffusion Tensor Analysis by Two-Dimensional Pair Correlation of Fluorescence Fluctuations in Cells. *Biophysical Journal* **111,** 841–851 (2016).
53. Aristov, A., Lelandais, B., Rensen, E., *et al.* ZOLA-3D Allows Flexible 3D Localization Microscopy over an Adjustable Axial Range. *Nature Communications* **9,** 2409 (2018).
54. Xu, F., Ma, D., MacPherson, K. P., *et al.* Three-Dimensional Nanoscopy of Whole Cells and Tissues with in Situ Point Spread Function Retrieval. *Nature Methods* **17,** 531–540 (2020).
55. Gustavsson, A.-K., Petrov, P. N. & Moerner, W. E. Light Sheet Approaches for Improved Precision in 3D Localization-Based Super-Resolution Imaging in Mammalian Cells [Invited]. *Optics Express* **26,** 13122–13147 (2018).
56. Mikhaylova, M., Cloin, B. M., Finan, K., *et al.* Resolving Bundled Microtubules Using Anti-Tubulin Nanobodies. *Nature communications* **6,** 1–7 (2015).
57. Ries, J., Kaplan, C., Platonova, E., *et al.* A Simple, Versatile Method for GFP-Based Super-Resolution Microscopy via Nanobodies. *Nature methods* **9,** 582 (2012).
58. Klein, T., Löschberger, A., Proppert, S., *et al.* Live-Cell dSTORM with SNAP-Tag Fusion Proteins. *Nature methods* **8,** 7–9 (2011).
59. Anders, C., Niewoehner, O., Duerst, A., *et al.* Structural Basis of PAM-Dependent Target DNA Recognition by the Cas9 Endonuclease. *Nature* **513,** 569–573 (2014).

9

Summary

Macromolecular motion is dictated by diffusion on >100 nm spatial scales, while specific interactions occur on the nanoscale based on Van der Waals, electrostatic, and hydrophobic/hydrophilic forces. Characterising macromolecular motion reveals fundamental insights when relating diffusional behaviour to the function of a macromolecule of interest. To adequately investigate diffusion, a technique is required that ideally 1) minimises sample invasion and destruction; 2) minimises spatiotemporal averaging; 3) reaches molecular specificity; 4) is accessible by non-experts of the technique; and 5) has a spatiotemporal resolution of at least ∼5-100 nm and ∼10 ms, and preferably even better.

Single-particle tracking fluorescence microscopy (sptFM) is a derivative of single-molecule localization microscopy (SMLM) and offers the possibility to investigate macromolecular motion while upholding these criteria. SMLM is a super-resolution optical microscopy methodology characterised by localizing point spread functions (PSFs) originating from single fluorescent molecules, with an accuracy surpassing the diffraction limit of light by roughly one order of magnitude. SptFM tracks single molecules moving through time, describing their position with ∼5-40 nm spatial resolution and good temporal resolution. These motions can then be quantitatively characterised and used to reveal macromolecular behaviour.

While sptFM is a promising technique to observe macromolecular motion, it can be further improved. SptFM can then be applied to study macromolecular diffusion in life science and soft matter. This thesis aims to advance the field of sptFM by increasing the achievable spatiotemporal resolution, and by increasing the accessibility of the hardware and software in sptFM. Next, sptFM, enriched by these advances, is applied to study dynamic CRISPR-Cas9 behaviour in vivo, and to study the spatiotemporal heterogeneity of κ-carrageenan hydrogels.

In **Chapter 2** we develop a novel single-molecule localization algorithm called phasor-based single-molecule localization microscopy (pSMLM). pSMLM can localize individual PSFs with a rate of $3{\cdot}10^6$ localizations/s on a regular central processing unit (CPU), ∼3 orders of magnitude faster than other localization algorithms, while keeping localization accuracies in line with other state-of-the-art algorithms. A region of interest surrounding a PSF is converted to two phasors by calculating the first Fourier coefficients in both the x- and y-dimension. The angles of these phasors when plotted in a phasor plot are representative of the emitter's lateral position. The ratio of the phasors' magnitudes describes the elongation of the PSF, which is used to obtain the emitter's axial position when employing astigmatism lenses. pSMLM can be used both as a stand-alone localization algorithm, as well as a starting point for iterative algorithms, and is integrated in the ThunderSTORM software for ImageJ and FIJI.

The pSMLM algorithm is expanded in **Chapter 3**, and the engineered PSFs known as double-helix (DH), saddle-point (SP), and tetra-pod (TP) are accurately localized in three dimensions via adaptations to the original pSMLM. For the DH PSF, pSMLM first identifies the two individual lobes with good accuracy while employing small regions of interest to prevent localization artefacts. Then, the two lobes are connected, and their relative rotation and distance are measures for the emitter's z-position. For the analysis of SP and TP PSFs, the distance between symmetrical lobes of a SP or TP PSF is extracted by deconvolution in phasor-space via an approach entitled circular-tangent pSMLM (ct-pSMLM). These novel pSMLM implementations are compared to the existing state-of-the-art software SMAP, and reveals that pSMLM delivers similar precision

and recall rates at signal-to-noise ratios typical for organic fluorophores. Importantly, the pSMLM software package increases the localization rate by a factor of ∼2-4, and achieves rates of up to 15 kHz (DH) or 250 kHz (SP/TP). pSMLM and its adaptations are implemented in an existing software package (SMALL-LABS), suitable for single-particle imaging and tracking.

While SMLM normally ignores spectral characteristics, the addition of spectral information (creating spectral SMLM or sSMLM) provides opportunities for fluorophore multiplexing and the characterisation of local chemical environments. A simple and minimal-dispersion method to obtain spectral as well as spatial information of single emitters is presented in **Chapter 4**. Existing implementations of sSMLM fall short in accessibility, as complex and expensive modifications were required to microscopes; or in signal-to-noise ratios, as the spectral information was spread out over 20-30 camera pixels. We placed a low-dispersion transmission grating as close to the camera as possible, leading to an implementation that is both low-cost (∼ €100) and that has a spectral dispersion of just 0.4 nm/pixel, orders of magnitude lower than typical sSMLM implementations. This results in a maximised signal-to-noise ratio and achievable emitter density. The obtained spatial and spectral profiles can both be analysed by typical single-molecule localization algorithms with high accuracy. This low-dispersion sSMLM is successfully applied in dSTORM and DNA-PAINT, showcasing spectral discrimination of fluorophores with just 10 nm spectral difference, and in single-molecule FRET, showcasing 0-to-15% FRET changes.

The applicability of single-particle tracking in the model lactic acid bacterium *Lactococcus lactis* is explored in **Chapter 5**. First, we qualitatively investigate the suitability of various non-photoactivatable and photoactivatable fluorophores in *L. lactis*. This is continued by creation a chimera of PAmCherry2, a red-emitting photoactivatable fluorescent protein, with dCas9, a dead variant of the *Streptococcus pyogenes* CRISPR-Cas9 used in genomic engineering procedures. We confirm the correct photoactivation of PAmCherry2 in combination with retained correct activity of dCas9. Last, a data analysis procedure for single-particle tracking of dCas9-PAmCherry2 is proposed and used to obtain information on single dCas9 proteins. This shows that dCas9 exists in three states in the absence of DNA targets: fully immobile, a transient state attributed to PAM screening, and fully mobile.

Single-particle tracking of dCas9-PAmCherry2 in *L. lactis* is continued in **Chapter 6**. The experimental data is acquired on a fully open-source SMLM microscope termed the miCube. The miCube combines high achievable data quality with low associated hardware costs, easy installation, and high modularity. Full details on all home-built components, including technical drawings and 3D models, and the commercial components are provided, allowing for reproduction of the miCube or derivative instruments.

The expected dynamic behaviour of dCas9 in the absence of DNA targets consists of a PAM-screening (slow diffusion) state, and a free (fast diffusing) state. Because the transitions between these states are expected to be on the same timescale as the individual frames (<30 ms), a novel analysis procedure termed Monte-Carlo Diffusion Distribution Analysis (MC-DDA) is created. MC-DDA is used to fit experimental diffusion data with a model describing protein motion with multiple diffusive states in confined environments, and can accurately predict observed diffusion of molecules experiencing fast state-changes.

Using the miCube and MC-DDA, we determine that dCas9 is screening PAMs ∼40% of the time, averaging 17 ± 4 ms per binding event, after which it remains 25 ± 8 ms in a diffusing state before it re-starts PAM-screening. Using heterogeneous dCas9 expression, we determine that ∼100 DNA target sites are present in individual cells. Moreover, we show that dCas9 is removed from its target on average every 100 seconds, possibly due to interference with polymerases, and in this state interferes with plasmid replication. The determined dynamic state-changing rates are used to predict the DNA target cleavage probability in *L. lactis* as a function of incubation time and cellular dCas9 copy number, inferring that a single Cas9 protein finds a single DNA target in ∼4 h.

In **Chapter 7**, the ability of sptFM to quantitatively assess spatiotemporal heterogeneity of the hydrogel κ-carrageenan is investigated. The tracking of infused fluorescent nanoprobes in κ-carrageenan reveals the existence of ∼1 µm dense network regions in a coarse bulk network. By quantifying the diffusion of the probes as a function of polymer concentration, we further determine that the individual fibres have a diameter of 3.2 ± 0.3 nm. Last, the use of sptFM reveals that the dense network regions are mobile on the seconds-to-minutes scale.

The findings presented in the previous chapters are discussed in **Chapter 8**, and their impact on the future development of sptFM is evaluated. Moreover, the challenges of applying sptFM in complex soft matter such as fibrous protein-based meat analogues are described and discussed.

Samenvatting

De beweging van grote moleculen (of macromoleculen) wordt bepaald door diffusie op groottes van >100 nm, terwijl specifieke interacties op de nanoschaal plaatsvinden op basis van Van der Waals, elektrostatische, en hydrofobische/hydrofiele krachten. Het karakteriseren van macromoleculaire beweging onthult fundamentele inzichten wanneer diffusiegedrag gerelateerd wordt aan de functie van een macromolecuul. Om diffusie adequaat te onderzoeken, is een techniek nodig die idealiter 1) het monster minimaal schendt of vernietigt; 2) minimale tijdsruimtelijke middeling teweegbrengt; 3) moleculaire specificiteit bereikt; 4) toegankelijk is voor non-experts van de techniek; en 5) een tijdsruimtelijke resolutie heeft van minstens ∼5-100 nm en ∼10 ms, maar idealiter zelfs beter dan dit.

Enkel-molecuul-volgen fluorescentie-microscopie (emvFM) is een techniek afgeleid van enkel-molecuul lokalisatie-microscopie (EMLM), en biedt de mogelijkheid om macromoleculaire beweging te onderzoeken met inachtneming van deze criteria. EMLM is een super-resolutie optische microscooptechniek waarbij puntspreidfuncties (PSFs), welke voortkomen vanuit enkele fluorescente moleculen, gelokaliseerd worden met een nauwkeurigheid die meer dan 10 keer beter is dan de diffractielimiet van licht. EmvFM volgt dan individuele moleculen door de tijd heen, waarmee hun positie wordt beschreven met ∼5-40 nm spatiële resolutie en goede temporele resolutie. Deze beweging kan daarna kwantitatief gekarakteriseerd worden om macromoleculair gedrag te onthullen.

Hoewel emvFM een veelbelovende techniek is om macromoleculaire beweging te observeren, kan het verder verbeterd worden. EmvFM kan daarna toegepast worden om macromoleculaire diffusie te bestuderen in de levenswetenschappen en in zachte materialen. Dit proefschrift heeft het doel om het veld van emvFM te bevorderen door de haalbare tijdsruimtelijke resolutie te verhogen, en door de toegankelijkheid van de hardware en software in emvFM te verhogen. Daarna wordt emvFM, verrijkt met deze verbeteringen, toegepast om dynamisch CRISPR-Cas9 gedrag te bestuderen in vivo, en om de tijdsruimtelijke heterogeniteit van κ-carrageenan hydrogellen te bestuderen.

In **Hoofdstuk 2** ontwikkelen we een enkel-molecuul lokalisatie-algoritme genaamd phasor-gebaseerde enkel-molecuul lokalisatie-microscopie (pEMLM). pEMLM kan individuele PSFs lokaliseren met een snelheid van $3{\cdot}10^6$ lokalisaties/seconde op een normale computerprocessor (centrale verwerkingseenheid, of CPU in het Engels), ∼3 ordes van grootte sneller dan andere lokalisatie-algoritmes, terwijl de lokalisatienauwkeurigheid niet afwijkt van andere geavanceerde algoritmes. Een gebied van interesse om de PSF heen wordt omgezet in twee phasors door de eerste Fourier coëfficiënten in de x- en y-richting te berekenen. De hoeken die deze phasors hebben als ze worden weergegeven in een phasordiagram zijn representatief voor de laterale positie van de PSF. De ratio van de grootte van de phasors beschrijft de mate van ellipticiteit van de PSF, die gebruikt kan worden om de axiale positie van het molecuul te bepalen als astigmatische lenzen worden gebruikt in de microscoop. pEMLM kan zowel gebruikt worden als een alleenstaand lokalisatie-algoritme alsmede als een startpunt voor iteratieve algoritmes, en is geïntegreerd in de ThunderSTORM software voor ImageJ en FIJI.

Het pEMLM algoritme is uitgebreid in **Hoofdstuk 3**, waarmee de ontworpen PSFs bekend als dubbele-helix (DH), zadel-punt (ZP), en tetra-pod (TP) nauwkeurig in drie dimensies gelokaliseerd worden via bewerkingen van de originele pEMLM. Voor de DH PSF indentificeert

pEMLM eerst de twee afzonderlijke lobben met goede nauwkeurigheid, terwijl kleine gebieden van interesse worden gebruikt om lokalisatie-artefacten te voorkomen. Daarna worden de twee lobben verbonden, en hun relatieve rotatie en afstand zijn maten voor de z-positie van het molecuul. Voor de analyse van ZP en TP PSFs, wordt de afstand tussen symmetrische lobben van een ZP of TP PSF berekend via deconvolutie in phasor-ruimte met een aanpak genaamd circulaire-raaklijn pEMLM (cr-pEMLM). Deze nieuwe pEMLM verwezenlijkingen worden vergeleken met de bestaande geavanceerde software SMAP, wat laat zien dat pEMLM vergelijkbare nauwkeurigheid heeft op signaal-ruis-verhoudingen typerend voor organische fluoroforen. Belangrijk is dat het pEMLM softwarepakket de lokalisatiesnelheid met een factor van ∼2-4 verhoogd, waarmee snelheden van 15 kHz (DH) of 250 kHz (ZP/TP) worden bereikt. pEMLM en de aanpassingen zijn geïntegreerd in een bestaand softwarepakket (SMALL-LABS) geschikt voor enkele-molecuul experimenten.

Hoewel EMLM normaal gesproken spectrale eigenschappen negeert, kan de toevoeging van spectrale informatie (spectrale EMLM of sEMLM) mogelijkheden creëren om meerdere fluoroforen tegelijkertijd te identificeren, of om lokale chemische omgevingen te karakteriseren. Een eenvoudige en minimale-dispersie methode om zowel spectrale als spatiële informatie van enkele moleculen te verkrijgen is beschreven in **Hoofdstuk 4**. Bestaande implementaties van sEMLM schieten tekort in toegankelijkheid, omdat complexe en dure aanpassingen nodig waren aan microscopen; of in signaal-ruis-verhoudingen, omdat de spectrale informatie uitgesmeerd werd over 20-30 camera pixels. Wij hebben een lage-dispersie transmissie diffractierooster zo dichtbij de camera als mogelijk geplaatst, wat leidt tot een uitvoering die zowel goedkoop is (∼ €100) en een spectrale dispersie van slechts 0.4 nm/pixel heeft, ordes van grootte kleiner dan bestaande sEMLM implementaties. Hierdoor wordt de signaal-ruis-verhouding en bereikbare molecuul-dichtheid gemaximaliseerd. De verkregen spatiële en spectrale profielen kunnen beide geanalyseerd worden door normale enkel-molecuuls lokalisatie-algoritmes met goede nauwkeurigheid. Deze lage-dispersie sEMLM techniek is toegepast in dSTORM en DNA-PAINT, waarmee fluoroforen met slechts 10 nm spectrale verschillen onderscheid kunnen worden, en in enkel-molecuuls FRET, welke veranderingen tussen 0 en 15% FRET laat zien.

De toepasbaarheid van enkel-molecuul-volgen in de melkzuur-modelbacterie *Lactococcus lactis* is onderzocht in **Hoofdstuk 5**. Ten eerste hebben wij de geschiktheid van verschillende non-foto-activeerbare en foto-activeerbare fluoroforen onderzocht in *L. lactis*. Daarna is een chimera gemaakt van PAmCherry2, een rood foto-activeerbaar fluorescent eiwit, met dCas9, een 'dode' variant van *Streptococcus pyogenes* CRISPR-Cas9 welke gebruikt wordt in DNA manipulatie. We bevestigen de correcte foto-activatie van PAmCherry2 in combinatie met behoudde activiteit van dCas9. Tenslotte wordt een data-analyse procedure voor enkel-molecuul-volgen van dCas9-PAmCherry2 voorgesteld, welke wordt gebruikt om informatie over enkele dCas9 eiwitten te verkrijgen. Dit laat zien dat dCas9 in drie staten bestaat als er geen DNA-doelen beschikbaar zijn: compleet immobiel, een kortstondige staat toegeschreven aan PAM-exploratie, en compleet mobiel.

Enkel-molecuul-volgen van dCas9-PAmCherry2 in *L. lactis* wordt voortgezet in **Hoofdstuk 6**. De experimentele data is verworven op een compleet open-source EMLM microscoop genaamd miCube. De miCube combineert goede data-kwaliteit met lage hardware-kosten, eenvoudige installatie, en hoge modulariteit. Volledige details van alle handgemaakte onderdelen, waaronder technische tekeningen en 3D modellen, en de commerciële onderdelen zijn verstrekt, zodat reproductie van de miCube of afgeleide microscopen mogelijk is.

Het verwachte dynamische gedrag van dCas9 als er geen DNA-doelen aanwezig zijn bestaat uit een PAM-exploratie (langzame diffusie) staat, en een vrije (snelle diffusie) staat. Omdat de transitie tussen deze staten waarschijnlijk op dezelfde tijdsschaal als de individuele frames van de camera (<30 ms) plaatsvinden, hebben we een nieuwe analysemethode genaamd Monte-Carlo Diffusie Distributie Analyse (MC-DDA) gemaakt. MC-DDA is gebruikt om experimentele diffusiedata passend te maken aan een model dat eiwitbeweging met meerdere diffusie-staten in een begrensde omgeving beschrijft, en kan nauwkeurig de waargenomen diffusie van moleculen die snelle staatsveranderingen ondergaan beschrijven.

Gebruik makend van de miCube en MC-DDA, hebben we vastgesteld dat dCas9 PAMs exploreert voor ∼40% van de tijd, waarbij iedere bindings-gebeurtenis gemiddeld 17 ± 4 ms duurt, waarna dCas9 25 ± 8 ms vrij diffundeert voordat het opnieuw PAMs gaat exploreren. Via heterogene productie van dCas9, bepalen we dat ∼100 DNA-doelen beschikbaar zijn in individuele cellen. Daarnaast laten we zien dat dCas9 gemiddeld elke 100 seconden van zijn doel wordt verwijderd, mogelijk via interferentie met DNA polymerases, en dat dCas9 in deze staat plasmidereplicatie belemmerd. Deze bepaalde dynamische staats-veranderingssnelheden zijn gebruikt om de kans op splijting van de DNA doelen in *L. lactis* als een functie van de incubatietijd en cellulaire dCas9 kopieën te bepalen, waaruit we ontdekken dat een enkel Cas9 eiwit een enkel DNA-doel in ∼4 uur vind.

In **Hoofdstuk 7** onderzoeken we de mogelijkheid van emvFM om kwantitatief de tijdsruimtelijke heterogeniteit van de hydrogel κ-carrageenan te bepalen. Het volgen van fluorescente nanosondes in κ-carrageenan onthult het bestaan van ∼1 µm dichte netwerkgebieden in een open bulknetwerk. Via het kwantificeren van de diffusie van de nanosondes als een functie van de polymeerconcentratie kunnen we verder bepalen dat de individuele netwerkstrengen een diameter van 3.2 ± 0.3 nm hebben. Tenslotte onthult emvFM dat de dichte netwerkgebieden mobiel zijn op een seconden-tot-minuten tijdsschaal.

De bevindingen van de eerdere hoofdstukken worden bediscusieerd in **Hoofdstuk 8**, en hun impact op de toekomstige ontwikkelingen van emvFM wordt geëvalueerd. Daarnaast worden de uitdagingen om emvFM toe te passen in complexe zachte materialen zoals vezelachtige plantaardige vleesvervangers beschreven en bediscusieerd.

10

Acknowledgements, about the author

Acknowledgements

Throughout my PhD, I have been lucky to work together with many people from many different disciplines, which all helped and motivated me to bring this thesis to completion. Without their effort, time, and kindness, this journey would not have been the same.

First and foremost, **Johannes Hohlbein**, thank you for the opportunity of doing my PhD thesis in your group, and for being my mentor these four years. Even though I was not sure about accepting this position, your promises of scientific freedom (and their fulfilment) convinced me, and looking back on it, I wouldn't have wanted it any other way. I have learned tremendously much under your wing, and I appreciate that you introduced me to the many facets of working in- and outside of academia. Thank you for your open-door policy and for your sincere interest in whatever wild idea I came to you with, and for trusting me to follow exciting research well outside the original scope of the project.

John van Duynhoven en **Aldrik Velders**, bedankt voor jullie moeite en steun tijdens het project. Jullie hebben mij beiden verschillende inzichten en waarden meegegeven in academia en daarbuiten waar ik veel van heb geleerd. John, bedankt voor het vertrouwen in mij om een PhD project aan te gaan na mijn stage bij jou. Aldrik, bedankt voor de wetenschappelijke vrijheid tijdens mijn PhD; ik stel jouw rotsvaste normen en waarden erg op prijs.

Many of my experimental chapters are the result of very fruitful collaborations inside and outside Wageningen. These collaborations have not only led to great scientific work, but also allowed to me meet wonderful people. **Atze Jan van der Goot**, bedankt voor de moeite die je hebt gestoken in het originele project, en voor jouw inzichten in de complexe wereld van voedselstructuur. **Birgit**, **Fiona**, and **Miek**, thank you for your assistance and insights in the protein-based meat analogues.

Bernd Rieger, thanks for your efforts in computational microscopy and for your advanced insights in our manuscripts and their publishing. **Lorenzo Albertazzi**, **Manos**, and **Roger**, thank you for the brief, but surely continuing, collaboration in the nanoparticle development. **Stan Brouns**, the collaborations with you and your group led to amazing work. Thank you for sharing your expertise with me. In the same breath, I have to acknowledge **Jochem**. Ik heb oprecht genoten van het onderzoek dat wij samen deden (en van het combineerde microscoop-werk en Tour-kijken), en ik kon er altijd op vertrouwen om diepgaande discussies met jou te voeren over de kleinste, en daarom belangrijkste, details in onze grote projecten. **Marnix**, bedankt voor de samenwerkingen in het begin van mijn PhD.

Michiel Kleerebezem en **Peter van Baarlen**, bedankt voor de mogelijkheid tot samenwerking in onze projecten, jullie zijn erg waardevol geweest in de biologische protocollen en in het interpreteren van de resultaten. **Simon**, ik heb erg genoten van onze samenwerking. Jij toonde veel enthousiasme in ons microscoopwerk, en ik hoop dat mijn enthousiasme over wat jij in het wet lab hebt kunnen bereiken niet verloren is gegaan. Je hebt me verrijkt met jouw biologische inzichten en diepgaande kennis, wat ik alleen maar kan hopen te evenaren in mijn toekomst. **Sam**, het zou jou te kort doen om je alleen als student te refereren. Je hebt ontzettend veel bijgedragen aan hele grote projecten, terwijl je jouw kennis in erg korte tijd hebt opgedaan. Bedankt voor jouw enthousiasme in de wetenschap in het algemeen, voor de moeilijke vragen die je stelde tijdens jouw thesis en daarna, en voor de ietwat esoterische urenlange filosofische discussies.

Next, I want to thank all colleagues I've had the pleasure of knowing during my four years. You've all helped in making me feel welcome and at ease, and contributed to a great working environment!

Mattia, I enjoyed spending four years with you in the same room and having all kinds of discussions on (bio-)physics, mathematics, but mostly on Dutch names for vegetables and Netflix shows. Thank you for introducing me to your overwhelming culture and family. **Sander**, wat leuk dat je zo lang geleden voor een thesis bij mij hebt gekozen. Ik ben fan van jouw no-nonsense aanpak in de wetenschap en het gemak waarmee wij gesprekken kunnen voeren. Thank you both for being my paranymphs.

Carel, **Suyeon**, **Abbas**, and **Mattia**, it has been fun to discuss our work with each other, and I hope you can forgive me for overwhelming you with information during the meetings. Thank you for taking your time to help me, and for the fun dinners, drinks, and conference-adventures we shared. **Julia**, als mijn enige 'volledige' collega kon je me steunen als ik weer eens te veel meetings had. Ik heb er erg veel vertrouwen in dat jij succesvol gaat worden in jouw academische carrière. **Tatiana**, your positivity and high spirits always rub off on others, me included. I won't forget your borrel-organisation skills or your dark side of the office! **Arjen**, bedankt voor je geduldige uitleg over het uitlijnen en schoonmaken van, voor mijn gevoel, elke lens die ik ooit vast heb gehad. **John Philippi**, bedankt voor je geduld met al mijn vreemde computer-gerelateerde vragen en zorgen. Je bent ontzettend goed in het maken en repareren van alles met een kabel, en zonder jouw inzet was veel van mijn werk nooit van de grond gekomen. **Herbert van Amerongen**, bedankt voor de ruimte op jouw groep, voor de wetenschappelijke vrijheid, en voor het faciliteren van een fijne omgeving. **Cor**, **Rob**, **Emilie**, **Frank**, ik vond het begeleiden van (werk)colleges ineens een stuk leuker toen ik er achter kwam dat ik lekker met jullie kon praten terwijl de studenten druk bezig waren. Bedankt dat jullie me hebben geholpen in het lesgeven en in het uitleggen van fundamentele natuurkunde als mijn kennis tekort schoot. Frank, ik kan nog altijd erg genieten van jouw willekeurige uitingen en opvolgende discussies over alles gerelateerd aan wis- en natuurkunde, vooral gebaseerd op YouTube-filmpjes. **Yashar**, **Donny**, **Ahmad**, **Esterii**, **Klaudia**, **Morwarid**, **Ludovico**, **Raquel**, **Wouter**, **Henk**, **Camilla**, **Netty**, and **Brenda**, thanks for contributing to the great atmosphere in the lively BIP group, and for all kinds of great discussions, borrels, and coffees!

Of course, my 'second life' at BioNT might not have consisted of as much lab-time as at Biophysics, but it made up for that with an increase in alcohol consumption. **Aldrik**, het aandringen op een borrel elke vrijdagmiddag zorgt zeker voor een goede sfeer op je groep. **Anton**, bedankt voor je hulp en geduld met mijn introductie in inorganische chemie. **Stan**, bedankt voor het eindeloze bierassortiment en voor jouw hulp met menig apparaat op het lab. **Vittorio**, always nice to discuss microscopes and twitter with you. **Jan Bart**, **Camilla**, **Laura**, **Rebecca**, **Gerben**, **Banu**, **Fatemeh**, **Ashkan**, and **Yurdanur**, thank you for the good times during borrels, dinners, discussions and meetings.

Ik heb het geluk gehad om ontzettend veel briljante en gezellige studenten te mogen begeleiden tijdens mijn PhD. Ze hebben mij allemaal geholpen in mijn projecten en daarbuiten. **Sam** en **Sander**, bedankt voor jullie grote inzet in onze projecten. **Vincent** en **Charlotte**, bedankt voor het bouwen van bruggen tussen biofysica en voedselstructuur. **Jan**, **George**, **Ben**, **Ezra**, de

resultaten die we samen hebben weten te bereiken op de grensvlakken van meerdere disciplines is noemingswaardig. Bedankt voor jullie inzet. **Adreas**, **Hans**, and **Koen**, thanks for your efforts during your time with me. Ik hoop dat jullie allemaal, naast wat geleerd te hebben, ook hebben genoten van jullie thesis of project - ik in ieder geval wel.

Lieve **pap en mam**, bedankt voor alles dat jullie hebben bijgedragen in mijn leven en jullie onvoorwaardelijke steun in mijn studies en academische carrière. Ik kan het erg waarderen dat jullie altijd proberen te begrijpen wat ik doe en heb gedaan. **Joyce**, **Max** (en Gijs), ik vind het erg fijn dat jullie mij met beide benen op de grond neerzetten met jullie nuchterheid. **Roelant**, ik vind het fijn om onze verwachtingen van een academische carrière op een nuchtere manier te kunnen bespreken. Lieve **Bianca**, bedankt voor jouw ongelofelijke steun. Bedankt voor de vele gesprekken, koffies, en grappen. Lieve **familie Kampers**, bedankt dat jullie me zo goed hebben opgenomen in jullie gezin. Ik hoop om nog heel veel onbijtjes, diners, en vakanties mee te gaan maken.

Lieve **Linde**, bedankt dat je jouw leven met mij wilt delen. Jij bent ongetwijfeld het belangrijkste in mijn leven. Bedankt dat je nog altijd luistert naar mijn chaotische verhalen over nieuwe artikelen, hulp biedt bij moeilijke situaties, en voor jouw onvoorwaardelijke steun in alles wat ik doe. Alleen met jou wil ik toekomstige avonturen aangaan.

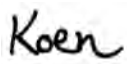

List of publications

This thesis

Koen J.A. Martens, Arjen N. Bader, Sander Baas, Bernd Rieger, and Johannes Hohlbein. "Phasor based single-molecule localization microscopy in 3D (pSMLM-3D): an algorithm for MHz localization rates using standard CPUs" *The Journal of chemical physics* **148**, no. 12 (2018)

Sam P.B. van Beljouw*, Simon van der Els*, **Koen J.A. Martens***, Michiel Kleerebezem, Peter A. Bron, and Johannes Hohlbein. "Evaluating single-particle tracking by photo-activation localization microscopy (sptPALM) in *Lactococcus lactis*" *Physical biology* **16**, no. 3 (2019)

Koen J.A. Martens*, Sam P.B. van Beljouw*, S. van der Els, Jochem N.A. Vink, Sander Baas, George A. Vogelaar, Stan J. J. Brouns, Peter van Baarlen, Michiel Kleerebezem, and Johannes Hohlbein. "Visualisation of dCas9 Target Search in vivo using an open-microscopy framework" *Nature Communications* **3552**, no. 10 (2019)

Koen J.A. Martens, John van Duynhoven, and Johannes Hohlbein. "Spatiotemporal Heterogeneity of κ-Carrageenan Gels Investigated via Single-Particle-Tracking Fluorescence Microscopy" *Langmuir* **36** no. 20 (2020)

Koen J.A. Martens, Abbas Jabermoradi, Suyeon Yang, and Johannes Hohlbein. "Integrating engineered point spread functions into the phasor-based single-molecule localization microscopy framework" *Methods* (2020)

Other publications

Koen J.A. Martens, Gerard van Dalen, Patricia C.M. Heussen, Mihai A. Voda, Tatiana Nikolaeva, and John P.M. van Duynhoven. "Quantitative structural analysis of fat crystal networks by means of Raman confocal imaging" *Journal of the American Oil Chemists' Society* **95** no.3 (2018)

Tatiana Nikolaeva, Ruud den Adel, Ruud van der Sman, **Koen J.A. Martens**, Henk Van As, Mihai A. Voda, and John P.M. van Duynhoven. "Manipulation of recrystallization and network formation of oil-dispersed micronized fat crystals" *Langmuir* **35** no.6 (2019)

Jochem N.A. Vink, **Koen J.A. Martens**, Marnix Vlot, Rebecca E. McKenzie, Cristóbal Almendros, Boris Estrada Bonilla, Daan J.W. Brocken, Johannes Hohlbein, and Stan J.J. Brouns. "Direct visualization of native CRISPR target search in live bacteria reveals Cascade DNA surveillance mechanism" *Molecular Cell* **77** no. 1 (2020)

* indicates shared authorship.

Completed training activities

Discipline specific activities	Organizing institute(s)	Year
DutchBiophysics	FOM	2016
DutchBiophysics	FOM	2017
DutchBiophysics	FOM	2018
Focus on Microscopy 2017	Bordeaux University, Amsterdam University	2017
TI-COAST: Forum for Analytical Science and Technology	COAST	2017
TI-COAST: Forum for Analytical Science and Technology	COAST	2018
SMLMs Berlin	Max-Planck Society	2018
SMLMs Delft	TU Delft	2019
PicoQuant Single Molecule Workshop	PicoQuant	2019
Dutch Photonics Event	Photonics NL	2019
General courses		
Competence Assessment	WGS	2017
VLAG PhD week	VLAG	2017
Scientific Writing	WGS	2018
Mobilising your - scientific - network	WGS	2019
Writing grant proposals	Wageningen in'to languages	2019
Optionals		
Preparation of research proposal	BIP	2016
Weekly group meetings	BIP	2016-2020
Weekly group meetings	BNT	2016-2020
BNT-51306	BNT	2016

About the author

Koen Jacobus Adrianus Martens was born on March 27th 1993 in Breda, the Netherlands. After graduating high school (Mencia de Mendoza-lyceum, Breda), he started his studies in Biotechnology at Wageningen University, finishing with a thesis at the Laboratories of Organic Chemistry and Microbiology entitled 'The isolation, immobilization and characterization of hydroxy-acid oxidase on platinum surfaces'. He directly continued his studies with a MSc in Biotechnology, with a specialization on cellular and molecular processes. In 2011, he finished his MSc thesis at the Laboratory of Biochemistry entitled 'Evaluating a FRET calcium sensor in Complex Core Micelles', and continued with a 6-month internship at Unilever Research and Development Vlaardingen, focusing on quantitative imaging of fat structures using confocal Raman microscopy. In 2016, he started as a PhD candidate in the Laboratories of Biophysics and BioNanoTechnology at Wageningen University & Research, the results of which are presented in this thesis.

Colophon

The research described in this thesis was performed at the Laboratory of Biophysics, Wageningen University & Research, The Netherlands, and at the Laboratory of BioNanoTechnology, Wageningen University & Research, The Netherlands, and was financially supported by VLAG (Advanced studies in Food Technology, Agrobiotechnology, Nutrition and Health Sciences), The Netherlands.

Financial support from the Laboratory of Biophysics, Wageningen University, for printing this thesis is gratefully acknowledged.

Cover designed by the author.

Printed by: ProefschriftMaken